UNIVERSITY OF CALIFORNIA
SANTA CRUZ

THE LINK BETWEEN GALAXY STRUCTURE AND STAR FORMATION ACROSS COSMIC TIME

A dissertation submitted in partial satisfaction of the
requirements for the degree of

DOCTOR OF PHILOSOPHY

in

ASTRONOMY AND ASTROPHYSICS

by

Jerome Joseph Fang

June 2015

The Dissertation of Jerome Joseph Fang
is approved:

Professor Sandra M. Faber, Chair

Professor David C. Koo

Professor Joel R. Primack

Dean Tyrus Miller
Vice Provost and Dean of Graduate Studies

Table of Contents

List of Figures **vi**

List of Tables **viii**

Abstract **ix**

Dedication **xi**

Acknowledgments **xii**

1 Introduction **1**
1.1 Structural Imprints of Quenching 3
1.2 Pathways through the Green Valley 6
1.3 The Diversity of Star-forming Galaxies 7

2 A Link between Star Formation Quenching and Inner Galaxy Structure **10**
2.1 Introduction 10
2.2 Data and Sample Selection 19
2.2.1 Photometry and Structural Parameters 19
2.2.2 Sample Selection 20
2.2.3 M/L Relation and Mass Surface Density Profiles 26
2.3 The Relation between Inner Surface Mass Density and Color . . . 29
2.4 Surface Brightness and Mass Density Profiles 39
2.4.1 Median Surface Brightness and Mass Density Profiles as a Function of Color 39
2.4.2 Light-weighted versus Mass-weighted Radii 45
2.5 Comparing Inner Surface Mass Density with Velocity Dispersion . 50
2.5.1 The Relation between Velocity Dispersion and Stellar Mass 50

2.5.2 The Relation between Σ_1 and Velocity Dispersion 51
2.5.3 A New Black Hole Mass Scaling Relation? 59
2.6 Discussion 60
2.6.1 Evolving Galaxies or Evolving Thresholds? 60
2.6.2 The Utility of Σ_1 and σ_1 as Quenching Predictors 63
2.6.3 On the Verticality and Scatter of Evolutionary Tracks . . . 67
2.6.4 Constraints on Rejuvenated SF 70
2.6.5 Is Quenching a Two-Step Process? 72
2.7 Summary and Conclusions 75
2.8 Appendix: Seeing Effects on Σ_1 Measurements 78

3 Extended Star Formation in $z \sim 0.1$ Green Valley Early-type Galaxies 82
3.1 Introduction 82
3.2 Data and Reduction 89
3.2.1 SDSS and *GALEX* Data 90
3.2.2 Aperture Photometry 96
3.3 Results 99
3.3.1 UV-Optical Color Profiles 99
3.3.2 Stellar Population Analysis of the ESF-ETGs 107
3.3.3 Stacked SDSS Spectra 113
3.3.4 The SR2010 ESF-ETGs in Context 117
3.3.4.1 SR2010's Selection Criteria 118
3.3.4.2 Searching for Additional ESF-ETGs in the Green Valley 121
3.3.4.3 The Contribution of ESF-ETGs to the GV 130
3.3.4.4 Constraining the Timescale of Recent SF in the ESF-ETGs 133
3.4 How Do ESF-ETGs Move through the Green Valley? 136
3.5 Summary and Conclusions 145

4 The Shifting Demographic Landscape of Star-forming Galaxies since $z = 2.5$ 149
4.1 Introduction 149
4.2 Data and Sample Selection 154
4.2.1 Multi-wavelength Photometric Catalogs 155
4.2.2 Redshifts and Rest-frame Photometry 155
4.2.3 Stellar Masses and Dust Attenuation 156
4.2.4 Structural Parameters 157
4.2.5 Mid- and Far-infrared Data 158
4.2.6 Star-formation Rates 158

4.2.7 Sample Selection 159
4.2.8 Residuals from the SSFR-Mass and Mass-Size Relations . 160
4.3 Systematic Trends in the UVJ Diagram 166
4.3.1 A (Universal) Relation between $(U-V)'$ Color and SSFR 169
4.3.2 Spectral Energy Distributions in UVJ Bins 176
4.3.3 Dust-corrected UVJ Diagram 181
4.3.4 "Fading" Galaxies 185
4.4 Correlations between Dust Attenuation and Galaxy Structure . . 188
4.4.1 Effects of Dust and Inclination in the UVJ Diagram . . . 188
4.4.2 Reddened Star-forming Galaxies 194
4.5 The Observed Shape Distributions of Star-forming Galaxies . . . 199
4.6 A Lack of Correlation between SSFR and Galaxy Structure 212
4.7 Discussion 218
4.7.1 The Impact of Galaxy Structure on Star Formation and Dust Attenuation 218
4.7.2 Connecting Galaxies to Dark Matter Halos 222
4.8 Summary and Conclusions 226
4.9 Appendix: On the Validity of Dust-corrected, UV-based SSFR . . 229
4.9.1 Systematic Biases in $L_{\rm IR}$ Estimates 230
4.9.2 Comparing $\rm SSFR_{UV,corr}$ and $\rm SSFR_{UV+IR}$ 237

Bibliography **242**

List of Figures

1.1 Schematic color-stellar mass diagram 4

2.1 NUV$-r$ color-stellar mass diagram 22
2.2 Stellar mass vs. redshift 25
2.3 M/L_i vs. $g-i$ color 27
2.4 Σ_1 vs. stellar mass for galaxies with $0.005 < z < 0.075$ 31
2.5 Σ_1 vs. stellar mass divided by color 33
2.6 NUV$-r$ vs. Σ_1 in stellar mass bins 34
2.7 Representative surface brightness and mass profiles 41
2.8 Median surface brightness and mass profiles 43
2.9 Montage of SDSS postage stamps 46
2.10 Bias in radii measurements for blue and red galaxies 48
2.11 Scaled velocity dispersion vs. stellar mass 52
2.12 NUV$-r$ vs. σ_1 in stellar mass bins 54
2.13 Σ_1 vs. σ_1 for galaxies with $0.005 < z < 0.075$ 56
2.14 Σ_1 vs. σ_1 in stellar mass bins 58
2.15 NUV$-r$ vs. Σ_1 in tilted mass bins 66
2.16 Angular size corresponding to 1 kpc vs. redshift 79
2.17 Σ_1 vs. redshift for blue, green, and red galaxies 81

3.1 FUV$-r$ color-stellar mass diagram 93
3.2 Comparison between *GALEX* FUV and *HST* FUV magnitudes . 98
3.3 Montage of four ESF-ETGs 100
3.4 FUV$-r$ color profiles of the ESF-ETGs 102
3.5 FUV$-r$ color profiles of the ESF-ETGs, continued 103
3.6 FUV$-g$ vs. $g-r$ color-color diagrams 108
3.7 Stacked SDSS spectrum of the ESF-ETGs 115
3.8 FUV$-r$ vs. Hα equivalent width 124
3.9 *GALEX* FUV FWHM vs. FUV$-r$ 127

3.10 Stellar mass vs. *GALEX* FUV FWHM 129

4.1 SSFR vs. stellar mass relations 163
4.2 Mass-size relations 165
4.3 UVJ diagram for CANDELS sample 168
4.4 Mass growth tracks on grid diagram 170
4.5 Subdivided UVJ diagram, color-coded by $\mathrm{SSFR_{UV,corr}}$ 171
4.6 Subdivided rotated UVJ diagram, color-coded by $\mathrm{SSFR_{UV,corr}}$ . . 173
4.7 Median $\mathrm{SSFR_{UV,corr}}$ across the rotated UVJ diagram 175
4.8 $\mathrm{SSFR_{UV,corr}}$ vs. $(U-V)'$ 177
4.9 SEDs in UVJ bins, color-coded by redshift 179
4.10 SEDs in UVJ bins, color-coded by mass 180
4.11 Dust-corrected UVJ diagram, color-coded by $\mathrm{SSFR_{UV,corr}}$ 182
4.12 Dust-corrected UVJ diagram with various model tracks 184
4.13 $\Delta \log \mathrm{SSFR_{UV,corr}}$ vs. $\Delta \log$ SMA, color-coded by A_V 187
4.14 Subdivided UVJ diagram for fading galaxies 189
4.15 Subdivided UVJ diagram, color-coded by A_V 191
4.16 Subdivided UVJ diagram, color-coded by b/a 193
4.17 Postage stamps in UVJ diagram 195
4.18 A_V vs. $\Delta \log$ SMA, color-coded by b/a 197
4.19 Postage stamps in A_V vs. $\Delta \log$ SMA 200
4.20 Axis ratio distributions for main sequence galaxies 203
4.21 Axis ratio b/a vs. $\Delta \log$ SMA 205
4.22 Axis ratio b/a vs. $\Delta \log$ SMA, color-coded by semi-minor axis . . 208
4.23 Axis ratio b/a vs. $\Delta \log$ SMA, color-coded by A_V 211
4.24 Postage stamps in b/a vs. $\Delta \log$ SMA for low-redshift galaxies . . 213
4.25 Postage stamps in b/a vs. $\Delta \log$ SMA for high-redshift galaxies . . 214
4.26 $\Delta \log \mathrm{SSFR_{UV,corr}}$ vs. Sersic, color-coded by A_V 217
4.27 Confusion in FIR images 232
4.28 L_{IR} (SED) compared to L_{IR} (R13) 234
4.29 $\mathrm{SSFR_{UV+IR}}$ (R13) compared with $\mathrm{SSFR_{UV,corr}}$ 239
4.30 Subdivided UVJ diagram, color-coded by $\mathrm{SSFR_{UV+IR}}$ (R13) . . . 241

List of Tables

2.1 Mass and Redshift Ranges and Galaxy Number Counts 24

3.1 Properties of the ESF-ETGs 94
3.2 Surface Brightness Measurements of the ESF-ETGs 104
3.3 Sample Sizes Using Original SR2010 ESF-ETG Selection Criteria 120
3.4 Sample Size Using Modified Criteria to Find ESF-Candidates . . 123
3.5 Contribution of ESF-ETGs to the GV 132

4.1 Sample Selection Cuts 161
4.2 Parameters of SSFR-Mass Fits 162
4.3 Parameters of Mass-Size Fits 164

Abstract

The Link between Galaxy Structure and Star Formation across Cosmic Time

by

Jerome Joseph Fang

The processes that fuel and quench star formation in galaxies are expected to leave imprints on their structure. Moreover, these imprints can serve as signposts to identify galaxies at various stages of their evolution. In this dissertation, we describe our efforts to characterize changes in galaxy structure (1) as star formation is going out, (2) after star formation has ostensibly quenched, and (3) during active star formation, with the goal of elucidating the relevant processes that regulate star formation in each case.

In Chapter 2, we use a local ($z \sim 0$) sample of galaxies drawn from the Sloan Digital Sky Survey (SDSS) to investigate the first two cases. We find that, as galaxies quench, their outer stellar mass density profiles remain essentially constant. However, their inner stellar mass density (within 1 kpc) increases, even while galaxies are still star-forming, until it reaches a mass-dependent threshold, at which point quenching can occur. The existence of this threshold indicates that quenching is connected with processes that grow bulges.

In Chapter 3, we then study the morphologies and color profiles of 19 $z \sim 0$ early-type galaxies located in the green valley. Combining high-resolution *Hubble*

ultraviolet images with SDSS optical photometry, we find that these objects harbor low-level star formation that is clearly detectable in the ultraviolet. Moreover, the recently formed stars are distributed in symmetric rings that often span the entire optical extent of the galaxy. The presence of an old underlying population in their outer parts suggests that star formation in these galaxies is either gradually fading out or possibly rejuvenated by smooth accretion from the intergalactic medium. Such galaxies comprise $\approx 13\%$ of green valley galaxies of similar mass and color, and they may linger in the green valley for several Gyr.

Finally, in Chapter 4, we focus on the evolution of star-forming galaxies since $z = 2.5$, leveraging the rich multi-wavelength datasets produced by the Cosmic Assembly Near-infrared Deep Extragalactic Legacy Survey (CANDELS). By finely dissecting our sample into narrow mass and redshift slices, we are able to uncover several striking trends, including evidence for mass-dependent evolution in terms of disk formation and the buildup of metals and dust, i.e., massive galaxies are more evolved at all epochs. However, at fixed mass, no correlation between structure and specific star-formation rate is seen for galaxies on the star-forming "main sequence." This behavior persists at all redshifts, despite the considerable diversity in size and shape among star-forming galaxies. This suggests that, on the main sequence, star formation is regulated primarily by external factors, e.g., halo accretion rate, rather than the internal structure of the galaxy.

When I consider your heavens,

the work of your fingers,

the moon and the stars,

which you have set in place,

what is mankind that you are mindful of them,

human beings that you care for them?

You have made them a little lower than the angels

and crowned them with glory and honor.

Psalm 8:3–5

Acknowledgments

The journey that has culminated in this dissertation could not have been completed without the guidance of my advisor, Sandy Faber. Her critical eye, skilled creativity, and uncanny ability to ask just the right questions have truly been inspiring. Working with you these past six years has been a wonderful privilege. Thank you for sharing your love of the universe with me, your thoughtful counsel, and, most of all, your constant support as I learned the ropes of becoming a scientist. Thanks also to my other committee members, David Koo and Joel Primack, who never failed to provide that second (or third) opinion to challenge and refine my views. My work is the richer because of their input and advice.

My deep appreciation goes to the astronomy and physics departments for giving me numerous opportunities to work with students as a classroom instructor. I am particularly grateful to Stan Woosley, who agreed to hire me as a TA for his Astronomy 12 course during my first year of grad school, and nearly every year since. I've thoroughly enjoyed working with you and for the freedom you gave me as a TA. Thanks to Michael Dine and Greg Laughlin for letting me try my hand at teaching full-on courses. I'm also thankful for the advice of Adriane Steinacker, whose tireless devotion to her students is unmatched and a true inspiration for me. A big thank you as well to the many students who I've had the privilege of working with—best wishes for your future! Many thanks also to Maria Sliwinski

for her encouragement and always being willing to tell it like it is.

My grad student experience was infinitely more enjoyable thanks to the community of friends that I've been blessed with here in Santa Cruz. A warm thank-you to my fellow astro grads for being such a supportive group of people who knew when to work and when to play. I'm particularly grateful to Rosalie McGurk and Angie Wolfgang for their friendship these past six years. I couldn't have asked for better people to share the grad school experience (and a house) with.

The Lord saved me partway through grad school, a turning point in my life for which I am eternally thankful. I am grateful for His constant love and grace, and for surrounding me with an awesome community of fellow believers. Thanks to my friends in the Graduate Christian Fellowship and at Santa Cruz Bible Church, who welcomed a broken and seeking individual with open arms and didn't let go. I especially want to thank Peter, Janet, Caleb, Chad, Leila, Rachel, Adam, Richard, Abraham, Kyle, Matt, Terry, Tim, and Zack for their steadfast love, encouragement, and friendship. I can't express how much you've helped me grow to be a better person.

Finally, my family has been an invaluable source of support through it all. They have been my biggest cheerleaders, always encouraging, always loving. Being 400 miles away from them these past six years has made me even more excited to be returning home. Thanks, Mom, Dad, and DD, for your patience and support,

for always being willing to listen, and for believing in me, even when I didn't. I love you dearly.

The text of this dissertation includes reprints of the following previously published material: (1) Fang, Faber, Koo, & Dekel 2013, ApJ, 776, 63, and (2) Fang, Faber, Salim, Graves, & Rich 2012, ApJ, 761, 23. One of the co-authors listed in these publications (S. M. Faber) directed and supervised the research which forms the basis for this dissertation. I am the first author of each of these papers. All of the analysis presented here is my own work, including the text, figures, and tables. The content of these publications makes up Chapters 2 and 3 of this dissertation. Chapter 4 includes work that will be submitted to a journal in the near future.

Chapter 1

Introduction

One hundred years ago, our knowledge of the cosmos was essentially confined to our Solar System and other stars within our own Milky Way Galaxy. Since then, our cosmic horizon has expanded, quite literally, to the edge of the universe. In particular, cosmology has matured into a precision science, and we are now able to describe the formation of galaxies and large-scale structure within a well-established theoretical framework: cold dark matter (e.g., White & Rees, 1978; Blumenthal et al., 1984; White & Frenk, 1991) plus a cosmological constant (e.g., Lahav et al., 1991; Riess et al., 1998; Perlmutter et al., 1999). Observations of galaxies, both near and far, have confirmed key predictions of the theory, while at the same time spurring further refinements in the model. Thanks to this synergy between theory and observations, the overall picture of how galaxies evolve with

time is continually being refined.

Even during my six years as a graduate student, our knowledge of how galaxies grow and change has expanded significantly, both in the local universe and (especially) at high redshift. Much of this is thanks to the rise of big data in astronomy. All-sky surveys have provided information on literally millions of galaxies at low redshift, and large-scale programs targeting more distant galaxies have produced catalogs with tens of thousands of objects. Simulations are becoming increasingly sophisticated, routinely generating terabytes of output to analyze. Given this abundance of data, astronomers can ask (and answer) questions that were unthinkable just a few decades ago.

Galaxy evolution is a vast subject, with many unsolved puzzles ripe for investigation. The questions that I explore in this dissertation are: (1) What structural changes occur as galaxies transition from star-forming to quiescent? (2) Is this transition always a one-way process? (3) What is the intrinsic variation in the properties of star-forming galaxies and how do these properties correlate with each other? In the rest of this section, I briefly set up the context for each of these questions and summarize the key findings of this work. Further background can be found in the introductions to each chapter.

1.1 Structural Imprints of Quenching

Galaxies exhibit a bimodal distribution in color (e.g., Strateva et al., 2001; Kauffmann et al., 2003a; Brammer et al., 2009). Galaxies in the "blue cloud" are actively forming stars, while most objects located on the "red sequence" have ceased forming stars. This bimodality is most apparent in the color-stellar mass diagram, schematically illustrated in Figure 1.1.[1] The "green valley" represents the transition region between the blue and red populations. It has been shown that there is a net flow of objects from the blue cloud onto the red sequence (e.g., Bell et al., 2004; Faber et al., 2007; Martin et al., 2007). Hence, some blue galaxies must shut down, or "quench", their star formation in some way, though our understanding of the relevant processes and their associated timescales is still uncertain. In this work, "quenching" refers to any process that halts star formation, regardless if it is rapid or slow.

Identifying the processes that quench galaxies has since become a central goal of galaxy evolution studies. The fundamental requirement for quenching is that the gas supply feeding a galaxy must be depleted or removed, and various mechanisms have been proposed to accomplish this, e.g., AGN feedback (e.g., Croton et al., 2006; Hopkins et al., 2006), morphological quenching (Martig et al., 2009), and halo quenching (e.g., Rees & Ostriker, 1977; Silk, 1977; Blumenthal et al.,

[1]The "pile-up" of galaxies on the red sequence is most obvious for optical colors, which are less sensitive to low-level star formation than e.g., a UV-optical color (see Chapter 3).

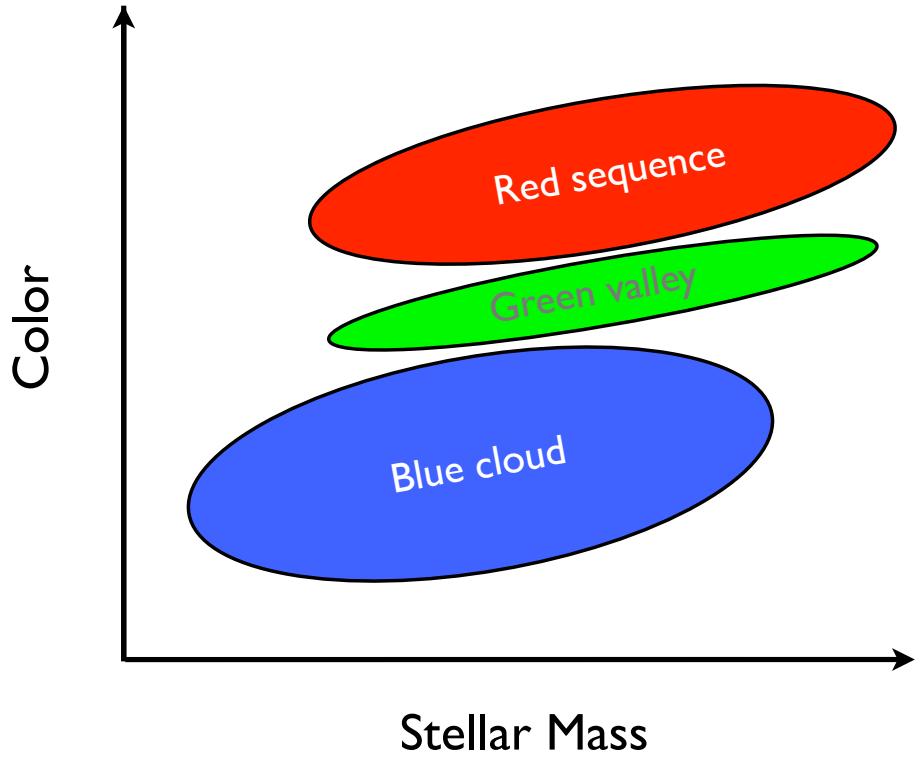

Figure 1.1: Schematic galaxy color-stellar mass diagram, representative of the local universe. Blue cloud galaxies are actively star-forming, whereas red sequence objects are quiescent. Galaxies in the green valley are in transit between the blue and red populations. Chapter 2 studies how galaxy structure changes as objects move from blue to red, while Chapter 3 examines the properties of a subset of green valley galaxies harboring recent, low-level star formation. We explore the redshift evolution of correlations between structure and star formation among blue galaxies in Chapter 4.

1984; Kereš et al., 2005; Dekel & Birnboim, 2006; Woo et al., 2013). Each of these processes have successfully quenched galaxies in theoretical models, but direct observational support is frustratingly thin (e.g., Fabian, 2012).

One way to constrain these processes is to study how a galaxy's internal structure changes as it quenches, which may help discriminate between the various quenching channels. For example, AGN feedback and morphological quenching are linked to the central bulge, so studying bulge growth may provide insight into how these processes operate. Even halo quenching, which operates on much larger scales, depends on the mass of the halo (Dekel & Birnboim, 2006), which in turn is linked to the strength of the gravitational potential experienced by the galaxy, which may be reflected in e.g., its central mass density or velocity dispersion.

Chapter 2 presents a detailed analysis of the internal structure of a sample of $z \sim 0$ central galaxies drawn from the Sloan Digital Sky Survey (SDSS). By tracing galaxies as they evolve from blue to red, we find clear evidence for bulge growth while galaxies are still star-forming. Once their central mass density reaches a critical value, galaxies are able to quench and evolve through the green valley onto the red sequence. Moreover, the most pronounced structural changes occur only in the inner regions; the outer mass profiles remain remarkably constant as galaxies evolve from blue to red (at fixed mass). These findings point toward bulge-related mechanisms (e.g., AGN feedback) as possible drivers of quenching,

at least for our centrals-only sample. We do not explore the role of environment on quenching, which primarily affects satellite galaxies (e.g., Peng et al., 2010; Woo et al., 2013).

1.2 Pathways through the Green Valley

As galaxies quench, they move through the green valley (GV) on their way to the red sequence, and this is the dominant pathway at late times. However, it is not guaranteed that once a galaxy is quenched, it remains quiescent forever. For example, a fresh supply of gas can be accreted onto the galaxy via cooling flows or a gas-rich merger, triggering a renewed episode of star formation. Such "rejuvenation" can be sufficient to drive a galaxy from the red sequence *back into* the GV. This is especially true when galaxies are studied in the ultraviolet (UV), since UV light is particularly sensitive to even small amounts of star formation. Hence the GV may represent a mix of galaxies with diverse, yet overlapping properties. Clearly distinguishing between quenching and rejuvenated galaxies is necessary in order to better constrain how galaxies go out and how common rejuvenation is, as well as their respective timescales.

Chapter 3 tackles these issues by studying the photometric and spectroscopic properties of a sample of 19 early-type GV galaxies selected to be optically red, yet blue in the UV. By analyzing high-resolution UV images, we find that such

objects have experienced recent star formation on extended, galaxy-wide scales. Moreover, this star formation is invisible in the optical, but is clearly seen in the UV. We find that star formation in these objects is either gradually fading out or possibly rejuvenated via smooth accretion occurring on long timescales. Indeed, their morphologies show no obvious disturbances, suggesting that the recent star formation is not due to violent processes like major mergers. We identify candidate objects with similarly extended star formation and find that they comprise $\approx 13\%$ of similarly massive GV galaxies at $z \sim 0$. In addition, these objects may linger in the GV for several Gyr.

1.3 The Diversity of Star-forming Galaxies

In the local universe, (massive) blue cloud galaxies are primarily objects possessing disk-dominated morphologies and active star formation (e.g., Blanton & Moustakas, 2009). However, this uniformity in structure breaks down at higher redshift. In particular, star-forming galaxies at $z \sim 2$ come in a variety of shapes, from clumpy disks (e.g., Wuyts et al., 2012; Mandelker et al., 2014; Guo et al., 2015) to compact nuggets (e.g., Barro et al., 2014; Williams et al., 2014). This diversity reflects the more violent and rapid nature of star formation at early times. At the same time, star-forming galaxies follow numerous scaling relations whose functional form remains nearly invariant with redshift (modulo possible

zeropoint evolution). Such relations include the star formation "main sequence" (e.g., Noeske et al., 2007; Whitaker et al., 2014), the mass-size relation (Shen et al., 2003; van der Wel et al., 2014a), and the fundamental metallicity relation (Mannucci et al., 2010). Given the strikingly different physical processes that form stars at high redshift compared to today, this invariance is rather surprising.

Despite this apparent regularity, star-forming galaxies show intrinsic scatter in these and other relations. Determining whether such scatter is correlated with other parameters can fine-tune our understanding of the interplay between the various processes that shape how galaxies evolve. In addition, studying how such correlations change with time can provide additional insight into the changing demographics of star-forming galaxies and help constrain key milestones in their evolution, e.g., the epoch of disk formation.

Chapter 4 presents a comprehensive exploration of star-forming galaxies over the past ~ 10 Gyr of cosmic time. This study is made possible by the rich datasets produced by the Cosmic Assembly Near-infrared Deep Extragalactic Legacy Survey (CANDELS). We study the evolution of key galaxy properties, including specific star-formation rate (SSFR), size, shape, and dust attenuation, and how these parameters correlate with each other as a function of stellar mass and redshift. A key analysis tool is the UVJ diagram, from which we extract several interesting results, including (1) a correlation between SSFR and location in the UVJ

diagram and (2) evidence for a previously unidentified population of compact, dusty star-forming galaxies at all redshifts. We also find that disk formation and the increase in metallicity and dust content follow a mass-dependent trend, i.e., massive galaxies are more evolved at any given epoch. In addition, we find that SSFR is independent of galaxy structure for objects on the main sequence. These findings confirm and extend previous results, and they have deep implications for how star formation is regulated in galaxies.

Chapter 2

A Link between Star Formation Quenching and Inner Galaxy Structure

2.1 Introduction

Our knowledge about galaxy formation and evolution has blossomed in recent years thanks to ever-larger observational surveys and increasingly sophisticated theoretical models. However, a full understanding of the processes by which star formation (SF) shuts down in galaxies and their connection to galaxy structure remains elusive. Observationally, galaxies exhibit a bimodal distribution in color

that persists even at high redshifts (e.g., Strateva et al., 2001; Kauffmann et al., 2003a; Brammer et al., 2009). The bimodality has been interpreted as an evolutionary path: blue and star-forming galaxies undergo one or more processes that ultimately shut down (or "quench") SF and cause them to migrate toward redder colors (Bell et al., 2004; Faber et al., 2007; Martin et al., 2007). Much work has been done to elucidate possible quenching processes, primarily from a theoretical perspective. Our focus in this work is on quenching in *central* galaxies, so we do not discuss processes that can quench SF in satellite galaxies.

The ultimate source of fuel for SF is (molecular) gas. In order to quench SF, the process(es) must remove such gas, heat it/prevent it from cooling, or stabilize it against gravitational collapse. Powerful AGN feedback (i.e., "quasar mode" feedback) is widely invoked as a means to expel gas from a galaxy (e.g., Di Matteo et al., 2005; Hopkins et al., 2006). Such feedback is predicted to be the result of a major gas-rich merger that initially fuels a powerful starburst as well as later activates the AGN, which subsequently blows out any remaining gas, thereby quenching SF. After the quasar phase, low-level AGN feedback continues to heat the surrounding gas and prevents it from cooling and settling (back) into the galaxy (i.e., "radio mode" feedback; Croton et al., 2006). The combination of these two AGN-driven processes effectively stifles any future SF.

An alternative method to suppress SF is to make any gas stable against grav-

itational collapse. In such a process, gas does not have to be expelled from the galaxy itself. Recently, Martig et al. (2009) proposed that the buildup of a central bulge is sufficient to stabilize the surrounding gas disk from collapsing and forming stars. Stability is achieved because the deeper gravitational potential well of the bulge increases the shear in the disk, making it difficult for the gas to form bound clumps (i.e., its Toomre $Q > 1$). Such "morphological quenching" can persist over several Gyr, and it is effective even if gas is continually accreted from external sources.

The quenching processes discussed so far operate *within* a galaxy. Of course, galaxies reside within dark matter halos, and it is not surprising that the halo itself may play a critical role in quenching SF. Simulations have shown that as halos reach a critical mass of $\sim 10^{12} M_{\odot}$, infalling gas in the halo becomes shock-heated to the virial temperature and is no longer able to cool efficiently (e.g., Birnboim & Dekel, 2003; Kereš et al., 2005; Dekel & Birnboim, 2006). The formation of a virial shock thus prevents gas from accreting onto the galaxy, robbing it of fuel for additional SF. Such "halo quenching" is not predicted to be a sharp, well-defined transition; theoretical predictions and observational evidence both indicate a large scatter in the critical halo mass of at least ~ 1 dex (Kereš et al., 2005; Dekel & Birnboim, 2006; Woo et al., 2013). Note that halo quenching does not require the presence of an AGN in order to operate.

A complementary approach to understanding quenching via gas physics has been to empirically examine how galaxy structure changes as galaxies evolve from blue to red. This approach is motivated by observed correlations between various structural parameters (e.g., mass concentration, velocity dispersion) and some measure of SF activity (e.g., color, specific SF rate). Presumably, the change in such a structural parameter as a galaxy evolves would be indicative of the relevant quenching process(es) at work.

Studies of SDSS galaxies have demonstrated the existence of critical or threshold values of structural parameters that define a transition in the recent SF histories of galaxies. For example, below a critical stellar mass, $M_* \sim 3 \times 10^{10}\, M_\odot$, galaxies typically are young and actively forming stars, while above this value, galaxies are predominantly old and not star-forming (Kauffmann et al., 2003b). A similar threshold in effective stellar surface mass density ($\propto M_*/R_{\rm eff}^2$) has also been seen: above a value of $\sim 3\times10^8\, M_\odot\,{\rm kpc}^{-2}$, galaxies are generally old and quiescent, while the opposite is true below this threshold (Kauffmann et al., 2003b, 2006). Moreover, Kauffmann et al. (2003b) showed that surface density, rather than stellar mass, is more strongly correlated with $D_n(4000)$, a proxy for galaxy age. This latter result is an indication that the *distribution* of mass within a galaxy may be the key tracer (or driver?) of quenching in galaxies. Indeed, a similar threshold has been found when examining the Sersic index (Sersic, 1968),

which quantifies the mass (more precisely, the light) distribution (Driver et al., 2006; Schiminovich et al., 2007; Bell, 2008). In particular, galaxies above a Sersic value of $n \approx 2.5$ tend to be quiescent.[1] The existence of structural thresholds in galaxies has also been seen at higher redshift (Franx et al., 2008; Bell et al., 2012; Cheung et al., 2012).

The results discussed above focus on the *general* galaxy population. For completeness, we mention here the existence of two classes of galaxies that have atypical quenching characteristics: post-starburst galaxies and low surface brightness galaxies. Post-starburst (or E+A) galaxies (Dressler & Gunn, 1983; Quintero et al., 2004; Goto, 2005) are rapidly quenched objects that likely underwent a recent merger-induced starburst (e.g., Hopkins et al., 2006; Snyder et al., 2011). These objects are rare in the local universe (a few percent, Wong et al., 2012; Mendel et al., 2013) and do not contribute much to the "quenching budget" at late times. However, they may represent the dominant quenching channel in the early universe (e.g., Whitaker et al., 2012; Barro et al., 2013). Understanding the connection between their structure and SF quenching is the subject of a recent SDSS study (Yesuf et al., 2014).

Low surface brightness galaxies are characterized by a central surface brightness fainter than ≈ 22 mag arcsec^{-2} in B (e.g., Impey & Bothun, 1997). Detecting

[1]However, as discussed in Section 2.4, the difference in Sersic index between blue and red galaxies is primarily due to the presence or lack of a bright, star-forming disk; it does not necessarily signal any large difference in the *mass* distribution.

these objects has been greatly enhanced thanks to surveys like SDSS. With larger samples, it has been found that these galaxies span a wide range in e.g., colors, SF rates, masses, gas content, and sizes (Galaz et al., 2002, 2011; Zhong et al., 2008, 2010). This diversity makes it unclear if SF in these objects plods along at a very low rate (Wyder et al., 2009), or if they experience bursty episodes followed by periods of quiescence (Boissier et al., 2008; Zhong et al., 2010). Understanding how SF is quenched in low surface brightness galaxies remains an important issue, though in this work we do not discuss them in detail since they are a tiny fraction of our sample (see Section 2.2).

Despite the existence of the structural thresholds discussed above, several challenges make it difficult to conclude that the structural configuration of a galaxy is sufficient to predict its SF history. First, the existence of thresholds in structural parameters does not immediately imply that *all* galaxies quench once they reach such a threshold. This is borne out in the data as a non-negligible fraction of "outlier" galaxies that are above a putative threshold value, e.g., Sersic index $n > 2.5$, yet are still blue and star-forming (Schiminovich et al., 2007; Bell, 2008; Bell et al., 2012; Cheung et al., 2012). In other words, being above the threshold is a necessary, but not sufficient, condition in order to be quenched. This suggests that quenching SF may be a multi-step process in which having the necessary galaxy structure is merely one component.

Another obstacle in linking structure with quenching is determining whether such thresholds are in fact fixed triggers (i.e., mass-independent and/or redshift-independent) over which galaxies evolve, or whether the thresholds evolve and "sweep up" galaxies (whose structural parameters were established early on and are now unchanging). Given that galaxies inevitably change their structure as they evolve, it is difficult to disentangle these two interpretations of thresholds.

Yet another question is whether thresholds are causative or merely correlative, with both parameters descending from a separate, third cause. In this paper, we are conservative and infer only that a correlation exists and that causation has not yet been proved. Thus, in showing a strong correlation between quenching and inner mass surface density (Section 2.3), we do not conclude that high mass density definitively causes quenching, but rather only that it tends to predict it.

A final challenge in connecting structure with quenching is deciding whether one structural parameter is superior to others in its ability to predict a galaxy's SF history and how that parameter is related to the actual physics of quenching. It is not expected that *one* parameter can fully encapsulate all the relevant physical processes; nevertheless, one might gain insight into the *dominant* mechanism at work by determining the most important structural parameter. It has been argued that Sersic index is the parameter that best discriminates between star-forming and quiescent galaxies (Bell et al., 2012). However, Wake et al. (2012b) conclude

that velocity dispersion (measured within one-eighth of an effective radius) shows an even better correlation with galaxy color in SDSS galaxies. Regardless of the exact details, both Sersic index and velocity dispersion reflect the *inner* mass distribution, which may therefore play a critical role in quenching SF. For example, both AGN feedback and morphological quenching rely on the presence of a sufficiently massive bulge in order to quench SF. A link to velocity dispersion might even exist in the halo quenching picture if it is indeed a better indicator of halo mass than stellar mass is (Wake et al., 2012a, but see Li et al. (2013)). But in this case the galactic structural parameter would signify the role of the halo rather than itself being the causative agent.

The growing appreciation that quenching correlates closely with galaxy structure has spurred further work recently. Cheung et al. (2012), using a sample of galaxies at $z \sim 0.8$ drawn from the AEGIS survey (Davis et al., 2007), investigated the utility of various structural parameters at predicting galaxy color. A novel feature was their use of the stellar surface mass density within a radius of 1 kpc, denoted Σ_1 hereafter, as a parameter to probe the inner regions of a galaxy. They found that Σ_1 shows an even tighter correlation with color than Sersic index, suggesting that it is the *inner mass distribution* that is a critical indicator of quenching.

While the result of Cheung et al. (2012) is tantalizing, it remains to be verified

with the larger samples available at lower redshifts. In this work, we harness the rich datasets available from the SDSS and *Galaxy Evolution Explorer* (*GALEX*) surveys to study the correlation of Σ_1 with color found by Cheung et al. (2012) in more detail. Specifically, we examine trends in narrow mass slices as a way to uncover possible systematic trends with mass. A key feature of our work is the use of *GALEX* UV data rather than rest-frame optical $U-B$ color in order to better resolve the transition region between star-forming and quiescent galaxies (i.e., the green valley). This allows us to separate galaxies that have recently quenched from redder galaxies that presumably quenched at earlier epochs (and may have built up mass post-quenching via dry mergers). In addition, we take advantage of high-quality aperture photometry from SDSS that enables measurements of mass profiles for a large sample of galaxies as a function of mass and color.

The chapter is organized as follows. Our sources of data, sample selection, and method of computing mass profiles are discussed in Section 2.2. A novel and intriguing mass-dependent relation between inner surface density and NUV$-r$ color is presented in Section 2.3. Section 2.4 presents average surface brightness and mass profiles and highlights our finding that mass buildup in the central regions is a key correlate of quenching in galaxies. We also compare the use of light-weighted versus mass-weighted quantities in studying galaxy structure. Section 2.5 presents a comparison between inner mass density and velocity dispersion as

tracers of quenching. Finally, our discussion and conclusions follow in Sections 2.6 and 2.7. All magnitudes are on the AB system (Oke, 1974). We assume a concordance ΛCDM cosmology with $\Omega_m = 0.3, \Omega_\Lambda = 0.7$, and $H_0 = 70\,\mathrm{km\,s^{-1}\,Mpc^{-1}}$.

2.2 Data and Sample Selection

2.2.1 Photometry and Structural Parameters

For this study, six-band integrated photometry (NUV from *GALEX*, *ugriz* from SDSS) was obtained from the cross-matched *GALEX* GR6/SDSS DR7 catalog available through the *GALEX* CASJobs interface[2]. For *GALEX* magnitudes, `mag_auto` values are used; for SDSS, model magnitudes are used. The photometry was corrected for Galactic extinction and k-corrected to $z = 0$ using version 4.2 of the `kcorrect` code package described in Blanton & Roweis (2007).

In addition to integrated photometry, the SDSS pipeline measures surface brightness profiles in all five (*ugriz*) bands in a series of circular annuli of fixed angular size. For this work, the apertures chosen range in radius from $0\farcs23$ to $11\farcs42$. The annular photometry was corrected for Galactic extinction and k-corrected by computing independent k-corrections in each annulus. The k-corrected surface brightness profiles were then smoothly interpolated following the method outlined in Stoughton et al. (2002). Briefly, a spline was fit to the *cumulative* light profile

[2] `http://galex.stsci.edu/casjobs/`

(in order to conserve flux), which was then differentiated to obtain the final surface brightness profile interpolated over a fixed grid of angular sizes in $0\farcs1$ intervals.

Spectroscopic redshifts, fiber velocity dispersions, and total stellar masses were obtained from the MPA/JHU DR7 value-added catalog[3]. The stellar masses were computed by fitting the integrated SDSS photometry with stellar population models [similar in spirit to the method used in Salim et al. (2007)]. We additionally obtain the group membership (central or satellite) of the galaxies using the catalog of Yang et al. (2012).

2.2.2 Sample Selection

Our sample was selected from the *GALEX* GR6/SDSS DR7 cross-matched catalog. The sample was selected (1) to have redshift $0.005 < z < 0.12$, (2) to be within the central $0\fdg55$ of the *GALEX* field of view, and (3) to be detected in the NUV bandpass of the *GALEX* Medium Imaging Survey. In addition, to exclude dusty, star-forming galaxies whose dust-reddened colors would move them into the green valley, only galaxies with axis ratio $b/a > 0.6$ were kept. Finally, since we are interested in the quenching of central galaxies, not satellites, we selected only objects listed as the most massive group member in the SDSS DR7 group catalog of Yang et al. (2012).

Figure 2.1 presents the NUV$-r$ color-stellar mass diagram for our sample. The

[3] `http://www.mpa-garching.mpg.de/SDSS/DR7/`

sensitivity of the UV to even low-level SF is clearly demonstrated: galaxies cleanly separate into two well-delineated populations (the blue and red sequences[4]), with a clear transition region in between (the green valley). Included in Figure 2.1 are contours indicating the completeness of the sample above a given redshift (indicated in the figure). Each contour encloses 95% of the total points in each redshift range. The loss of lower-mass galaxies with increasing redshift is due to the SDSS spectroscopic limit ($r = 17.77$) and the *GALEX* NUV magnitude limit (NUV = 23).

Throughout this paper we divide the sample into mass slices 0.25 dex wide in this color-stellar mass diagram. We emphasize that this is possible thanks to the large number of galaxies available in SDSS. Dividing by mass can uncover trends that are washed out when considering a wide range of stellar masses all together. An implicit assumption made later on is that galaxies evolve and redden without significantly increasing their stellar mass. Indeed, existing quenching scenarios predict either very little stellar mass growth or at most a doubling of stellar mass (via major mergers) between the blue and red sequences (see Section 2.3 for further discussion). In addition, one benefit of using NUV$-r$ color rather than an optical color is that the former is much more sensitive to low-level SF and hence can be used to identify galaxies that have *recently* quenched. The clear green valley seen

[4]In this paper, the terms "blue sequence" and "blue cloud" are used interchangeably. The former is a more accurate description of the distribution of star-forming galaxies in a UV-optical color-mass diagram.

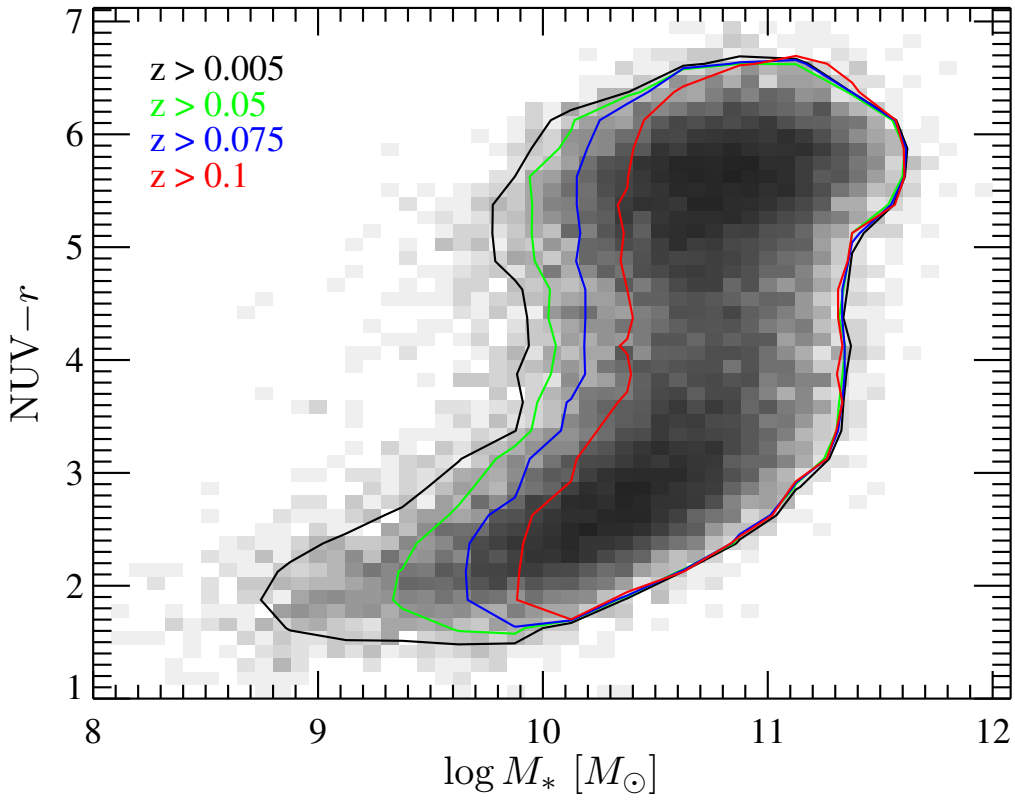

Figure 2.1: NUV$-r$ color vs. stellar mass for SDSS galaxies with *GALEX* NUV detections. The 2D histogram (grayscale) shows the distribution of central, face-on ($b/a > 0.6$) galaxies with redshift $0.005 < z < 0.12$, clearly showing the well-defined blue and red sequences, with the green valley located in between at intermediate colors. The contours enclose those galaxies located above the redshift limits listed at upper left, indicating the approximate completeness limit at those redshifts. In this work, our final sample is restricted to $z < 0.075$.

in Figure 2.1 is dominated by those galaxies that are currently transitioning from star-forming to quiescent.

To construct a sample that does not exclude the reddest galaxies yet contains as many objects as possible, we select our final sample in the following way. As can be seen in Figure 2.1, the upper envelope of the red sequence lies around NUV$-r \approx 6.5$. Given that the NUV magnitude limit is 23, this implies that, to ensure detection of the reddest objects, galaxies must have $r < 16.5$. Figure 2.2 shows stellar mass versus redshift for galaxies with $r < 16.5$ and NUV$-r > 4$. Indicated in the figure are the six mass bins used throughout this paper. Each bin is 0.25 dex wide, and we consider the interval $9.75 < \log M_*/M_\odot < 11.25$. For each mass bin, a volume-limited sample is constructed by defining the minimum and maximum redshifts between which red galaxies are detected. Note that the volumes chosen are different for each mass bin. Hereafter, we refer to this sample of 2361 galaxies as the "volume-limited sample," even though it is not formally restricted to a single volume for all galaxies. For reference, Table 2.1 lists the mass and redshift ranges defining the volume-limited sample, as well as the numbers of galaxies in each bin. The fraction of blue, green, and red galaxies in each mass bin are also provided. Throughout this paper, blue galaxies are defined to have NUV$-r < 4$, green galaxies have $4 <$ NUV$-r < 5$, and red galaxies have NUV$-r > 5$.

Table 2.1. Mass and Redshift Ranges and Galaxy Number Counts

Mass Range ($\log M_*/M_\odot$)	Redshift Range	$N_{\rm blue}$[a]	$N_{\rm green}$[b]	$N_{\rm red}$[c]	$N_{\rm tot}$
$[9.75, 10.00]$	$[0.025, 0.035]$	53 (70%)	10 (13%)	13 (17%)	76
$[10.00, 10.25]$	$[0.025, 0.04]$	91 (55%)	21 (13%)	52 (32%)	164
$[10.25, 10.50]$	$[0.0275, 0.05]$	134 (42%)	45 (14%)	140 (44%)	319
$[10.50, 10.75]$	$[0.035, 0.07]$	265 (33%)	112 (14%)	423 (53%)	800
$[10.75, 11.00]$	$[0.045, 0.075]$	184 (27%)	112 (16%)	392 (57%)	688
$[11.00, 11.25]$	$[0.055, 0.075]$	38 (12%)	49 (16%)	227 (72%)	314
		765 (32%)	**349 (15%)**	**1247 (53%)**	**2361**

[a]Galaxies with NUV$-r < 4$.

[b]Galaxies with $4 <$ NUV$-r < 5$.

[c]Galaxies with NUV$-r > 5$.

Our use of the SDSS spectroscopic sample can, in principle, bias our sample against specific types of galaxies. Fiber collisions exclude $\sim 6\%$ of photometrically detected objects (Strauss et al., 2002). These excluded galaxies tend to be found in very dense environments or in close pairs. We do not expect the loss of these few objects to alter our conclusions. The sample may also be biased against low surface brightness galaxies. To test this, we identified low surface brightness galaxies using the criteria in Galaz et al. (2011). Within the redshift limits of our volume-limited sample, we find that we are complete in low surface brightness galaxies for each mass bin. Such objects comprise only 1.6% of the volume-limited sample overall and are not expected to affect our conclusions.

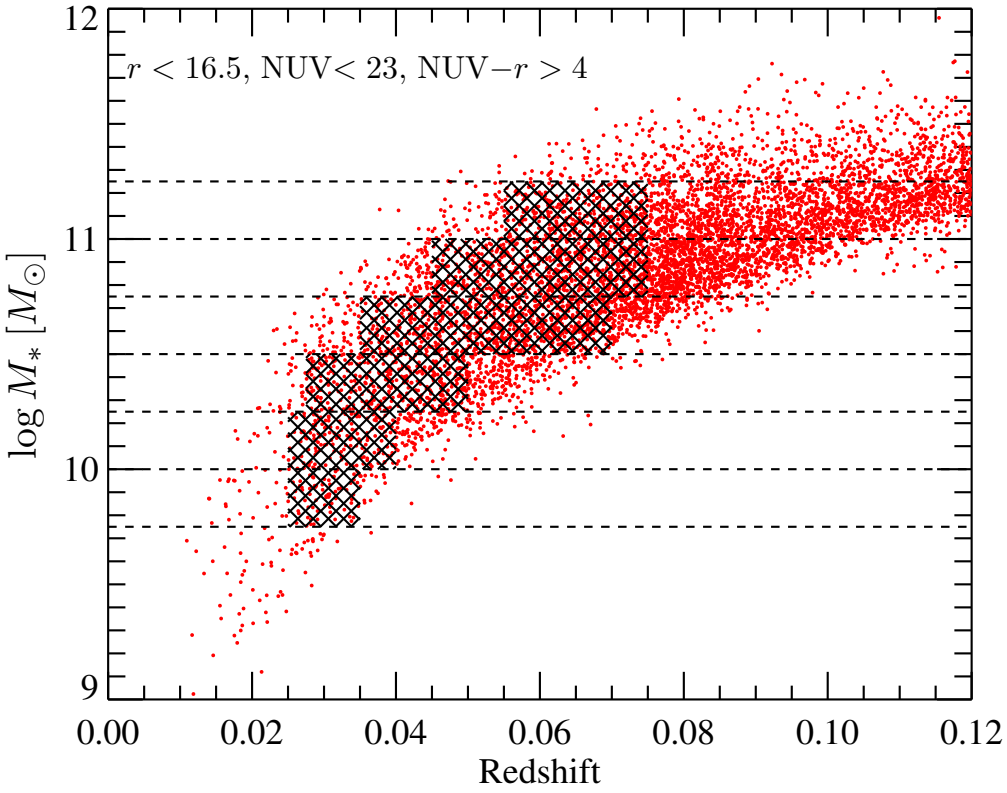

Figure 2.2: Stellar mass vs. redshift for galaxies in our sample with $r < 16.5$, NUV< 23, and NUV$-r > 4$ (red points). The magnitude limits ensure that we are not excluding the reddest objects from the sample (Section 2.2.2). The horizontal dashed lines indicate the mass bins used in defining our sample. The hatched regions indicate the redshift ranges used to define our "volume-limited sample." This approach maximizes the number of galaxies in each mass bin. Redshift limits and number counts are provided in Table 2.1. The size of the SDSS PSF limits our useable redshift range to $z < 0.075$ (see Section 2.8).

2.2.3 M/L Relation and Mass Surface Density Profiles

A major focus of this paper is studying the buildup of stellar mass in the inner regions of galaxies and its relation to quenching. To trace the mass distribution and its evolution, we compute stellar mass surface density profiles for each galaxy using the surface brightness profiles described in Section 2.2.1. To do so requires knowledge of the stellar mass-to-light ratio, M/L, to convert surface brightness into mass surface density. We calibrate a relation between M/L_i (i.e., stellar mass divided by i-band luminosity) and rest-frame $g-i$ color using the integrated photometry and stellar masses of our sample. Figure 2.3 presents the derived calibration, $\log M/L_i = (1.15^{+0.11}_{-0.07}) + (0.79^{+0.07}_{-0.10})(g-i)$. The calibration is derived from a linear least-squares fit to the data, incorporating errors in the stellar mass estimates (typically ~ 0.1 dex; photometric errors are a few percent at most). The uncertainties in the slope and zeropoint are 16th and 84th percentile confidence limits obtained by bootstrap resampling the data points within their errors and recalculating the fit. This relation is consistent, within the uncertainties, with the M/L_i calibration determined by Taylor et al. (2011) for a larger sample of SDSS galaxies. This M/L_i relation is used in conjunction with the interpolated surface brightness profiles to calculate mass density profiles. The 1σ scatter about the relation is 0.04 dex, which is taken to be the uncertainty in M/L_i when calculating errors later on.

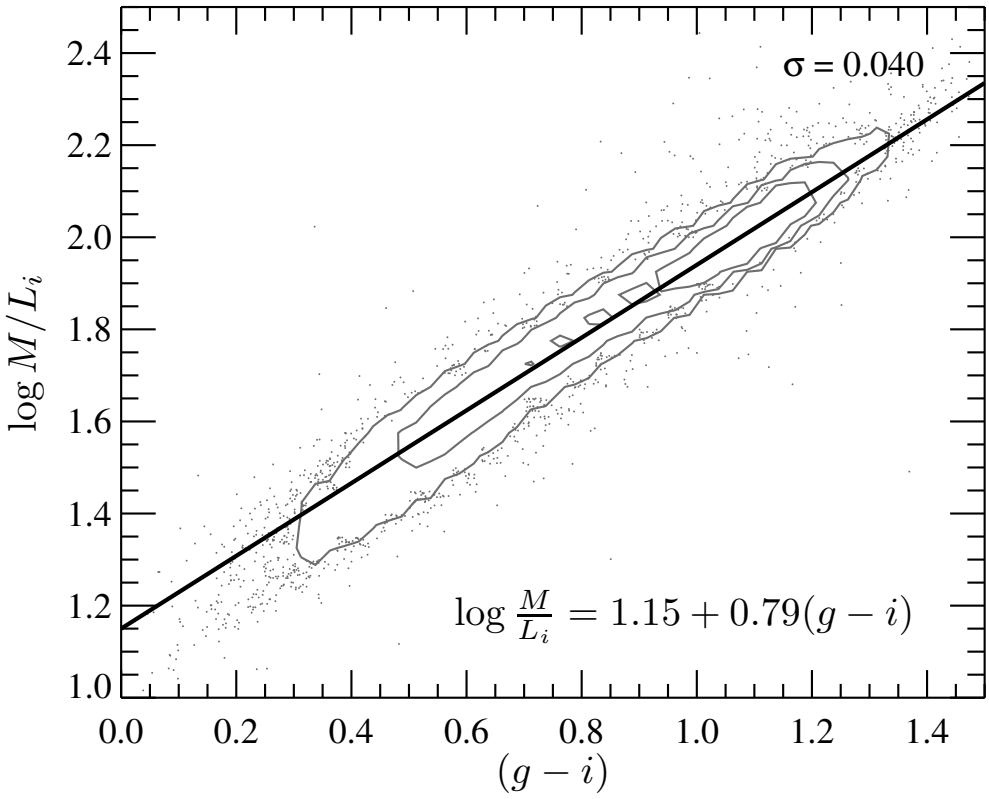

Figure 2.3: Integrated stellar mass-to-light ratio M/L_i (i-band luminosity) vs. rest-frame $g-i$ color for SDSS galaxies in our sample (gray contours and points). Stellar masses are from the MPA/JHU catalog. The best-fit linear relation is plotted, $\log M/L_i = (1.15^{+0.11}_{-0.07}) + (0.79^{+0.07}_{-0.10})(g-i)$. Confidence limits for the slope and zeropoint were computed by bootstrap resampling. This relation is used to convert i-band surface brightness profiles into mass surface density profiles. The 1σ scatter about the relation (0.04 dex) is indicated in the upper right.

A potential concern is how variations in stellar population parameters (e.g., SF history, dust, metallicity, initial mass function) affect our derived M/L relation. In particular, such variations may cause galaxies to scatter off the linear relation, leading to an incorrect estimate of the mass density. However, broadly speaking, such variations conspire together to shift galaxies *along* the relation rather than off it (e.g., Bell & de Jong, 2001; Szomoru et al., 2013).

To verify empirically that metallicity does not bias M/L, we measured the M/L relation using masses and colors determined within the SDSS 3″ fiber. Since the fiber subtends the inner regions of each galaxy ($\lesssim 3$ kpc), we can probe regions with higher metallicities and see if they are located off the relation in Figure 2.3. We find that the fiber-based M/L relation lies on top of the relation in Figure 2.3, with slightly smaller scatter (0.035 dex). No systematic offset is seen, suggesting that metallicity effects do not introduce a systematic bias in our measurements of M/L. We have also verified that low surface brightness galaxies follow the main relation and do not lie systematically off it.

Variations in the initial mass function (IMF) can also result in inaccurate estimates of M/L. To first order, changing the IMF shifts the zeropoint of the M/L relation but preserves its slope (e.g., Bell & de Jong, 2001). If the IMF varies systematically with, e.g., galaxy luminosity, our use of a single calibration would be inappropriate. Indeed, increasing evidence points to systematic variations in

the IMF, such that steeper IMFs (more bottom-heavy) are inferred in (early-type) galaxies with higher velocity dispersions (e.g., Cappellari et al., 2012; Conroy & van Dokkum, 2012; La Barbera et al., 2013). If this trend applies to our sample, then our estimates of M/L would be systematically underestimated for more massive and redder galaxies. Fortunately, this effect works in our favor by *increasing* the measured difference in inner stellar surface mass densities between red and blue galaxies, strengthening our claim that quenched galaxies have higher inner mass densities (see Section 2.3). Thus, the changes in our resulting mass density profiles may, in fact, be lower limits to the actual mass distribution changes in quenched galaxies.

2.3 The Relation between Inner Surface Mass Density and Color

Following in the footsteps of Cheung et al. (2012), which presented evidence that quenching is linked with *inner stellar mass density* in $z \sim 0.8$ galaxies, we explore the link between color and inner mass density with our nearer sample. The average surface mass density within a circular aperture of radius 1 kpc, denoted as Σ_1, is computed by directly integrating the mass profiles from the innermost point out to $R = 1$ kpc. Our analysis is limited to galaxies with redshift $z <$

0.075, where the HWHM of the SDSS PSF (0.″7) is comparable to the smallest aperture corresponding to 1 kpc (0.″68). The appendix to this chapter (Section 2.8) discusses this issue in more detail.

Figure 2.4 shows the distribution of Σ_1 as a function of stellar mass and NUV$-r$ color for galaxies with $0.005 < z < 0.075$. It is clear that green valley and red sequence galaxies trace out a well-defined, power-law relation. A least-squares fit to only the green and red galaxies is included in the plot, incorporating errors in Σ_1. The best-fit relation obtained is

$$\log \Sigma_1 = (9.29^{+0.10}_{-0.10}) + (0.64^{+0.23}_{-0.20})(\log M_* - 10.25), \tag{2.1}$$

with a 1σ scatter for green and red galaxies about the relation of 0.16 dex. The units are $M_\odot$ for M_* and $M_\odot\,\mathrm{kpc}^{-2}$ for Σ_1. The errors are calculated using bootstrap resampling of the data and represent the 16th and 84th percentile confidence limits. This correlation between Σ_1 and stellar mass implies that the threshold value of Σ_1 above which galaxies are seen to quench grows with stellar mass. It thus challenges the notion of a *fixed, mass-independent* surface density threshold (see Kauffmann et al., 2006; Franx et al., 2008).

Figure 2.4 offers a new way to trace the structural changes in a galaxy as it evolves from star-forming to quiescent. Since blue galaxies have systematically lower Σ_1 than green and red galaxies, Figure 2.4 implies that a galaxy increases

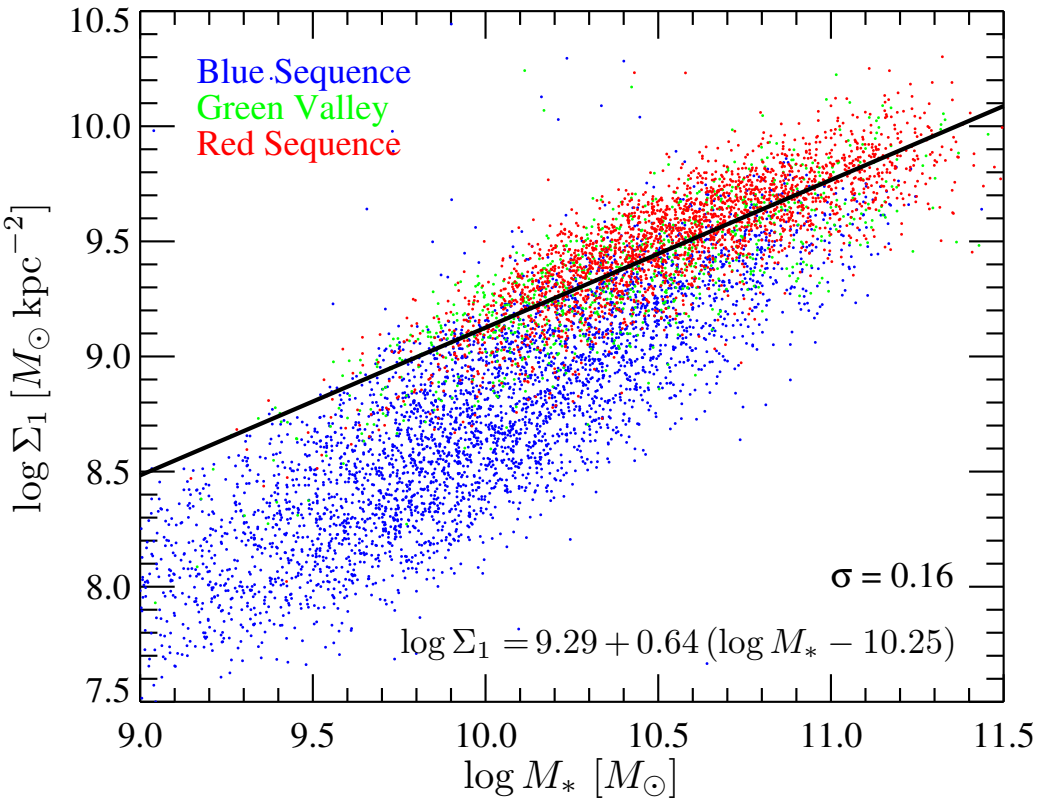

Figure 2.4: Σ_1 vs. stellar mass for galaxies with $0.005 < z < 0.075$. Points are color-coded according to NUV$-r$ color. A strong trend between both parameters is seen for green and red galaxies, while blue galaxies lie below the ridge line of the relation. The line is a least-squares fit to the green valley and red sequence galaxies only (NUV$-r > 4$), $\log \Sigma_1 = (9.29^{+0.10}_{-0.10}) + (0.64^{+0.23}_{-0.20})(\log M_* - 10.25)$. The quoted confidence limits were obtained using bootstrap resampling of the data. The 1σ vertical scatter of green and red galaxies about the fit is indicated in the figure (0.16 dex). The strong trend with stellar mass challenges the notion of a fixed, mass-independent threshold surface mass density above which galaxies can quench.

its Σ_1 as it evolves from blue to red. This is more clearly demonstrated in Figure 2.5, which plots the mass-Σ_1 relation for blue, green and red galaxies separately. At all stellar masses, blue galaxies (on average) fall *below* the best-fit relation (Equation 2.1) and the locus of points occupied by quenched galaxies (indicated by the red contour). Thus quenching of star formation is accompanied by an increase in Σ_1. The implications of this link are explored further in Section 2.6.

A major advantage of our sample is that we have sufficient numbers to investigate the mass dependence of this trend in finer detail. Figure 2.6 shows the relation between Σ_1 and NUV$-r$ color in six mass bins 0.25 dex wide ranging from $\log M_*/M_\odot = 9.75$ to $\log M_*/M_\odot = 11.25$. Dividing the sample into narrow mass bins uncovers systematic trends that are smeared out when examining the whole sample together. In particular, a striking regularity is seen in each mass bin: blue galaxies with NUV$-r < 4$ span a relatively larger range in Σ_1, compared to galaxies in the green valley and red sequence (i.e., NUV$-r > 4$), which span a *narrower* range in Σ_1. The general shape of the distribution resembles a hook, and remains roughly the same across all mass bins. The typical spread in Σ_1 for blue galaxies is ~ 0.7 dex, while in the green valley and red sequence the spread is smaller, ~ 0.4 dex.

Since it is known that galaxies evolve from blue to red (e.g., Bell et al., 2004; Faber et al., 2007; Martin et al., 2007), it is tempting to interpret the loci seen

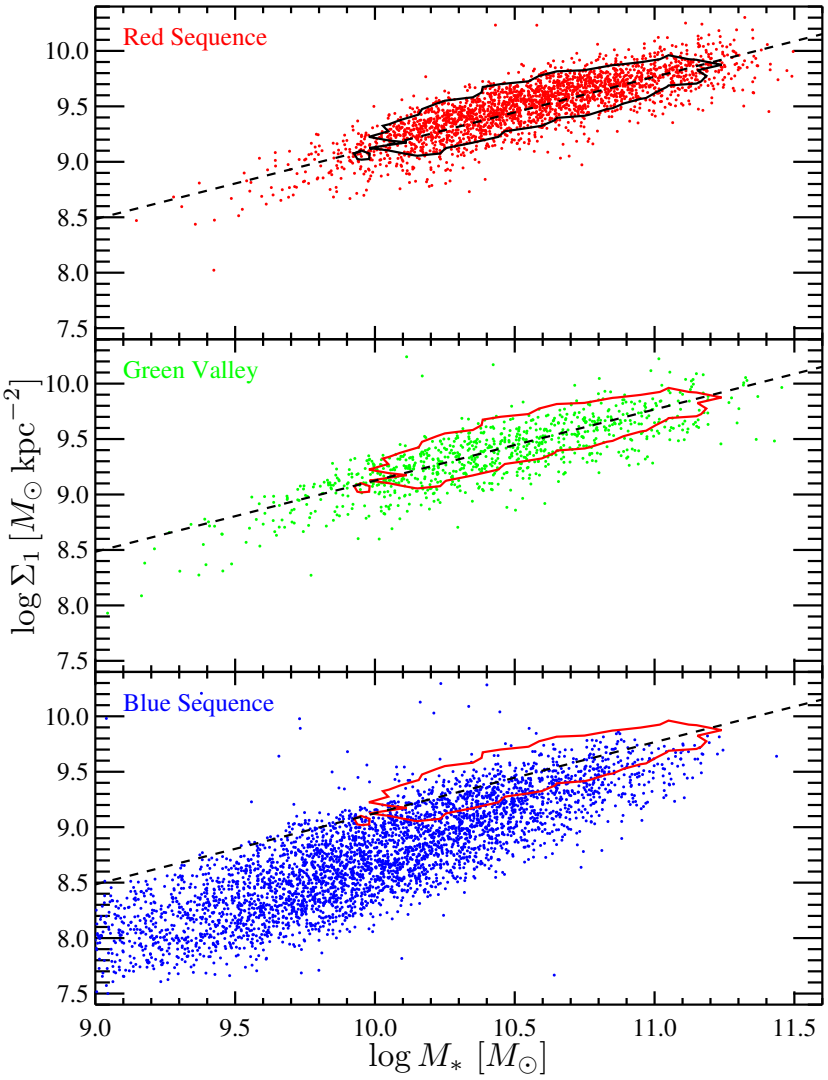

Figure 2.5: Σ_1 vs. stellar mass for galaxies with $0.005 < z < 0.075$. Each panel includes only galaxies in the blue sequence, green valley, and red sequence (bottom to top). The black contour defined by the red galaxies in the top panel is repeated in the other panels in red as a visual aid. The best-fit line from Figure 2.4 is also shown in each panel. In general, blue galaxies have lower Σ_1 than quenched galaxies at all stellar masses, showing that quenching is linked with an increase in Σ_1. Moreover, the blue galaxies within the contour suggest that a dense bulge is necessary but not sufficient to quench SF.

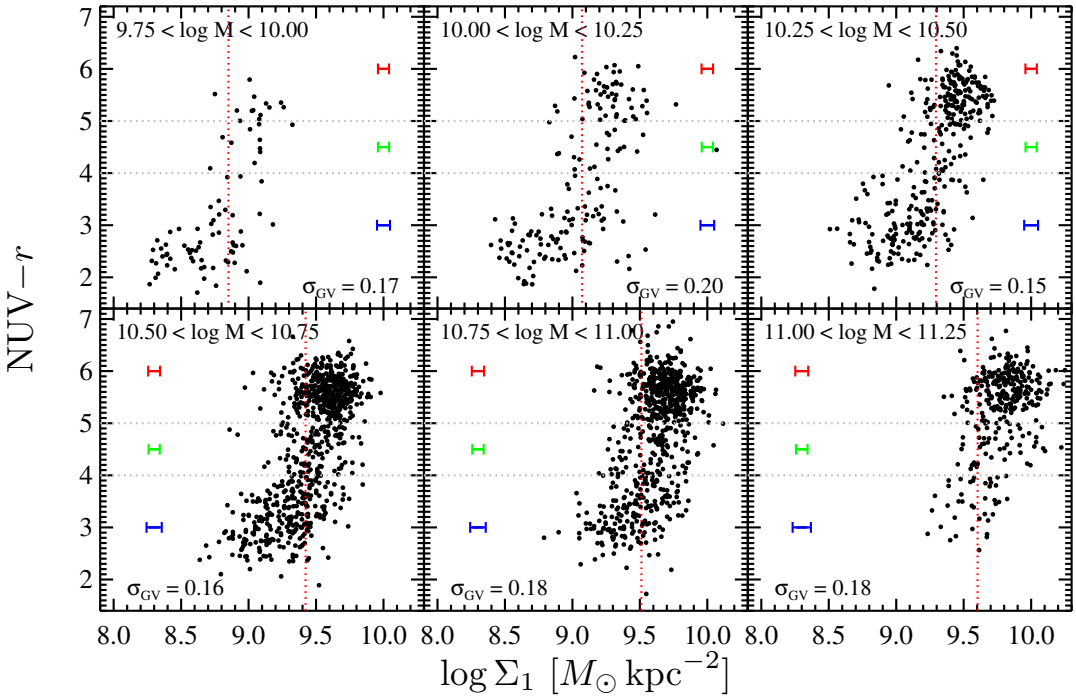

Figure 2.6: NUV$-r$ vs. Σ_1, plotted for the volume-limited sample in six stellar mass bins. Values of Σ_1 are computed from the mass density profiles discussed in Section 2.2.3. The error bars indicate the median error in Σ_1 for blue, green, and red galaxies in each mass bin. Dotted gray lines indicate the division between blue, green, and red galaxies. The "hook"-shaped distribution in seen in nearly every mass bin. The horizontal scatter in dex of the distribution in the green valley is indicated at the bottom of each panel. Assuming that galaxies evolve at fixed mass, this suggests that galaxies in the blue sequence build up their bulges (i.e., increase Σ_1) and then quench and redden. The near-vertical distribution of green and red galaxies suggests that inner bulge buildup does not continue (much) once a galaxy leaves the blue sequence. In addition, the distribution "marches" toward higher Σ_1 with increasing stellar mass. Dotted red lines indicate the value of Σ_1 above which 80% of the red galaxies lie in each mass bin.

in Figure 2.6 as possible evolutionary tracks, with galaxies evolving roughly horizontally through the blue cloud and then upward onto the red sequence *at fixed stellar mass*. To determine if this is plausible, we divide the proposed path into two segments: (1) evolution through the blue cloud and (2) quenching through the green valley onto the red sequence. For each segment, we compare an appropriately defined "evolutionary" timescale with an estimate of the mass doubling time. If both evolutionary timescales are shorter than the mass doubling time, then our claim that galaxies evolve at fixed mass is reasonable.

We first examine the second evolutionary segment by comparing the quenching timescale with the mass doubling timescale. In the local universe, the quenching time (i.e., the time to move across the UV-optical green valley) is of the order 1 Gyr or less (Martin et al., 2007). The mass growth timescale can be estimated using the results of e.g., Wechsler et al. (2002), McBride et al. (2009), and Dekel et al. (2013). In particular, these authors find that the mass growth of a dark matter halo can be parameterized as an exponential: $M(z) = M_0 e^{-\alpha z}$, with the best-fitting $\alpha \approx 0.7$. Using this formula, we find that the time to double the halo mass is ≈ 8 Gyr (i.e., the time elapsed since $z \approx 1$). A similar doubling time for the stellar mass is found in semi-analytic models of galaxy growth (Behroozi et al., 2013). Since this time is much longer than the quenching timescale, we can safely assume that galaxies do not significantly increase their mass as they

quench, i.e., they remain in the same mass bin as they leave the blue cloud, move through the green valley, and arrive on the red sequence. This picture neglects major mergers, but they are expected to be rare at low redshifts (Lotz et al., 2011) and an insignificant contribution to the overall mass growth (Moustakas et al., 2013). In summary, since the quenching timescale is much shorter than the mass doubling time, galaxies will, on average, evolve through the green valley onto the red sequence *at fixed stellar mass*.

Some of the green valley objects in Figure 2.6 are prime candidates for rapid SF quenching, namely, post-starburst galaxies. While we do not explicitly identify them in this work (since we do not discuss spectral information), other studies find that post-starbursts lie in the green valley and have compact structure (high Σ_1), consistent with the evolutionary tracks in Figure 2.6 (Wong et al., 2012; Mendel et al., 2013; Yesuf et al., 2014).

We now turn to the first segment of the proposed path and ask if blue galaxies can increase Σ_1 without a significant (factor of 2) increase in stellar mass. We can appeal to another timescale argument to verify this. We assume a mass doubling time of $\sim$ 8 Gyr, as above. If the growth in Σ_1 is due to e.g., violent disk instabilities, the timescale for clumps in the disk to fall toward the center is of order tens of dynamical times (i.e., a few Gyr; Dekel et al., 2009). However, violent disk instabilities are believed to be more common at high redshift and are

unlikely to be the main driver of bulge buildup in our galaxies. On the other hand, secular evolution (via, e.g., bar-driven processes) is believed to be a key player at late times and can also increase the inner mass density on timescales of a few Gyr (Kormendy & Kennicutt, 2004). While these bulge buildup timescales are smaller than the mass doubling time, we caution that these estimates are somewhat uncertain. Despite this caveat, it is nevertheless plausible that galaxies can build up their inner regions while maintaining roughly constant stellar mass since $z \sim 1$. Thus our interpretation of each panel of Figure 2.6 as an evolutionary track is reasonable.

Our interpretation is also consistent with the data themselves. Specifically, the distribution of points in Figure 2.6 (especially at lower masses) forms a "hook" shape, with some blue galaxies having lower Σ_1 than green and red galaxies of the same mass. The lack of quenched galaxies with *low* Σ_1 in each mass bin is strong evidence that blue galaxies cannot simply fade onto the red sequence without increasing their inner mass density. If they could, we would expect to see the scatter in Σ_1 for green and red galaxies to be comparable to the scatter in Σ_1 for blue galaxies. This is not seen in Figure 2.6. Our interpretation is consistent with Cheung et al. (2012), who find that the inner mass concentration of galaxies at $z \sim 0.8$ must increase in order for galaxies to quench. Our result moreover shows that this mass rearrangement occurs *at fixed stellar mass*. We note that

the few low surface brightness galaxies in our sample lie in the low-Σ_1 tail of the blue cloud in Figure 2.6, along with the many other normal galaxies with low Σ_1. Thus such objects do not bias our interpretation of the figure.

In addition to the hook-shaped distribution, Figure 2.6 reveals other trends. One is the "disappearance" of blue sequence galaxies in higher mass bins (Table 2.1). This is not surprising because the blue sequence is tilted in color-mass space (see Figure 2.1), with the bluest objects found only at low stellar masses. Put another way, the ratio of blue galaxies to red galaxies decreases with stellar mass (Table 2.1). If galaxies do evolve as we have described, then Figure 2.6 also implies that such evolution is more complete at higher masses. That is, the dearth of massive blue galaxies is consistent with more massive galaxies completing their evolution onto the red sequence at earlier times. This is consistent with downsizing and also the fact that more massive spheroidal galaxies are found to possess more evolved stellar populations (e.g., Thomas et al., 2005; Cattaneo et al., 2008; Graves et al., 2010; Barro et al., 2013; Moustakas et al., 2013). Our new results imply that more massive galaxies are more dynamically evolved as well.

2.4 Surface Brightness and Mass Density Profiles

In this section we examine the mass profiles for further insight into the global mass distribution among galaxies of different colors. Our main goal is to compare the profiles of galaxies in the blue sequence, green valley, and red sequence at fixed stellar mass to determine how they differ and if they shed light on a plausible evolutionary path. We also highlight important differences between mass-weighted radii and light-weighted radii as measures of galaxy size.

2.4.1 Median Surface Brightness and Mass Density Profiles as a Function of Color

Before presenting profiles for the whole sample, we show, in the top row of Figure 2.7, i-band surface brightness (SB) profiles, $\mu_i(R)$, for a random sample of 20 blue, green, and red galaxies in a single mass and redshift slice. To facilitate comparison, we overplot blue and red galaxies in the left column and green and red galaxies in the right column. Starting with the upper-left panel, we see that blue galaxies have systematically brighter outer regions than red galaxies but have fainter inner regions. In the upper-right panel, we see that green and red galaxies have rather similar i-band profile shapes. Taken together, these SB profiles show

that as galaxies evolve from blue to red (at fixed mass), their outer disks fade and their inner regions get brighter.

The bottom row of Figure 2.7 converts these brightness profiles to surface mass density (SD) profiles, $\Sigma(R)$, using the M/L relation in Figure 2.3. Despite their brighter outer disks, blue galaxies have *nearly identical* outer mass profiles as red galaxies. This can be explained as a consequence of the lower mass-to-light ratios of blue galaxies (i.e., while blue galaxies have bright disks due to young stars, those stars do not dominate the total stellar mass). Despite the similar outer mass profiles, it can be seen that red galaxies have, on average, higher mass densities in the inner regions ($R \lesssim$ a few kpc) than blue objects. The lower-right panel shows that the SD profiles of green and red galaxies are very similar at all radii.

We now move beyond a single mass and redshift bin to examine the SB and SD profiles of all galaxies in the volume-limited sample. Figure 2.8 presents the median i-band SB and SD profiles for galaxies in the sample, divided into the same mass bins used in Figure 2.6. In each mass bin, galaxies are divided into blue, green, and red galaxies based on NUV$-r$ color. The conclusions drawn from Figure 2.7 are essentially the same for the whole sample. Beginning with the SB profiles, what is apparent from the figure is that the SB profiles of green and red galaxies are remarkably similar at all radii in all mass bins. This suggests that

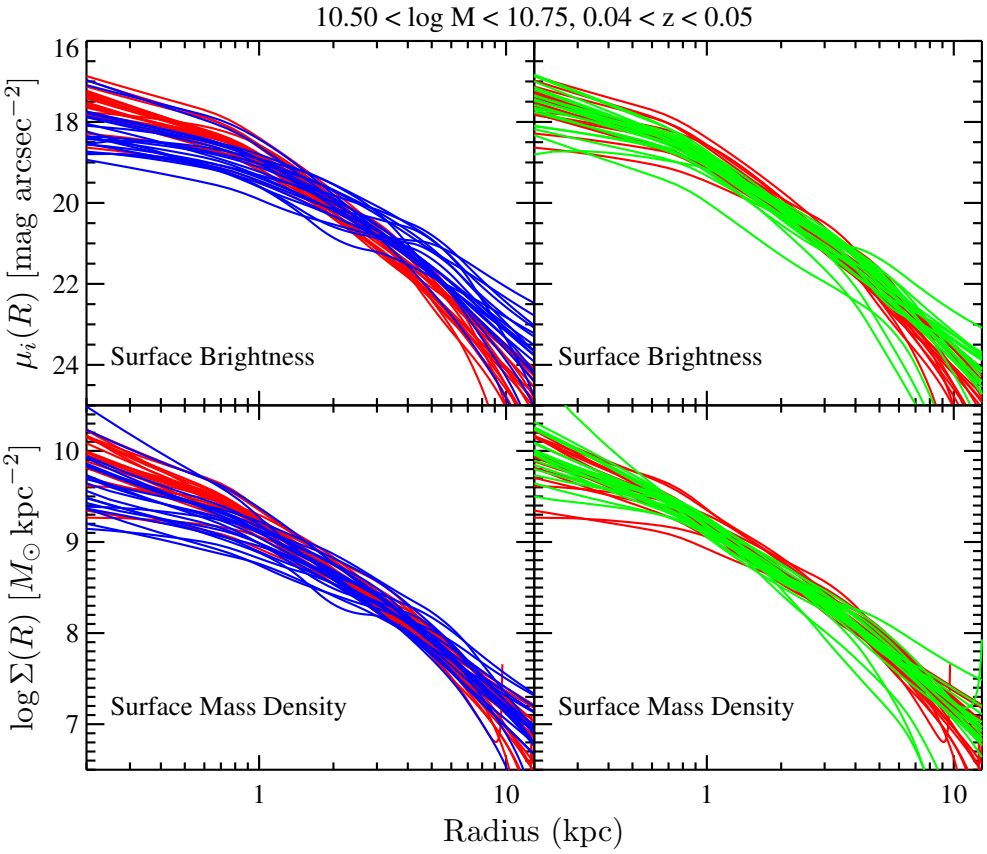

Figure 2.7: Top row: SDSS i-band surface brightness profiles for 20 representative blue, green, and red galaxies with stellar mass $10.5 < \log M_*/M_\odot < 10.75$ and redshift $0.04 < z < 0.05$. Bottom row: Stellar surface mass density profiles for the same galaxies (derived from the i-band profiles). While blue galaxies have brighter surface brightness profiles at large radii, their outer mass profiles are very similar to those of green and red galaxies. In addition, blue galaxies have lower inner mass densities compared to the (quenched) green and red objects.

green and red galaxies are structurally very similar. The second notable aspect is the difference between the SB profiles of the blue and green/red galaxies. In particular, the blue galaxies have significantly brighter outer regions. This is not surprising given the fact that blue galaxies predominately have extended (bright) disks.

Turning to the SD profiles, inspection of Figure 2.8 reveals that the outer parts of *all* galaxies in a mass bin have similar values of $\Sigma(R)$, especially at higher mass. This stands in contrast to the SB profiles, where we noted that blue galaxies have systematically brighter outer profiles than green and red galaxies. In addition, the mass profiles highlight that the main difference in $\Sigma(R)$ between galaxies of different colors is found in their inner regions ($R \lesssim 1$ kpc). At fixed mass, green and red galaxies have inner surface densities systematically larger than blue galaxies by about a factor of 2–3. As mentioned in Section 2.2.3, recently reported IMF variations would *increase* the difference in inner $\Sigma(R)$ between blue and red galaxies.

Taking the view that galaxies evolve from blue to red at fixed mass, we are led to conclude that mass is building up in the inner (bulge-dominated) regions as galaxies evolve. Moreover, most of this buildup occurs *before the galaxy leaves the blue cloud*. This last point is indicated by the observation that the SD profiles of green and red galaxies are nearly identical in their inner regions. If, instead, mass

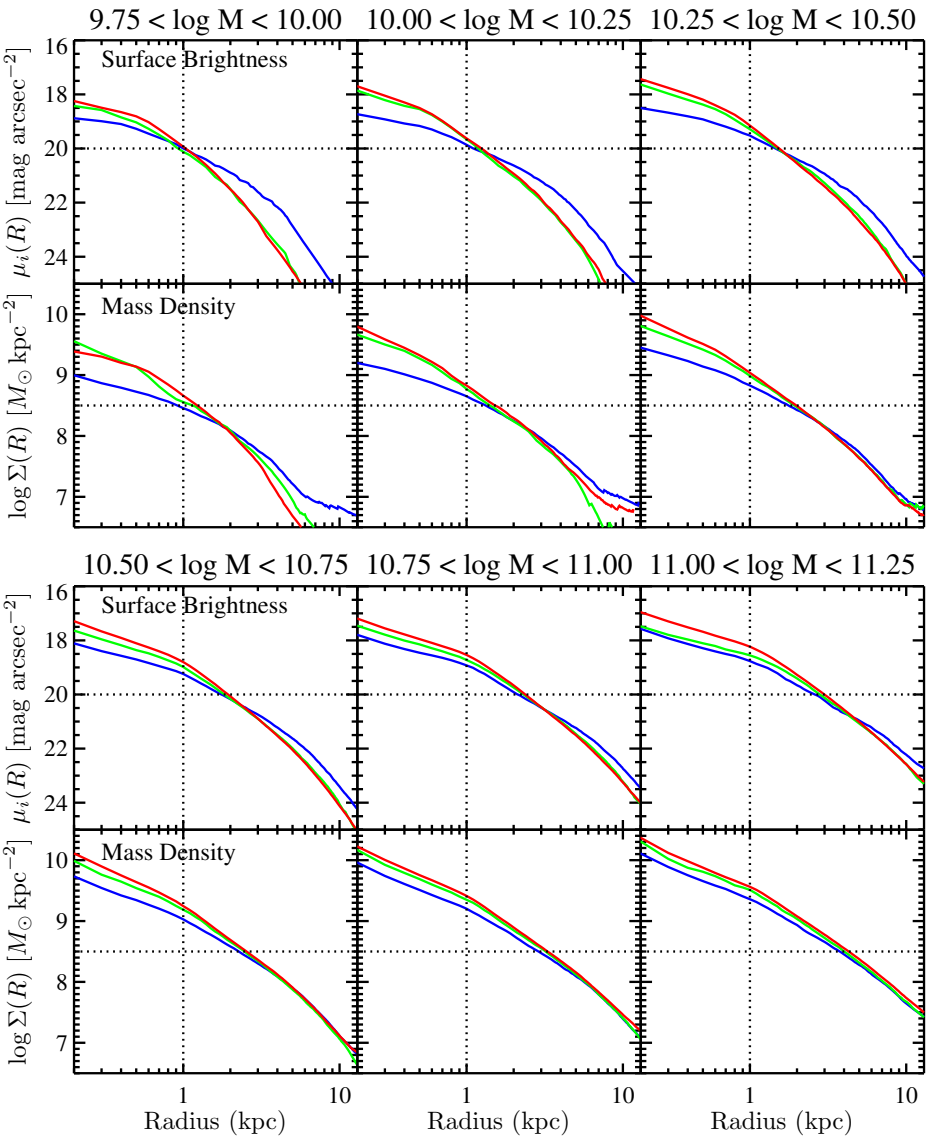

Figure 2.8: Median SDSS i-band surface brightness profiles and mass surface density profiles (derived from the i-band profiles) for galaxies in six stellar mass bins for the volume-limited sample. Profiles are color-coded to correspond to galaxies in the blue sequence, green valley, and red sequence. While the surface brightness profiles for green and red galaxies are nearly identical, blue galaxies have dimmer centers and brighter outer disks; this effect is more pronounced at lower masses. However, the outer mass density profiles are nearly identical for galaxies of all colors, particularly at higher masses. Dotted lines in each panel are the same and serve to guide the eye.

buildup occurred gradually as a galaxy transitioned from blue to red, we would expect to see the green valley mass profiles take on values more intermediate between the blue and red galaxy profiles. This expectation is strengthened by referring back to Figure 2.6. In each mass slice, especially at lower stellar masses where the blue cloud is well-populated, the distribution of galaxies in color-Σ_1 space is consistent with an interpretation in which galaxies increase their inner mass densities while still in the blue cloud. Once they reach a critical value of Σ_1, galaxies are able to quench and move into the green valley. Moreover, Σ_1 remains nearly constant after a galaxy is quenched; this manifests itself as the nearly vertical tracks in Figure 2.6.

Figure 2.9 gives a visual sense of the diversity of galaxy morphologies, even at fixed mass. This montage of SDSS color postage stamps shows a random sampling of galaxies with redshifts between 0.04 and 0.05 and stellar masses $10.25 < \log M_*/M_\odot < 10.5$. The narrow redshift slice was chosen to ensure that the images have comparable physical extent (25 kpc). The top row shows blue galaxies with low Σ_1. As can be seen, these galaxies have extended blue disks and weak central bulges. Given their dim centers, low surface brightness galaxies fall into this category (e.g., the fourth object in the top row). The second row in Figure 2.9 displays blue galaxies with higher Σ_1. For consistency, both rows show galaxies with NUV$-r < 3$. What is striking is the radically different optical sizes

and visual morphologies of the galaxies in the second row compared to those in the top row. These high-Σ_1 objects have much smaller disks and more pronounced bulges.

The third and fourth rows of Figure 2.9 show examples of green valley and red sequence galaxies, respectively. Their sizes and morphologies are very similar to the high-Σ_1 blue cloud objects in the second row. This lends further support to a scenario where nearly all of the bulge buildup takes place while galaxies are still in the blue cloud. Thus, the mass rearrangement must be essentially complete *before* galaxies move into the green valley.

2.4.2 Light-weighted versus Mass-weighted Radii

Figure 2.8 shows that the SB profiles show systematic differences from the SD profiles. For example, at fixed mass, blue galaxies have brighter SB profiles at large radii than quenched objects, yet their outer mass profiles are nearly identical to those of quenched galaxies. This implies that apparent differences in e.g., sizes of blue and red galaxies are likely exaggerated simply because sizes are measured using SB profiles, which are affected by bright blue stars in the disks of star-forming galaxies. This effect has been called "outshining" in some contexts (Reddy et al., 2012; Wuyts et al., 2012), whereby light from recently formed stars biases measurements of radii, stellar population ages, or other parameters.

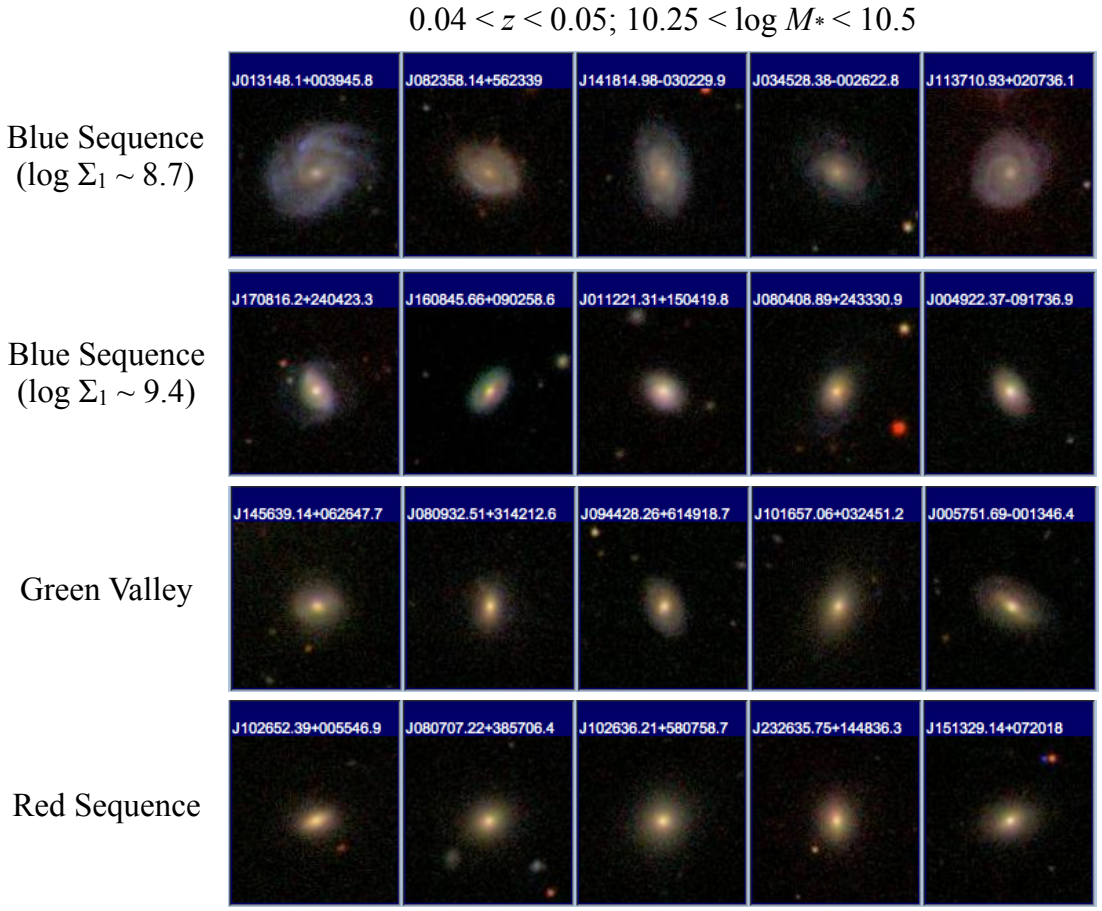

Figure 2.9: Montage of SDSS postage stamps ($\sim$ 25 kpc on a side) for a selection of galaxies with redshifts $0.04 < z < 0.05$ and stellar masses $10.25 < \log M_*/M_\odot < 10.5$. Top row: Blue sequence galaxies with relatively low Σ_1 ($\log \Sigma_1 \approx 8.7$). Second row: Blue sequence galaxies with relatively high Σ_1 ($\log \Sigma_1 \approx 9.4$). Note the striking differences between even blue sequence galaxies at the same mass. Third row: Green valley galaxies. Bottom row: Red sequence galaxies. Note that green and red galaxies have similar sizes and more prominent bulges than the blue galaxies in the top row. However, the blue galaxies in the second row bear a strong resemblance to the green and red galaxies. It is plausible that the green and red galaxies are the quenched and faded counterparts of the high-Σ_1 blue galaxies in the second row.

Figure 2.10 highlights the effects of outshining by comparing measures of galaxy size using light-weighted radii and mass-weighted radii. The ratio of the mean radius for blue galaxies to the mean radius for green and red galaxies, $\langle R_{50,\mathrm{BC}} \rangle / \langle R_{50,\mathrm{GV/RS}} \rangle$, is plotted as a function of stellar mass. Three radius definitions are used: g-band half-light radius, i-band half-light radius, and half-mass radius. Half-light radii are the 50% Petrosian radii from the SDSS database, and half-mass radii are computed from the SD profiles.

For each radius definition, the general trend is that the size difference between star-forming and quenched galaxies decreases slightly with stellar mass. This trend is consistent with the observed increase in bulge-to-total ratios with stellar mass (e.g., Kauffmann et al., 2003b). That is, more massive galaxies, regardless of color, tend to be more bulge-dominated than lower-mass objects, which reduces the difference in size between blue and red galaxies. What is striking, however, is the comparison between different radius definitions at a fixed mass. In particular, for $M_* \gtrsim 10^{10.25}\,M_\odot$, light-weighted radii significantly exaggerate the difference in size between blue and green/red galaxies, when compared to mass-weighted radii, which ostensibly represent "true" sizes. As expected, the effect is slightly more pronounced when using the bluer g-band radii, which are more sensitive to younger stars than i. That the half-mass size ratio is always larger than unity indicates that quenched galaxies are more compact than their star-forming progenitors when

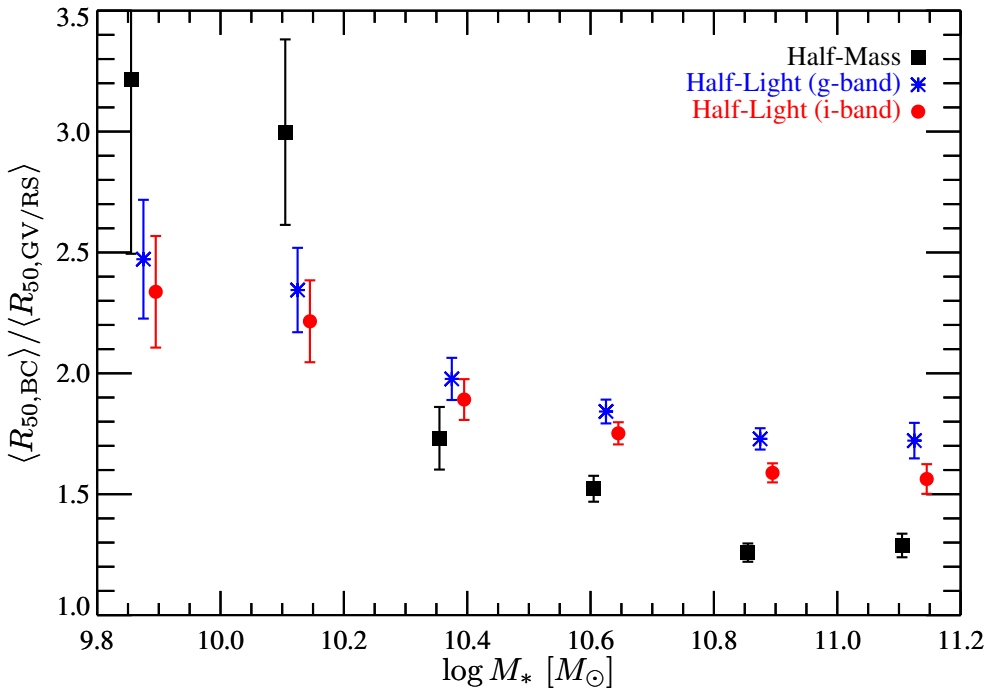

Figure 2.10: Ratio of mean galaxy radius of blue cloud galaxies to quenched galaxies, $\langle R_{50,\mathrm{BC}}\rangle / \langle R_{50,\mathrm{GV/RS}}\rangle$, as a function of stellar mass. Each symbol represents a different definition of radius: g-band half-light radius (blue stars), i-band half-light radius (red circles), and half-mass radius (black squares). While at lower masses all three radii give consistent ratios, light-weighted radii exaggerate the difference in size between star-forming and quenched galaxies at higher masses. Individual points have been offset horizontally for clarity. Error bars indicate the uncertainty in the mean ratio, and are large at lower masses due to the small number of objects in those bins.

using mass-weighted sizes. This is due, presumably, to the growth of the bulge as galaxies evolve.

Because of outshining, light-based structural parameters are not generally indicative of the underlying stellar mass distribution of a galaxy. Szomoru et al. (2013) show that mass-weighted radii are $\sim 25\%$ smaller than light-weighted radii for massive galaxies out to $z \sim 2$. A similar result is seen in Wuyts et al. (2012) using resolved mass maps of massive, star-forming galaxies out to $z \sim 2.5$. Our analysis sharpens these results by separating objects according to both color and mass and discussing how outshining affects star-forming and quiescent galaxies *differentially*. Indeed, we caution that this differential outshining may exaggerate apparent trends in e.g., Sersic index as a function of color. It is well-known that blue galaxies have mainly low Sersic indices ($n \approx 1$) while red galaxies predominately have higher values ($n \approx 4$). This is in part due to the higher bulge-to-total ratios in red galaxies. However, as the SB profiles show, while it is clear that the bulge component increases in strength from blue to red, the outer disks also *fade* as galaxies redden. These two effects act together to increase the apparent difference in n. Our analysis shows that the underlying mass density profile is nearly the same among blue and red galaxies, especially in the outer parts, i.e., the mass density does not "fade" as a galaxy reddens. It thus appears that the "bimodality" of Sersic values is exaggerated by fitting light profiles rather than

mass profiles. A comparison between light-weighted and mass-weighted Sersic indices is urgently needed, but it is beyond the scope of this work.

2.5 Comparing Inner Surface Mass Density with Velocity Dispersion

Our results thus far have revealed that Σ_1 is correlated with the SF state of galaxies and may serve as a useful diagnostic of quenching. In this section, we examine the use of velocity dispersion as an alternative tracer of quenching, as proposed in Wake et al. (2012b), and compare it with Σ_1. We also discuss how measurements of Σ_1 may offer a new method of examining black hole growth in galaxies.

2.5.1 The Relation between Velocity Dispersion and Stellar Mass

Figure 2.11 plots velocity dispersion scaled to a circular aperture of radius 1 kpc, σ_1, versus stellar mass for galaxies with $0.005 < z < 0.075$. Points are color-coded according to their NUV$-r$ color. A least-squares fit to green and red galaxies is also plotted:

$$\log \sigma_1 = 2.09^{+0.05}_{-0.08} + (0.29^{+0.13}_{-0.10})(\log M_* - 10.25), \tag{2.2}$$

with the uncertainties corresponding to the 16th and 84th percentile confidence limits obtained by bootstrap resampling the data within their errors. SDSS fiber velocity dispersions were scaled using the relation in Cappellari et al. (2006) calibrated using the early-type galaxies in the SAURON survey, $\sigma \propto R^{-0.66}$. The use of σ_1 facilitates comparison with Σ_1.

The distribution of points in Figure 2.11 is very similar to that seen in Figure 2.4. In particular, green and red galaxies lie on a well-defined, mass-dependent relation, while blue galaxies scatter below the ridge line. Since σ_1 is determined spectroscopically, it is a more direct (dynamical) tracer of the total mass distribution (baryonic + dark matter) in the inner regions. This allows us to use σ_1 as an independent check of our previous result that the inner mass distribution builds up as galaxies evolve from blue to red. The consistent mass dependence of both Σ_1 and σ_1 imply that this buildup is a robust result and not simply due to possible systematics in converting light to mass when measuring Σ_1.

2.5.2 The Relation between Σ_1 and Velocity Dispersion

To test recent claims that velocity dispersion is better correlated with color than other structural parameters (Wake et al., 2012b), Figure 2.12 plots NUV$-r$

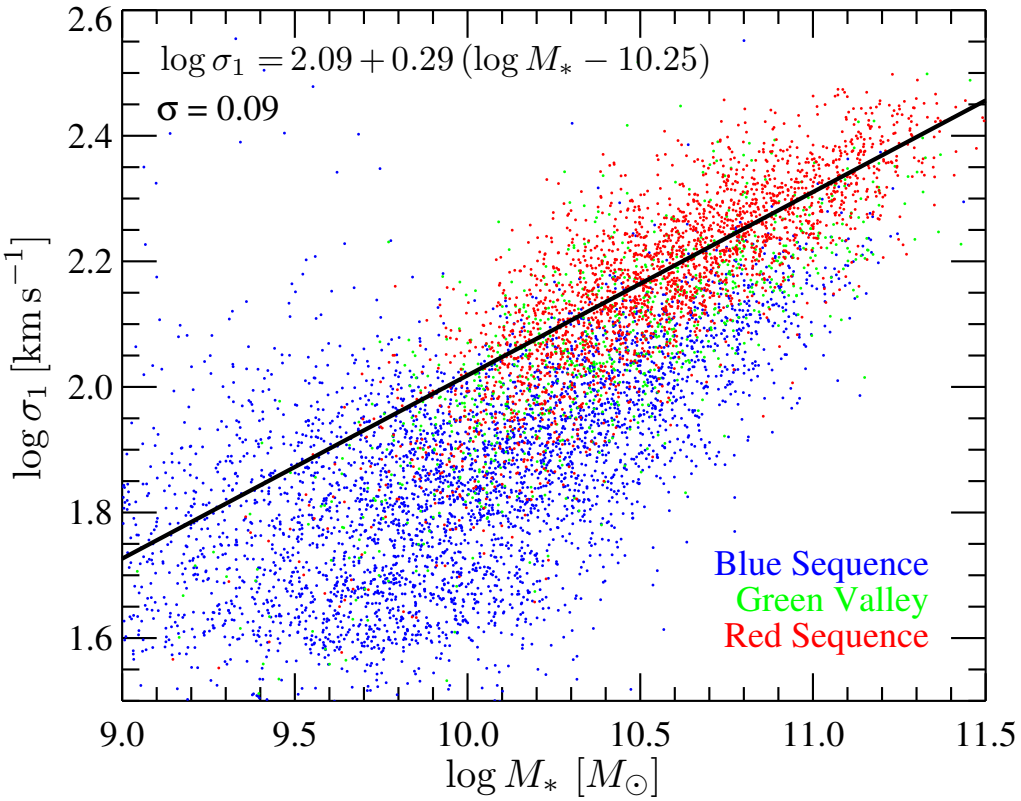

Figure 2.11: Velocity dispersion scaled to a 1-kpc aperture, σ_1, vs. stellar mass for galaxies with $0.005 < z < 0.075$. The points are color-coded by NUV$-r$ color. The line is a least-squares fit to green and red galaxies only, $\log \sigma_1 = 2.09^{+0.05}_{-0.08} + (0.29^{+0.13}_{-0.10})(\log M_* - 10.25)$. The 1σ vertical scatter of green and red galaxies about the relation is indicated in the figure (0.09 dex). The strong trend with stellar mass supports the notion of a mass-dependent quenching threshold, previously seen in Figure 2.4.

color against velocity dispersion in six stellar mass bins. This plot can be compared to Figure 2.6. Inspection of Figure 2.12 shows that σ_1 is fairly well-correlated with NUV$-r$ color in galaxies more massive than $\sim 10^{10.25}\,M_\odot$. However, at lower masses, the correlation is less obvious because the distribution shows increased scatter, possibly due to increased measurement errors in σ_1. This is in contrast to the behavior of Σ_1, which shows comparatively little scatter in all mass bins (Figure 2.6). Except for this, the two figures are remarkably similar.

Σ_1 and σ_1 are compared directly in Figure 2.13. As can be seen, the two quantities are strongly correlated. The line is a least-squares fit of all galaxies, incorporating errors in both Σ_1 and σ_1,

$$\log \Sigma_1 = (9.18^{+0.04}_{-0.05}) + (1.99^{+0.22}_{-0.16})(\log \sigma_1 - 2.0) \tag{2.3}$$

with Σ_1 in $M_\odot\,\mathrm{kpc}^{-2}$ and σ_1 in $\mathrm{km\,s}^{-1}$. Bootstrap resampling was used to compute uncertainties in the slope and zeropoint. The 1σ vertical scatter about the relation is 0.24 dex. The scatter is reduced to 0.18 dex when considering only green and red galaxies. Intriguingly, the power-law slope of ~ 2 between Σ_1 and σ_1 is consistent with predictions from simple scaling arguments. Neglecting projected mass outside a radius R and assuming homologous structure, the surface density $\Sigma \propto M/R^2$, and the mass is related to velocity dispersion and radius by the virial

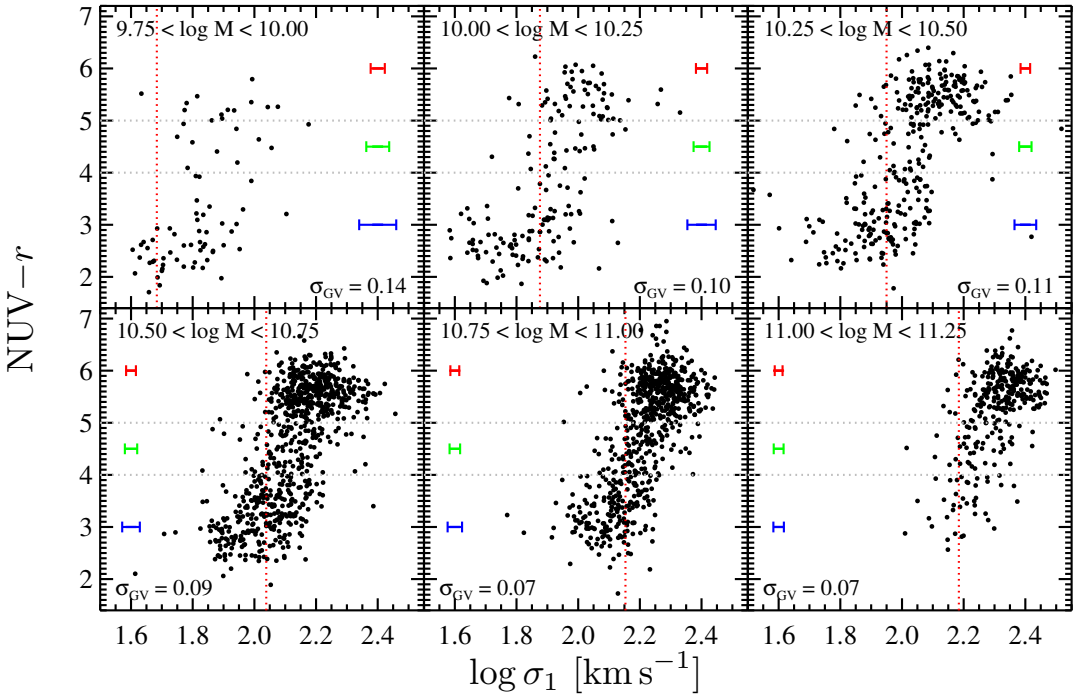

Figure 2.12: NUV$-r$ vs. σ_1 in six stellar mass bins for the volume-limited sample. Error bars indicate median errors in σ_1 for blue, green, and red galaxies in each mass bin. Dotted gray lines indicate the division between blue, green, and red galaxies. The horizontal scatter in dex of the distribution in the green valley is indicated at the bottom of each panel. The dotted red lines indicate the value of σ_1 above which 80% of the red galaxies are found in each mass bin. Though a correlation between σ_1 and NUV$-r$ color is apparent, the scatter and measurement errors in σ_1 become increasingly severe toward lower masses.

theorem ($M \propto \sigma^2 R$). Combining these relations we obtain

$$\Sigma \propto \frac{\sigma^2}{R}, \tag{2.4}$$

or, assuming all quantities are measured within a constant aperture of 1 kpc,

$$\Sigma_1 \propto \sigma_1^2. \tag{2.5}$$

Thus simple scaling arguments predict a power-law relation with a slope of 2, which matches the observationally determined slope. We stress that our use of the virial theorem assumes that galaxy bulges are homologous, which is not necessarily the case, considering the large diversity of galaxy morphologies in our sample, and it also neglects contributions to the surface mass density from regions that are outside a 1-kpc radius sphere centered on the nucleus. In spite of this, the consistency between the observed and predicted relations is an intriguing result.

The tight correlation between Σ_1 and σ_1 implies that the value of one quantity can be predicted given knowledge of the other (especially for quenched galaxies, where the scatter is smaller). In particular, this relation might be used to estimate velocity dispersions in local galaxies without the need to obtain time-consuming spectra. Given the relative abundance of high-resolution photometry of high-redshift galaxies, the result might even be a useful tool in studying the dynamical

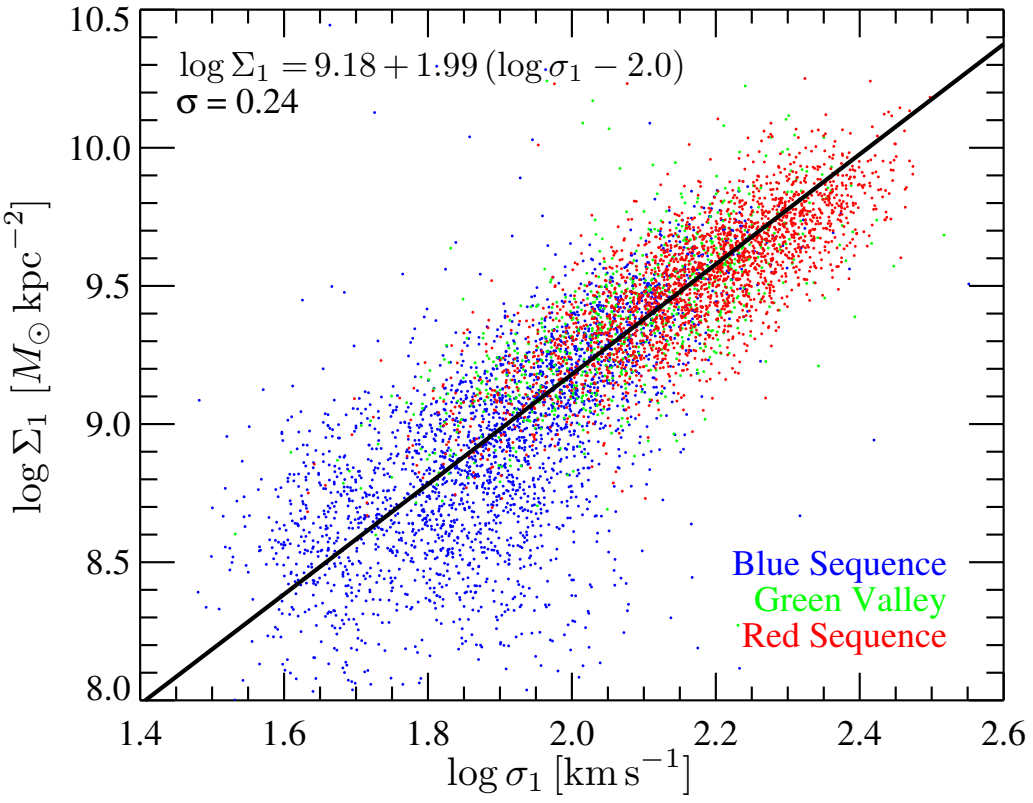

Figure 2.13: Σ_1 vs. σ_1. Galaxies with $9.75 < \log M_*/M_\odot < 11.25$ and $0.005 < z < 0.075$ are plotted. Points are color-coded according to NUV$-r$ color. The line is a least-squares fit to *all* galaxies in the plot incorporating errors in both quantities. There is a strong correlation between the inner surface density and velocity dispersion, $\log \Sigma_1 = (9.18^{+0.04}_{-0.05}) + (1.99^{+0.22}_{-0.16})(\log \sigma_1 - 2.0)$. The slope of the relation is consistent with simple dynamical arguments (see text). The existence of such a relation suggests that both quantities are sensitive to bulge buildup. The 1σ vertical scatter about the relation is indicated at upper left (0.24 dex). The scatter is reduced to 0.18 dex when including only the green and red galaxies.

properties of more distant objects. Of course, it would first have to be established that this correlation between mass density and velocity dispersion remains valid at higher redshifts.

To further investigate the relation between surface mass density and velocity dispersion, Figure 2.14 plots Σ_1 against σ_1 in bins of stellar mass. In each panel, the best-fit least-squares line is included, and the slope of each relation is indicated. The slopes are all consistent with each other and with the value of 1.99 found in Figure 2.13. What this implies is that a tight correlation between inner surface density and velocity dispersion exists even at fixed stellar mass. In other words, both quantities are equally sensitive to central bulge buildup, and this behavior is independent of stellar mass. However, Σ_1 is attractive in a practical sense because it is more accurate even in lower-mass galaxies, where σ_1 has large errors or cannot be measured reliably (in SDSS) at all.

Recently, Wake et al. (2012b) asserted that galaxy color is best correlated with velocity dispersion rather than with stellar mass, effective surface mass density, or Sersic index. Their conclusion was reached by examining the strength of *residual* color correlations when one parameter is held fixed: only weak residual correlations between color and any of the remaining parameters were found at fixed velocity dispersion. But, such correlations manifestly do exist, especially for $\sigma \lesssim 200\,\mathrm{km\,s^{-1}}$ (their Figure 4). To examine structural correlations with quench-

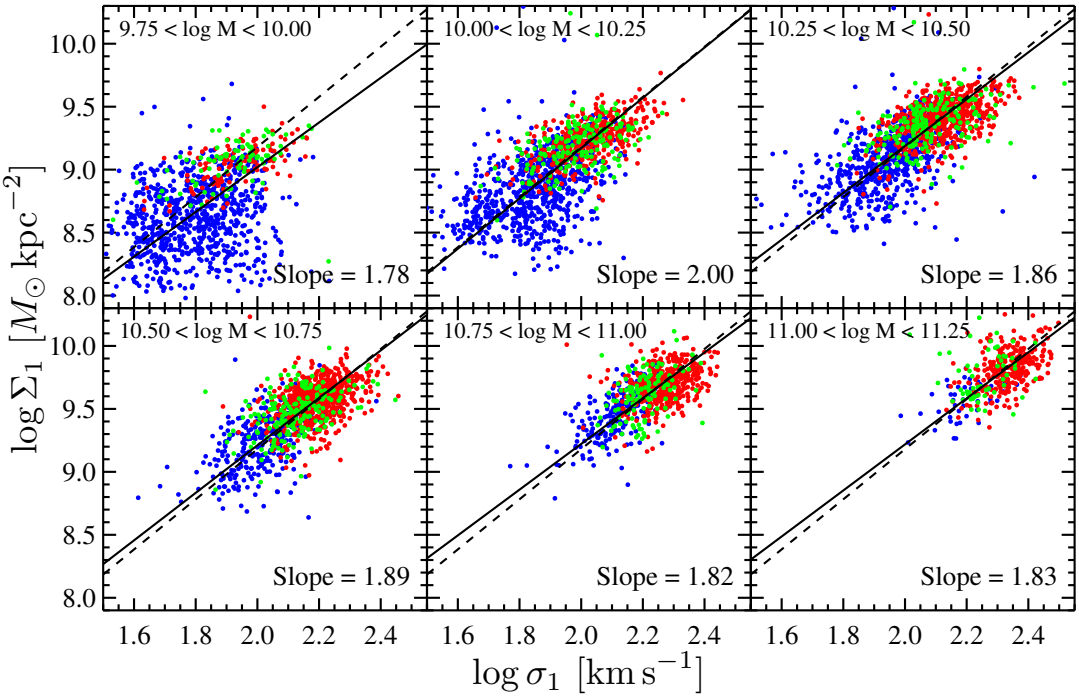

Figure 2.14: Σ_1 vs. σ_1 in six stellar mass bins for galaxies with $0.005 < z < 0.075$. Points are color-coded according to NUV$-r$ color as in Figure 2.13. In each panel, the solid line is a least-squares bisector fit to all galaxies in each mass bin. The slope of the best-fit relation is indicated. For reference, the dashed line is the global relation from Figure 2.13. The individual relations are consistent with that found by fitting to all galaxies simultaneously. The existence of a relation between Σ_1 and σ_1 at fixed mass suggests that both quantities are indeed sensitive to mass increase in the *inner* regions, i.e., to bulge buildup.

ing, it is necessary to follow trends *along evolutionary paths*, and thus at fixed stellar mass. Once this is done, Σ_1 and σ_1 look equally predictive, except that Σ_1 is more accurately measured in small galaxies.

2.5.3 A New Black Hole Mass Scaling Relation?

At low redshift, the new, tight relation between Σ_1 and σ_1 might also be utilized in studies of the $M_{\rm BH}$-σ relation. Again, since determining σ is time-consuming, one might use Σ_1 as a proxy for velocity dispersion and reassess the implication for the properties of black holes in various galaxies. Alternatively, one might try to establish an entirely parallel $M_{\rm BH}$-Σ_1 relation and explore its implications. Calculating Σ_1 is made easy thanks to the wide availability of high-resolution images of nearby galaxies. Specifically, assuming a $M_{\rm BH}$-σ relation of the form $M_{\rm BH} \propto \sigma^4$ (e.g., Tremaine et al., 2002; Gültekin et al., 2009), and substituting our relation $\Sigma_1 \propto \sigma_1^{1.99}$, we find that $M_{\rm BH} \propto \Sigma_1^{2.0}$. It will be interesting to verify if this prediction is indeed valid for nearby red sequence and green valley galaxies. It will also be interesting to see whether blue galaxies, which lie on the Σ_1-σ_1 relation, lie on or off the $M_{\rm BH}$-Σ_1 relation.

A $M_{\rm BH}$-Σ_1 relation could also be utilized to estimate the amount of growth in black hole mass as a galaxy evolves through the blue cloud and onto the red sequence. Such information would provide useful constraints on the coevolution

of black holes and their host galaxies while they are still forming stars. This is particularly relevant given recent results indicating that AGNs may preferentially exist in star-forming galaxies (e.g., Mullaney et al., 2012; Trump et al., 2013). Assuming that galaxies evolve through the blue cloud at roughly constant stellar mass, Figure 2.6 implies that a galaxy can increase its Σ_1 by a factor of ~ 4 while evolving through the blue cloud. Using our predicted relation, $M_{\rm BH} \propto \Sigma_1^{2.0}$, the black hole would then grow by a factor of ~ 16.

2.6 Discussion

Our discussion addresses several key questions raised earlier. We present alternative interpretations of the thresholds in structural parameters. A brief discussion about rejuvenated SF follows. Finally, we speculate on the possible mechanisms that quench SF and how they relate to the buildup of galaxy bulges and the properties of dark matter halos.

2.6.1 Evolving Galaxies or Evolving Thresholds?

Our interpretation of Figure 2.6 is that galaxies increase their inner mass density (Σ_1) during their evolution through the blue cloud. Once Σ_1 reaches a (mass-dependent) threshold value, galaxies are able to quench. An alternative interpretation is that a galaxy's Σ_1 is set at some early epoch and remains fixed

through time and that the threshold value evolves down in time to "sweep up" galaxies, rather than galaxies building up Σ_1 over time. Indeed, Franx et al. (2008) and Williams et al. (2010) claim to find an evolving threshold surface density that decreases with time[5].

There are two arguments why the interpretation of an evolving threshold is less preferred. First, if the threshold were moving over time, one would expect to see signs of this in the Σ_1 distributions of more massive galaxies today. Assuming that the Σ_1 distributions of massive blue galaxies exhibited a spread comparable to that seen in present-day, *less* massive blue galaxies (i.e., ≈ 0.6 dex total width; Figure 2.6), we would then expect to see a similarly broad Σ_1 distribution in their quenched descendants if Σ_1 is fixed as galaxies move through the green valley. This broad Σ_1 distribution in red sequence galaxies of higher mass is not seen. Rather, the total spread of red galaxies *decreases* with mass from ≈ 0.4 dex in the lowest mass bin to ≈ 0.3 dex in the highest mass bin.

Another way of seeing this is that, if only the threshold moves and Σ_1 does not evolve, the motion of points in Figure 2.6 would all be strictly vertical. Hence, the total width of the Σ_1 distribution from the bottom of the blue sequence to the top of the red sequence would remain the same in all mass bins. This is also not seen: in each mass bin, the width of the Σ_1 distribution narrows toward redder colors.

[5]More precisely, Franx et al. (2008) and Williams et al. (2010) use *effective* surface density ($\propto M_*/R_{\rm eff}^2$), and their samples are not divided into stellar mass bins when obtaining this result.

Both viewpoints imply that the Σ_1 distribution either must start out narrower at higher mass, or, as is more plausible, galaxies are individually evolving upwards in Σ_1 and converging on the limiting value that is set by their stellar mass (Figure 2.4).

Second, galaxies do not live in a vacuum and are not frozen in time. Numerous processes exist which tend to make inner mass densities increase. These processes can be ranked according to whether they are rapid or slow, but all of them depend on the ability of dynamical subpopulations in the galaxy to exchange energy and angular momentum with one another. Examples from fast to slow include gas-rich major mergers (e.g., Toomre & Toomre, 1972), violent disk instabilities (e.g., Dekel et al., 2009; Ceverino et al., 2010; Cacciato et al., 2012), gas-rich minor mergers (e.g., Mihos & Hernquist, 1994), and bar and related non-axisymmetric disk instabilities (e.g., Kormendy & Kennicutt, 2004). All of these processes raise inner mass density by driving gas toward the center in a dissipative manner.

Thus, we *know* that galaxy inner mass densities are increasing, the only question is by how much and how fast. To assess this, it is appropriate to note that our SDSS data reflect galaxies at the present epoch, which have mostly settled down into dynamical equilibrium. It is thus appropriate to consider bulge-building processes that are operative now, which leads us to focus on the slower processes listed above. Reliable rates for inner mass density buildup in mature disk galaxies

require very accurate hydrodynamic simulations, which are only now becoming feasible. As an alternative, we cite the analytic toy model of Forbes et al. (2012), which models the rather modest effects of gravitational disk instabilities. The net result from that process alone is a buildup in inner mass density by a factor ~ 2 since $z \approx 2$. This is consistent with the average difference in inner mass density between blue and red galaxies seen in our data (Figure 2.8), which suggests that this process could be a significant contributor. Also, Patel et al. (2013) present *observational* evidence that blue, star-forming galaxies *continually* grow their inner mass density as they evolve from $z \sim 1$ to the present day.

2.6.2 The Utility of Σ_1 and σ_1 as Quenching Predictors

The results presented above highlight the connection between inner mass density and the quenching of SF. It is not obvious whether the trends seen are causative or merely predictive of quenching. For now, we discuss the predictive nature of the correlation between color and Σ_1 (Figure 2.6). In this, we follow previous authors who also looked for structural parameters that are predictive of quenching (Kauffmann et al., 2006; Bell, 2008; Franx et al., 2008; Wake et al., 2012b; Cheung et al., 2012). Those efforts were only partially successful because every parameter tried (e.g., stellar mass, effective surface density, or Sersic index) proved to show scatter, i.e., at a fixed value of the parameter, one could find

both blue and red galaxies. In this respect, our new parameter Σ_1 has a similar weakness. Nevertheless, our approach has several merits worth discussing.

A key feature of our analysis is the use of narrow mass slices to remove global trends with stellar mass. By doing so, we have been able to identify plausible evolutionary tracks (Figure 2.6). Such tracks would have been strongly blurred out if we had considered all galaxies together because of the strong trend between Σ_1 and stellar mass in Figure 2.4. In addition, our use of UV data from *GALEX* provides a clearer separation between star-forming and quenched galaxies. The improved dynamic range permits a more detailed study of galaxies that are *currently* transitioning from blue to red, an advantage that has not been exploited previously.

The validity of our assumption that galaxies quench at essentially fixed mass bears further discussion. In Section 2.3, we appealed to simple physical arguments that show that galaxies do not increase their mass significantly over the expected quenching timescale ($\sim$ 1 Gyr). Indeed, the mass doubling time is several Gyr (from $z \approx 1$ to 0; Marchesini et al., 2009; Behroozi et al., 2013), suggesting that our assumption of evolution through the green valley at constant mass is reasonable. Nevertheless, it is worth verifying explicitly how such mass growth would affect our results. Figure 2.15 presents the relation between NUV$-r$ and Σ_1 for galaxies in our sample, this time divided into mass bins that are tilted in the color-mass

diagram, with the slope of the tilt corresponding to a growth in stellar mass by a factor of 2 from the blue cloud to the red sequence. Compared with Figure 2.6, it is apparent that the overall distributions remain essentially unchanged, and the total increase in Σ_1 along an evolutionary path is, if anything, increased. Thus, our results are robust even when incorporating realistic mass growth rates explicitly.

Other potentially valid structural parameters include total stellar mass and inner velocity dispersion. However, the former is known to be a poor predictor of quenching (Franx et al., 2008; Bell et al., 2012; Cheung et al., 2012), and the latter is seemingly equivalent to Σ_1 in its predictive power (see below).

Thus, the situation is fundamentally different for color overlap in Σ_1 compared to color overlap in stellar mass. The latter reflects the fact that mass by itself is a genuinely poor predictor of color whereas the former (at fixed stellar mass) reflects the fact that galaxies evolve rapidly in color after attaining a certain value of Σ_1. The key difference is that galaxies evolve in Σ_1 (and color changes) in a single mass bin whereas the locus of points in the color-mass diagram does *not* reflect a *single* evolutionary track.

A benefit of using Σ_1 as a tracer of quenching is that it is measured from galaxy *mass* profiles, rather than from *light* profiles. As shown in Figures 2.8 and 2.10, the surface brightness profiles exaggerate the difference in structure between

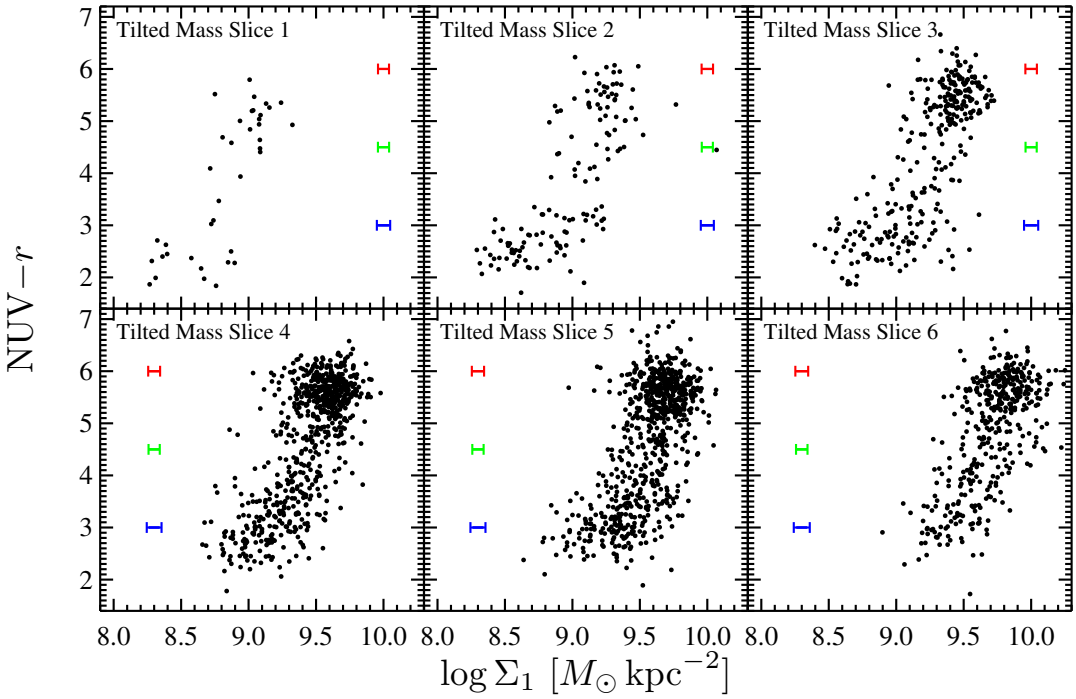

Figure 2.15: NUV$-r$ vs. Σ_1 for the volume-limited sample. Each panel corresponds to a *tilted* mass slice in the color-mass diagram, with the slope of the tilt corresponding to a growth in stellar mass by a factor of 2 from the blue sequence to the red sequence. Compared to Figure 2.6, the shape of the distribution in each panel remains nearly the same, implying that our results remain unchanged even when incorporating realistic mass growth rates explicitly.

blue and red galaxies. This impacts measurements of other structural parameters (e.g., effective surface density, effective velocity dispersion, and Sersic index), which are traditionally based on light profiles. In other words, this "outshining" may exaggerate previously seen trends between color and these parameters, such that the strong differences between the structure of red and blue galaxies is simply dependent on whether a galaxy is star-forming or not. Using mass-weighted versions of these parameters would decrease the apparent strength of these trends. With the availability of high-resolution data at increasingly large redshifts, the use of mass profiles in characterizing structure is becoming more common in galaxy evolution studies (e.g., van Dokkum et al., 2010; Wuyts et al., 2012; Patel et al., 2013; Szomoru et al., 2013).

2.6.3 On the Verticality and Scatter of Evolutionary Tracks

As seen in Figures 2.6 and 2.12, green and red galaxies trace out a nearly vertical distribution in each mass bin. What are the implications of the verticality of these plausible evolutionary tracks? What does the width of the distribution, particularly in the green valley, tell us about the relation between galaxy structure and quenching?

To address these questions, suppose that the distribution in Figure 2.6 were a *perfectly narrow* step function, but that Σ_1 has scatter caused by measurement

errors. The step function would then be blurred, and both red and blue galaxies would be found at the same value of Σ_1. Thus, under a highly non-linear trend like a step function, standard measures of prediction accuracy, such as the relative number of red and blue galaxies at fixed Σ_1, would tend to break down due to the confounding effects of measurement error on an intrinsically narrow distribution.

An alternative way to view this is relative timescales. If galaxies quench at fixed mass, the verticality of the tracks in Figure 2.6 is due to rapid evolution in color after reaching a critical value of Σ_1. Thus, it is impossible, in principle, to find a structural parameter that perfectly predicts the quenching state (color) if the quenching timescale is very rapid compared to the evolution timescale of the relevant structural parameter. In other words, the change in structure "lags behind" the change in galaxy color.

One way to proceed is to ask whether it is possible to narrow the scatter still further below that seen in Figure 2.6. If so, this may indicate that galaxies indeed evolve over a step function in Σ_1 and that the observed scatter is (solely) due to measurement error. We attempted to reduce the scatter by retreating more closely to the original data. Specifically, instead of Σ_1, we used the average i-band surface brightness, μ_1, within a 1-kpc radius aperture. This eliminates the M/L conversion, which has a scatter of 0.04 dex. To reduce other sources of uncertainty, we selected a narrowly defined subsample for this test: only galaxies

in our volume-limited sample with $10.25 < \log M_*/M_\odot < 10.5$ located between $0.045 < z < 0.055$ were chosen. The chosen redshift range permits us to calculate μ_1 without having to interpolate between SDSS apertures. The scatter in μ_1 for the green valley is 0.151 dex ($0.38\,\mathrm{mag\,arcsec^{-2}}$), comparable to the 0.154 dex seen in Figure 2.6 for galaxies in the same mass bin. Thus, it appears that the scatter in Σ_1 is not due solely to these measurement uncertainties.

How does velocity dispersion fare in this regard? As seen in Figure 2.12, the typical rms scatter in σ_1 for green valley galaxies is $\lesssim 0.1$ dex. In order to make a fair comparison with Σ_1, the scatter must be multiplied by 2 (the slope of the Σ_1-σ_1 relation in Figure 2.13). Doing so, we find that the scatter in σ_1 is larger than that for Σ_1 for lower-mass galaxies ($< 10^{10.5} M_\odot$), but is comparable to or smaller than that for Σ_1 for high-mass galaxies ($> 10^{10.5} M_\odot$). The reduced scatter in σ_1 would suggest that σ_1 offers a slightly cleaner measure of the intrinsic scatter in the green valley, at least for high-mass galaxies.

It thus appears that the intrinsic scatter in Σ_1 and σ_1 through the green valley is not zero, and hence it is unclear if a narrow step function is a correct description of the trends seen in Figures 2.6 and 2.12. To be sure, we have not accounted for all possible factors that could contribute to the scatter (e.g., dust effects, inclination, rejuvenated SF [see below]). It would be interesting to investigate systematically these effects with, e.g., semi-analytic models to better understand the behavior

observed in Figures 2.6 and 2.12. Regardless, our results present useful constraints that theoretical models of galaxy evolution need to match.

2.6.4 Constraints on Rejuvenated SF

While the dominant "flow" of galaxies is believed to be from blue to red (e.g., Bell et al., 2004; Faber et al., 2007; Martin et al., 2007), an increasing number of observations have uncovered evidence of previously quiescent galaxies undergoing "rejuvenated" SF as a result of recently acquired gas (e.g., Kaviraj et al., 2007; Salim & Rich, 2010; Thilker et al., 2010; Lemonias et al., 2011; Marino et al., 2011; Fang et al., 2012; Salim et al., 2012). Such a rejuvenated galaxy is driven from the red sequence back into the green valley (or blue sequence). Kauffmann et al. (2006) hypothesized that galaxies with effective surface densities below the threshold value of $\sim 10^{8.5}\,M_{\odot}\,\mathrm{kpc}^{-2}$ undergo increasingly bursty episodes of SF triggered by stochastic gas accretion that can drive red galaxies toward bluer colors. Moreover, these rejuvenation events were predicted to be so rapid and frequent that the color bimodality of galaxies at fixed mass (or effective surface density) was due *purely* to jumping between the blue and red states.

While our results do not rule out that rejuvenation is occurring in some galaxies, we can constrain how it must proceed. We assume first that the stellar mass growth during rejuvenation is small so that the constant-mass slices in Figure 2.6

still apply. Figure 2.6 then shows that galaxies can move from red to blue (at fixed mass) as long as no significant central mass growth occurs. In other words, rejuvenated galaxies are allowed to move vertically in Figure 2.6, with the consequence that any new SF occurs mainly in the outer parts. This is indeed seen in UV images of candidate rejuvenated galaxies, where young stars are seen to form in extended disks and rings (Kauffmann et al., 2007; Salim & Rich, 2010; Thilker et al., 2010; Fang et al., 2012; Salim et al., 2012). Extended UV emission is also seen in some low surface brightness galaxies, and their UV colors are also consistent with rejuvenated SF (Boissier et al., 2008).

According to this interpretation, at least some of the vertical spread in NUV$-r$ color at fixed Σ_1 in Figure 2.6 may be caused by rejuvenation. This is an interesting hypothesis as it picks out certain galaxies that are prime candidates for rejuvenation, namely, those with high Σ_1 but blue colors, and these could be studied further. However, an equally important use of Figure 2.6 is to *limit* the amount of transiting back and forth between the blue and red sequences that can occur. In particular, increasing Σ_1 is a one-way trip—it cannot be undone, at least not easily. Hence, the *net* difference in Σ_1 between blue and red galaxies is important; if all galaxies were making multiple trips back and forth between the red and blue sequences, we would expect their Σ_1 to be more equal, and this is not seen. Even stronger constraints may come from Figure 2.12, which uses

velocity dispersion rather than Σ_1. The tilt of the "hooks" is larger in this figure, further limiting the amount of hopping back and forth that can be taking place at (presumably) fixed σ. The overall conclusion is that the new data permit some degree of rejuvenation, but it cannot be a wholesale phenomenon. Better models and better understanding of the horizontal scatter in Figures 2.6 and 2.12 may be able to tightly limit this process in the future.

2.6.5 Is Quenching a Two-Step Process?

As discussed in the introduction, several processes have been proposed that can shut down SF in galaxies by stabilizing, expelling, and/or heating up any gas in the galaxy or surrounding halo. Broadly speaking, these mechanisms can be divided into two classes: those that are governed by the conditions of the dark matter halo (virial shock-heating of gas) and those that are driven by bulge buildup (e.g., morphological quenching, AGN feedback, and stellar and supernova feedback in a central starburst). Conventional wisdom typically assumes that any one of these processes working alone is sufficient to quench a galaxy's SF. However, the results presented in this paper necessitate a closer examination of this assumption.

We have emphasized that our results imply that galaxy quenching requires the presence of a bulge, but that a bulge alone is not enough to ensure the complete

cessation of SF. This is reflected in e.g., the large vertical scatter in color in Figure 2.6: galaxies with high Σ_1 can be both blue or red. In addition, the critical value of Σ_1 above which galaxies can quench is seen to be a strong function of stellar mass (Figure 2.4). Both observations suggest that a single structural parameter is insufficient to fully predict the quenching state of a galaxy; two parameters may be necessary.

But if one parameter is indeed insufficient, what would be the physical basis for two? A possible answer may be found by realizing that genuine quenching requires that *two* conditions be met: 1) gas internal to a galaxy must be heated/expelled *and* 2) external gas accretion must be permanently halted. The first requirement that internal gas be prevented from forming stars can be achieved by the influence of a strong bulge and its attendant AGN feedback and/or disk stabilization (e.g., Di Matteo et al., 2005; Croton et al., 2006; Martig et al., 2009), or supernova feedback from a central starburst triggered by inflowing gas (e.g., Dekel & Silk, 1986; Hopkins et al., 2006). The state of the bulge is thus one physical property that is plausibly linked to quenching, and can be traced by a parameter like Σ_1. Preventing subsequent gas accretion onto the galaxy, however, is a halo-regulated process; gas becomes shock-heated once the halo reaches some critical mass ($\sim 10^{12}\,M_\odot$; Birnboim & Dekel, 2003; Dekel & Birnboim, 2006). Thus, our sought-after second parameter must be able to trace the state of a galaxy's

dark matter halo. Direct observational measurements of halo properties (mass, size, etc.) are impossible, and hence indirect indicators are needed. Candidate parameters include a galaxy's velocity dispersion (Wake et al., 2012a) or its total stellar mass (Li et al., 2013).

Having recognized that quenching is a two-step process best described using two structural parameters, the next issue is to understand the connection between bulge-driven and halo-driven quenching processes. In other words, how does the bulge know about the halo, or vice versa? We speculate on some potential methods to link the two together. Recent galaxy simulations have shown that the formation of a stable virial shock can be triggered by a minor merger that sets off a shock wave in the unstable gas in a halo around the critical mass (A. Dekel, private communication). In addition, the minor merger can bring gas into the center of the galaxy, form additional stars (increasing Σ_1), and perhaps trigger an AGN. Another possibility is that AGN feedback is most effective at heating and driving out gas only in halos that have reached the critical mass (Dekel & Birnboim, 2006).

To summarize, the results of this paper and related work point to the importance of the bulge in quenching, namely, that the growth of the bulge is a necessary condition for a galaxy to be quenched, whether by stabilizing or removing any gas. However, in order to prevent further gas accretion, the halo must

also be massive enough to maintain a shock that heats infalling gas and prevents it from cooling onto the galaxy. Moreover, if these two processes do not happen in perfect synchrony, it could result in the horizontal scatter seen in e.g., Figure 2.6. A clear quenching threshold would only emerge in a two-dimensional parameter space that *combines* the operative bulge and halo properties. We have not yet explored what this two-dimensional parameter space looks like. The present paper is a first step, but our measures of halo properties, such as stellar mass or velocity dispersion, are still rather indirect. The next step is to extend the present analysis using a more direct measure of halo properties, such as halo mass, to see if the predictions sharpen further. Such an analysis has been presented in Woo et al. (2015).

2.7 Summary and Conclusions

This paper studies the connection between the quenching of star formation and the growth of the stellar mass surface density in bulges of a sample of central SDSS galaxies with $9.75 < \log M_*/M_\odot < 11.25$ and $z < 0.075$. Bulge growth is traced by the stellar mass surface density within a radius of 1 kpc, Σ_1, and star formation is traced through NUV$-r$ color, which can select galaxies in the green valley that are *currently* transitioning from blue to red. A key and novel aspect of our work is dividing the sample into narrow mass slices, which plausibly selects

groups of galaxies that are traveling along nearly the same evolutionary track. Our main results are as follows.

1. The critical value of Σ_1 above which galaxies are predominantly quenched increases with stellar mass, $\Sigma_1 \propto M_*^{0.64}$; it is not a fixed universal value. This suggests that at least two structural parameters that are not fully correlated are necessary to shut down star formation.

2. At fixed stellar mass, a galaxy's color is closely related to Σ_1. Specifically, Σ_1 seems to increase in the blue cloud until it reaches a mass-dependent threshold value, then star formation quenches, and color starts to redden. Reaching this threshold is a necessary, but not sufficient, condition to be quenched.

3. The surface brightness profiles of blue galaxies are brighter (fainter) in the outer (inner) parts compared to green and red galaxies of the same stellar mass. However, the outer *mass* density profiles are remarkably similar for all galaxies in a given mass slice regardless of color. The one difference is a slightly lower mass surface density in blue galaxies by a factor of $\sim$ 2–3 within 1 kpc. This indicates that the growth of the bulge is the key structural change related to galaxy quenching. In addition, the common use of light profiles to measure quantities like sizes exaggerate structural

differences between blue and red galaxies; stellar mass profiles should be used instead.

4. A strong correlation between Σ_1 and velocity dispersion σ_1 is seen for galaxies of all colors, $\Sigma_1 \propto \sigma_1^{2.0}$. The scaling is consistent with simple dynamical arguments and highlights the fact that both parameters are useful tracers of the central bulge. Using this result, we predict a black hole mass scaling relation of the form $M_{\rm BH} \propto \Sigma_1^{2.0}$, in analogy to the established $M_{\rm BH} \propto \sigma^4$ relation.

5. Our finding that at least two structural parameters are needed to predict quenching (e.g., stellar mass and Σ_1 or σ_1) may be able to reconcile the two broad classes of quenching theories. On the one hand, gas already inside the galaxy must be expelled, heated, or stabilized from forming stars. This process (e.g., AGN feedback, morphological quenching) requires a sufficiently dense bulge and can be traced by Σ_1. This by itself is not sufficient to guarantee quenching, however. Gas accretion onto the galaxy must also be halted, and the relevant process for this (virial shock-heating) activates once the halo reaches a threshold mass.

The results of this work highlight the need to better understand the interplay between the inner conditions of galaxies and their surrounding dark matter halos during the quenching process. In addition, the scaling relations presented here

offer useful constraints on the structural evolution of galaxies that can be compared to theoretical models. It will also be interesting to study the behavior of high-redshift galaxies in these parameter spaces and examine how they differ from the galaxies studied here.

2.8 Appendix: Seeing Effects on Σ_1 Measurements

A concern is that the resolution of the SDSS imaging may compromise the reliability of our measurements of Σ_1, especially at the highest redshifts considered in the volume-limited sample (Figure 2.2). Here we motivate our adoption of $z = 0.075$ as the maximum allowed redshift for the two highest mass bins. Figure 2.16 shows the angular extent corresponding to 1 kpc physical size as a function of redshift. Two dashed lines are plotted indicating (1) the SDSS seeing HWHM of $0\farcs7$ and (2) the smallest aperture radius used in the SDSS pipeline ($R = 0\farcs68$) that is comparable to the seeing. As can be seen, the $0\farcs68$ aperture photometry is usable out to $z = 0.075$, and this value is adopted as the maximum redshift limit to ensure reliable values of Σ_1 for the most massive galaxies in the sample.

To check the validity of this redshift limit, Figure 2.17 presents the values of Σ_1 as a function of redshift for blue, green, and red galaxies. The diamonds indicate

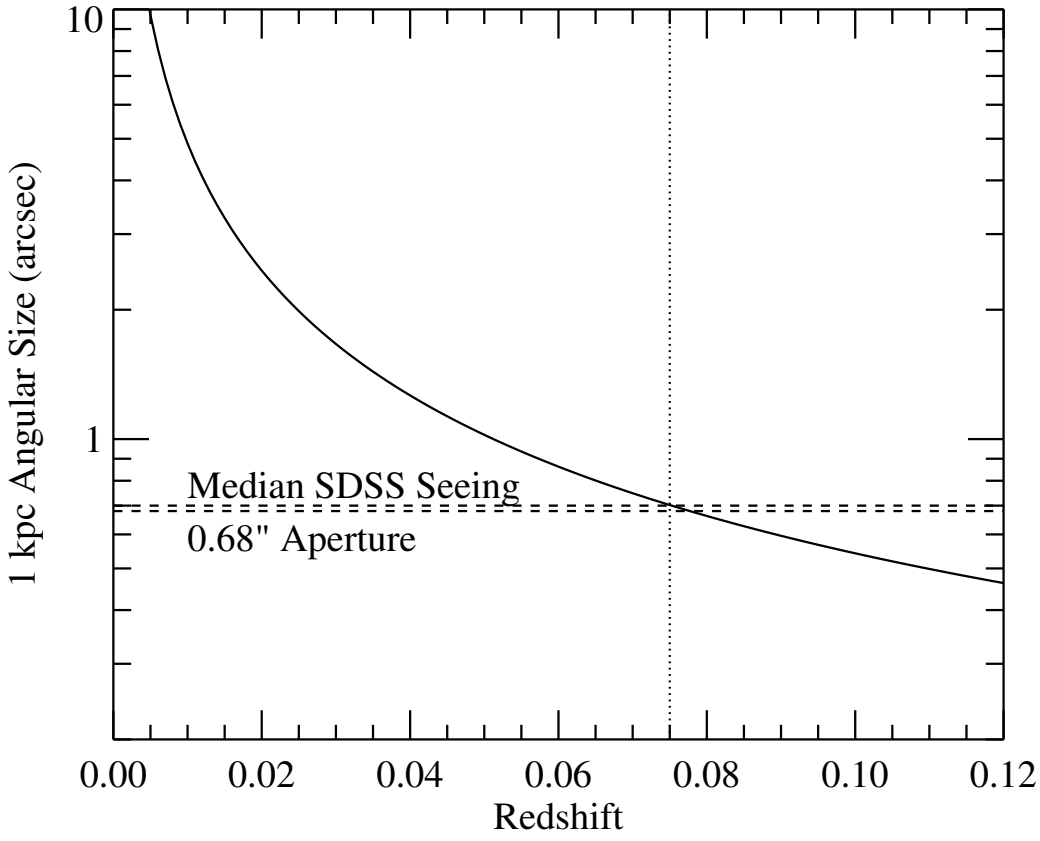

Figure 2.16: The angular size (in arcsec) corresponding to 1 kpc physical size as a function of redshift. The upper dashed line indicates the median SDSS seeing (HWHM = $0\farcs7$). The lower dashed line corresponds to the smallest aperture ($R = 0\farcs68$) used in the SDSS pipeline that is comparable in size to the seeing. To reduce scatter in our measurements of Σ_1 due to seeing, we restrict the redshift range to $z < 0.075$ (vertical dotted line) for the most massive galaxies when defining the volume-limited sample.

the median value of Σ_1 in redshift bins, and the error bars indicate the 1σ scatter of Σ_1 in each bin. In each panel, the vertical dashed line indicates the redshift limit adopted for each mass bin in defining the volume-limited sample (Figure 2.2). The vertical dotted line indicates the redshift $z = 0.075$, above which seeing affects the reliability of measurements of Σ_1. For galaxies of all colors, the median value of Σ_1 and the scatter are essentially constant within the redshift ranges adopted, and even out to $z = 0.075$.

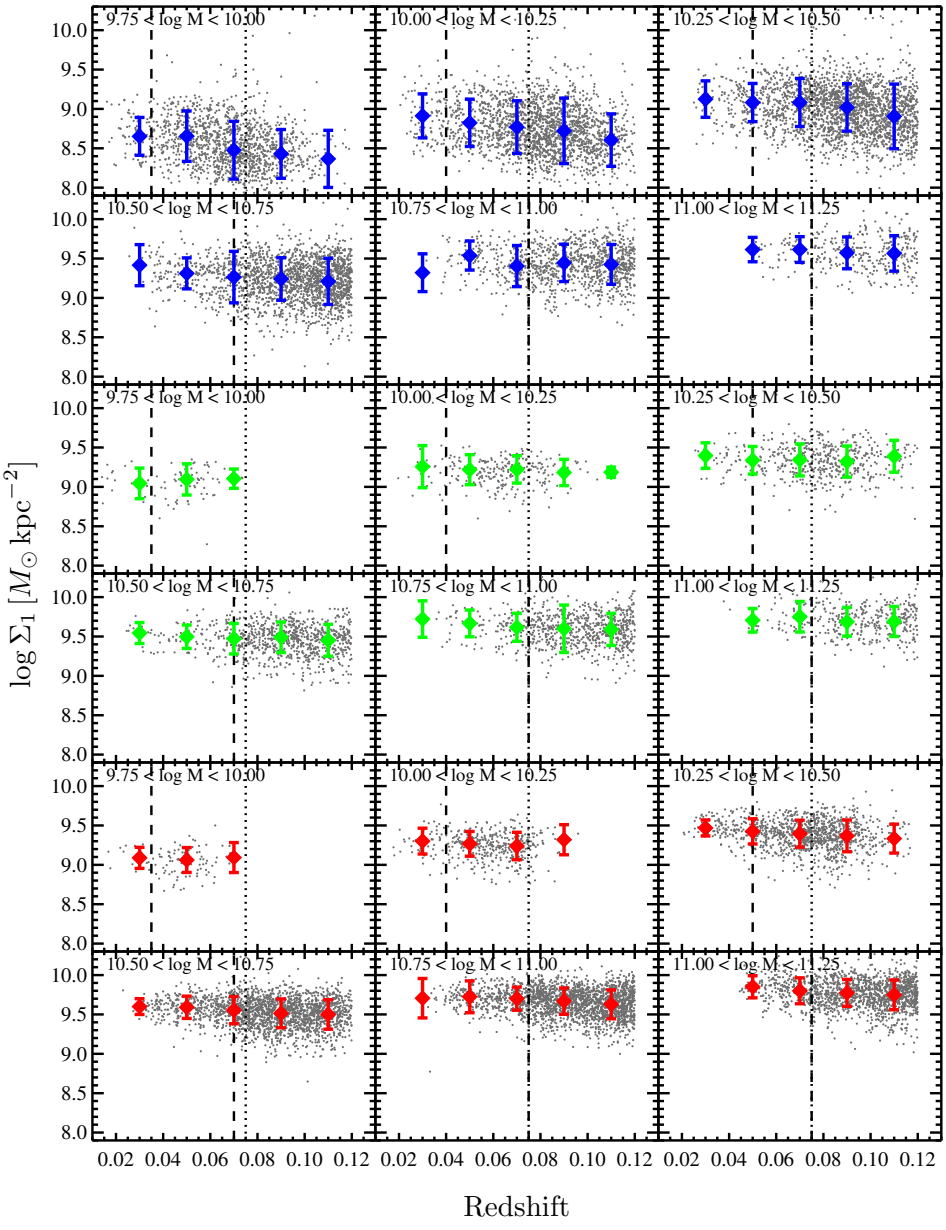

Figure 2.17: Σ_1 vs. redshift for blue (top), green (middle), and red (bottom) galaxies in six stellar mass bins. Diamonds indicate the median Σ_1 in five redshift bins, and the error bars represent the 1σ scatter. The vertical dashed line in each panel indicates the maximum redshift used to define the volume-limited sample for each mass bin (Figure 2.2). The median and scatter in Σ_1 remain essentially constant within the redshift limits for each mass bin. The dotted line indicates the redshift ($z = 0.075$) where the size of the PSF is comparable to 1 kpc.

Chapter 3

Extended Star Formation in $z \sim 0.1$ Green Valley Early-type Galaxies

3.1 Introduction

Early-type galaxies (ETGs) are no longer viewed as a homogeneous population of "red and dead" systems that have ceased forming stars at late times. A mounting wealth of evidence indicates that some ETGs have experienced recent or ongoing star formation (SF). In the nearby universe, the SAURON survey (de Zeeuw et al., 2002) has uncovered recent SF in a subset of the ETGs in its sam-

ple. (Note that the SAURON galaxies are only a representative sample of local ETGs rather than a complete, volume-limited sample.) Shapiro et al. (2010) found that the $\sim 30\%$ of SAURON galaxies with infrared signatures of SF (i.e., PAH emission) are preferentially classified as "fast rotators" (galaxies harboring an embedded disc component), while the non-star forming galaxies are "slow rotators" (spheroidal, kinematically hot systems). This result was corroborated by a stellar population analysis of absorption line maps of the SAURON galaxies: a subset of the fast rotators have SSP-equivalent ages consistent with recent SF, while slow rotators have uniformly old ages (Kuntschner et al., 2010). Intriguingly, the fast rotators tend to be morphologically classified as S0 (lenticular) galaxies, while the slow rotators are almost exclusively E (elliptical) galaxies (Emsellem et al., 2007). This suggests a possible morphological dependence on the observed SF in ETGs, with recent SF preferentially occurring in S0 galaxies.

Evidence for recent or ongoing SF in ETGs is also found in much larger samples available from all-sky surveys, including the Sloan Digital Sky Survey (SDSS; Stoughton et al., 2002), and the *Galaxy Evolution Explorer* (*GALEX*; Martin et al., 2005). The latter provides UV measurements that are crucial in constraining recent SF (Kaviraj et al., 2009). Utilizing both SDSS and *GALEX* photometry, Yi et al. (2005) showed that at least $\sim 15\%$ of their sample of 160 nearby ($z \lesssim 0.1$) ETGs have blue UV-optical colors that they argue can only be attributed to low-

level recent SF. With a larger sample of $\sim$ 2100 morphologically selected SDSS ETGs, Kaviraj et al. (2007) concluded that $\sim$ 30% of their sample have UV-optical colors consistent with SF occurring within the past 1 Gyr, forming $\sim$ 1%–3% of the total stellar mass.

Given these results, it is clear that recent SF in ETGs is more prevalent than once believed. What remains uncertain is how to interpret such SF in the context of galaxy evolution. As is well known, galaxies exhibit a bimodal color distribution, with star-forming galaxies located in the "blue cloud" and passively evolving objects located in the "red sequence" (e.g., Strateva et al., 2001). In between the blue cloud and red sequence lies the "green valley" (GV), which is most apparent when studying UV-optical colors. The movement of galaxies through the GV is presumed to be a net flow from blue to red as a result of the quenching of SF in blue cloud galaxies and the resultant reddening of their colors (Bell et al., 2004; Faber et al., 2007; Martin et al., 2007). Within this framework, the ETGs with recent SF are a mystery: is the observed SF the most recent phase of the original (fading?) star formation, or is it a subsequent episode that has been triggered in a hitherto quiescent galaxy?

Much attention has been focused on the latter explanation of the recent SF in ETGs, which has been termed "rejuvenation" in the literature (e.g., Rampazzo et al., 2007; Thomas et al., 2010; Thilker et al., 2010; Marino et al., 2011). The

newly triggered SF could drive a galaxy *back into* the GV from the (UV-optical) red sequence. In this paper, "rejuvenation" is used to describe SF that causes a quiescent red sequence galaxy to move back into the GV.

One possible cause of rejuvenated SF is gas accretion during gas-rich minor mergers (e.g., Kaviraj et al., 2009). Recently, Thilker et al. (2010) showed that the SF observed by *GALEX* in the outer regions of the nearby S0 galaxy NGC 404 is most likely fueled by an external reservoir of H I gas formed during a recent merger with a gas-rich dwarf galaxy (del Río et al., 2004). Gas-rich major mergers can also trigger nuclear SF; however, the infalling gas is also predicted to trigger strong AGN feedback that expels or heats up the remaining cold gas, effectively quenching SF (e.g., Di Matteo et al., 2005; Hopkins et al., 2006).

Another possible trigger for rejuvenated SF is smooth accretion from the intergalactic medium (IGM). Direct evidence for such accretion has been difficult to observe. However, the presence of extended reservoirs of neutral gas around ETGs has been shown to be a fairly common phenomenon (e.g., Morganti et al., 2006; Catinella et al., 2010). The formation of some of these H I disks has been attributed to accretion from the IGM (e.g., Finkelman et al., 2011; Wang et al., 2011). Cortese & Hughes (2009) found that the "H I-normal" galaxies in their sample of GV galaxies are experiencing recent SF that in a few cases may be rejuvenated, owing to evidence for recently accreted H I disks (i.e., the H I disks

show disturbed or ring-like morphologies indicative of external accretion).

It is important to note that the UV flux seen in ETGs is not necessarily due to recent SF. An excess of UV flux seen in elliptical galaxies (the "UV upturn") is believed to be caused by hot, evolved stars (e.g., horizontal branch stars; Code, 1969; O'Connell, 1999). In this case, the UV emission is expected to be smoothly distributed and follow the optical light profile of the galaxy. Note, however, that UV upturn ETGs are found in the UV-optical red sequence and not in the GV (Yi et al., 2005). AGN activity can also contribute to the UV light seen in ETGs (e.g., Agüeros et al., 2005).

Our understanding of recent SF and rejuvenation in ETGs has been drastically improved thanks to the large samples provided by SDSS and *GALEX*. However, due to the limited spatial resolution of *GALEX* and the typical redshift of SDSS galaxies ($z \sim 0.1$), it has not been possible to resolve the actual physical location of the SF that is inferred based on integrated UV-optical colors. Combining high-resolution UV imaging with the large sample sizes of all-sky surveys could provide important information about the nature and origin of recent SF in ETGs.

As a follow-up to the SDSS/*GALEX* studies mentioned above, Salim & Rich (2010, hereafter SR2010) reported first results from high-resolution *HST* UV imaging of a sample of 29 SDSS ETGs detected by *GALEX*. These galaxies were chosen to have high SDSS concentration and blue UV-optical colors, yet no detectable

emission lines in the 3″ SDSS fiber spectra. This unique combination was intended to select centrally quiescent ETGs yet with high UV excess. The emission line cut also had the effect of discarding ETGs with emission lines due to AGN activity, including most LINERs.

SR2010 found that $\sim 2/3$ of their sample show *extended* UV emission in rings, clumps, and/or spiral arms due to ongoing or recent SF. In Salim et al. (2012, hereafter Paper I), these galaxies were named "extended star-forming early-type galaxies" (ESF-ETGs), and we do the same in this work. The remaining $\sim 1/3$ of their sample had only small-scale SF or centrally compact[1] UV emission. According to SR2010, the ESF-ETGs on average have fairly low far-UV (FUV) dust attenuation and large UV sizes with respect to other galaxies with similar specific star formation rates. The large UV sizes and low FUV dust attenuation were consistent, they argued, with rejuvenated SF taking place in large outer reservoirs of gas acquired in mergers with gas-rich dwarfs or directly from the IGM. However, fading of the original SF could not be ruled out in at least part of the ESF-ETG sample.

A more comprehensive exploration of the same sample is presented in Paper I, supplemented with deep, good-seeing R-band images taken with the WIYN telescope. The discussion there is focused on the qualitative morphologies of the ESF-ETGs as determined from optical and UV images. Galaxies were classified

[1]These compact-UV objects are referred to as "unresolved" UV objects in Paper I.

according to their optical Hubble types as well as by their UV morphologies. Some key conclusions from Paper I are (1) the ESF-ETGs have smooth optical morphologies without signatures of recent merger activity, (2) the origin of the gas is either internal or smoothly accreted from the IGM, and (3) the extended SF phenomenon is preferentially found in S0s and not ellipticals.

The intriguing results discussed in SR2010 and Paper I call out for additional data and analysis to provide further insight into the nature of ESF-ETGs in the GV. Quantitative photometry from the optical and UV images can provide additional information about the stellar populations in the ESF-ETGs. In addition, a more careful comparison between the ESF-ETGs and the SDSS/*GALEX* parent population from which they were selected can help elucidate whether these objects are rare or common. To tackle these issues, we take advantage of the available UV and optical imaging to present a quantitative analysis of the star formation *within* each galaxy via aperture photometry and stellar population modeling. We show that the ESF-ETGs have characteristically red centers containing old stars and blue outer disks due to recent SF, which is expected given how they were selected. The outer disks have a significant population of old stars as well, and we show that the colors are consistent with either the gradual decline of SF or rejuvenation occurring on extended timescales. In addition, we show that a sizable fraction of massive GV galaxies are potentially ESF-ETGs.

The chapter is structured as follows. We describe the SR2010 sample of 29 ETGs, sources of data, and data reduction in Section 3.2. Section 3.3.1 presents optical and UV photometry of the sample, revealing similarities among the ESF-ETGs. An analysis of the stellar populations in the outer disks of the ESF-ETGs is presented in Section 3.3.2. Section 3.3.3 presents stacked SDSS spectra of the bulges of the ESF-ETGs, revealing old central ages and hints of weak emission activity with LINER-like ratios. We search for additional candidate ESF-ETGs from a large sample of SDSS galaxies and estimate the ESF-ETG contribution to the GV in Section 3.3.4. An examination of various possible scenarios to explain the SF in the ESF-ETGs is given in Section 3.4. Our main conclusions are summarized in Section 3.5.

All magnitudes are on the AB system (Oke, 1974). A concordance ΛCDM cosmology with $\Omega_m = 0.3, \Omega_\Lambda = 0.7$, and $H_0 = 70\,\mathrm{km\,s^{-1}\,Mpc^{-1}}$ is assumed.

3.2 Data and Reduction

Descriptions of the sample selection criteria used in SR2010 as well as specifics about the UV and optical imaging are discussed in detail in Paper I. Briefly, a sample of 30 quiescent ETGs with strong UV excess (FUV$-r < 5.3$) were selected from a cross-matched SDSS DR4/*GALEX* IR1.1 catalog (Seibert et al., 2005). High-resolution *HST* Solar-Blind Channel FUV images were obtained for

29 objects. The numbering scheme used in Paper I to identify these objects is retained in this paper, e.g., SR01 is the first object in the sample. Objects are ordered by increasing FUV$-r$ color.

As discussed in Paper I, two objects (SR22 and SR26) were removed from the analysis because of incorrect *GALEX* IR1.1 FUV magnitudes that resulted in erroneously blue FUV$-r$ colors. It was shown that the remaining galaxies divide nicely into three categories based on their UV morphology: extended SF (UV rings and/or arms, 19 objects), small-scale SF (6 objects), and compact (central UV source only, 2 objects). Because the ESF-ETGs represent the majority of the sample and may furthermore represent the behavior of many massive GV galaxies, we focus exclusively on them in the rest of this paper.

3.2.1 SDSS and *GALEX* Data

Placing the ESF-ETGs into the broader context of evolution through the GV requires a broad suite of ancillary data. In particular, we take advantage of additional structural and spectral data available from the SDSS and *GALEX* databases. To make use of updated data since SR2010, we used SDSS DR7 (Abazajian et al., 2009) and *GALEX* GR6 for both the ESF-ETGs and a larger SDSS sample. This larger sample was constructed using the SDSS DR7/*GALEX* GR6 cross-matched catalog available through the *GALEX* CASJobs interface[2].

[2] `http://galex.stsci.edu/casjobs/`

SDSS galaxies with redshifts $0.005 < z < 0.12$ having a *GALEX* NUV and/or FUV detection in the Medium Imaging Survey (MIS) within a $5''$ radius were selected. Objects were excluded if they were more than $0.^{\circ}55$ from the center of the *GALEX* detector to ensure reliable photometry. The resulting $\sim 57,000$ galaxies are referred to in this paper as the "SDSS master sample." In Section 3.3.4, we select galaxies from this sample and compare their properties with the 19 *HST* ESF-ETGs.

For both the ESF-ETGs and the SDSS master sample, integrated magnitudes in *GALEX* FUV, NUV, and SDSS $u, g, r, i,$ and z were retrieved. Spectroscopic redshifts, Galactic extinction, optical Petrosian radii (enclosing 50% of the Petrosian flux), isophotal axis ratios (`isob_r/isoa_r`), and *GALEX* FWHM measurements (a measure of UV diameter) were also collected; the *GALEX* resolution is $\approx 5''$ FWHM. All integrated magnitudes were corrected for Galactic extinction and k-corrected to $z = 0$ using the `kcorrect` code, version 4.2 (Blanton & Roweis, 2007). For reference, the median k-correction for blue cloud (red sequence) galaxies is $\Delta(\mathrm{FUV}-r) = 0.08$ (0.17) and $\Delta(g-r) = 0.06$ (0.17), where Δ(color) is the difference between observed and rest-frame color. Stellar mass estimates and emission line measurements were obtained from the MPA/JHU value-added catalogs for SDSS DR7[3]. Table 3.1 lists the various SDSS and *GALEX* quantities

[3]A Chabrier IMF was assumed in calculating stellar masses. Catalogs are available at `http://www.mpa-garching.mpg.de/SDSS/DR7`

described above for the ESF-ETGs. We also obtained *ugriz* aperture photometry for the ESF-ETGs from the SDSS DR7 database's `frames` pipeline. These data consist of radially averaged surface brightness profiles measured in a series of circular annuli centered on each object. Aperture colors are corrected for Galactic extinction only, i.e., they have not been k-corrected. The optical aperture photometry is used in conjunction with the *HST* UV photometry to measure color profiles (Section 3.3.1). Flux-calibrated SDSS spectra for the ESF-ETGs were also obtained for use in characterizing their central bulges (Section 3.3.3).

Figure 3.1 shows the distribution of the ESF-ETGs and the SDSS master sample in FUV$-r$ color versus stellar mass. This figure demonstrates how cleanly FUV$-r$ separates the main galaxy population into well-defined blue and red sequences, with a clear GV in between. This is a major advantage of using a UV-optical color; we can easily separate fully quenched objects from those that have only recently quenched. An optical color does not have the dynamic range to do this, which is why the optical red sequence appears more prominent. In other words, the red sequence in Figure 3.1 appears less well-defined due to the "resolving power" of FUV$-r$ color. In addition the figure does not show a volume-limited sample, which reduces the number of low-mass, red objects in the plot. Note that the ESF-ETGs are located among the higher-mass galaxies in the GV (and blue sequence).

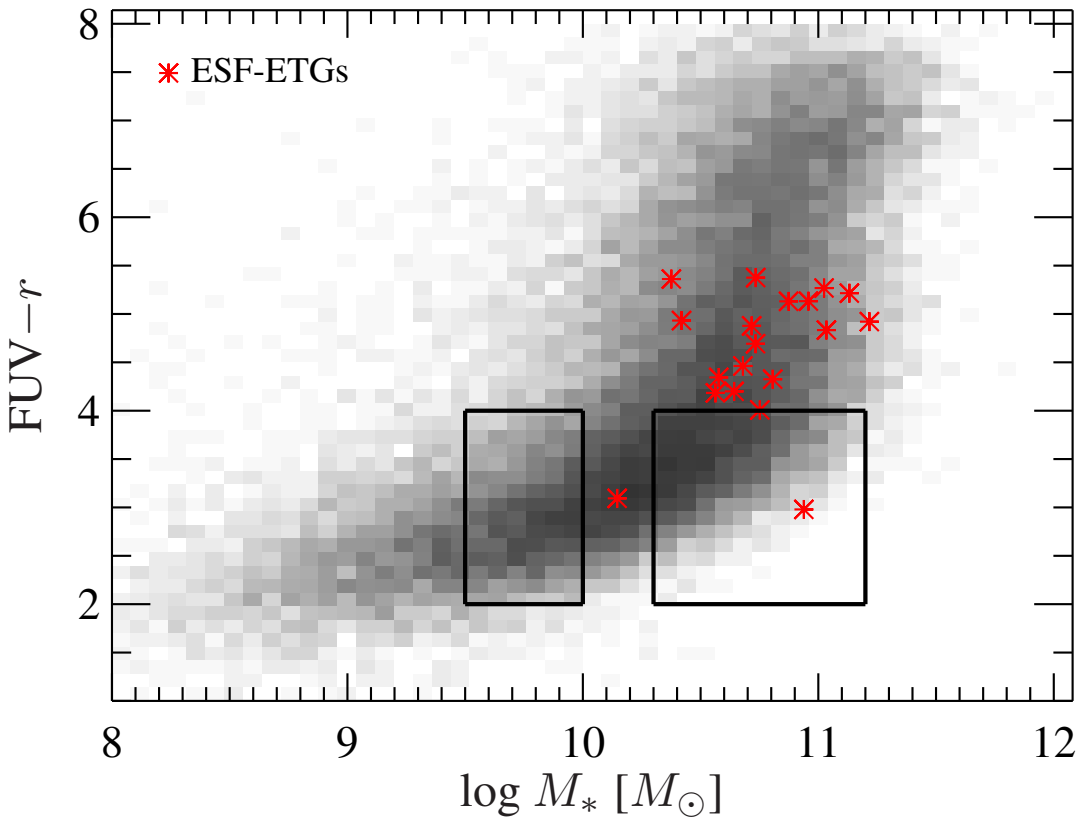

Figure 3.1: FUV$-r$ color-stellar mass diagram, with the SDSS master sample plotted as the gray histogram and the ESF-ETGs plotted as red points. AB magnitudes are used. Stellar masses are from the MPA/JHU SDSS DR7 Value-Added Catalog. The ESF-ETGs are concentrated in the bluer part of the green valley ($4 \lesssim$ FUV$-r \lesssim 5.3$) and are relatively massive ($\log M_*/M_\odot \gtrsim 10.5$). The rectangles enclose low-mass and high-mass blue galaxies with *integrated* FUV$-r$ colors similar to the *outer* FUV$-r$ colors of the ESF-ETGs ($2 <$ FUV$-r < 4$). Colors of objects within the rectangles are compared to the outer colors of the ESF-ETGs in Figure 3.6.

Table 3.1. Properties of the ESF-ETGs

Object	Redshift	$\log M_*$ $[M_\odot]$	M_r	r	FUV$-r$	$E(B-V)$	FUV FWHM (kpc)	Hα EW (Å)	b/a
SR01	0.119	10.94	-21.99	16.72	2.98	0.059	91.87	1.251	0.86
SR02	0.081	10.15	-20.11	17.72	3.09	0.044	57.60	0.603	0.92
SR03	0.057	10.58	-20.69	16.35	4.34	0.016	43.19	0.200	0.61
SR04	0.114	10.64	-21.34	17.28	4.20	0.028	60.38	1.352	0.68
SR05	0.101	10.56	-21.10	17.24	4.18	0.061	23.14	2.098	0.56
SR06	0.095	10.81	-21.68	16.51	4.33	0.040	44.57	0.587	0.56
SR07	0.107	10.73	-21.44	17.04	4.69	0.036	31.42	1.406	0.75
SR08	0.111	10.75	-21.46	17.10	4.01	0.027	57.57	0.514	0.75
SR09	0.092	10.42	-20.72	17.39	4.93	0.042	25.58	0.645	0.57
SR10	0.111	11.22	-22.51	16.04	4.92	0.026	41.76	0.714	0.65
SR11	0.077	10.68	-21.48	16.25	4.46	0.027	47.33	0.779	0.76

Table 3.1 (cont'd)

Object	Redshift	$\log M_*$ $[M_\odot]$	M_r	r	FUV$-r$	$E(B-V)$	FUV FWHM (kpc)	Hα EW (Å)	b/a
SR12	0.114	11.03	-22.36	16.26	4.83	0.024	54.43	0.852	0.57
SR14	0.085	11.02	-22.00	15.93	5.27	0.088	29.48	0.736	0.42
SR17	0.118	10.96	-22.01	16.69	5.13	0.051	38.78	2.061	0.75
SR18	0.116	10.72	-21.35	17.31	4.88	0.022	34.67	2.232	0.46
SR20	0.114	10.87	-21.66	16.97	5.13	0.025	45.98	2.160	0.59
SR23	0.114	11.13	-22.30	16.32	5.22	0.039	55.80	0.799	0.95
SR28	0.104	10.73	-21.38	17.02	5.38	0.033	33.82	2.326	0.48
SR29	0.059	10.38	-20.73	16.37	5.36	0.014	18.10	0.889	0.70

Note. — Redshifts, stellar masses, and Hα equivalent widths from the SDSS DR7 MPA/JHU value-added catalog. Optical photometry and axis ratios (b/a) from the SDSS DR7 database. FUV magnitudes, FUV FWHM, and color excess from the *GALEX* GR6 database. All photometry in table k-corrected to $z = 0$ and corrected for Galactic extinction using the $E(B-V)$ values listed.

3.2.2 Aperture Photometry

Aperture photometry of the UV images was measured using Source Extractor, version 2.8.6 (Bertin & Arnouts, 1996). To be consistent with the SDSS optical measurements, UV fluxes were measured using the circular apertures defined by the SDSS `frames` pipeline. The radii of the apertures used are $R = 0\farcs23, 0\farcs68, 1\farcs03, 1\farcs76, 3''$, $4\farcs63, 7\farcs43$, and $11\farcs42$. While elliptical apertures are better suited for this particular sample, we show below that the typical color profile in the outer parts of the galaxies is fairly flat, and thus our measurements are not that sensitive to the exact shape of the aperture. To check this, we compared the SDSS r-band surface brightness profiles to those measured in elliptical apertures from deeper R-band images taken with the WIYN telescope (presented in Paper I); no significant difference was found between the shapes of the SDSS and WIYN profiles. The WIYN data are not used here because they exist for only 16 of the 19 ESF-ETGs and because they have not been flux-calibrated. To avoid spurious color gradients, the *HST* UV images were first smoothed to match the $1\farcs4$ seeing (1σ) of the SDSS telescope. In a few cases (SR08 and SR17) nearby UV companions located within the outermost aperture were masked out prior to measuring photometry.

The UV sky background in each individual frame was determined by measuring fluxes in a number of 100×100-pixel boxes placed in source-free regions of the

image. The average value of all the box fluxes was taken to be the sky value and was subtracted from each individual frame prior to co-adding them (Paper I). The sky is not uniform across the image, and this represents an additional source of uncertainty in the photometry. We accounted for this by measuring the rms scatter of the residual sky values in the co-added frames, defined to be the standard deviation of the distribution of box fluxes in source-free regions. The total error in each aperture flux measurement consists of Poisson noise of the source and sky and the rms scatter in the residual sky, all added in quadrature. Note that the SBC detector has no read noise. Flux errors in the optical photometry are small (a few percent at most), and the errors on the colors are dominated by the UV measurements.

To check for any zeropoint offset between the *GALEX* FUV and *HST* FUV filters,[4] we compared integrated magnitudes measured from the *HST* images to the *GALEX* GR6 `mag_auto` magnitudes. As seen in Figure 3.2, the agreement between the two measurements is generally good, with a median offset of $HST - GALEX = -0.19$ mag. Since the offset is much smaller than the FUV$-r$ colors, no correction was made to the *HST* magnitudes. Note that the magnitudes in Figure 3.2 have not been corrected for Galactic extinction.

[4]Our adopted *HST* zeropoint was obtained at `stsci.edu/hst/acs/analysis/zeropoints`.

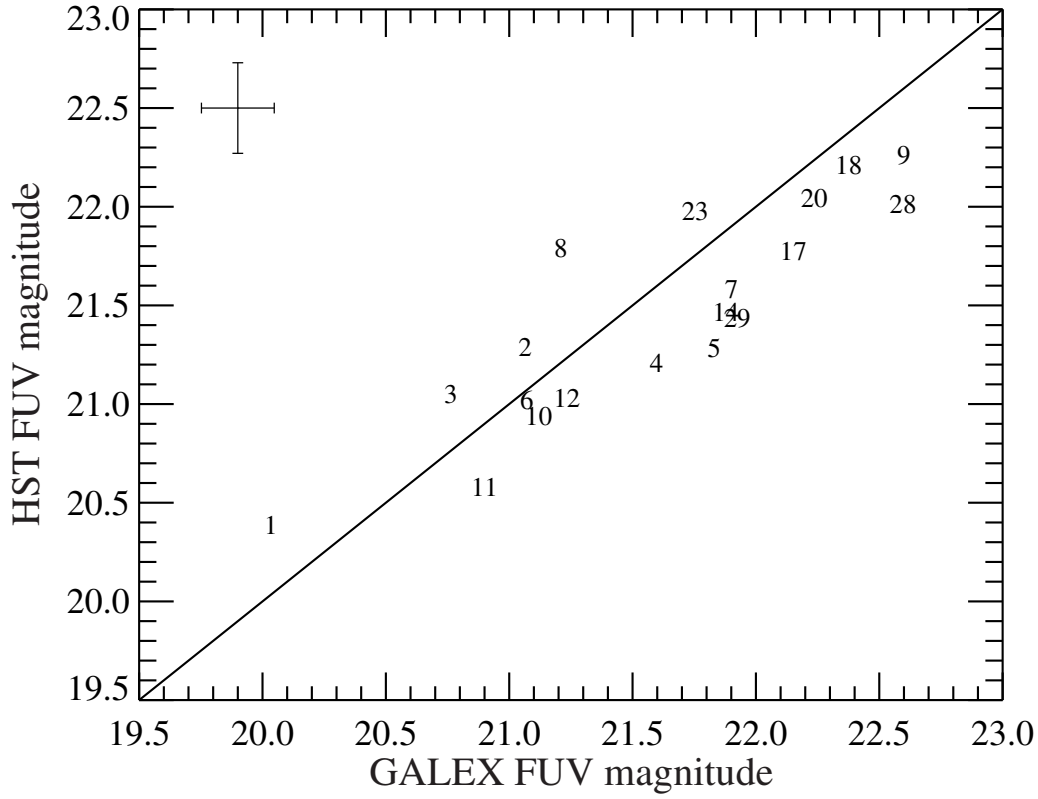

Figure 3.2: Comparison between *GALEX* FUV ($\lambda_e = 1530\,\text{Å}$) and *HST* FUV (F125LP filter, $\lambda_e = 1430\,\text{Å}$) magnitudes for the ESF-ETGs. The magnitudes have not been corrected for Galactic extinction. The points are labeled by object number (1 = SR01, etc.). The cross indicates median errors in the magnitudes. The one-to-one line is indicated. The *HST* magnitudes were measured within a circular aperture of radius $R = 11\farcs42$. The agreement between the *GALEX* and *HST* magnitudes is generally good, with a median offset of $HST - GALEX = -0.19$ mag. Because this is smaller than the FUV$-r$ colors, no zeropoint correction is made to the *HST* magnitudes.

3.3 Results

3.3.1 UV-Optical Color Profiles

To give an idea of the UV morphologies seen in the ESF-ETGs, Figure 3.3 presents a montage of four ESF-ETGs in the sample. As discussed in Paper I, UV rings are seen in all but one of the ESF-ETGs, and clear spiral arms are found in two objects. Crucially, the UV emission is *extended* over tens of kpc in all cases. Compact, central UV emission is also seen in nearly all the ESF-ETGs. The reader is referred to Paper I for a compilation and discussion of the UV and optical images and morphologies of the complete sample.

New in this paper are the SDSS r-band and *HST* UV surface brightness and color profiles, presented in Figures 3.4 and 3.5. Surface brightness measurements are also listed in Table 3.2 for reference (negative fluxes are arbitrarily assigned a surface brightness of 35 mag arcsec^{-2}). Since the surface brightness values are averages within each annulus, each point has been plotted at the midpoint of each annulus. To facilitate comparison between galaxies, the radial coordinate has been scaled to the Petrosian half-light radius (R_{50}) for each galaxy. The photometry quantitatively highlights the disconnect between optical and UV light in tracing young stars and underscores the leverage one gains with UV data when studying recent SF in ETGs. Compared to the r-band surface brightness profiles, the UV

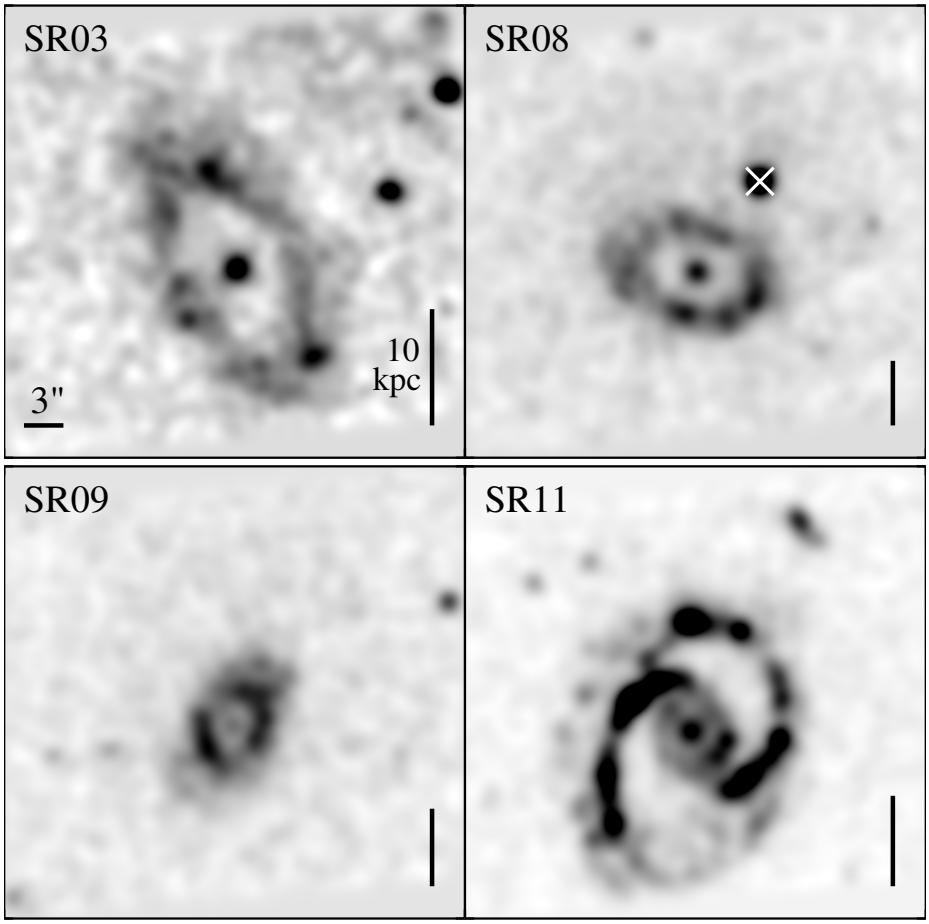

Figure 3.3: A montage of four ESF-ETGs highlighting the typical UV morphologies observed in these galaxies. The *HST* UV images have been smoothed to match the seeing of SDSS and are $\sim 30''$ on a side. For scale, the horizontal bar indicates the $3''$ diameter of the SDSS spectroscopic fiber, and the vertical bar in each panel equals 10 kpc. The companion marked "$\times$" was masked when measuring photometry. Unmarked companions are located outside the maximum aperture used ($11.42''$). Extended UV emission is located *outside* the fiber. The majority of the 19 ESF-ETGs in the sample have similar UV rings. SR11 is one of two objects with pronounced spiral arms. High-resolution images of all 29 *HST* UV galaxies are presented in Paper I, along with SDSS optical and WIYN R-band images.

profiles are much shallower in general, particularly in the outer parts. In principle, one could measure UV surface brightnesses to larger radii to investigate where the UV light falls off. However, larger apertures would often reach beyond the edge of the detector, making accurate sky measurements difficult, especially for the larger galaxies.

Another feature seen in Figures 3.4 and 3.5 is the broad similarity in the overall shape of the color profiles of the ESF-ETGs. The FUV$-r$ color profiles show that their centers are quite red: they typically have a color FUV$-r \gtrsim 6$, which is consistent with old, red sequence stellar populations (Figure 3.1; Rich et al., 2005; Donas et al., 2007). This is not too surprising given that the ESF-ETGs were selected to have no central emission. By contrast, their outer parts ($R/R_{50} \gtrsim 2$, or $\gtrsim 7$ kpc) show very blue FUV$-r$ colors, typically between 2 and 4. These are values typical of star-forming, blue cloud galaxies (Figure 3.1). Note that, despite the visual prominence of the central UV emission in the images, it only accounts for $\sim 5\%$ of the total UV flux in each galaxy and negligibly contributes to the integrated FUV$-r$ colors. A similar observation was made by Kauffmann et al. (2007), who showed that the UV flux in their sample of GV ETGs was primarily due to SF on extended scales, even in objects with AGN activity.

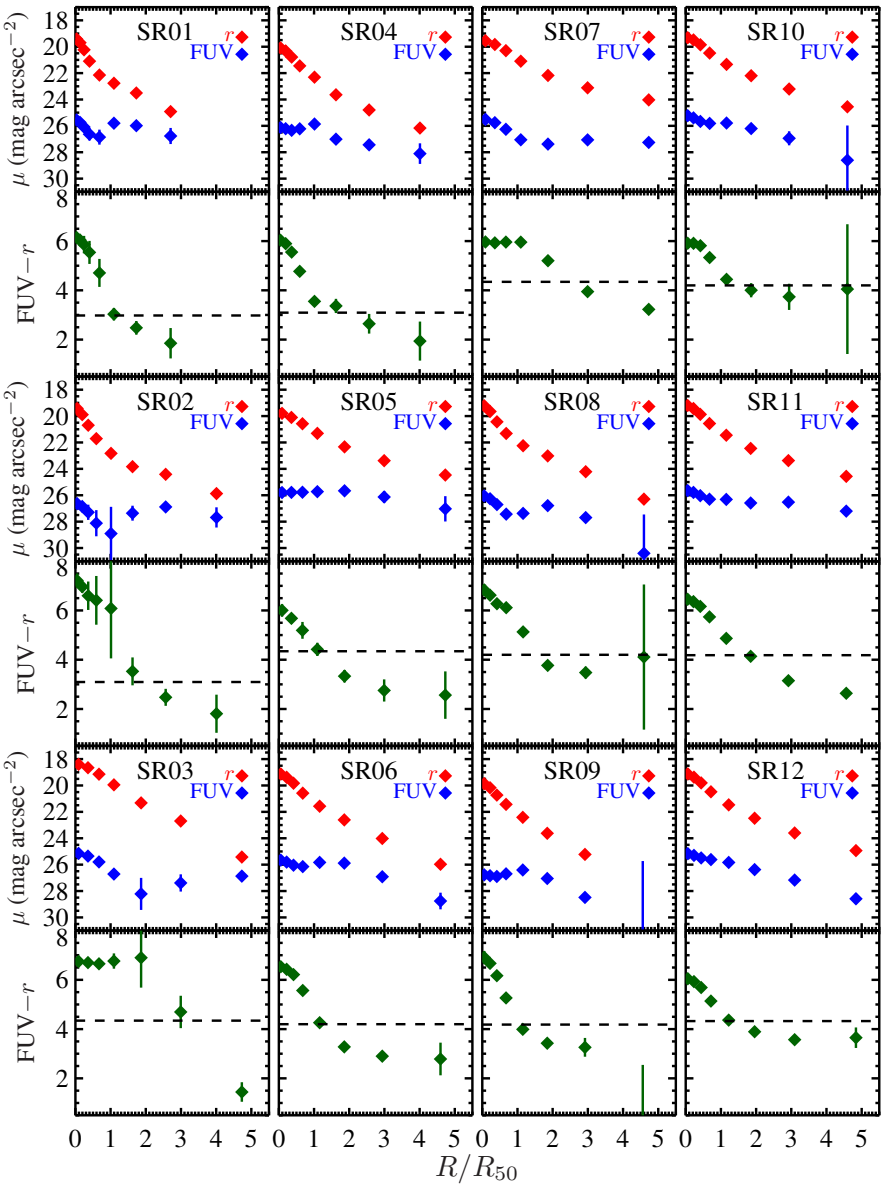

Figure 3.4: FUV and r-band surface brightness and FUV$-r$ color profiles of the ESF-ETGs. The x-axis is scaled to the half-light radius (R_{50}) of each galaxy. The dashed line indicates the integrated FUV$-r$ color of each galaxy from Table 3.1. The general shape of the color profiles is similar among the ESF-ETGs; the centers are typically red (FUV$-r \gtrsim 6$), and the outer regions are quite blue ($2 \lesssim$ FUV$-r \lesssim 4$). Photometry has been corrected for Galactic extinction but not k-corrected. Measurements are tabulated in Table 3.2.

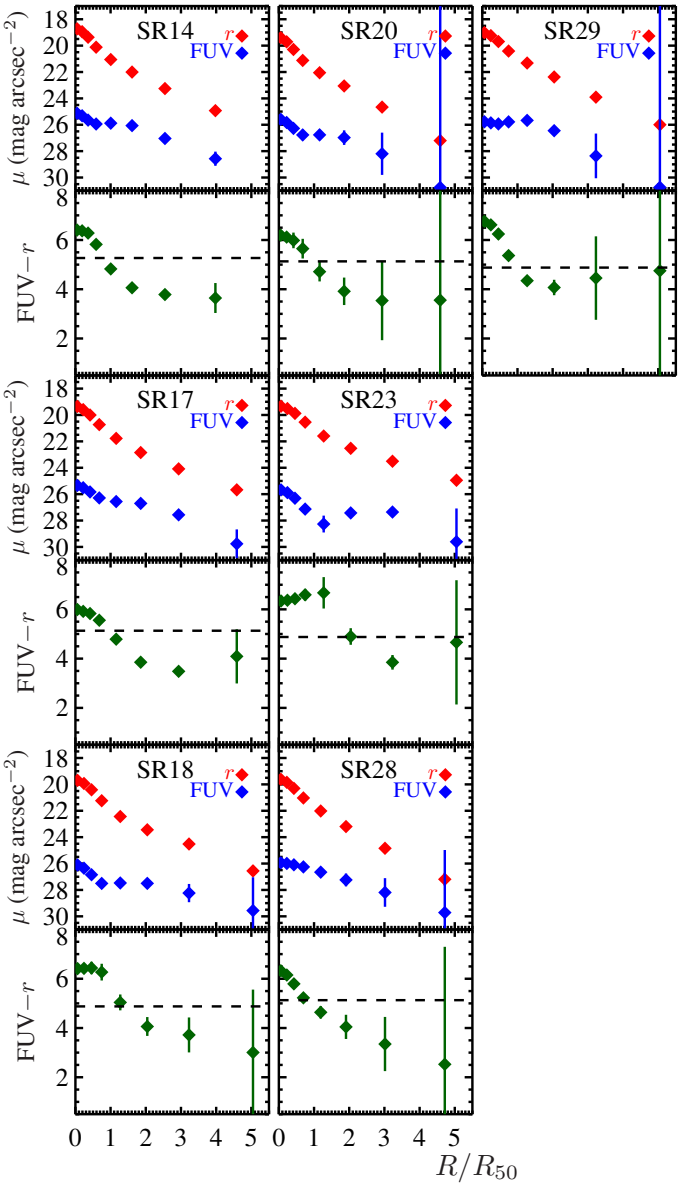

Figure 3.5: Same as Figure 3.4 for the remaining ESF-ETGs.

Table 3.2. Surface Brightness Measurements of the ESF-ETGs

Object	$R = 0\farcs23$	$R = 0\farcs68$	$R = 1\farcs03$	$R = 1\farcs76$	$R = 3\farcs00$	$R = 4\farcs63$	$R = 7\farcs43$	$R = 11\farcs42$
SR01	26.040 ± 0.193	26.221 ± 0.160	26.574 ± 0.353	27.120 ± 0.468	27.339 ± 0.568	26.283 ± 0.249	26.470 ± 0.277	27.253 ± 0.611
	19.571 ± 0.027	19.854 ± 0.006	20.393 ± 0.015	21.256 ± 0.014	22.308 ± 0.015	22.928 ± 0.026	23.668 ± 0.027	25.078 ± 0.090
SR02	27.000 ± 0.288	27.214 ± 0.242	27.653 ± 0.577	28.481 ± 0.990	29.267 ± 2.028	27.721 ± 0.566	27.248 ± 0.343	28.043 ± 0.766
	19.542 ± 0.026	20.010 ± 0.005	20.814 ± 0.017	21.828 ± 0.018	22.944 ± 0.032	23.953 ± 0.032	24.534 ± 0.045	25.995 ± 0.114
SR03	25.276 ± 0.118	25.484 ± 0.079	25.927 ± 0.176	26.844 ± 0.310	28.348 ± 1.214	27.519 ± 0.654	27.002 ± 0.380	27.979 ± 1.004
	18.442 ± 0.030	18.697 ± 0.004	19.188 ± 0.008	19.994 ± 0.018	21.363 ± 0.050	22.736 ± 0.068	25.469 ± 0.114	29.288 ± 0.616
SR04	26.358 ± 0.192	26.446 ± 0.113	26.570 ± 0.186	26.454 ± 0.125	26.092 ± 0.087	27.241 ± 0.285	27.668 ± 0.394	28.336 ± 0.781
	20.169 ± 0.037	20.395 ± 0.002	20.863 ± 0.010	21.529 ± 0.021	22.386 ± 0.029	23.718 ± 0.046	24.871 ± 0.070	26.243 ± 0.138
SR05	26.303 ± 0.251	26.289 ± 0.210	26.278 ± 0.342	26.234 ± 0.268	26.169 ± 0.252	26.637 ± 0.448	27.536 ± 0.960	29.510 ± 6.347
	19.960 ± 0.035	20.269 ± 0.003	20.746 ± 0.009	21.475 ± 0.016	22.499 ± 0.037	23.547 ± 0.040	24.635 ± 0.075	26.979 ± 0.361
SR06	25.985 ± 0.154	26.134 ± 0.071	26.369 ± 0.107	26.476 ± 0.067	26.158 ± 0.042	26.213 ± 0.047	27.244 ± 0.110	29.085 ± 0.631
	19.235 ± 0.023	19.489 ± 0.003	19.939 ± 0.008	20.692 ± 0.011	21.681 ± 0.029	22.718 ± 0.062	24.126 ± 0.097	26.081 ± 0.203
SR07	25.812 ± 0.144	26.059 ± 0.073	26.560 ± 0.140	27.356 ± 0.170	27.682 ± 0.202	27.363 ± 0.170	27.557 ± 0.188	28.903 ± 0.696
	19.647 ± 0.029	19.930 ± 0.002	20.400 ± 0.007	21.198 ± 0.008	22.279 ± 0.015	23.215 ± 0.026	24.130 ± 0.037	26.025 ± 0.099
SR08	26.269 ± 0.176	26.486 ± 0.088	26.926 ± 0.163	27.651 ± 0.191	27.593 ± 0.162	27.007 ± 0.107	27.912 ± 0.227	30.621 ± 2.943
	19.291 ± 0.023	19.721 ± 0.004	20.507 ± 0.013	21.391 ± 0.014	22.319 ± 0.016	23.092 ± 0.030	24.289 ± 0.062	26.368 ± 0.141

Table 3.2 (cont'd)

Object	$R = 0\farcs23$	$R = 0\farcs68$	$R = 1\farcs03$	$R = 1\farcs76$	$R = 3\farcs00$	$R = 4\farcs63$	$R = 7\farcs43$	$R = 11\farcs42$
SR09	27.119 ± 0.259	27.186 ± 0.118	27.244 ± 0.159	27.043 ± 0.083	26.751 ± 0.055	27.397 ± 0.106	28.830 ± 0.358	31.768 ± 5.695
	19.979 ± 0.036	20.287 ± 0.006	20.845 ± 0.009	21.548 ± 0.019	22.531 ± 0.028	23.741 ± 0.067	25.340 ± 0.134	35.000 ± 1.918
SR10	25.440 ± 0.137	25.606 ± 0.099	25.876 ± 0.196	26.025 ± 0.177	25.997 ± 0.170	26.414 ± 0.287	27.154 ± 0.532	28.814 ± 2.633
	19.388 ± 0.025	19.557 ± 0.003	19.924 ± 0.006	20.554 ± 0.009	21.411 ± 0.010	22.270 ± 0.022	23.278 ± 0.027	24.625 ± 0.072
SR11	25.870 ± 0.144	26.006 ± 0.065	26.253 ± 0.096	26.522 ± 0.064	26.537 ± 0.050	26.809 ± 0.067	26.742 ± 0.057	27.425 ± 0.112
	19.269 ± 0.023	19.500 ± 0.002	19.943 ± 0.006	20.637 ± 0.011	21.525 ± 0.028	22.525 ± 0.028	23.447 ± 0.026	24.642 ± 0.056
SR12	25.368 ± 0.137	25.501 ± 0.060	25.695 ± 0.083	25.818 ± 0.046	26.035 ± 0.038	26.578 ± 0.060	27.372 ± 0.105	28.789 ± 0.403
	19.189 ± 0.022	19.438 ± 0.001	19.873 ± 0.005	20.546 ± 0.010	21.537 ± 0.024	22.551 ± 0.042	23.669 ± 0.057	25.004 ± 0.104
SR14	25.856 ± 0.144	26.042 ± 0.066	26.373 ± 0.103	26.667 ± 0.068	26.604 ± 0.048	26.788 ± 0.058	27.764 ± 0.124	29.298 ± 0.537
	18.968 ± 0.019	19.185 ± 0.003	19.607 ± 0.008	20.359 ± 0.012	21.294 ± 0.026	22.243 ± 0.070	23.494 ± 0.141	25.169 ± 0.284
SR17	25.763 ± 0.137	25.934 ± 0.062	26.255 ± 0.095	26.707 ± 0.069	26.983 ± 0.061	27.122 ± 0.070	27.989 ± 0.137	30.186 ± 1.094
	19.489 ± 0.026	19.733 ± 0.005	20.144 ± 0.008	20.869 ± 0.007	21.913 ± 0.010	22.987 ± 0.015	24.225 ± 0.038	25.813 ± 0.125
SR18	26.289 ± 0.183	26.535 ± 0.113	27.029 ± 0.253	27.688 ± 0.339	27.656 ± 0.319	27.685 ± 0.377	28.419 ± 0.693	29.746 ± 2.523
	19.758 ± 0.029	19.993 ± 0.005	20.472 ± 0.016	21.299 ± 0.024	22.497 ± 0.042	23.504 ± 0.066	24.580 ± 0.150	26.619 ± 0.397
SR20	25.800 ± 0.160	26.036 ± 0.133	26.483 ± 0.317	26.979 ± 0.399	26.974 ± 0.395	27.183 ± 0.553	28.407 ± 1.601	30.964 ± 18.104
	19.470 ± 0.025	19.780 ± 0.003	20.362 ± 0.006	21.193 ± 0.018	22.124 ± 0.024	23.128 ± 0.073	24.731 ± 0.134	27.270 ± 0.238

Table 3.2 (cont'd)

Object	$R = 0\farcs23$	$R = 0\farcs68$	$R = 1\farcs03$	$R = 1\farcs76$	$R = 3\farcs00$	$R = 4\farcs63$	$R = 7\farcs43$	$R = 11\farcs42$
SR23	26.002 ± 0.155	26.209 ± 0.084	26.635 ± 0.166	27.459 ± 0.239	28.591 ± 0.638	27.750 ± 0.337	27.682 ± 0.296	29.933 ± 2.523
	19.443 ± 0.027	19.621 ± 0.003	19.985 ± 0.004	20.650 ± 0.007	21.702 ± 0.011	22.635 ± 0.010	23.614 ± 0.025	25.056 ± 0.032
SR28	26.211 ± 0.187	26.265 ± 0.117	26.367 ± 0.195	26.527 ± 0.174	26.925 ± 0.244	27.514 ± 0.483	28.465 ± 1.086	29.990 ± 4.745
	19.706 ± 0.030	19.934 ± 0.006	20.393 ± 0.016	21.121 ± 0.022	22.106 ± 0.059	23.288 ± 0.089	24.935 ± 0.178	27.282 ± 0.483
SR29	25.890 ± 0.169	25.975 ± 0.125	26.052 ± 0.214	25.897 ± 0.148	25.785 ± 0.132	26.566 ± 0.311	28.478 ± 1.693	30.862 ± 16.334
	19.057 ± 0.020	19.283 ± 0.004	19.731 ± 0.007	20.452 ± 0.012	21.360 ± 0.020	22.417 ± 0.034	23.946 ± 0.077	26.034 ± 0.110

Note. — For each object, the top (bottom) row gives *HST* FUV (SDSS r-band) surface brightnesses (in mag arcsec^{-2}). Values are measured in circular annuli with outer radii specified in the column headings. Measurements are corrected for Galactic extinction but are not k-corrected. Negative fluxes are assigned the value $\mu = 35.0$.

3.3.2 Stellar Population Analysis of the ESF-ETGs

The color profiles in Figures 3.4 and 3.5 quantitatively show that young stars exist in the outer disks of the ESF-ETGs, confirming the result in SR2010 and Paper I. However, one cannot immediately determine whether those stars represent the vestiges of the original, fading SF or whether those young stars were produced in a rejuvenated burst of SF following a quiescent phase. Fortunately, a key question that *can* be answered using broadband photometry is whether the outer disks consist purely of young stars or whether the young-star light is frosting on top of an older stellar population.

Figure 3.6 presents color-color diagrams showing the *outer* colors of the ESF-ETGs (magenta diamonds). Depending on the UV extent of each galaxy, the outer colors (FUV$-g$ and $g-r$) were computed by adding up the flux within the annuli that enclosed the outer UV rings/arms. The typical range of radii was between $4\farcs63$ and $11\farcs42$. Note that the outer colors have been corrected for Galactic extinction but have not been k-corrected.

Included in Figure 3.6 is a selection of stellar population models constructed using the 2007 version of the Bruzual & Charlot (2003) synthesis code. The models were generated assuming (1) a Chabrier IMF, (2) solar metallicity, and (3) a formation age of 12 Gyr. The various tracks were chosen to represent a range of possible SF histories for the ESF-ETGs (discussed in Section 3.4). The

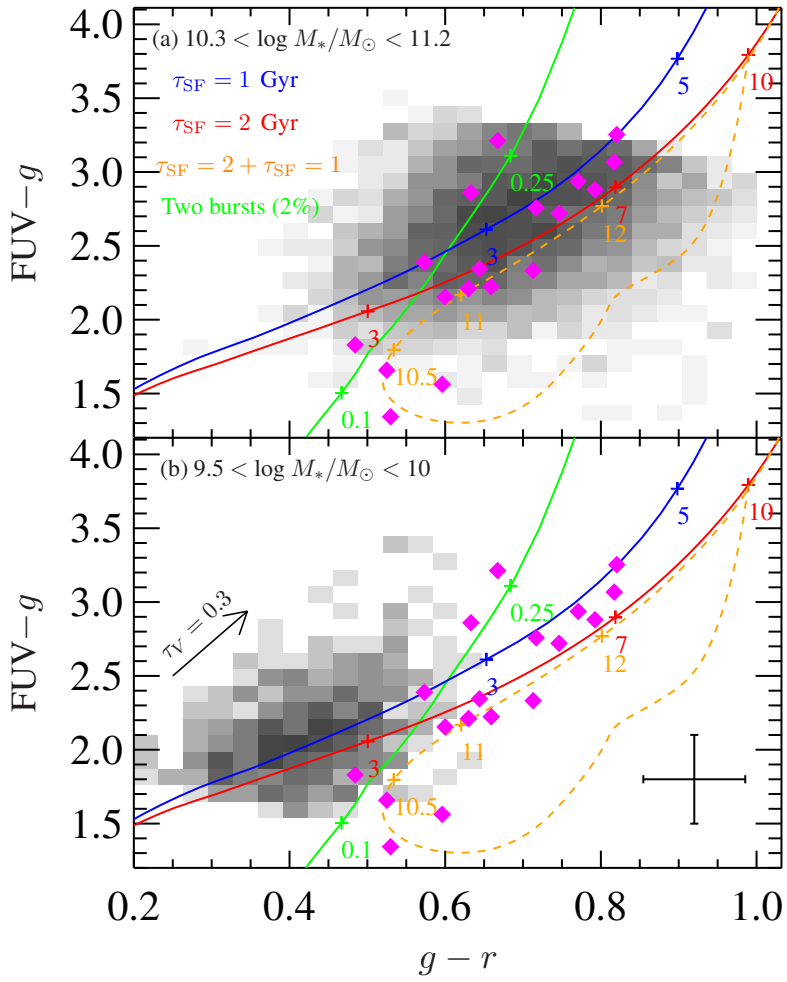

Figure 3.6: FUV$-g$ vs. $g-r$ color-color diagrams. In both panels, the outer disk colors of the ESF-ETGs are indicated (magenta diamonds), with median errors indicated by the cross in the bottom panel. Integrated colors of two SDSS comparison samples are shown: (a) high-mass and (b) low-mass blue cloud galaxies; these samples are indicated by the boxes in Figure 3.1. Various Bruzual & Charlot models (age = 12 Gyr at $z = 0.1$) are shown as colored lines, with ages indicated in Gyr (for the two-burst model, ages are after the second burst). The Calzetti et al. (2000) reddening vector is indicated for reference. The ESF-ETG outer colors are well-matched by the declining τ-models (blue, red, and orange tracks) and also by the high-mass comparison sample, both of which contain old stars. The two-burst model (green track) also contains old stars, but the colors evolve very rapidly, implying that bursty rejuvenation is unlikely the cause of the SF in most ESF-ETGs (Section 3.3.4).

blue and red tracks in the figure are two exponentially declining SF histories (τ-models), with e-folding times $\tau_{\rm SF} = 1$ and 2 Gyr, respectively. The orange track describes a "double-τ" model: the first τ-model has $\tau_{\rm SF} = 2$ Gyr on top of which a second $\tau_{\rm SF} = 1$ Gyr model is added 10 Gyr later (which produces 7% of the total stellar mass). All three of these tracks include the two-component dust model of Charlot & Fall (2000). The default dust model parameters were chosen, i.e., the effective optical depth suffered by stars younger than 10^7 yr is assumed to be $\hat{\tau}_V = 1.0$, and the fraction of the attenuation due to the diffuse ISM is taken to be $\mu = 0.3$. Finally, the green track assumes an instantaneous burst at $t = 0$ and a second instantaneous burst 0.25 Gyr before the epoch of observation (taken to be $z = 0.1$) that produces 2% of the total stellar mass. This model is dust-free. For consistency with the ESF-ETG outer colors, which have not been k-corrected, all the tracks show observed-frame colors at $z = 0.1$, the median redshift of the ESF-ETGs.

Before comparing to the data, we first discuss the behavior of the models themselves. The τ-models represent gradually declining SF and are meant to represent the gradual decline of SF expected in massive blue galaxies (e.g., Noeske et al., 2007). As Figure 3.6 shows, at a fixed age, a longer $\tau_{\rm SF}$ results in bluer colors. This is because the SF rate at a given age is higher in longer $\tau_{\rm SF}$ models, and thus the colors "hover" at bluer values for longer than a model with shorter

$\tau_{\rm SF}$. Overall, the τ-models span about 7 Gyr in age for the ESF-ETG color range plotted in Figure 3.6. The double-τ track is identical to the $\tau_{\rm SF} = 2$ Gyr track up to $t = 10$ Gyr, when the second episode of SF begins. The colors then become bluer before looping back and approaching the original $\tau_{\rm SF} = 2$ Gyr track. In other words, the double-τ model is virtually indistinguishable from the single-τ model ~ 1 Gyr after the second SF episode begins.

By contrast, the behavior of the two-burst model is rather different and simulates the effect of rapidly rejuvenated SF in a quiescent galaxy. The second burst occurs on top of an evolved stellar population, and thus affects the FUV$-g$ color (which is sensitive to young stars) more strongly than the $g - r$ color (which is dominated by older stars). This causes the track to rapidly redden in FUV$-g$ as the OB stars die off while the optical $g - r$ color changes little. As seen in the figure, the FUV$-g$ color reddens within ~ 200 Myr, implying that any significant bluing in the UV due to bursty SF would have to be short-lived.

What do the models tell us about the stellar populations in the outer disks of the ESF-ETGs? As seen in Figure 3.6(a), the outer ESF-ETG colors are generally consistent with the declining τ-models (both single-τ and double-τ) and imply intermediate to old ages for the underlying stellar populations in these galaxies. By contrast, the two-burst model colors are somewhat offset from the mean $g - r$ colors of the ESF-ETGs. One could argue that adjusting the mass fraction of

the second burst (set to 2% in the figure) or incorporating dust reddening could bring the colors more in agreement. However, regardless of the values used, bursts evolve *very quickly* through the region occupied by the ESF-ETGs, and thus it is statistically unlikely that most ESF-ETGs are bursts unless they are exceedingly rare objects. We return to this issue in Section 3.3.4 and show that this is probably not the case.

Collectively, this comparison shows that the SF in the outer disks of the ESF-ETGs is taking place *in regions with old stars*. Moreover, it demonstrates that *bursty* rejuvenation is not likely responsible for the SF we see. This last point is consistent with SR2010's selection against galaxies with post-starburst signatures or optical disturbances indicative of recent, short-duration bursts.

In addition to the model comparison above, it is useful to demonstrate the existence of old stellar populations in the ESF-ETG disks in an empirical manner. To that end, we now compare the outer disk colors of the ESF-ETGs to two sets of galaxies chosen from the SDSS master sample. These sets are indicated by the rectangles in Figure 3.1. The comparison sample in Figure 3.6(a) consists of high-mass ($10.3 < \log M_*/M_\odot < 11.2$) galaxies matched in redshift to the ESF-ETGs ($0.08 < z < 0.12$) that have the same *integrated* FUV$-r$ color as the *outer* parts of the ESF-ETGs, namely $2 <$ FUV$-r < 4$, i.e., they reside in the blue cloud. The integrated colors of these galaxies have been corrected for Galactic extinction but

are not k-corrected. We note that the k-correction to $z = 0.1$ is small, i.e., < 0.1 mag for FUV$-g$ and < 0.04 mag for $g - r$. As can be seen, the outer ESF-ETG colors are fully consistent with the integrated colors of these comparison galaxies. Because the latter are massive, they have significant old stellar populations, and hence red $g - r$ colors (the effect of dust attenuation is discussed below). This bolsters the conclusion from comparing to models above that old stars are present in the outer disks of the ESF-ETGs.

By contrast, the sample in Figure 3.6(b) is comprised of low-mass ($9.5 < \log M_*/M_\odot < 10.0$) blue cloud galaxies within the same redshift range as the ESF-ETGs ($0.08 < z < 0.12$). Their $g - r$ colors seem systematically too blue compared to the ESF-ETGs, reflecting the fact that they have higher specific SF rates than their more massive counterparts (e.g., Salim et al., 2007). This results in a higher fraction of younger, and hence bluer, stars in the low-mass objects, driving their $g - r$ color blueward. Indeed, visual inspection of the SDSS color images of the low- and high-mass comparison galaxies clearly shows that the former have blue disks, while the latter have red bulges and disks. The point is that the integrated colors of more massive, optically redder comparison galaxies are a good match to the outer colors of the ESF-ETGs whereas the less massive, optically bluer comparison sample does not match. Thus we have seen that both data and theory lead to the same conclusion: old stars are abundant in the outer

star-forming regions of the ESF-ETGs.

Our discussion so far has neglected the effects of dust attenuation on the observed colors of the comparison galaxies. Indeed, the amount of dust attenuation in SF galaxies increases with stellar mass (e.g., Brinchmann et al., 2004; Salim et al., 2007; Wuyts et al., 2011a), potentially complicating our comparison with the ESF-ETGs, especially for the massive sample shown in Figure 3.6(a). We attempted to remove the most dust-reddened objects by excluding edge-on systems with axis ratio $b/a < 0.5$. This makes no difference in the distribution of points in Figure 3.6. In any case, assuming that the dust-corrected colors of the comparison galaxies are bluer than shown in Figure 3.6 only strengthens our conclusion that the outer disks of the ESF-ETGs contain *old* stars.

3.3.3 Stacked SDSS Spectra

The SDSS fiber spectra, which probe the central $3''$ (~ 5 kpc at $z \sim 0.1$), can provide additional insight into the stellar populations and any potential emission activity that may be responsible for the central UV light seen in nearly all the ESF-ETGs. Also, they can inform our discussion about how SF is evolving in the ESF-ETGs, particularly the possible role of AGN feedback in shutting down SF (e.g., Schawinski et al., 2007). SR2010 tentatively ascribed the central UV emission to weak AGN activity based on a stacked BPT classification. Stacking

was necessary because the ESF-ETGs do not have securely detected emission lines, meaning any (potentially weak) emission features will not be readily apparent in the individual spectra.

We reach similar conclusions based on stacking the spectra themselves. The stacking method is detailed in Graves et al. (2009a). Figure 3.7 shows the resulting stacked spectrum of the ESF-ETGs. Interestingly, weak emission lines due to [O II] $\lambda 3727$ and [N II] $\lambda 6584$ that were not apparent in the individual spectra are clearly evident in the stack. These emission lines are characteristic of LINER emission (e.g., Heckman, 1980; Yan et al., 2006; Graves et al., 2007). If LINERs are indeed a weak phase in the AGN life cycle, this might indicate that AGN feedback played a role in shutting down SF, at least in the centers of these galaxies. However, AGN feedback has historically been proposed as a mechanism that quenches SF *globally* in a galaxy, not just in the center (e.g., Di Matteo et al., 2005; Hopkins et al., 2006). Given the extended SF seen in the outer parts of the ESF-ETGs, it would appear that AGN feedback is most effective at removing (or heating up) the *central* gas and less so at disrupting SF in the outer parts. Interestingly, recent observations of X-ray-selected AGN hosts at $z \sim 1$ may suggest that AGN feedback quenches SF only within the central kpc (Ammons et al., 2011).

It is also possible that the LINER emission observed in ESF-ETGs is unrelated

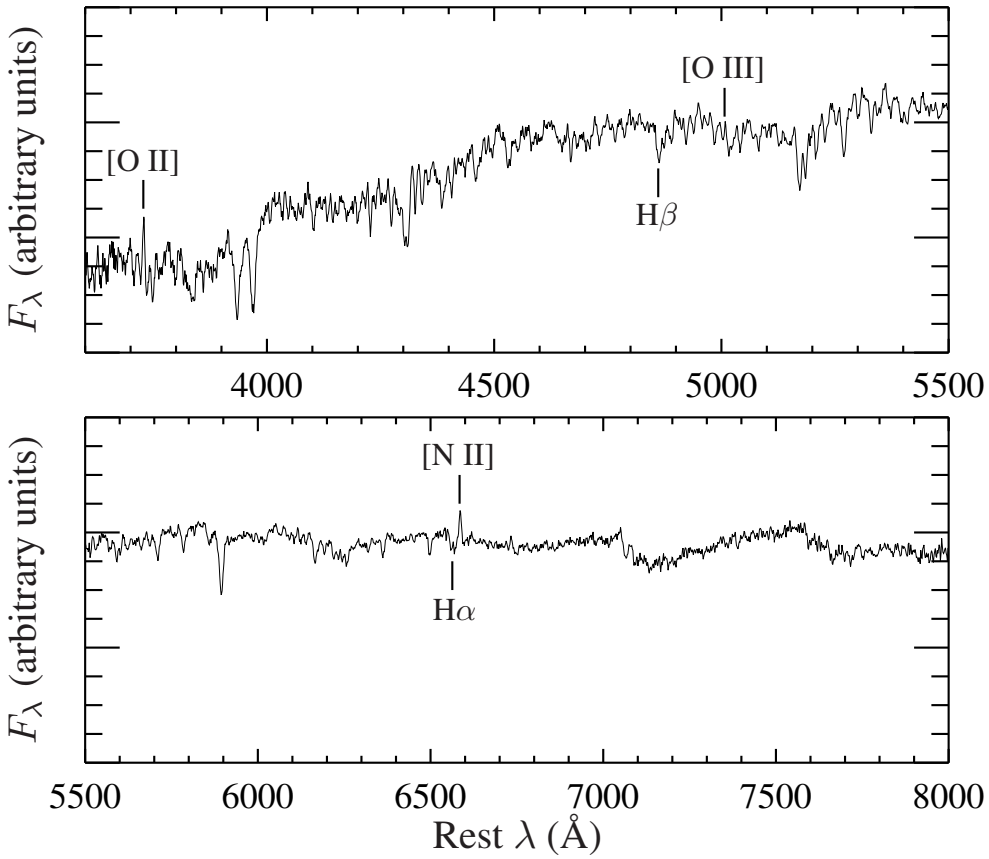

Figure 3.7: Stacked SDSS spectrum of the ESF-ETGs. While the continuum is that due to an old stellar population, emission lines of [O II] $\lambda\,3727$ and [N II] $\lambda\,6584$ are clearly detected, and [O III] $\lambda\,5007$ is barely visible. These features are characteristic of LINER emission. Hα and Hβ are also labeled for reference. The strength of the Hβ absorption line, together with $\langle$Fe$\rangle$, is used to estimate an average luminosity-weighted stellar population age of $\sim$ 7 Gyr (see text for details).

to AGN (e.g., Filippenko, 2003). It has been suggested that LINER emission is dominated by emission from hot gas in the ISM ionized by extended UV sources, such as post-AGB stars, rather than an AGN (e.g., Binette et al., 1994; Goudfrooij et al., 1994; Sarzi et al., 2010; Yan & Blanton, 2012). In any case, the emission in the stacked spectrum is both weak and uncharacteristic of young stars, which is the point we wish to establish.

With our resolved photometry we are able to say more about the nature of the central UV emission in the ESF-ETGs. The central FUV$-r$ colors of the ESF-ETGs (FUV$-r \gtrsim 6$) in Figure 3.4 are consistent with old, red sequence galaxies (Figure 3.1; Rich et al., 2005; Donas et al., 2007). The possibility that LINER emission is due to ionization by old, UV-bright (e.g., post-AGB) stars bolsters the observation that the central UV emission is not due to recent SF. To summarize, the stacked spectra indicate weak LINER-like activity, but the red FUV$-r$ colors do not require anything besides old UV upturn stars.

With spectra one can also compute mean ages of the central stellar populations from absorption features. To gain quantitative insight into the typical age of the stars in the central regions of the ESF-ETGs, the publicly available code `EZ_Ages` (Schiavon, 2007; Graves & Schiavon, 2008) was used to compute a mean luminosity-weighted age from the stacked spectrum. Stellar absorption templates are fit to the spectrum, and an age is derived based on the calculated strength of

age-sensitive absorption features, such as Hβ. Caution must be taken to account for any absorption line infill due to nearby emission. The Hβ absorption line strength measured here was corrected for infill by first determining the EW of the [O III] emission [visible only in the continuum-subtracted spectrum (not shown)], then calculating the appropriate Hβ correction using Equation (A1) of Appendix A in Graves & Faber (2010). The correction was subtracted from the Hβ line strengths before estimating ages. The resulting mean luminosity-weighted age (determined using primarily Hβ and $\langle$Fe$\rangle$) of the central regions of the ESF-ETGs is $6.8^{+2.1}_{-1.7}$ Gyr. This derived age is younger than a pure, maximally old passively evolving stellar population, but it is consistent with light-weighted ages of the central regions of other ETGs in the local universe (e.g., Trager et al., 2000). Moreover, an age of $\sim$ 7 Gyr is not consistent with any significant contribution from young stars. For example, the SAURON galaxies with recently formed young stellar populations have Hβ-based light-weighted ages younger than $\sim$ 3 Gyr (Kuntschner et al., 2010).

3.3.4 The SR2010 ESF-ETGs in Context

With their characteristic blue outer colors and distinctive UV rings, the ESF-ETGs represent a clearly identifiable stage of evolution of massive ETGs through the GV. While the UV properties of only a small number of ESF-ETGs have been

presented in this work, it is useful, if possible, to place our results in the broader context of evolution through the GV. To do so requires answering two questions. First, are ESF-ETGs rare or common among the GV population? Second, what is the "residence time" of ESF-ETGs in the GV? The answer to the first question can help establish whether or not extended SF is a dominant phenomenon among GV galaxies. Answering the second question can help distinguish between plausible SF histories of the ESF-ETGs, such as those discussed in Section 3.3.2.

Accordingly, in this section a search is conducted for further potential ESF-ETG candidates in the SDSS master sample defined in Section 3.2.1. We first review the selection cuts made by SR2010 in defining their *HST* sample and explain the motivations behind them. Then we apply a modified version of the SR2010 cuts on the SDSS master sample and examine the properties of the resulting objects, many hundreds of which we also believe to be ESF-ETGs. Sources of contamination that need to be accounted for when counting GV galaxies are discussed, and a rough estimate of the fraction of ESF-ETGs in the GV is presented. This is followed by a discussion of the ESF-ETG GV residence time and its use in constraining potential SF histories for the ESF-ETGs.

3.3.4.1 SR2010's Selection Criteria

At first blush, the small number of galaxies selected by SR2010 would seem to suggest that ESF-ETGs comprise an insignificant part of the GV. In the following

sections we show that this is not the case. Recall that SR2010 selected an initial sample of ~ 60 objects with strong UV excess and no spectral signatures of SF or AGN activity starting with a cross-matched SDSS DR4/*GALEX* IR1.1 catalog (Seibert et al., 2005) containing 18,127 galaxies[5]. The second column of Table 3.3 shows the number of galaxies we obtain from the same catalog that satisfy each successive SR2010 cut, until the final sample is obtained. To review, the first cut made by SR2010 selected for ETGs by choosing galaxies with r-band concentration $C > 2.5$. To exclude objects with emission due to SF or AGN, only galaxies in the "Unclassifiable" category as defined by Brinchmann et al. (2004) were kept (these are galaxies with generally weak emission). To further prune remaining galaxies with weak emission, SR2010 required Hβ S/N < 3 and excluded any galaxies located within the LINER region of the BPT diagram, i.e., $-0.2 < \log([\text{N II}]/\text{H}\alpha) < 0.5$ and $-0.3 < \log([\text{O III}]/\text{H}\beta) < 0.8$, regardless of line S/N. Finally, a color cut was made to select galaxies with strong UV excess (FUV$-r < 5.3$). As can be seen in the second column of Table 3.3, their very small final sample is due mainly to the cuts on "Unclassifiable" galaxies and FUV$-r$ color. We note that among these ~ 60 objects are galaxies with clear optical disturbances, late-type morphologies and post-starburst signatures. To arrive at their final sample of 30 objects, SR2010 excluded these contaminants.

[5]This number includes the subset of galaxies with both NUV and FUV detections and redshift $z < 0.12$ located within $0.^{\circ}55$ of the center of the *GALEX* field of view. The catalog sky coverage is 645 deg^2.

Table 3.3. Sample Sizes Using Original SR2010 ESF-ETG Selection Criteria

Cut	DR4/IR1.1[a]	SDSS Master Sample[b]
Initial Sample[c]	18127 (100%)	31763 (100%)
Conc > 2.5	8119 (44.8%)	15617 (49.2%)
"Unclassifiable"[d]	1819 (10.0%)	4152 (13.1%)
Hβ S/N < 3[e]	1761 (9.7%)	4026 (12.7%)
Not LINER[f]	1008 (5.6%)	2338 (7.4%)
FUV$-r < 5.3$	**67** (0.37%)	**186** (0.59%)

[a]SDSS/*GALEX* catalog from which SR2010 selected ESF-ETGs.

[b]SDSS DR7/*GALEX* GR6 catalog used in this work.

[c]Redshift $0.005 < z < 0.12$, NUV- and FUV-detected in MIS, and within $0.^{\circ}55$ of the center of the *GALEX* field of view.

[d]Galaxies lacking statistically significant emission lines according to Brinchmann et al. (2004).

[e]A further cut to ensure weak emission; see text.

[f]"Unclassifiable" galaxies outside the LINER region of the BPT diagram.

This is discussed further in Section 3.3.4.3.

We applied the SR2010 cuts on the SDSS master sample, which is based on SDSS DR7 and *GALEX* GR6 data and is roughly twice as large as the Seibert et al. (2005) dataset used by SR2010. This results in a sample of 186 galaxies, as shown in the third column of Table 3.3. Both samples include only galaxies with redshift $z < 0.12$ that are detected in FUV at *GALEX* MIS depths. Starting with this larger sample yields a bigger bottom line, but apart from that the effect of the various cuts is very similar in the two samples. In other words, it appears that

ESF-ETGs selected using the strict SR2010 criteria are still rather uncommon, comprising only $\sim 0.6\%$ of the entire SDSS master sample. It should be noted that the original goal of SR2010's selection strategy was to study objects with unusually strong UV excess that was not obviously related to SF or AGN activity. Therefore, they purposely imposed very strict criteria on spectroscopic quiescence to reduce possible UV contamination from SF or AGN. Their selection criteria were not designed to obtain a *complete* sample of ESF-ETGs. To achieve that we modify some of their criteria below.

3.3.4.2 Searching for Additional ESF-ETGs in the Green Valley

The hallmark of ESF-ETGs is that they are characterized by extended SF in their outer parts, while their centers are devoid of SF. Nevertheless, as demonstrated in Section 3.3.3, their central regions may harbor weak emission consistent with LINERs. Regardless of the source of the LINER emission (Section 3.3.3), such emission may be a common feature of ESF-ETGs and may hold clues to their evolution through the GV. Thus a search for ESF-ETGs ought not to exclude *a priori* galaxies with weak (LINER) emission since such emission unlikely affects the UV flux (Section 3.3.3). Because SR2010 explicitly excluded galaxies with *any* central emission, their exclusion of LINERs probably also excluded many genuine non-star-forming galaxies. In what follows, we relax the SR2010 selection criteria to accept LINERs, and thereby demonstrate that a larger sample of ESF-

candidates exists and that such a sample indeed shares many similarities with the ESF-ETGs observed by *HST*.

In selecting our new "ESF-candidate sample", the most salient SR2010 selection criteria were retained, namely, the morphological cut (concentration $C > 2.5$) and the FUV$-r$ color cut (FUV$-r < 5.3$). However, we avoided selecting galaxies based on the spectral categories defined by Brinchmann et al. (2004), which relied on S/N cuts and BPT classification. Instead, weak central-star-forming galaxies were chosen based on Hα equivalent width (EW). Because the EW measures the continuum-normalized line strength, it can be used to compare the emission properties in galaxies with different intrinsic luminosities in a relatively uniform manner. Since we are interested in selecting (bright) galaxies with weak Hα emission, the EW provides a cleaner indicator of Hα line strength than a S/N cut on the emission line flux.

Shown in Figure 3.8(a) is the FUV$-r$ versus Hα EW distribution of the SDSS master sample, with the ESF-ETGs overplotted. We see that the ESF-ETGs lie within (or below) the GV in FUV$-r$ (by selection) and also have low Hα EWs for their FUV$-r$ color. The low EWs are consistent with SR2010's selection against detectable emission lines using S/N cuts. The maximum Hα EW among the ESF-ETGs is approximately log Hα EW [Å] ≈ 0.4, and we adopt this as the upper boundary for the ESF-candidates. Thus our final sample of new ESF-

Table 3.4. Sample Size Using Modified Criteria to Find ESF-Candidates

Cut	SDSS Master Sample
Initial Sample	31763 (100%)
Conc > 2.5	15617 (49.2%)
log Hα EW < 0.4	6732 (21.2%)
FUV$-r < 5.3$	**1226**[a] (3.9%)

[a]Before correction for potential contamination, which reduces this number by half (Section 3.3.4.3).

candidate galaxies satisfies the following criteria: (1) FUV$-r < 5.3$, (2) i-band concentration[6] $C > 2.5$, and (3) log Hα EW < 0.4. Because galaxies are now included regardless of spectral classification, the ESF-candidate sample includes objects spectroscopically categorized as LINERs but still excludes star-forming galaxies, which have higher Hα EWs. By casting a wider net, we now find that the ESF-candidate sample contains 1226 galaxies, almost seven times more than the SR2010 criteria returned. Moreover, like the ESF-ETGs, the ESF-candidate galaxies lie on the optical red sequence despite their blue FUV$-r$ colors. Table 3.4 lists the number of galaxies remaining after each of the new selection cuts. Evidently including galaxies with weak emission yields many more galaxies.

Figure 3.8(b) presents the distribution of the original ESF-ETGs and the new ESF-candidate sample in FUV$-r$ versus Hα EW. ESF-candidates classified as

[6]SR2010 selected galaxies using r-band concentration. However, the difference between the r- and i-band concentrations is negligible.

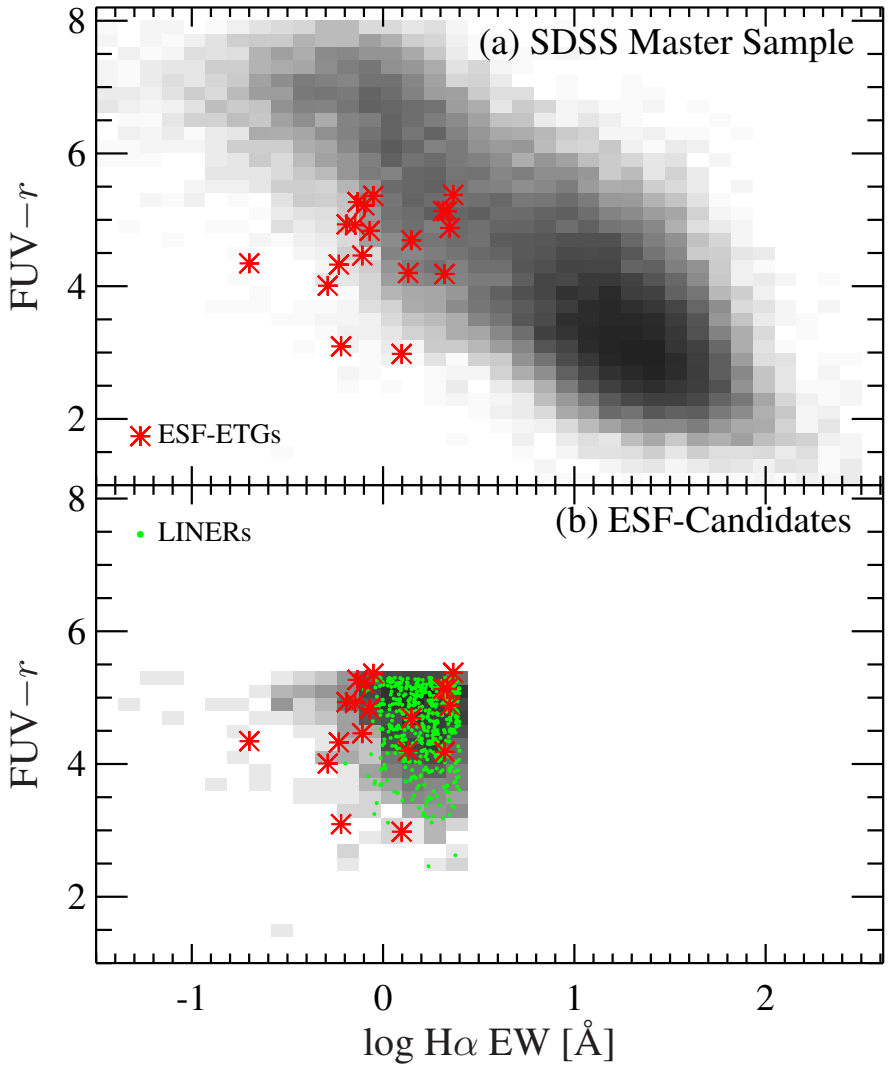

Figure 3.8: FUV$-r$ vs. Hα equivalent width (EW). (a) The SDSS master sample (gray histogram) is plotted along with the ESF-ETGs (red points). By selection, the ESF-ETGs have FUV$-r < 5.3$, concentration $C > 2.5$, and weak Hα emission. (b) A new ESF-candidate sample (gray histogram, ~ 1200 objects) chosen to match the ESF-ETGs and selected using FUV$-r < 5.3$, $C > 2.5$, and a simple cut on Hα EW (log Hα EW < 0.4). Galaxies classified as LINERs by Brinchmann et al. (2004) (534 objects) are plotted as green dots. The distribution of the ESF-ETGs in this parameter space is consistent with that of the ESF-candidates. Also, the LINERs fall generally within the same region as both the ESF-ETGs and the ESF-candidate sample.

LINERs according to Brinchmann et al. (2004) are plotted as green dots. Three things to note are: (1) The new ESF-candidate sample has a similar distribution as the ESF-ETGs, (2) the LINERs make up a significant fraction of the ESF-candidate sample ($534/1226 \approx 44\%$), and (3) most of the original ESF-ETGs have Hα EWs comparable to the LINERs. Point (1) is simply due to selecting galaxies with similar color and EWs as the ESF-ETGs. Point (2) suggests that many of the ESF-candidates have weak emission that in the stronger cases has been classified as LINERs. Point (3) is consistent with the results of Section 3.3.3, where LINER emission lines, including Hα, were detected in the stacked spectrum of the ESF-ETGs. If one assumes that LINER activity is common in aging stellar populations, then it is reassuring to find that a significant fraction of the ESF-candidate sample are LINERs. Moreover, it is of interest to see whether the LINER galaxies have other properties in common with the ESF-ETGs.

A notable characteristic of the ESF-ETGs is their large UV sizes (SR2010). This is important because it may be a clue to the origin of the gas fueling the extended SF. SR2010 showed that the *GALEX* FUV FWHM sizes of the ESF-ETGs (roughly their UV diameters) tend to be larger than other GV galaxies with similar specific SF rates (their Figure 5). We obtain a similar result in Figure 3.9(a), where the distribution of FUV FWHM versus FUV$-r$ color is plotted in a similar style as Figure 3.8. Figure 3.9(a) shows the ESF-ETGs compared to the

full SDSS master sample. Clearly, the ESF-ETGs are systematically larger than the average of *all other GV galaxies of similar FUV−r color*.

Since we aim to establish the similarity between the true ESF-ETGs and the ESF-candidates, we proceed to compare the UV sizes of the ESF-ETGs with the ESF-candidates. We refrain from making comparisons with the rest of the GV. Figure 3.9(b) shows the UV sizes of the ESF-ETGs and ESF-candidates. Since the latter were chosen in a similar way as the ESF-ETGs, it is not too surprising that their UV sizes are roughly consistent with those of the ESF-ETGs. The higher-Hα galaxies in the GV prove to have smaller UV sizes, and agreement with the ESF-ETG sample is improved when they are eliminated.

To quantify any remaining offset between the ESF-candidates and the ESF-ETGs, a linear fit was made to the ESF-candidate sample and the residuals in FUV FWHM of the ESF-ETGs were computed. The median FUV FWHM residual for the ESF-ETGs is 0.13 ± 0.03 dex. This implies that the ESF-ETGs are $\sim 35\%$ larger than the ESF-candidate galaxies. This slightly larger size may be because the ESF-ETGs were chosen to satisfy strict criteria that may have biased the sample to larger UV sizes, whereas the ESF-candidate sample has not been vetted in a similarly stringent manner. In particular, SR2010 excluded post-starburst galaxies and other blue interlopers, which tend to have smaller UV sizes. We also note that the LINERs in Figure 3.9(b) are not systematically larger or smaller than

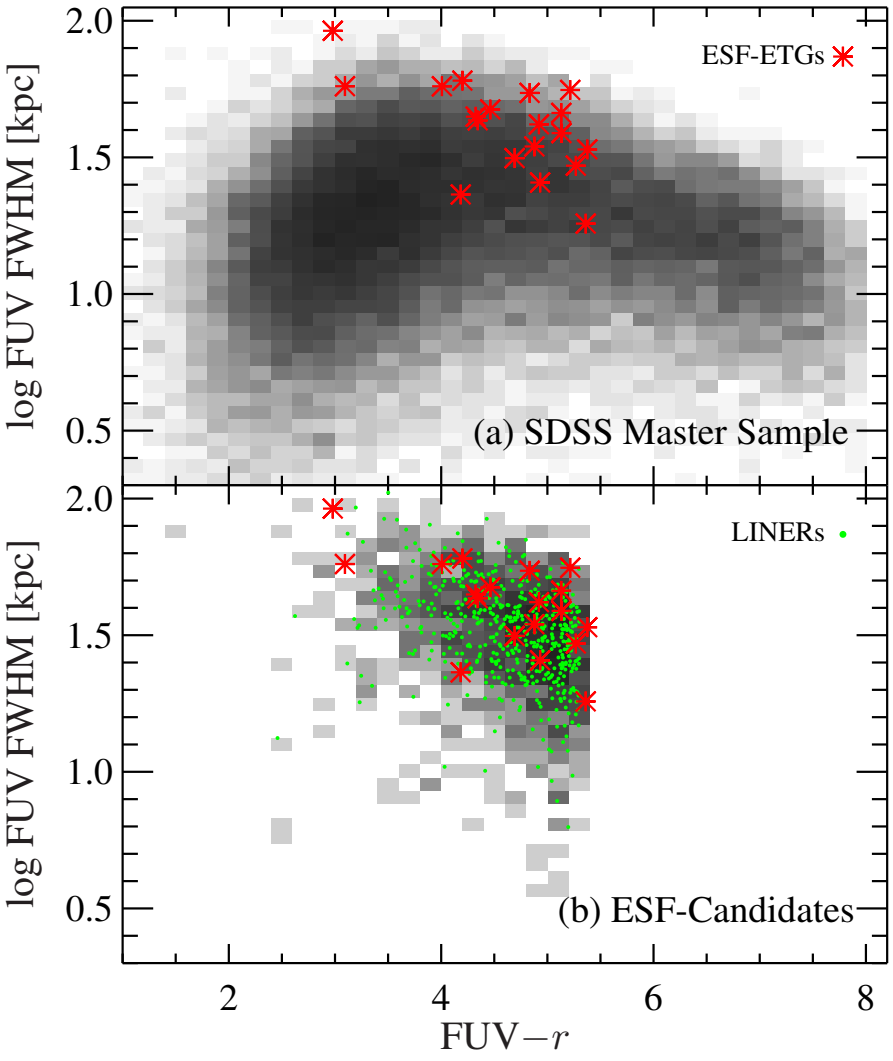

Figure 3.9: *GALEX* FUV FWHM (a measure of UV diameter) vs. FUV$-r$. (a) The distribution of the entire SDSS master sample (gray histogram) and the ESF-ETGs (red points). The finding of SR2010 is confirmed that the ESF-ETGs tend to lie high when compared to all GV galaxies of similar color: their median size is $\sim$ 0.38 dex above the SDSS master sample. (b) The same distribution but now restricted to the ESF-candidate sample of $\sim$ 1200 galaxies chosen to match the original ESF-ETGs with FUV$-r < 5.3$, concentration $C > 2.5$, and log Hα EW < 0.4 (gray histogram). Overplotted are galaxies identified as LINERs by Brinchmann et al. (2004) (green dots). The median offset in size of the ESF-ETGs is now only 0.13 dex above a linear fit to the ESF-candidates.

the ESF-candidates or the ESF-ETGs. This similarity between the ESF-ETGs and LINERs reinforces our assertion that many of the LINER galaxies have large UV diameters consistent with the ESF-ETGs, and that a larger population of GV galaxies with extended UV emission exists.

An additional comparison is made in Figure 3.10, where we show the distribution of FUV size as a function of stellar mass. Figure 3.10(a) shows the SDSS master sample, while Figure 3.10(b) plots only the ESF-candidate sample. A strong trend is apparent in both panels, with more massive galaxies having larger UV diameters. Notably, the ESF-ETGs are consistent with this trend. The median FUV FWHM residual of the ESF-ETGs from a linear fit to the ESF-candidate sample is now only 0.08 ± 0.04 dex, i.e., at fixed stellar mass, the ESF-ETGs are $\sim 20\%$ larger. This median UV size residual is *smaller* than in the previous comparison in Figure 3.9(b), which did not take into account the strong trend with stellar mass. Again, the existence of LINER galaxies with similarly large UV sizes strengthens our point that such UV-extended galaxies comprise a non-negligible fraction of massive GV ETGs (see below).

To summarize, we conclude that the stellar masses and UV sizes of the 19 *HST* ESF-ETGs are consistent with a much larger sample of ESF-candidate objects. This analysis lends support to our claim that the ESF-ETGs are only a small subset of a larger population of galaxies with similar properties.

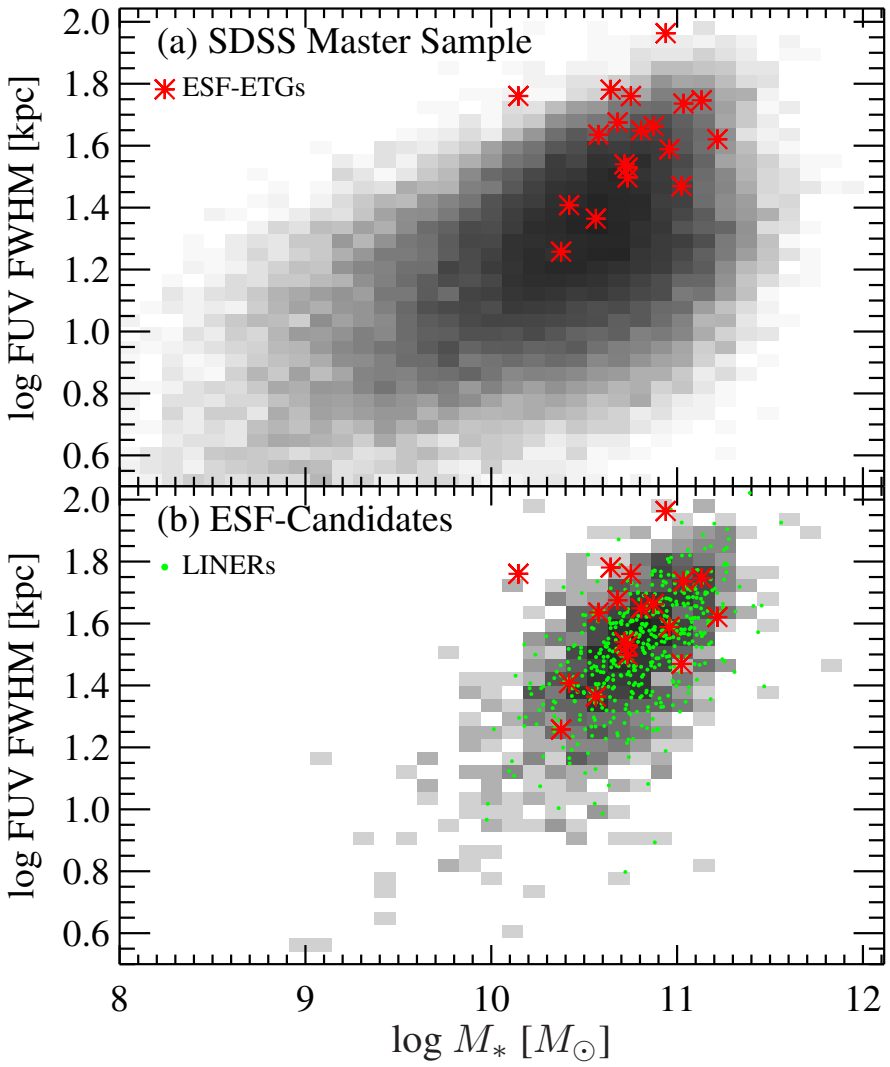

Figure 3.10: Galaxy stellar mass M_* vs. *GALEX* FUV FWHM (a measure of UV diameter). (a) The entire SDSS master sample (gray histogram) and the ESF-ETGs (red points). The ESF-ETGs lie high by ~ 0.3 dex. (b) The same distribution but now restricted to the ESF-candidate sample of ~ 1200 galaxies chosen to match the original ESF-ETGs with FUV$-r < 5.3$, concentration $C > 2.5$, and log Hα EW < 0.4 (gray histogram). Overplotted are galaxies identified as LINERs by Brinchmann et al. (2004) (green dots). The median offset in UV size of the ESF-ETGs is now only 0.08 dex above a linear fit to the ESF-candidates.

3.3.4.3 The Contribution of ESF-ETGs to the GV

Investigating a sample with weak or marginally detected properties is always challenging because of the inherent inhomogeneities present within it due to measurement error or misidentification. The ESF-candidate sample is no exception, and properly screening its members is necessary to obtain useful results. Indeed, prior to formulating their final *HST* program, SR2010 visually inspected their $\sim$ 60 candidate objects for possible contamination due to nearby companions, tidal disturbances, or post-starburst galaxies and wound up discarding half of them on these accounts. We repeated this exercise on their $\sim$ 60 objects and found 20 contaminants, or 1/3 of the sample. Most of the contamination is due to nearby UV-bright objects that in some cases induce a large ($\gtrsim 3''$) offset between the SDSS and *GALEX* positions. Five contaminants have post-starburst spectra and appear rather blue in optical color; these were eliminated by SR2010 because their UV emission is obviously due to SF. In addition to the 1/3 of the sample excluded by our new visual inspections, *HST* UV imaging revealed that about 1/3 of the actually imaged galaxies had UV morphologies unlike the ESF-ETGs; their UV emission is either compact or on small scales (Section 3.2 and Paper I). Taken together, these cuts imply that almost half of the galaxies in the initial sample of $\sim$ 60 are not bona fide ESF-ETGs. Assuming that this fraction is representative of the larger ESF-candidate sample, the estimated number of true ESF-ETGs is

reduced from ~ 1200 to ~ 600.

A key question is whether the ESF-candidate sample represents the typical galaxy evolving through the GV. However, determining this requires some care. Because the ESF-ETGs and the ESF-candidates have high stellar masses ($\gtrsim 10^{10.5} M_{\odot}$), we can only make statements about the *massive* end of the GV. We define the massive end of the GV in FUV$-r$ color-mass space to be bounded by $4 <$ FUV$-r < 5.3$ and $10.3 < \log M_*/M_{\odot} < 11.2$. This mass range spans most of the ESF-ETGs and contains ~ 5200 galaxies in the SDSS master sample. To avoid potential contamination due to dust-reddened, star-forming galaxies, we further exclude highly inclined galaxies with axis ratio $b/a \leq 0.5$. This is a significant cut that removes ~ 1800 galaxies. This cut is motivated by the observation that nearly all of the ESF-ETGs tend to be nearly face-on, with $b/a > 0.5$ (Table 3.1). To be consistent with the cuts made to identify massive GV galaxies, we cut the ESF-candidate sample to have the same range in stellar mass, FUV$-r$ color, and axis ratio. This results in 670 galaxies, and implies that the relative fraction of ESF-candidates among massive GV galaxies in this UV color-mass bin is $670/3400 \approx 20\%$. Exact numbers are presented in Table 3.5 for reference.

Note that this quoted fraction has not been corrected for contamination by superposed companions, post-starburst galaxies, etc., as discussed above. If such contamination is random, then the resulting fraction remains unchanged. How-

Table 3.5. Contribution of ESF-ETGs to the GV

Cut	SDSS Master Sample
Initial Sample	31763 (100%)
Massive GV[a]	5199 (16.4%)
Face-on ($b/a > 0.5$)	3389 (10.7%)
ESF-Candidates[b]	670 (2.1%)

[a]Galaxies with $10.3 < \log M_*/M_\odot < 11.2$ and $4 < \mathrm{FUV} - r < 5.3$.

[b]ESF-candidates (Table 3.4) located in the massive GV.

ever, if some forms of contamination affect the ESF-candidate sample more than the general GV population, then the fraction can be smaller. For example, post-starburst galaxies ought to be excluded from the ESF-candidates but not the general GV because they are truly transitioning from blue to red but are not ESF-ETGs. We have attempted to estimate this "differential contamination" by applying cuts to the ESF-candidate sample that mimic the results of the visual inspection described earlier. Specifically, contaminants are excluded if they satisfy any of the following conditions: (1) $\mathrm{H}\delta_A > 1.65$ to remove post-starbursts, (2) FUV-to-optical size ratio < 2.15 to remove galaxies without extended SF, or (3) *GALEX*-SDSS separation $> 2\farcs2$ to remove obvious superpositions. Applying these cuts lowers the ESF-candidate fraction to $\approx 13\%$, i.e., contamination may reduce the fraction by $\approx 30\%$.

By defining a suitable ESF-candidate sample, we have shown that many other

objects exist with similar properties (FUV$-r$ color, Hα EW, stellar mass, and UV size) to the original ESF-ETGs. Within these selection cuts, ESF-candidates classified as LINERs have similar properties as well. This bolsters our belief that ESF-ETGs are accompanied by weak LINER-like emission. We have therefore shown that the 19 ESF-ETGs studied in this paper are part of a larger population of similar galaxies. Moreover, we have shown that extended SF in ETGs is not a rare phenomenon among massive GV galaxies.

3.3.4.4 Constraining the Timescale of Recent SF in the ESF-ETGs

In the previous section we showed that a modest fraction (13%) of massive GV galaxies are likely to be ESF-ETGs. However, this by itself does not constrain the star formation *timescale* of the ESF-ETGs. This quantity is important as it will be used later to identify plausible SF histories for the ESF-ETGs, in particular focusing on the recent SF traced by the UV. In this section we estimate the contribution of rapid, bursty SF as triggered by a minor merger to the fraction of ETGs in the GV. The goal of this analysis is to determine if such bursty SF is sufficient to explain the abundance of ESF-candidates in the GV identified in the previous section.

The expected number of ETGs found in the GV due to minor-merger-driven SF is calculated as follows. We assume the progenitors are ETGs in the UV-optical red sequence (FUV$-r > 6$) or not detected at all in FUV. This color cut is made

on the assumption that ESF-ETG progenitors were initially quiescent and not star-forming and that the subsequent, rejuvenated SF moved them back into the GV. The progenitors are restricted to galaxies with (1) $10.3 < \log M_*/M_\odot < 11.2$, (2) concentration $C > 2.5$, and (3) axis ratio $b/a > 0.5$. These cuts are made to be consistent with the ESF-candidates, which are the presumed descendants. This gives 11875 galaxies.

The minor merger rate is estimated using the theoretical predictions given in Kaviraj et al. (2009). Specifically, a minor merger rate of 0.03 Gyr^{-1} (1:10 mass ratio) is assumed. In addition we estimate the time spent in the GV due to enhanced SF to be $\sim$ 750 Myr. This estimate assumes three pericentric passages of the satellite, each causing an enhancement of the SF rate (and bluer FUV$-r$ colors) lasting for $\sim$ 250 Myr (Kaviraj et al., 2009; Peirani et al., 2010). Note that the final coalescence is not included in this estimate because the resulting SF is expected to be centrally concentrated and hence unlike the SF seen in the ESF-ETGs. Combining these values, we estimate $\approx$ 270 ETGs to be present in the GV due to (ring-like) minor-merger-driven SF. Compared with the 670 ESF-candidates identified in the previous section, we see that bursty SF resulting from minor mergers can only account for $\sim$ 40% of ESF-candidates. It is interesting to note that this fraction is not too different from the $\sim$ 30% differential contamination presented in the previous section. In other words, the contaminating galaxies

are quite possibly a subset of the minor-merger-driven SF galaxies. Note that the above discussion is meant to constrain the role of bursty *star formation* due to minor mergers; we are not requiring that the *gas* fueling the observed SF cannot have come from minor mergers.

It should be noted that the 40% estimate is subject to uncertainties in both the merger rate and GV residence time. In particular, (minor) merger rates are uncertain at the factor of ~ 2 level at least (e.g., Hopkins et al., 2010; Lotz et al., 2011). Also, the GV residence time is sensitive to the duration of each burst of SF and the number of passages, which depend on the merger geometry, mass ratio, etc. (e.g., Cox et al., 2008; Peirani et al., 2010). It is difficult to quantify such uncertainties, and the 40% contribution estimated above should be viewed as a rough estimate at best. Thus we tentatively suggest that bursty SF is unlikely to be the dominant cause of the SF in the ESF-ETGs, though it cannot be firmly ruled out by this analysis. However, Section 3.4 below highlights other evidence that indicates that the SF in the majority of ESF-ETGs is likely due to more gradual processes.

3.4 How Do ESF-ETGs Move through the Green Valley?

Given the photometric and spectroscopic results presented for the ESF-ETGs, along with the selection and examination of the ESF-candidates, we are now in a stronger position to interpret the recent SF observed in the ESF-ETGs. The main question motivating this study is whether the ESF-ETGs are fading out or are rejuvenated. This question is directly tied to how these galaxies are evolving through the GV. To provide a framework for discussion, we present three possible evolutionary scenarios to explain the SF in the ESF-ETGs: (1) rapid quenching, (2) disk rejuvenation (SF in a pre-existing disk), and (3) gradual decline. We evaluate the plausibility of each scenario in light of the results in this paper and Paper I. The present discussion supplements the close examination in Paper I of the origin of the gas fueling the extended SF in the ESF-ETGs.

(1) Rapid quenching. In this scenario, SF is quickly truncated as a result of a (gas-rich) major merger that triggers a rapid starburst and/or AGN. Centrally concentrated SF is expected to occur in galaxies undergoing such an event due to the funneling of gas toward the center during the merger (e.g., Hernquist & Mihos, 1995; Hopkins et al., 2006). The gas can also power an AGN that ejects any remaining gas out of the galaxy (Di Matteo et al., 2005). The timescale for

SF is expected to be short (a few 100 Myr; Di Matteo et al., 2005; Hopkins et al., 2008), owing to the strong AGN feedback that effectively quenches any remaining SF. The resulting remnant is predicted to have spheroidal morphology. Note that this scenario applies equally well to a galaxy that is moving from the blue cloud to the red sequence for the first time or has been rejuvenated back into the GV.

Though it is possible that the ESF-ETGs have undergone rapid quenching in the past, the *recent* SF observed is unlikely to be related to the end phase of such an event. Their optical morphologies, while bulge-dominated, include a disk component, are undisturbed, and do not reveal any signs of recent mergers or interactions with nearby companions (SR17 is an exception; Paper I). In addition, we find that the stellar populations at the centers of the ESF-ETGs are uniformly old, arguing against centrally concentrated recent SF. There does exist evidence for rapid quenching of SF via major mergers in certain kinds of galaxies, notably post-starburst galaxies. However, the spectra of such objects show signatures of a few 100-Myr old stellar population superimposed on old stars (e.g., Quintero et al., 2004), and many are morphologically disturbed. In contrast, none of the SDSS spectra of the ESF-ETGs displays the strong Balmer lines characteristic of post-starbursts, as expected from how they were selected. We note that only five of the original 60 SR2010 candidates were excluded because they appeared to be post-starbursts based on their large $H\delta_A$ values; these may be the post-major

merger objects. The lack of central SF in the ESF-ETGs is not too surprising given the SR2010 selection criteria, which selected galaxies without detectable emission in the centers yet had blue FUV$-r$ colors. This unique combination of parameters is thus a useful method of finding GV galaxies dominated by *extended* UV emission.

Based on their undisturbed morphologies and lack of centrally concentrated SF, we conclude that the ESF-ETGs have not experienced recent rapid quenching and that their SF is the result of some other, less violent process. We are not implying, however, that such a scenario is impossible for at least some GV galaxies. Rapid quenching is seriously considered as the main channel for some galaxies to evolve onto the red sequence (Faber et al., 2007; Martin et al., 2007).

(2) Disk rejuvenation. In this scenario recent SF takes place in an *existing* (formerly quiescent) stellar disk, such as those found in S0 galaxies. The newly formed stars cause the FUV$-r$ color to become bluer. Because the new young stars form on top of the existing old stellar population, galaxies undergoing disk rejuvenation would be expected to have similar colors to the outer colors seen in the ESF-ETGs in our sample. In the nearby universe, this phenomenon is exemplified by the discovery of extended-UV (XUV) disks (e.g., Thilker et al., 2005, 2007). XUV-disk galaxies are characterized by extended UV emission located beyond the SF threshold. In most cases, this translates to SF being located

beyond the optical extent of the galaxy, though in some objects the XUV emission is found *within* the optical extent. XUV-disks have been found in galaxies of all Hubble types, notably even in E/S0 galaxies (Lemonias et al., 2011; Moffett et al., 2012). Thus it is possible that the ESF-ETGs are examples of early-type XUV-disks, especially since their SF occurs primarily in the outskirts of the optical disks (Figures 3.4 and 3.5; Paper I).

Thilker et al. (2007) adopted a threshold UV surface brightness of $\mu_{\rm FUV} = 27.25$ AB mag arcsec^{-2} to characterize XUV disks, which corresponds to a threshold SF surface density of $\Sigma_{\rm SFR} = 3 \times 10^{-4}\, M_{\odot}\, {\rm yr}^{-1}\, {\rm kpc}^{-2}$. According to that criterion, our ESF-ETG UV disks hover near that level, as may be seen in Figures 3.4 and 3.5, thus qualifying them as XUV disks or very near that level. Indeed, a study of the space density of XUV-disk galaxies by Lemonias et al. (2011) has shown that XUV-disks are more common among red sequence and GV galaxies. In one respect, however, our galaxies differ strongly in that their outer FUV$-r$ colors are a full 1.5–2.5 mag bluer than their integrated FUV$-r$ colors. In Lemonias et al., by contrast, outer FUV$-r$ colors correlate closely with integrated FUV$-r$ colors, and there are no blue outer disks at all among their red galaxies (their Figure 12). Thus, it is not clear that they are detecting the same phenomenon that we are.

Different mechanisms can deliver gas into the outer regions of a galaxy and trigger disk rejuvenation. Lemonias et al. (2011) proposed that cold gas accretion

from the intergalactic medium (IGM) is responsible for triggering SF in the XUV-disks. This picture is a possible manifestation of late-time cold mode accretion predicted in simulations (Kereš & Hernquist, 2009). In addition, minor, gas-rich mergers can also trigger recent SF in ETGs (Kaviraj et al., 2009), perhaps leading to disk rejuvenation in addition to nuclear SF.

Disk rejuvenation may be a viable explanation for the SF seen in at least some of the ESF-ETGs. All the ESF-ETGs in the sample are classified as S0 or later (Paper I), so the presence of extended UV emission is not unreasonable given the literature results discussed above. As discussed in Section 3.3.2, the outer disks of the ESF-ETGs contain a significant underlying old stellar population upon which new stars have formed. However, any disk rejuvenation cannot have been triggered recently or very rapidly. For one thing, the highly symmetric UV morphologies of the ESF-ETGs would require any gas to be resident in the galaxies for a few rotation periods, which in the outer parts is likely to exceed $\sim$ 1 Gyr. IGM accretion is consistent with this picture as long as it occurs smoothly on extended timescales, allowing the gas to settle into an axisymmetric disk before forming stars.

In addition, as Figure 3.6 indicates, a burst superimposed on an old stellar population reddens too quickly. We roughly estimated in Section 3.3.4.4 that bursty SF due to minor mergers produces less than half the number of ESF-

candidates identified in the GV (Section 3.3.4.3), tentatively suggesting that minor mergers are not the dominant cause of the SF in the ESF-ETGs. Moreover, the SF histories predicted from minor merger simulations are bursty with typical timescales of a few to several 100 Myr (Cox et al., 2008; Kaviraj et al., 2009). Also, the newly formed stars tend to be centrally concentrated (Cox et al., 2008; Peirani et al., 2010), in contrast with the red colors seen in the bulges of the ESF-ETGs (Figure 3.4). Taken together, these points suggest that disk rejuvenation is only viable if (1) the gas has not been recently accreted and (2) the resulting SF has been ongoing for an extended period of time.

In a study of the recent SF histories of SDSS galaxies, Kauffmann et al. (2006) hypothesized that galaxies above a transitional surface mass density experience intense bursty SF that consumes infalling gas on timescales of $\sim$ 1 Gyr. Such (rejuvenated) SF is likely to drive galaxies from the red sequence into the green valley. The morphological and photometric data of the ESF-ETGs can provide useful constraints on this model. In particular, assuming a rotation speed of $200\,\mathrm{km\,s^{-1}}$ at a radius of 10 kpc, and hence a rotation period of 300 Myr, recently infalling gas would have experienced $\sim$ 3 rotation periods in 1 Gyr. This is likely sufficient time for the gas to settle into an axisymmetric disk. The average galaxy would be observed halfway through this period, and one would expect to see a distribution of morphologies corresponding to various stages of gas rearrangement.

However, we do not see such diversity in the UV morphologies of the ESF-ETGs. In addition, stellar population analysis of the outer disks (Section 3.3.2) indicates that SF in the outer parts of the ESF-ETGs takes place on timescales longer than 1 Gyr. Also, the similarity between the outer colors of the ESF-ETGs and massive blue cloud galaxies [where SF proceeds on Gyr timescales (Noeske et al., 2007)] points to a longer gas consumption timescale than that suggested by Kauffmann et al. (2006).

(3) Gradual decline. In this scenario, a galaxy's *original* SF gradually shuts down as its existing gas supply is used to form stars (Noeske et al., 2007). No mergers or interactions are required to explain the recent SF, and the galaxy's original (disky) morphology is preserved. This model reflects the general expectation that most galaxies are evolving from blue to red for the first time. Gradual decline implies that SF is steadily decreasing over time, and hence that there exists an underlying population of older stars.

While the timescale for evolution from blue to red is generally believed to be fairly rapid ($\sim$ 1 Gyr; Martin et al., 2007), it is certainly not expected that *all* galaxies need transition through the GV in such a rapid manner. Indeed, local observations have shown the existence of a population of galaxies in the GV, primarily S0s, whose cold gas properties imply a much longer GV residence time (e.g., van Driel & van Woerden, 1991; Noordermeer et al., 2005; Cortese & Hughes,

2009). Specifically, radio observations of S0s have revealed that some harbor large H I reservoirs containing $\sim 10^9\,M_\odot$ of gas or more. The gas surface density in these reservoirs, $\Sigma_{\rm gas} \sim$ few $M_\odot\,{\rm pc}^{-2}$, fall within the H I-to-H_2 transition regime, where the SF rate declines non-linearly with $\Sigma_{\rm gas}$ (Krumholz et al., 2009). Specifically, the SF rate is predicted to be $\sim$ 10 times lower than in normal spiral galaxies, i.e., $\sim 0.1\,M_\odot\,{\rm yr}^{-1}$. These results imply a gas consumption time of up to 10 Gyr in these gas-rich S0s. In other words, there likely exists a subpopulation of GV galaxies whose SF can persist at a very low level for a very long time.

We find this gradual decline scenario to be another possible explanation for the recent SF seen in the ESF-ETGs. Their undisturbed and symmetric morphologies indicate a lack of recent mergers or interactions. The blue outer disks plus red bulges are a possible extension of morphologies of galaxies slightly later along the Hubble sequence, which sometimes show a hole in their central gas distributions and a lack of young stars in their bulges (Pahre et al., 2004; Gil de Paz et al., 2007). Moreover, the H I distributions of the S0 galaxies described above are typically ring-like with central depressions in gas surface density (e.g., van Driel & van Woerden, 1991; del Río et al., 2004; Noordermeer et al., 2005). Moreover, *GALEX* imaging of some of these S0s show UV rings reminiscent of those seen in the ESF-ETGs (Cortese & Hughes, 2009). Thus it is conceivable that the ESF-ETGs harbor similar reservoirs of low-surface-density cold gas. Obtaining radio

observations of the ESF-ETGs would be extremely useful in characterizing the amount and distribution of cold gas in these objects.

Finally, we showed in Section 3.3.2 that the stellar populations in the UV rings contain a significant contribution from old stars, and that their SF histories are consistent with fading τ-models. Assuming that the fading model applies to ESF-ETGs in general, and because fading is considered an important mode of evolution through the GV, one would expect to find a significant fraction of GV galaxies with ESF-like properties. Section 3.3.4.3 showed that $\approx 13\%$ of massive galaxies in the bluest part of the GV are ESF-candidates. Though not a majority in this region, ESF-candidates nonetheless make up a non-negligible portion of it, and we cannot rule out fading for at least a subset of these objects. We note that gas-rich GV galaxies comprise $\sim 12\%$ of the total GV sample presented in Cortese & Hughes (2009). The close agreement between their fraction and the 13% ESF-ETG GV fraction found here is intriguing and indicates that gradual decline of SF on Gyr timescales should not be discounted as an important evolutionary path through the GV for some objects.

To summarize, only certain models for the SF in the ESF-ETGs survive comparison with the results presented in this paper. The viable models are the slow decline of the original SF and/or (non-bursty) disk rejuvenation. SR2010 and Paper I reach similar conclusions based on the integrated properties of the ESF-

ETGs. In particular, both works found that the decline of the original SF is possible in a subset of the ESF-ETGs, and we come to a similar conclusion based on stellar population analysis of the outer disks of the ESF-ETGs.

SR2010 also argue that the SF in some of the ESF-ETGs is most consistent with rejuvenation because of their lower intrinsic dust content and larger-than-average UV sizes relative to the entire GV. While SR2010 supported rejuvenated SF, they were unable to constrain whether the necessary gas was accreted via mergers or directly from the IGM. We find that mergers (in the rapid quenching model) are unlikely to produce the observed morphologies and lack of central SF in the ESF-ETGs, but IGM accretion is permissible as long as it does not disrupt the galaxy and the resulting SF is not too recent and bursty. Paper I reaches a similar conclusion, finding that $\sim$ 55% of the ESF-ETGs have UV and optical morphologies consistent with smooth IGM accretion. Rejuvenation is permitted as long as the new stars began forming long ago in a gradual manner. We have not been able to think of tests that could tell the difference, definitively, between this kind of "extended rejuvenation" and a simple decline of the existing SF.

3.5 Summary and Conclusions

This paper complements the work of SR2010 and Paper I. Using high-resolution UV imaging from *HST* and optical photometry from SDSS, we measure surface

brightness and UV-optical color profiles of 19 ESF-ETGs selected from a cross-matched SDSS/*GALEX* catalog. These galaxies were selected to have high concentration, blue FUV$-r$ color, and no detectable emission lines within the SDSS fiber. This combination of selection criteria yielded a sample dominated by objects with *extended* UV emission. Our main results are summarized below.

1. The UV-optical color profiles of the ESF-ETGs all show red centers and blue outer parts, as expected given how they were selected. The central FUV$-r$ colors are consistent with red sequence galaxies (FUV$-r \gtrsim$ 6), implying that the observed central UV emission is unlikely due to recently formed stars. By contrast, the outer FUV$-r$ colors are all quite blue (FUV$-r \sim 2-4$), which is similar to star-forming, blue cloud galaxies. Blue colors together with well-formed UV structures in the regions of extended UV emission point to recent SF in the outer regions of these galaxies.

2. A comparison of the outer colors of the ESF-ETGs with blue cloud galaxies in different mass ranges shows that the stellar populations in the outer disks of the ESF-ETGs contain many old stars. Additionally, their outer colors are consistent with gradually declining τ-models that indicate old stellar population ages, as well as with a "double-τ" model representing a prolonged rejuvenation event. The colors are also marginally consistent with a recent-burst model. However, we roughly estimate that a bursty SF history

triggered by minor mergers underpredicts the number of ESF-candidates we find (Point 4 below) by a factor of ~ 2.

3. Based on stacked SDSS spectra, we determine a mean light-weighted age of $6.8^{+2.1}_{-1.7}$ Gyr for the centers of the ESF-ETGs, consistent with their red FUV$-r$ colors. We find evidence for weak LINER-like emission (i.e., [O II] and [N II] emission) in the central regions of the ESF-ETGs. If the emission is due to weak AGN activity, this suggests that AGN feedback may have played a role in quenching SF, particularly in the centers of these objects. If instead the LINER emission is caused by gas ionization due to old stars, then this strengthens our conclusion that the centers are dominated by evolved stellar populations.

4. By using a larger, updated SDSS/*GALEX* catalog, we find $\sim$ 600 ESF-candidate galaxies that have similar spectral and structural properties to the ESF-ETGs. The key change in sample selection that yielded a much larger number of ESF-candidates was admitting all Hα-weak objects, including LINERs. We find that the ESF-candidates and true ESF-ETGs have similar distributions in FUV$-r$ color, Hα EW, UV size, and stellar mass. A rough estimate suggests that ESF-ETGs comprise $\approx 13\%$ of massive GV galaxies in their UV color-mass range.

5. We present three possible scenarios to explain the recent SF in the ESF-

ETGs. Based on the results presented, we are able to rule out rapid quenching following a merger-induced starburst. However, our results are consistent with disk rejuvenation (via smooth IGM accretion) and/or the gradual decline of the original SF. Both scenarios can explain the regular morphologies of the ESF-ETGs and the presence of underlying stars in the regions of recent SF. The similarity of some ESF-ETGs to local, gas-rich S0s in the GV suggests that they are among a class of GV galaxies that may take Gyrs to fully quench and reach the red sequence.

The discovery of recent SF in ETGs has challenged traditional explanations of the evolution of these galaxies. Our understanding has benefitted greatly from all-sky surveys in the optical and, crucially, in the UV. The ability of the UV to detect even faint signatures of SF in seemingly quiescent objects highlights the richness and diversity of ETGs and raises many important questions, some of which we examined in this work. Our study of the ESF-ETGs represents an initial attempt to constrain the evolution of galaxies in the GV. Future work will systematically examine the properties and numbers of a wider range of galaxies to study the mass-dependent evolution of galaxies through the GV.

Chapter 4

The Shifting Demographic Landscape of Star-forming Galaxies since $z = 2.5$

4.1 Introduction

The life history of the typical galaxy is fairly well-understood, at least in general, having been refined through the years as observational samples have gotten larger and theoretical models more sophisticated. We know that galaxies grow in mass as they actively form stars. Over time, their star-formation rate (SFR) declines, and galaxies ultimately quench (either gradually or rapidly; e.g.,

Bell et al., 2004; Kauffmann et al., 2006; Faber et al., 2007). Their structure also changes as they evolve: nascent galaxies, fed by narrow flows of accreting gas, start out disturbed and asymmetric, gradually settling down into rotationally supported disks that grow with time (e.g., Trujillo et al., 2006; Dekel et al., 2009; Kassin et al., 2012; van der Wel et al., 2014a). Later on, they undergo further transformation to become centrally dense, bulge-dominated objects, which are eventually believed to become quenched (e.g., Kauffmann et al., 2003b; Franx et al., 2008; Bell et al., 2012; Cheung et al., 2012; Barro et al., 2013; Fang et al., 2013; Tacchella et al., 2015). A galaxy's interstellar medium (ISM) also becomes progressively enriched with metals as it evolves (e.g., Tremonti et al., 2004; Mannucci et al., 2010). Recent reviews summarizing key observational and theoretical results can be found in Silk & Mamon (2012), Madau & Dickinson (2014), and Somerville & Davé (2014).

The methods used to study galaxy demographics and how they change over time have become increasingly sophisticated. A basic overview of galaxies can be made via (1) univariate distribution functions, such as luminosity (or mass) functions (e.g., Schechter, 1976; Blanton & Moustakas, 2009; Marchesini et al., 2009; Muzzin et al., 2013), and (2) cosmic averages of, e.g., the star formation rate or luminosity (or mass) volume density (e.g., Madau et al., 1998; Pérez-González et al., 2005; Behroozi et al., 2013). While these quantities and their time evolution are foundational for describing galaxies, particularly in theoretical models, they

lack the "resolving power" to identify intrinsic variations among galaxies of the same luminosity/mass.

One way to better "resolve" galaxy populations is through the use of scaling relations, such as the SFR-(stellar) mass relation (e.g., Noeske et al., 2007; Salim et al., 2007), the mass-metallicity relation (e.g., Tremonti et al., 2004; Mannucci et al., 2010), and the mass-size relation (e.g., Shen et al., 2003; van der Wel et al., 2014a). These correlations have been well-studied and probe more deeply into the physical processes shaping galaxies as they evolve. However, scaling relations are not perfectly tight; they have intrinsic scatter that is often correlated with additional parameters in a systematic fashion (e.g., Graves et al., 2009b; Mannucci et al., 2010). These relations and their correlated scatter place even more stringent constraints on how galaxies evolve.

Discovering these trends, however, requires rich datasets with a large number of objects and additional measured parameters. Fortunately, large-scale surveys have produced vast quantities of data that can be leveraged to systematically explore the multi-dimensional parameter space traced out by galaxies. At low redshift, programs like the Sloan Digital Sky Survey (York et al., 2000) and complementary surveys at other wavelengths have enabled us to study galaxy evolution as a function of several parameters (e.g., stellar mass, color, morphology, environment) and uncover trends that are often hidden when galaxies are lumped

together under fewer parameters (Blanton & Moustakas, 2009). At high redshift, large amounts of data are being accumulated, thanks to coordinated campaigns using many ground- and space-based facilities, including the *Hubble Space Telescope*. The multi-wavelength datasets and ancillary products generated from these observations have paved the way toward a fuller understanding of distant galaxies. In particular, the Cosmic Assembly Near-Infrared Deep Extragalactic Legacy Survey (CANDELS; Grogin et al., 2011; Koekemoer et al., 2011) offers one of the richest troves of data to study the high-redshift universe, particularly around the era of peak star formation (and AGN) activity ($z \sim 2$). At these redshifts, the CANDELS observations are essentially complete down to $\sim 10^9\,M_\odot$ (Tal et al., 2014), enabling a statistically robust census of galaxy evolution over the past ~ 10 billion years of cosmic time.

In this work, we harness the large sample size and value-added catalogs made possible by CANDELS in order to provide a systematic overview of the star-forming galaxy population at $0.2 < z < 2.5$. Quiescent galaxies are not discussed extensively in this work, as their properties have already been the focus of numerous prior studies, many using CANDELS data (e.g., Fontana et al., 2009; Ilbert et al., 2010; Brammer et al., 2011; Barro et al., 2013; Bezanson et al., 2013; Muzzin et al., 2013; Szomoru et al., 2013; van de Sande et al., 2014). By comparison, star-forming galaxies, especially of lower stellar mass, have received relatively

less scrutiny, despite being arguably more diverse in terms of morphology, gas content, and star-formation activity. Existing studies have tended to focus on global scaling relations (e.g., Williams et al., 2010; Wuyts et al., 2011b; van der Wel et al., 2014a; Genzel et al., 2015), or on unique subclasses (e.g., "blue nuggets"; Barro et al., 2014; Williams et al., 2014). Our analysis, in contrast, examines a mass-complete sample of typical star-forming galaxies, with enough "parameter resolution" to thoroughly characterize their demographics and identify interrelationships among their structure, dust content, and SFR, as a function of stellar mass and redshift.

The chapter is organized as follows. In Section 4.2, we discuss the data used in our work and detail our sample selection. Our analysis begins in Section 4.3 with an examination of regularities among star-forming galaxies within the UVJ diagram (Wuyts et al., 2007; Williams et al., 2009). Specifically, we show that the location of an object in UVJ space at a given stellar mass and redshift is determined by its specific star-formation rate (SSFR) and dust attenuation. Section 4.4 presents a closer examination of dust attenuation as it relates to galaxy structure. This is followed by a census of galaxy shapes in Section 4.5, focusing on the evolution in the distribution of disky versus elongated (prolate) objects. A surprising lack of correlation between galaxy structure and SSFR is presented in Section 4.6. The implications of our results are discussed in Section 4.7, in-

cluding comments on the connection between galaxies and dark matter halos. We summarize our conclusions in Section 4.8. An appendix (Section 4.9) comparing our preferred, dust-corrected, UV-based SSFRs to infrared-based rates shows that both are consistent, justifying the use of our preferred method in the analysis.

All magnitudes are on the AB system (Oke, 1974). We assume a concordance ΛCDM cosmology with $\Omega_m = 0.3, \Omega_\Lambda = 0.7$, and $H_0 = 70\,\mathrm{km\,s^{-1}\,Mpc^{-1}}$.

4.2 Data and Sample Selection

This study makes use of the rich multi-wavelength and ancillary datasets produced by the Cosmic Assembly Near-Infrared Deep Extragalactic Legacy Survey (CANDELS; Grogin et al., 2011; Koekemoer et al., 2011). Out of the five fields targeted in the survey, we use data from two: the southern field of the Great Observatories Origins Deep Survey (GOODS-S, Giavalisco et al., 2004) and the UKIDSS Ultra-Deep Survey (UDS, Lawrence et al., 2007). Our catalogs are retrieved from the *Rainbow* database (Barro et al., 2011), a central repository of CANDELS-related data that can be accessed via a web-based interface.[1] Below, we summarize the catalogs used in our analysis as well as our sample selection criteria.

[1]The *Rainbow* database can be accessed at `http://rainbowx.fis.ucm.es`.

4.2.1 Multi-wavelength Photometric Catalogs

Multi-wavelength photometric catalogs exist for both GOODS-S (Guo et al., 2013) and UDS (Galametz et al., 2013), and the reader is referred to the cited papers for more details on source identification and measurement. Briefly, for both fields, the catalogs were constructed from a combination of ground- and space-based observations, spanning the U-band through to 8μm. Objects were selected from the *HST*/WFC3 F160W (H-band; 1.6 μm) images and cross-matched to the other datasets. Consistent multi-wavelength photometry was measured using TFIT (Laidler et al., 2007), as described in Galametz et al. (2013) for UDS and Guo et al. (2013) for GOODS-S.

4.2.2 Redshifts and Rest-frame Photometry

The redshifts used in this study include a combination of broadband photometric, moderate-resolution spectroscopic, and grism redshifts. Photometric redshifts are taken from the catalog of Dahlen et al. (2013), which provides median values of z for all five CANDELS fields, based on the spectral energy distribution (SED) fitting outputs from 11 different methods. When available, we use reliable-quality spectroscopic redshifts from the literature or redshifts based on *HST*/WFC3 grism spectroscopy (for GOODS-S only; Morris et al., 2015). Photometric redshifts were used for 72.6% of our final sample, spectroscopic redshifts for 22.3%, and grism

redshifts for 5.1%. The consistency among all three redshift classes has been previously validated (Dahlen et al., 2013; Morris et al., 2015). Rest-frame magnitudes in various standard filters, from FUV to K, were computed from the redshifts and multi-wavelength observations using the EAZY code (Brammer et al., 2008), which fits a set of galaxy SED templates to the observed photometry.

4.2.3 Stellar Masses and Dust Attenuation

As is common in extragalactic studies, the stellar masses and other stellar population parameters used here are derived from SED fitting procedures applied to the multi-wavelength photometry. Recently, the CANDELS collaboration released a catalog of "official" stellar masses that combine the results from 10 separate SED fitting methods (Santini et al., 2015). These median masses are more robust than any individual mass determination, as they average over variations in the assumptions used in each method (e.g., star formation histories, dust prescription, metallicity). The typical uncertainty in the median stellar masses is ~ 0.1 dex.

In addition to stellar masses, we also use the visual attenuation, A_V, derived from the SED fitting. To ensure that the values are robust, we combine results from five methods and compute the median A_V. The five methods were chosen based on their similar, simplifying assumptions (exponentially declining star-formation histories, the Calzetti dust law, and no nebular emission). The typical

scatter among the various methods relative to the median A_V is ~ 0.2 mag.

4.2.4 Structural Parameters

Galaxy structural parameters, as measured by GALFIT (Peng et al., 2002), are available for all CANDELS galaxies. Details on the measurement procedure and catalog construction are presented in van der Wel et al. (2012), to which the reader is referred for more information. Briefly, GALFIT was applied to the *HST*/WFC3 F160W (H-band) images. Each galaxy was fit with a single-Sersic model, and the best-fitting Sersic index, semi-major axis, ellipticity, axis ratio, and position angle were computed, along with estimates of their errors. In this work, we use the effective radii *along the major axis* (i.e., the semi-major axis, hereafter SMA), axis ratios (b/a), and Sersic indices (n). The typical uncertainty in these quantities is $\lesssim 10\%$ for galaxies in our sample (van der Wel et al., 2012). We use SMA as our indicator of galaxy size, rather than circularized effective radius, $R_{\rm eff}$, because the latter depends on viewing angle ($R_{\rm eff} \equiv \sqrt{b/a} \times {\rm SMA}$), while SMA is a more faithful indicator of *intrinsic* size. This distinction will prove crucial in the analysis of galaxy shapes below (Section 4.5).

4.2.5 Mid- and Far-infrared Data

Infrared (IR) observations from *Spitzer*/MIPS (24 μm) are available for both fields, and were obtained as part of the FIDEL survey (Pérez-González et al., 2008a). In addition, *Herschel* observations of both fields were taken as part of the GOODS-*Herschel* (Elbaz et al., 2011) and PEP (Magnelli et al., 2013) surveys. Data in our catalog include *Herschel* PACS 100 and 160 μm and SPIRE 250, 350, and 500 μm. These infrared data are used (as described in the appendix, Section 4.9) to estimate IR-based SFRs, which are compared to the UV-based rates that form the basis of our analysis.

4.2.6 Star-formation Rates

For this work, SFRs are derived from the rest-frame, near-ultraviolet (NUV) luminosities ($\lambda \approx 2800$ Å), after applying a dust correction based on the measured A_V values. The dust correction assumes foreground screen attenuation that follows the Calzetti et al. (2000) law, which gives $A_{\rm NUV} = 1.8 A_V$. After correcting the NUV luminosity by $A_{\rm NUV}$, we convert the NUV luminosity to a SFR using the Kennicutt & Evans (2012) calibration:

$$\mathrm{SFR}_{\rm UV,corr}\ [M_\odot\,\mathrm{yr}^{-1}] = 2.59 \times 10^{-10} L_{\rm NUV,corr}\ [L_\odot], \tag{4.1}$$

where the calibration constant assumes a Kroupa IMF (essentially identical to the Chabrier IMF used to compute stellar masses), and $L_{\rm NUV,corr} \equiv \nu L_\nu(2800\,\text{Å}) \times 10^{0.4A_{\rm NUV}}$. We present an extensive discussion of the reliability of $\rm SFR_{UV,corr}$ in the appendix (Section 4.9), where it is compared to SFRs based on a combination of UV and IR data. The main result is that $\rm SFR_{UV,corr}$ is generally consistent with these UV+IR rates, so we adopt $\rm SFR_{UV,corr}$ as our fiducial measure of star-formation activity, because rest-frame NUV measurements are available for all the galaxies in our sample. Indeed, only $\sim 25\%$ of the sample has photometry from *Spitzer* and only 60% of those objects are detected by *Herschel*. Given the severe reduction in sample size this presents, our analysis would be nearly impossible if we were confined to this small subset of IR-detected objects.

4.2.7 Sample Selection

The full GOODS-S and UDS catalogs contain 34,930 and 35,932 objects, respectively. The sample used in our analysis is constructed by applying the following selection cuts to the above data:

1. Observed F160W magnitude $H < 24.5$, as recommended by van der Wel et al. (2014a) to ensure robust GALFIT measurements

2. SExtractor flag = 0 to exclude spurious sources, e.g., star spikes, and hot pixels

3. SExtractor `CLASS_STAR` < 0.9 to reduce contamination by stars

4. Redshifts within $0.2 < z < 2.5$ and stellar masses within $9.0 < \log M_*/M_\odot < 11.0$ to maximize the sample size while maintaining mass completeness for the majority of our final sample (e.g., Tal et al., 2014)

5. Well-constrained GALFIT measurements (quality flag = 0; van der Wel et al., 2012)

The final sample contains 9,135 galaxies: 4,028 from GOODS-S and 5,107 from UDS, or roughly one-eighth of the original catalogs. Table 4.1 details the selection criteria and the resulting sample sizes after each cut. Of note is the GALFIT quality flag cut, which excludes $\approx 13\%$ of the selected objects lying within our mass and redshift limits. Visual inspection shows that these galaxies suffer from contamination from nearby objects or have exceptionally small angular sizes, precluding reliable fits (van der Wel et al., 2012).

4.2.8 Residuals from the SSFR-Mass and Mass-Size Relations

Some of our parameters (e.g., SFR, SMA) show strong trends with stellar mass and/or redshift. For our analysis, we "divide out" these M_*- and $z-$dependent trends and use quantities that are normalized to the typical galaxy of a given mass

Table 4.1. Sample Selection Cuts

Cut	GOODS-S	UDS	Combined
Full catalog	34,930 (100%)	35,932 (100%)	70,862 (100%)
F160W < 24.5	9,904 (28.4%)	12,223 (34.0%)	22,127 (31.2%)
SE flag $= 0$	9,607 (27.5%)	11,392 (31.7%)	20,999 (29.6%)
CLASS_STAR < 0.9	9,376 (26.8%)	11,090 (30.9%)	20,466 (28.9%)
$0.2 < z < 2.5$	7,656 (21.9%)	9,534 (26.5%)	17,190 (24.3%)
$\log M_* < 11.0$	7,585 (21.7%)	9,445 (26.3%)	17,030 (24.0%)
$9.0 < \log M_* < 11.0$	4,683 (13.4%)	5,810 (16.2%)	10,493 (14.2%)
GALFIT flag $= 0$	4,028 (11.5%)	5,107 (14.2%)	9,135 (12.9%)

and redshift. In particular, we calculate residuals in specific star-formation rate (SSFR) and SMA, based on the well-known SSFR-mass and mass-size relations.

Figure 4.1 plots the SSFR-mass relation for galaxies in our five adopted redshift bins. Only galaxies defined as star-forming by the UVJ criterion (Figure 4.3) are included. The distribution of points in the figure clearly traces out the "main sequence" of star formation (e.g., Daddi et al., 2007; Noeske et al., 2007; Salim et al., 2007; Whitaker et al., 2012). The red line in each panel is the best-fit linear relation. The fits are made after excluding outliers, as follows. An initial fit to all star-forming galaxies is made, then objects greater than 1.5σ away from the fit are excluded. A second fit is made on this pruned sample, with a new estimate of σ, and galaxies greater than 1.5σ away are removed. A third fit is made using this final sample, which is adopted as the final fit. (The parameters of the fits are provided in Table 4.2.) We opt for this approach in order to obtain relations that pass through the ridge line of the main sequence as closely as possible.

Table 4.2. Parameters of SSFR-Mass Fits

Redshift Range	Slope a	Zeropoint b
$0.2 < z < 0.5$	-0.013	-9.273
$0.5 < z < 1.0$	-0.089	-9.022
$1.0 < z < 1.5$	-0.217	-8.879
$1.5 < z < 2.0$	-0.274	-8.759
$2.0 < z < 2.5$	-0.331	-8.724

Note. — The best-fit linear relations are of the form $\log \mathrm{SSFR} = a(\log M_* - 10) + b$, with SSFR in yr^{-1} and M_* in $M_\odot$.

After the fits are in hand, vertical offsets from the relation are calculated for galaxies in each redshift bin. These residuals are denoted $\Delta \log \mathrm{SSFR}_{\mathrm{UV,corr}}$, with galaxies lying above (below) the best-fit relation defined to have positive (negative) residuals. $\Delta \log \mathrm{SSFR}_{\mathrm{UV,corr}}$ is used later to quantify the relative star-formation activity for galaxies in a given mass and redshift bin. Note that while the fits include data outside the nominal mass range of the sample, our use of differential quantities at fixed mass means our results are insensitive to the exact slope or zeropoint of the fits.

A similar approach is used to calculate residuals from the mass-size relation. Figure 4.2 shows the mass-size relation in the same redshift bins for star-forming galaxies only. The solid red lines indicate the best-fitting linear relation to all the galaxies in each panel. Because they will be needed later on, we repeat the fits after excluding "fading" galaxies, defined to have $\Delta \log \mathrm{SSFR}_{\mathrm{UV,corr}} < -0.4$ dex. These

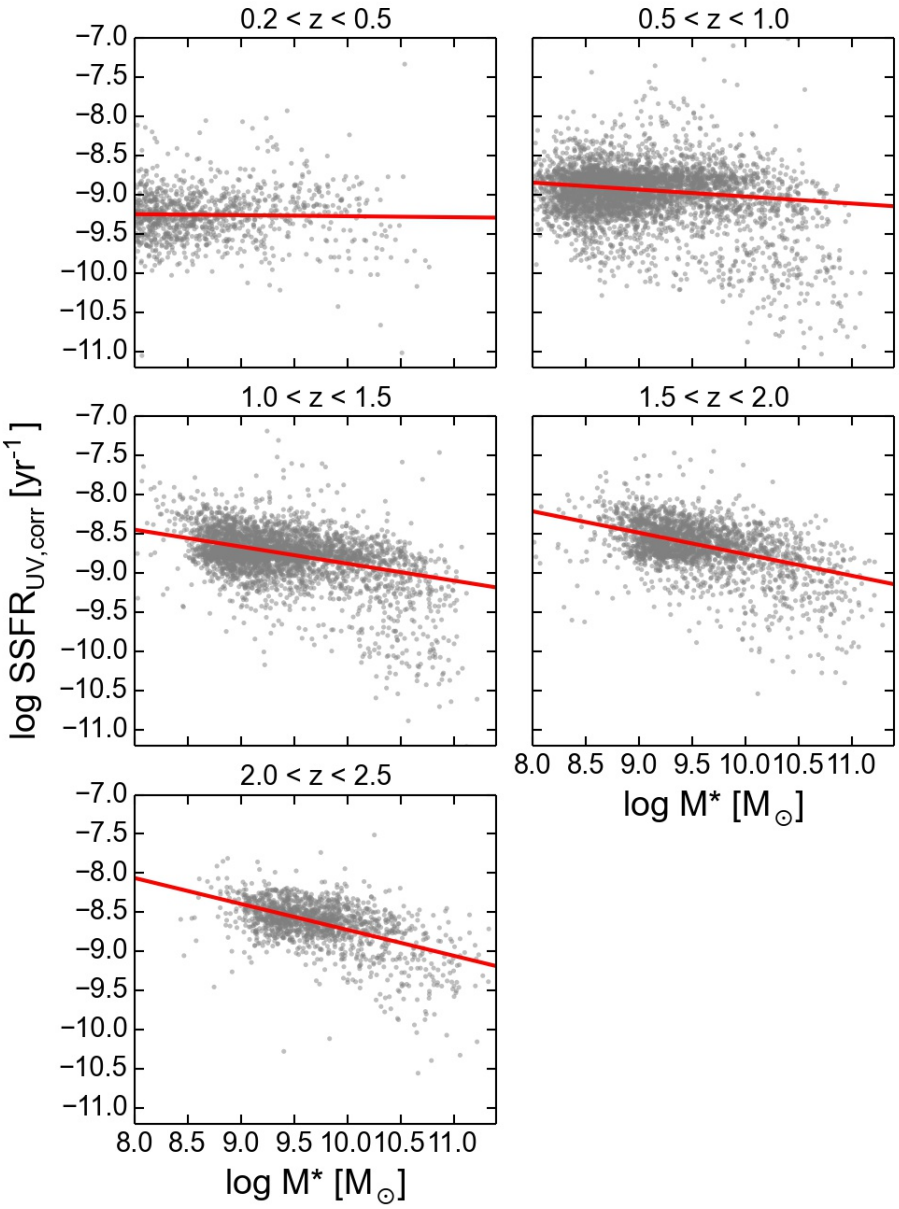

Figure 4.1: $\mathrm{SSFR_{UV,corr}}$ vs. stellar mass in the five redshift bins used in this study. Only UVJ-defined star-forming galaxies are shown. In each panel, the red line indicates the best-fit linear relation to galaxies located on the ridge-line of the main sequence. (See Table 4.2 for fit parameters.) The fits were performed by iteratively excluding outlying points (see text). Residuals from the fit, denoted $\Delta \log \mathrm{SSFR_{UV,corr}}$, are used later on to quantify the relative star-formation activity for galaxies in a given mass and redshift bin.

Table 4.3. Parameters of Mass-Size Fits

	All SF		No Fading	
Redshift Range	Slope a	Zeropoint b	Slope a	Zeropoint b
$0.2 < z < 0.5$	0.134	0.534	0.159	0.569
$0.5 < z < 1.0$	0.148	0.515	0.182	0.556
$1.0 < z < 1.5$	0.127	0.477	0.150	0.501
$1.5 < z < 2.0$	0.138	0.456	0.162	0.478
$2.0 < z < 2.5$	0.157	0.389	0.168	0.398

Note. — The best-fit linear relations are of the form $\log \mathrm{SMA} = a(\log M_* - 10) + b$, with SMA in kpc and M_* in $M_\odot$. "All SF" refers to fits made with all star-forming galaxies. "No fading" fits were performed after excluding objects with $\Delta \log \mathrm{SSFR}_{\mathrm{UV,corr}} < -0.4$ dex.

fits are indicated by the dashed blue lines. Such fading galaxies are smaller on average and more numerous at high mass (see Figure 4.13); they thus drive down the overall fit slightly (red lines). We calculate residuals from each set of fits, both denoted by $\Delta \log$ SMA (we will note later which version is used). Fit parameters are given in Table 4.3. Our slopes are systematically shallower by $\sim 0.05-0.1$ dex compared to the fits in van der Wel et al. (2014a). These discrepancies do not affect our results, since we are only concerned with *relative* size differences at fixed mass and redshift. Similarly, as stated above, including galaxies outside the mass range of the sample in the fits does not affect our conclusions, given that we are interested in differential, not absolute, size differences.

Before continuing, we remark that we are using the data directly from the catalogs and have not performed a detailed check for accuracy. Nevertheless,

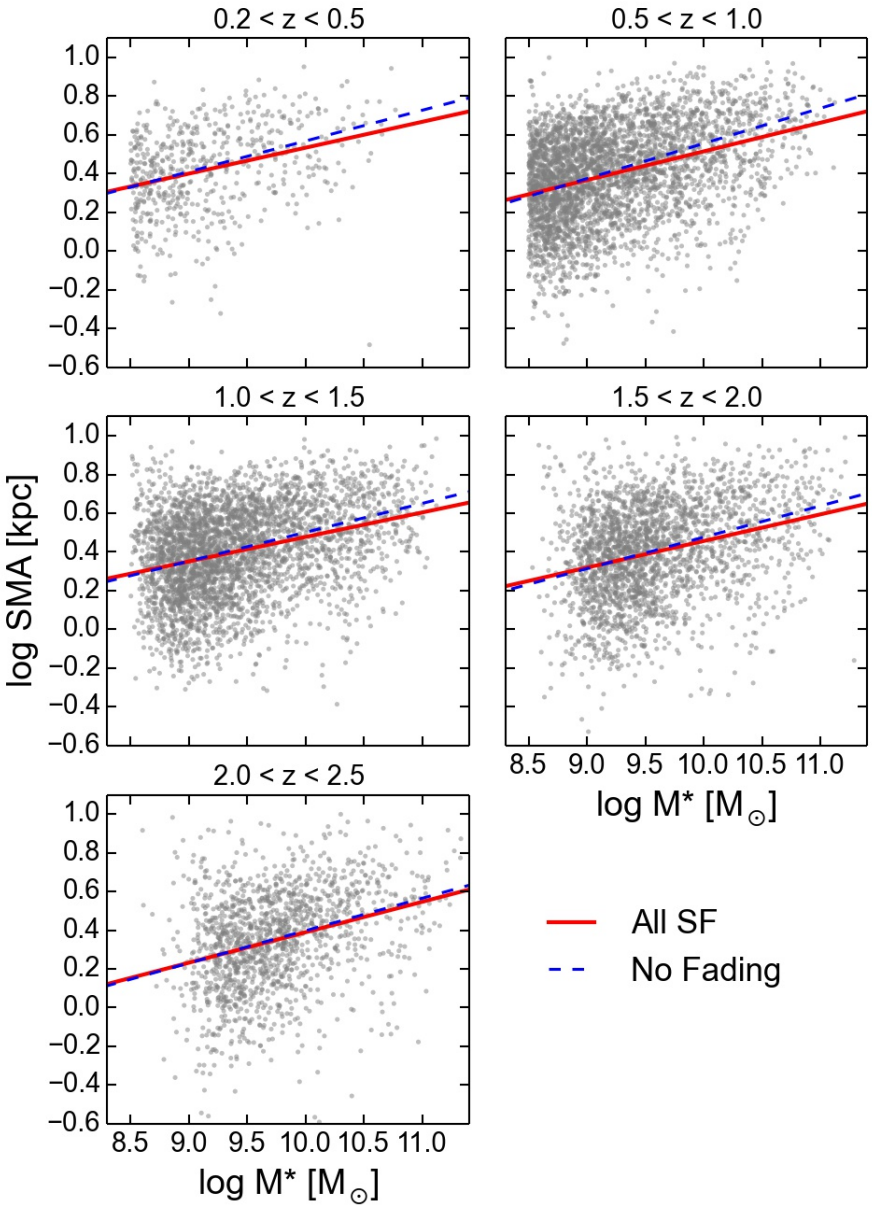

Figure 4.2: Galaxy semi-major axis (SMA) vs. stellar mass in the five redshift bins used in this study. Only UVJ-defined star-forming galaxies are shown. Solid red lines indicate the best-fit linear relation to all galaxies in each panel, while the dashed blue lines show the fit when fading galaxies ($\Delta \log \mathrm{SSFR}_{\mathrm{UV,corr}} < -0.4$ dex) are excluded. (See Table 4.3 for fit parameters.) Residuals from the fit, denoted $\Delta \log$ SMA, are used later on to characterize the relative sizes of galaxies in a given mass and redshift bin.

the trends we find based on these data are plausible, suggesting that no severe quality issues exist in our final sample. The present work can be considered a first attempt to study the overall star-forming and dust parameters of galaxies at $z < 2.5$. However, any future corrections to e.g., A_V and SSFR may result in modifications to our conclusions.

4.3 Systematic Trends in the UVJ Diagram

Figure 4.3 shows the rest-frame UVJ diagram for all galaxies in the final sample. The black lines separate the quiescent region, as defined by Williams et al. (2009) for $1 < z < 2$, from the star-forming galaxies, where most of our final sample lies. The UVJ diagram is frequently used to identify quiescent galaxies in high-redshift studies. However, our focus in this work is on the star-forming galaxies. In particular, we seek to tease out trends and regularities both along and perpendicular to the star-forming sequence seen in the UVJ diagram.

To aid this analysis, we define rotated coordinate axes, hereafter $(V - J)'$ and $(U - V)'$, that are parallel and perpendicular to the star-forming sequence, respectively. The set of axes in the lower right of Figure 4.3 shows the orientation of the rotated coordinates with respect to the standard UVJ axes. Specifically, the best-fit linear relation to all the star-forming galaxies in Figure 4.3 is calculated, and its slope is used to define $(V - J)'$ and $(U - V)'$ as a linear combination of

$V - J$ and $U - V$:

$$(V - J)' = (V - J)\cos\theta + (U - V)\sin\theta \quad (4.2)$$

$$(U - V)' = (U - V)\cos\theta - (V - J)\sin\theta, \quad (4.3)$$

where $\theta = 34.8°$ is the inverse tangent of the slope of the best-fit line.

A key feature of our analysis is dividing the sample into narrow redshift and mass bins. By doing so, underlying systematic trends can be uncovered, which would otherwise remain hidden. Our basic visualization tool is a diagram showing a grid of panels, each corresponding to a bin of redshift and stellar mass. Specifically, the grid is divided into four, 0.5 dex-wide mass bins between $9.0 < \log M_*/M_\odot < 11.0$ and five redshift bins between $0.2 < z < 2.5$. By plotting the sample in this diagram, one can more easily see trends as a function of redshift and/or mass.

In addition, the diagram can be used to track galaxies as they increase their mass over time. To illustrate this, Figure 4.4 shows a sample "grid diagram" overlaid with stellar mass growth tracks taken from Moster et al. (2013) and Papovich et al. (2015). Roughly speaking, galaxies move diagonally through the diagram. Variations in the trajectory slopes reflect the differing growth rates of low-mass and high-mass galaxies (e.g., Behroozi et al., 2013; Moster et al., 2013). In particular, high-mass galaxies accumulate their stellar mass earlier than low-

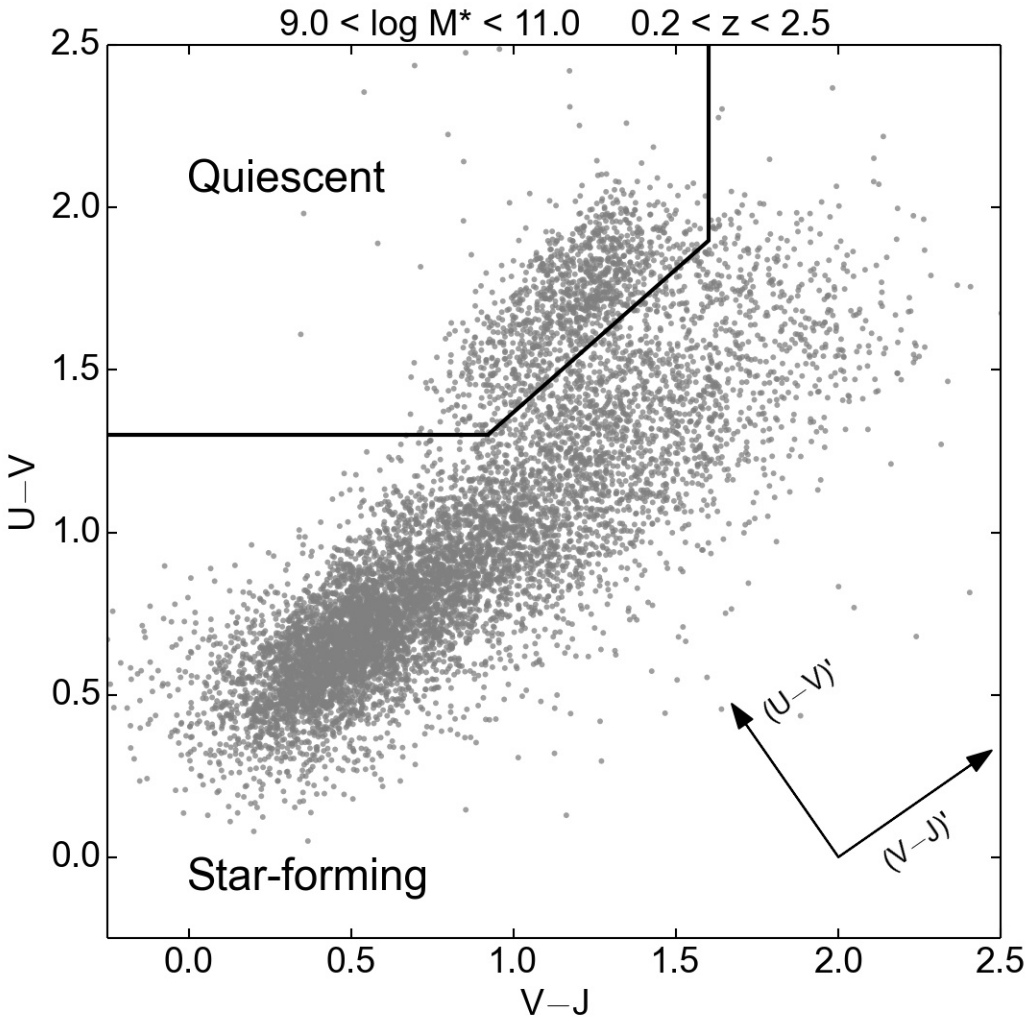

Figure 4.3: Rest-frame UVJ diagram for all 9,135 galaxies in the final sample ($9.0 < \log M_*/M_\odot < 11.0$ and $0.2 < z < 2.5$). The black lines separate quiescent and star-forming galaxies, according to the definition in Williams et al. (2009). Our analysis focuses on star-forming galaxies, in particular, teasing out trends both parallel and perpendicular to the diagonal star-forming sequence seen in the UVJ diagram. The set of axes in the lower-right corner indicates the rotated coordinates, $(V-J)'$ and $(U-V)'$, that are used to facilitate our analysis.

mass galaxies, a phenomenon loosely termed "downsizing." We will see other manifestations of such mass-dependent evolution throughout this work.[2]

4.3.1 A (Universal) Relation between $(U-V)'$ Color and SSFR

Figure 4.5 presents the UVJ diagram for the sample in the grid diagram. Points are color-coded by $\mathrm{SSFR}_{\mathrm{UV,corr}}$. Inspection of the figure reveals several notable trends. First, the location of the star-forming sequence shifts toward redder $(U-V)'$ with increasing galaxy mass and cosmic time. This behavior reflects the overall aging of stellar populations with time. Second, galaxies progressively fill in the dusty region of the star-forming sequence, toward redder $(V-J)'$, as they evolve. This is consistent with their having a higher dust content at late times and in more massive galaxies (e.g., Whitaker et al., 2012). Third, the buildup of quiescent galaxies with time is clearly evident at all masses; moreover, quiescent objects appear earlier at higher masses.

Another striking feature in nearly every panel of Figure 4.5 is the presence of a clear gradient in $\mathrm{SSFR}_{\mathrm{UV,corr}}$ running nearly parallel to $(U-V)'$. Such a gradient was previously noted by Williams et al. (2010), Patel et al. (2011), and Arnouts

[2]Because "downsizing" has been applied in many different contexts, some far removed from the original usage in Cowie et al. (1996), we instead adopt the expression "mass-dependent evolution" for clarity.

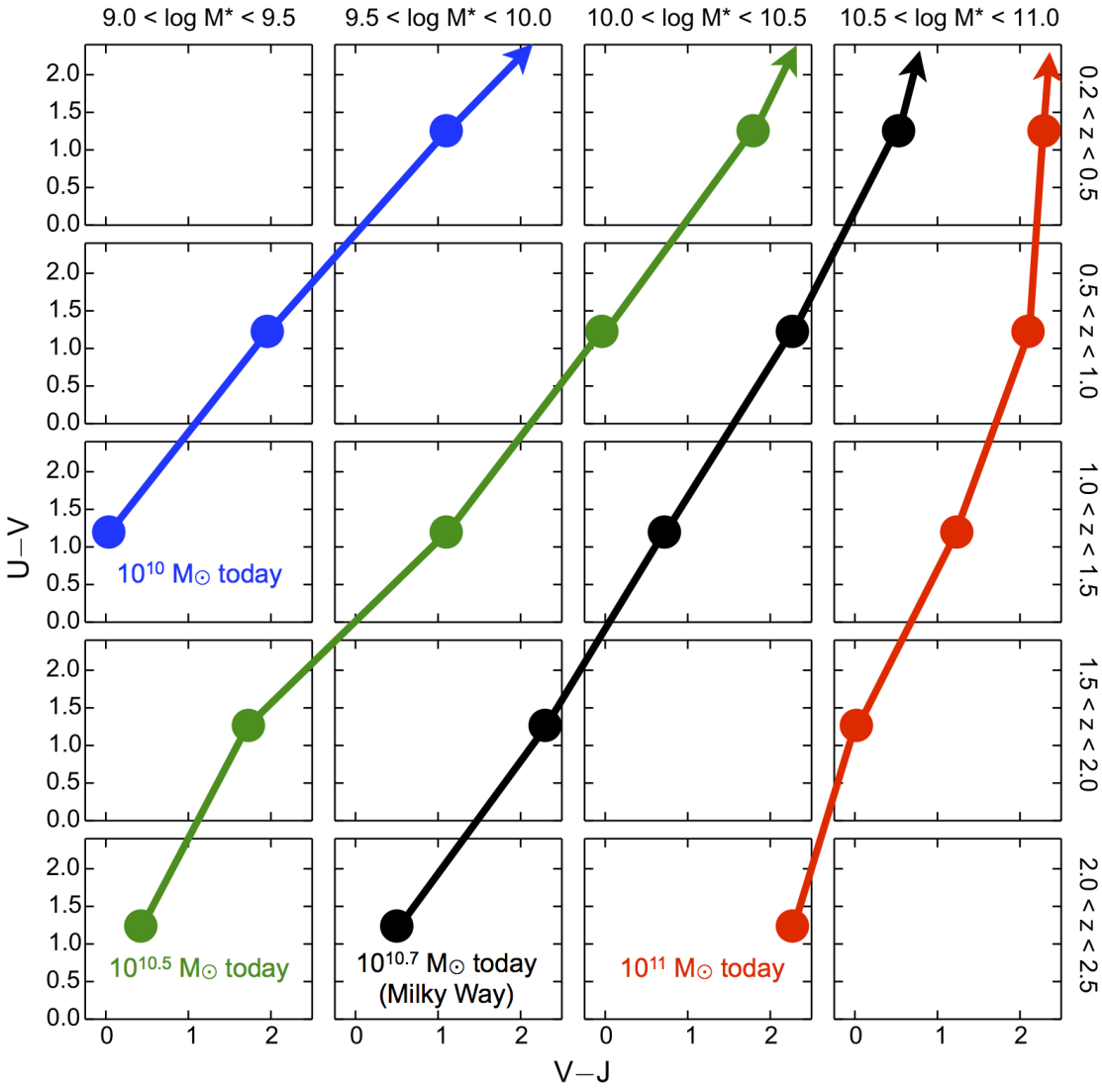

Figure 4.4: Grid diagram over-plotted with galaxy stellar mass growth tracks illustrating how galaxies move through our mass and redshift bins as they evolve. Four representative tracks are shown, labeled by the stellar mass at $z = 0$. The horizontal positions of the points assume that the vertical edges of each panel correspond to the mass limits of each bin. The observationally derived Milky Way track is from Papovich et al. (2015), while the others are theoretical predictions from Moster et al. (2013). Roughly speaking, galaxies move diagonally through the diagram.

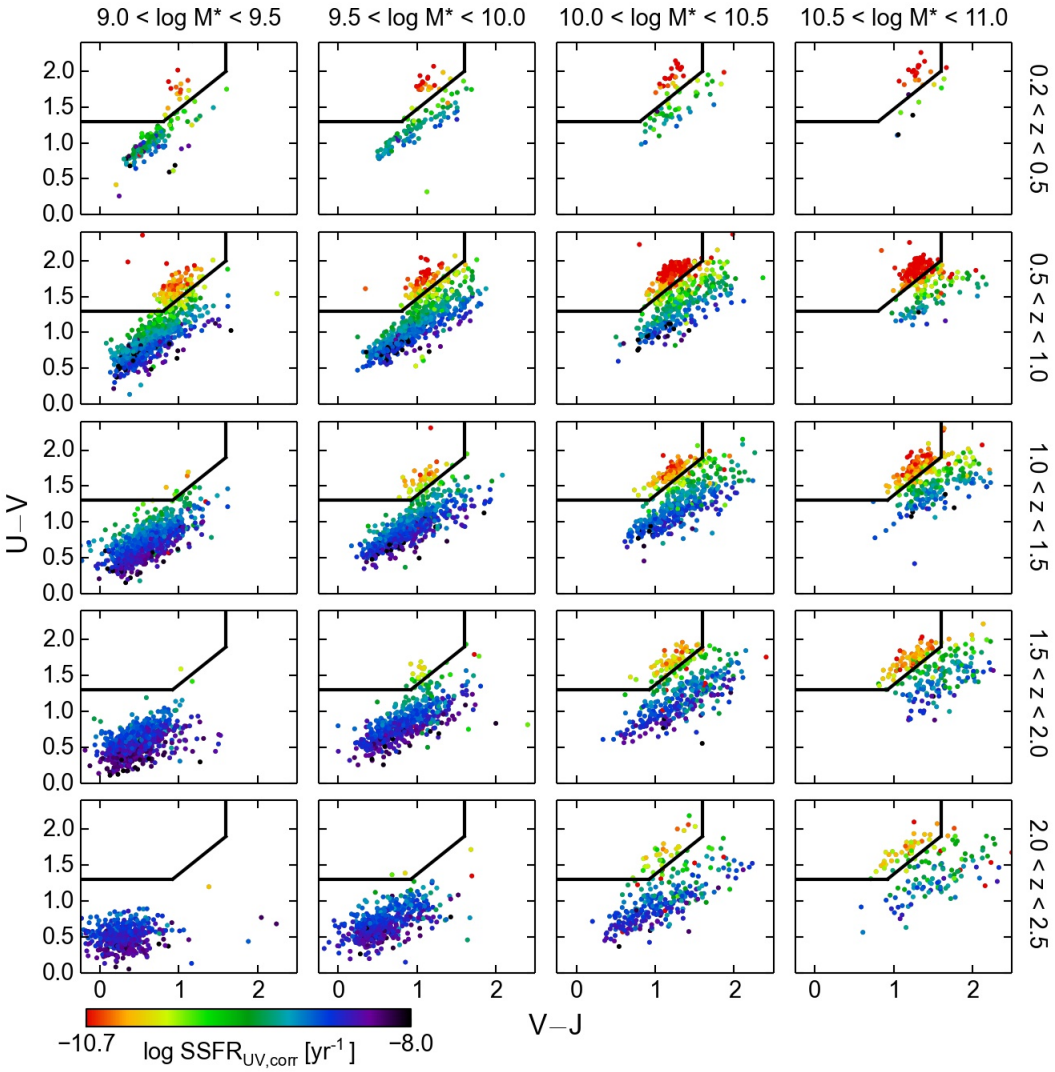

Figure 4.5: Rest-frame UVJ diagram, divided into narrow stellar mass and redshift bins, as indicated in the figure. Points are color-coded by the dust-corrected, UV-based specific star-formation rate, $\mathrm{SSFR_{UV,corr}}$. The star-forming sequence shifts to redder colors as age and dust content increase. The quiescent population is seen to form first at higher mass. Moreover, a clear gradient in $\mathrm{SSFR_{UV,corr}}$, running nearly parallel to $(U-V)'$, is seen in all panels except the bottom two with $\log M_*/M_\odot < 10.0$.

et al. (2013), though their samples were not divided into the narrow mass and redshift bins used here. The fact that a gradient is seen, even in narrow bins, suggests that $\mathrm{SSFR_{UV,corr}}$ is well-correlated with $(U-V)'$ across a large range in mass and redshift.

To more easily visualize the SSFR "stripes" in each panel, Figure 4.6 plots a modified UVJ diagram that uses the rotated colors $(U-V)'$ and $(V-J)'$ defined earlier. From this figure, it is apparent that the rotated colors do a good job at capturing the tilt of the star-forming sequence in UVJ space, i.e., lines of constant $\mathrm{SSFR_{UV,corr}}$ run nearly horizontally in the figure. The slight tilt between $(U-V)'$ and $\mathrm{SSFR_{UV,corr}}$ is likely due to our use of a global fit in all bins to define the $(U-V)'$ coordinate; fitting to each bin individually would take out most of the remaining tilt. A stronger disagreement is seen in the two leftmost bottom panels ($M_* < 10^{10} M_\odot$ and $2.0 < z < 2.5$), where the rotated colors are misaligned relative to the distribution of points in UVJ space.

To the eye, the $\mathrm{SSFR_{UV,corr}}$ gradient remains essentially fixed as a function of mass and redshift; i.e., at fixed $(U-V)'$, the same value of $\mathrm{SSFR_{UV,corr}}$ is found, independent of M_* and z. To investigate whether this is so, Figure 4.7 presents two versions of the "rotated" UVJ diagram, this time stacking together all galaxies in our sample (except the two leftmost bottom bins, i.e., $M_* < 10^{10} M_\odot$ and $2.0 < z < 2.5$, where the rotated colors are a poor fit to the star-forming sequence).

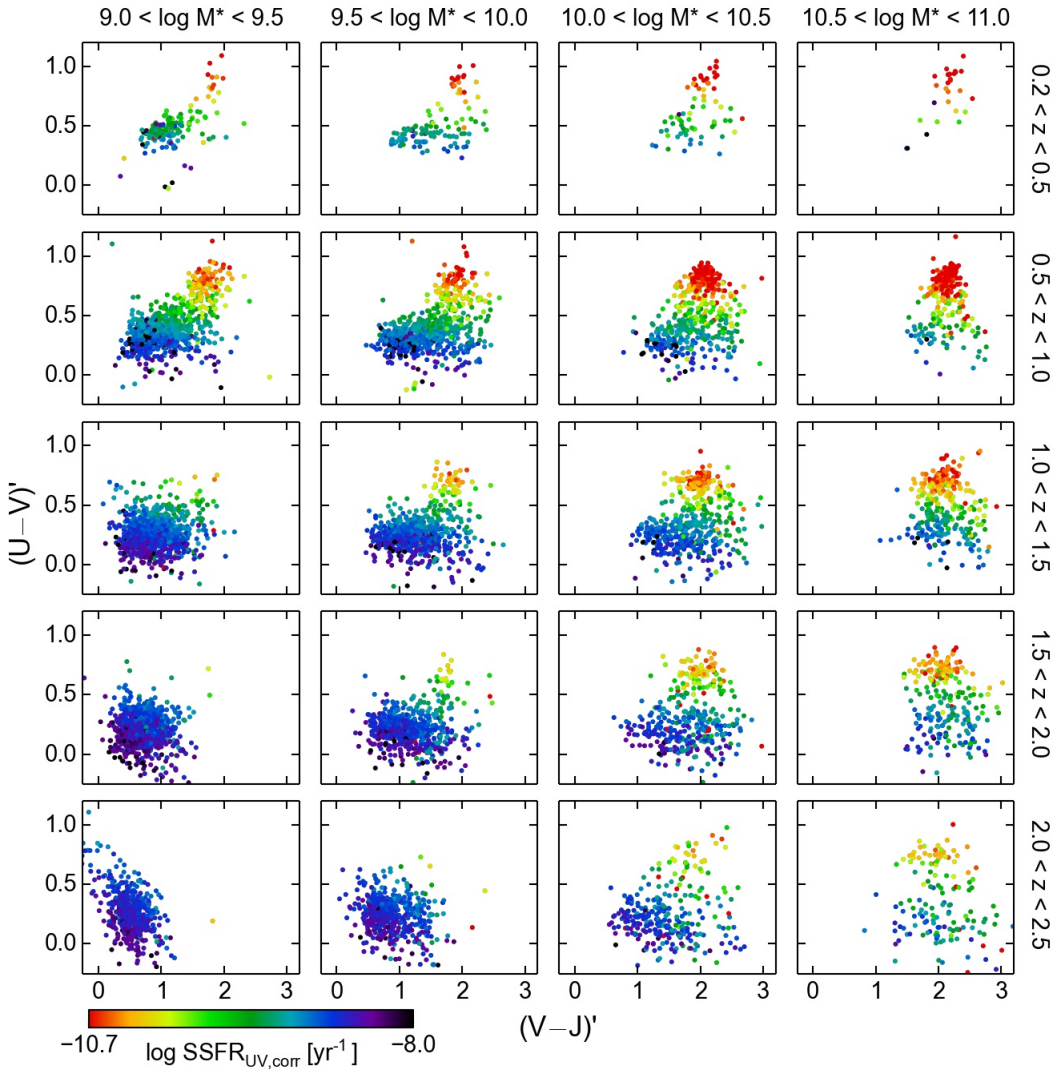

Figure 4.6: Modified UVJ diagram using the "rotated" colors $(U-V)'$ and $(V-J)'$, divided into narrow stellar mass and redshift bins, as indicated in the figure. Points are color-coded by $\mathrm{SSFR}_{\mathrm{UV,corr}}$. In this parameter space, the gradient in $\mathrm{SSFR}_{\mathrm{UV,corr}}$ runs nearly parallel to the vertical axis, $(U-V)'$. In the two leftmost bottom panels, the distribution of points and the gradient are skewed due to the definition of the rotated colors, which describe these galaxies poorly (Figure 4.5).

In the top panel, the color-coding shows the median value of log $\mathrm{SSFR}_{\mathrm{UV,corr}}$ in each pixel. The gradient in $\mathrm{SSFR}_{\mathrm{UV,corr}}$ is clearly seen, even when including galaxies over a wide range in mass and redshift. This supports the hypothesis that the gradient is indeed a fixed pattern "embedded" in UVJ space through which galaxies move as they evolve.

To further confirm this, it is necessary to check whether the *dispersion* in $\mathrm{SSFR}_{\mathrm{UV,corr}}$ at each location in UVJ is small. In the bottom panel of Figure 4.7, the color-coding indicates the 1σ scatter in log $\mathrm{SSFR}_{\mathrm{UV,corr}}$ in each pixel. Indeed, the typical scatter in a pixel is $\lesssim 0.35$ dex (factor of 2.2), implying a remarkably tight relation between $(U-V)'$ and $\mathrm{SSFR}_{\mathrm{UV,corr}}$ over a factor of 100 in mass and 10 Gyr of cosmic time.

Assuming the $\mathrm{SSFR}_{\mathrm{UV,corr}}$ values are correct, the tightness of the relation between $\mathrm{SSFR}_{\mathrm{UV,corr}}$ and $(U-V)'$ means that a galaxy's SSFR can be estimated just by knowing its location in the UVJ diagram. Figure 4.8 further illustrates this by plotting $\mathrm{SSFR}_{\mathrm{UV,corr}}$ versus $(U-V)'$ for the entire sample, excluding the low-mass, high-redshift objects for which $(U-V)'$ is not reliable. The color-coding in the top (bottom) panel is redshift (stellar mass). The dashed line roughly divides the sample into star-forming and quiescent objects. The figure supports the conclusion that the gradient seen in the UVJ diagram is a fixed relation: for star-forming galaxies, there is little systematic offset between galaxies of different

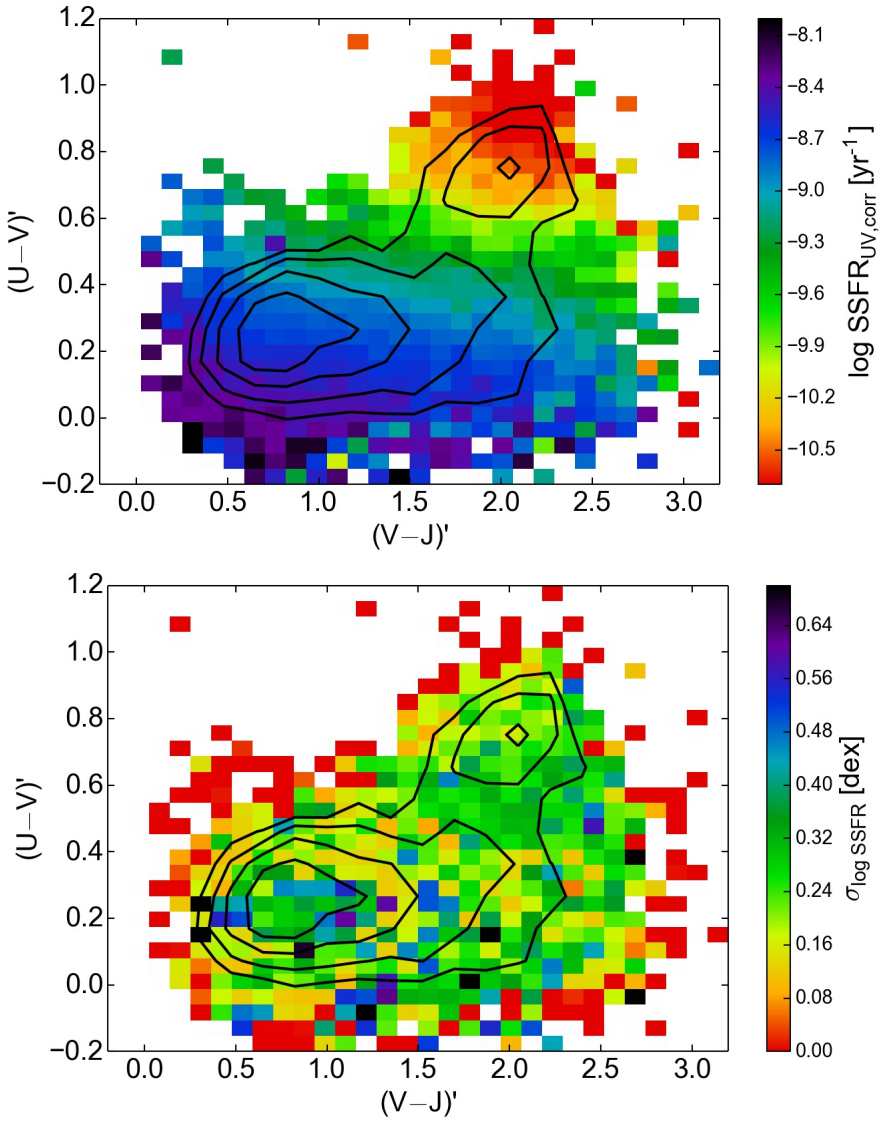

Figure 4.7: Two-color diagram using the "rotated" colors $(U-V)'$ and $(V-J)'$. The entire sample is plotted, except those with $M_* < 10^{10} M_\odot$ and $2.0 < z < 2.5$. Black contours are logarithmically spaced and indicate the density of points. The colored 2D histograms show the median value (top panel) and the 1σ dispersion (bottom panel) in log $\mathrm{SSFR}_{\mathrm{UV,corr}}$ in each pixel. The gradient in $\mathrm{SSFR}_{\mathrm{UV,corr}}$ is clearly seen in the top panel, while the bottom panel indicates that the typical dispersion in log $\mathrm{SSFR}_{\mathrm{UV,corr}}$ in a pixel is $\lesssim 0.35$ dex, suggesting that the gradient is a fixed pattern "embedded" into the UVJ diagram through which galaxies move as they evolve.

masses/redshifts from the backbone of the relation. However, it is interesting that a systematic trend with redshift is seen for quiescent galaxies. This is likely an age sequence, with galaxies at lower redshift having redder $(U-V)'$ due to progressive aging of their stellar populations.

4.3.2 Spectral Energy Distributions in UVJ Bins

The small dispersion in $\mathrm{SSFR_{UV,corr}}$ across the UVJ diagram (Figure 4.7) implies that galaxies with the same $U-V$ and $V-J$ colors have similar SSFRs. Turning it around, do galaxies with similar SSFR have similar colors, i.e., similar spectral energy distribution (SED) shapes? To explore this question, we study the SEDs, spanning the rest-frame far-UV to the near-infrared, of star-forming galaxies in small bins in the UVJ plane (see also Reddy et al., 2015). The rest-frame photometry is derived from EAZY (Section 4.2), and we use magnitudes in the FUV, NUV, U, B, V, R, I, J, H, and K bandpasses to construct the SEDs.

Figures 4.9 and 4.10 present a montage of SEDs for a sampling of UVJ bins for star-forming galaxies. The panels are organized by the $(U-V)'$ and $(V-J)'$ colors of each bin. The average colors and number of objects in each bin are indicated in each panel. Individual SEDs are color-coded by redshift in Figure 4.9 and by mass in Figure 4.10. Several trends are seen in these figures. First, the SEDs get steeper with increasing $(V-J)'$, which mainly reflects the increased reddening

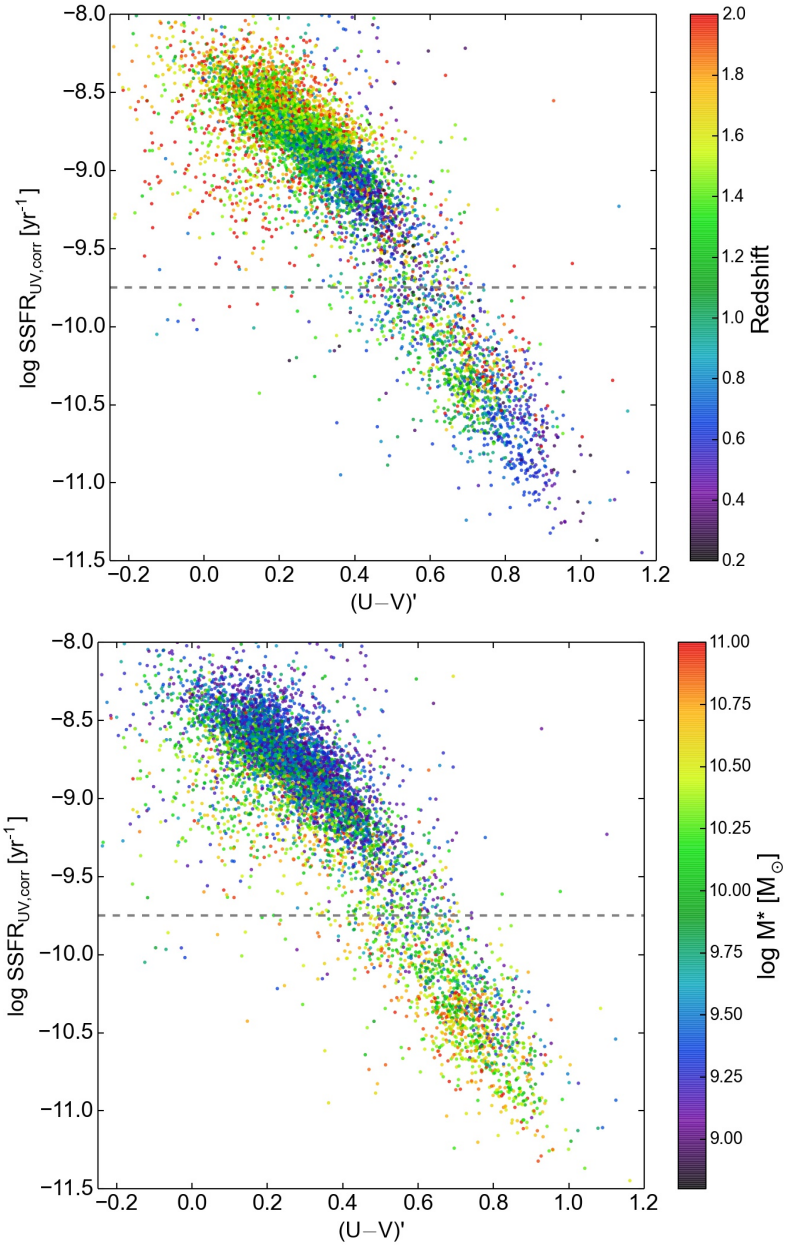

Figure 4.8: $\mathrm{SSFR_{UV,corr}}$ vs. $(U-V)'$, for our sample (excluding the low-mass, highest-redshift objects for which $(U-V)'$ is not reliable; Figure 4.5). Galaxies are color-coded by redshift (top panel) and stellar mass (bottom panel). The gray dashed line roughly divides the sample into star-forming and quiescent objects. For star-forming galaxies, a tight correlation exists between $\mathrm{SSFR_{UV,corr}}$ and $(U-V)'$ that is independent of both redshift and mass, allowing one to estimate a galaxy's SSFR just based on its $(U-V)'$.

due to dust (Figure 4.15). Second, the average redshift decreases toward redder $(U-V)'$ (Figure 4.9), reflecting the aging of the overall stellar populations with time. Third, the average mass increases with $(V-J)'$ (Figure 4.10), consistent with increasing dust content in more massive galaxies (e.g., Whitaker et al., 2012). Moreover, a closer inspection of the residual trends with redshift in each bin in Figure 4.9 reveals that the scatter in SED shape correlates mildly with z, particularly at redder $(V-J)'$: the UV slope becomes steeper toward lower redshift. This is consistent with the increase in dust content (and metallicity) in galaxies with time. However, no residual trend is seen with stellar mass (Figure 4.10).

A general conclusion from these figures is that the overall dispersion in the SEDs of a given bin is surprisingly small at nearly all wavelengths (though a larger dispersion is seen in the FUV and K-band data, likely due to increased errors in the measured photometry). This suggests that one can infer the average SED shape of a galaxy just from its UVJ colors. Moreover, stacking SEDs with similar UVJ colors can offer a useful tool to study mean properties of galaxies, including dust attenuation. In a future work, we will use these SEDs to derive an average dust attenuation law as a function of mass, redshift, and structural properties.

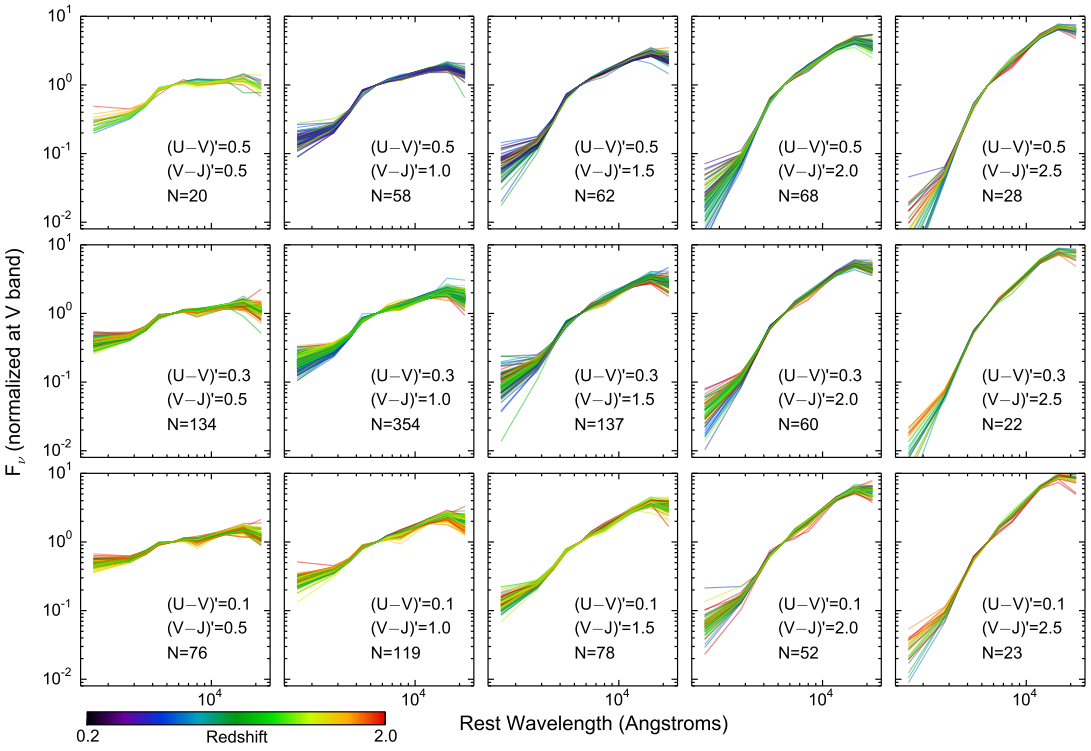

Figure 4.9: Rest-frame SEDs of star-forming galaxies in the sample, illustrating the uniformity of the overall SEDs, spanning FUV to K, among samples of galaxies selected by UVJ. Galaxies are divided into bins 0.1 mag wide in $(U-V)'$ and 0.2 mag wide in $(V-J)'$, centered around the values indicated in each panel. The number of objects in each bin is given. SEDs are in F_ν, normalized at V, and color-coded by redshift. The effect of dust reddening on the SED shape is clearly seen; SEDs steepen with $(V-J)'$. In a bin, the SEDs show very little dispersion (except in the FUV and K bands, which may be less accurate). Among the reddest SEDs (rightmost column), a clear trend is seen: UV slopes steepen toward lower redshift, consistent with aging stars and increasing dust with time. Aside from this, at most minor trends with redshift are seen in the other bins.

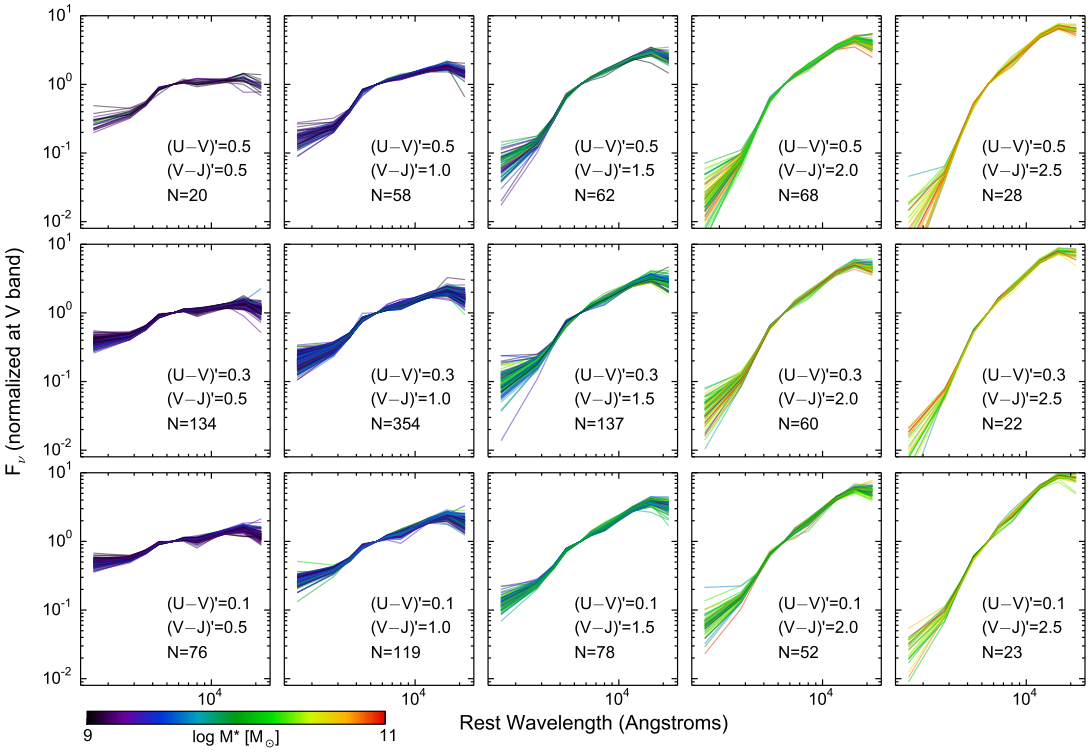

Figure 4.10: Rest-frame SEDs of star-forming galaxies in the sample, illustrating the uniformity of the overall SEDs, spanning FUV to K, among samples of galaxies selected by UVJ. Galaxies are divided into bins 0.1 mag wide in $(U-V)'$ and 0.2 mag wide in $(V-J)'$, centered around the values indicated in each panel. The number of objects in each bin is given. SEDs are in F_ν, normalized at V, and color-coded by stellar mass. The effect of dust reddening on the SED shape is clearly seen as $(V-J)'$ increases. In a bin, the SEDs show very little dispersion (except in the FUV and K bands, which may be less accurate). Mass is strongly correlated with $(V-J)'$. No residual trend with mass is seen in the individual bins.

4.3.3 Dust-corrected UVJ Diagram

The extent of the locus of star-forming galaxies along $V - J$ is mainly due to varying amounts of dust reddening (see Figure 4.15 below). Yet, Figure 4.5 reveals that galaxies with different A_V can also have the same SSFR. To what extent, then, are the *intrinsic* colors of star-forming galaxies similar? Because we have estimates of dust attenuation (A_V), we can correct the observed colors and examine the resulting distribution in the UVJ diagram.

To perform the correction, we take the measured A_V and apply the Calzetti et al. (2000) attenuation law to determine the appropriate attenuation in U and J, i.e., $A_U = 1.5A_V$, $A_J = 0.35A_V$. The resulting dust-corrected UVJ diagram is shown in Figure 4.11, where the points are color-coded by $\mathrm{SSFR_{UV,corr}}$. Star-forming galaxies now define a fairly narrow locus that extends diagonally upward, with $\mathrm{SSFR_{UV,corr}}$ decreasing along the sequence. The magenta curve in each panel is a Bruzual & Charlot (2003) dust-free, exponentially declining ($\tau = 3\,\mathrm{Gyr}$) model with solar metallicity. The distribution of points remains quite stable with time, and traces the theoretical model remarkably well.

One may claim that the striking agreement between the data and the model track is merely a consequence of using τ-models in the SED fitting procedures to derive the galaxy parameters, including A_V. On the other hand, the scatter in the dust-corrected colors is not zero and possibly points to intrinsic variations in the

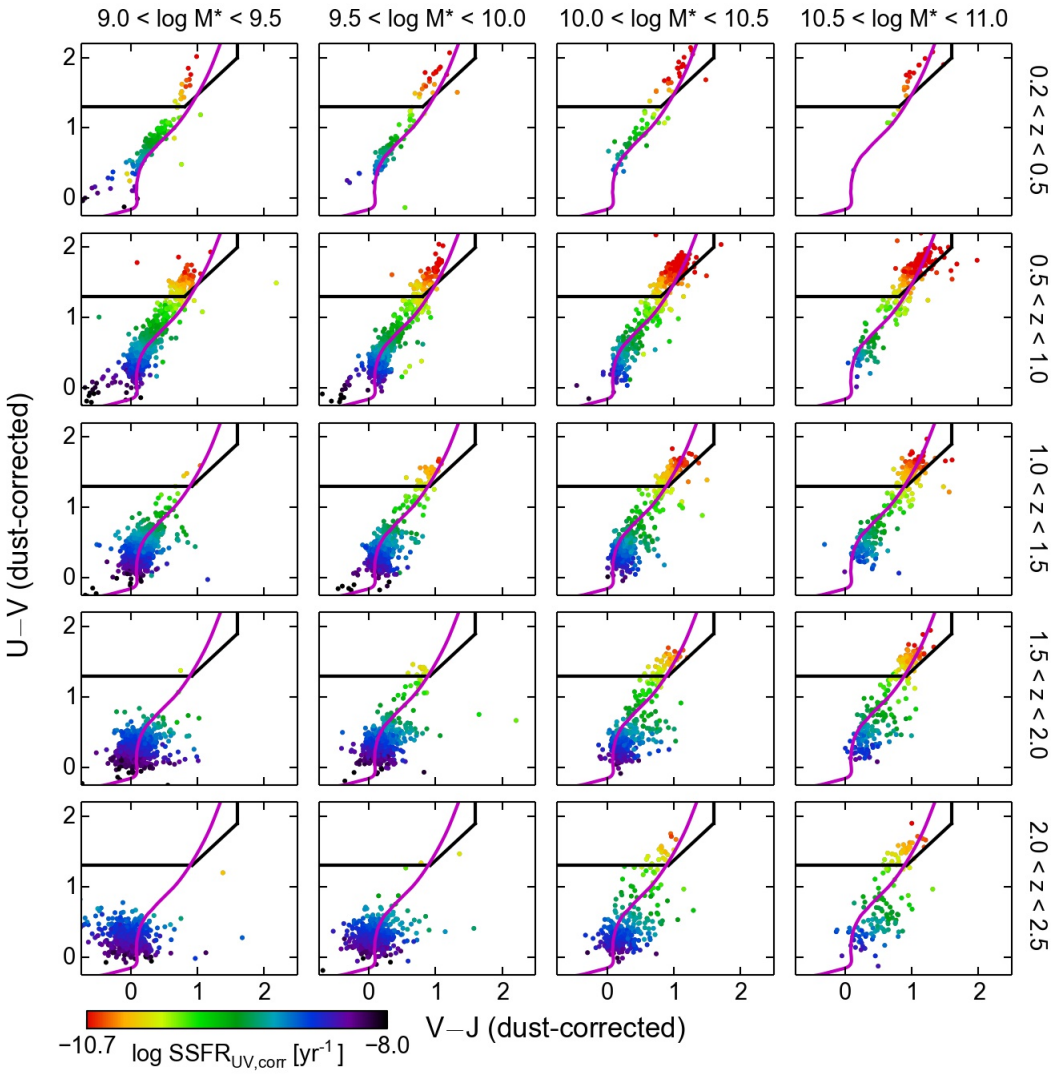

Figure 4.11: Rest-frame *dust-corrected UVJ* diagram, divided into narrow stellar mass and redshift bins, as indicated in the figure. Points are color-coded by $\mathrm{SSFR}_{\mathrm{UV,corr}}$. The magenta curve shows the evolutionary track for a dust-free, $\tau = 3$ Gyr, solar-metallicity stellar population model from Bruzual & Charlot (2003). The dust correction shifts points blueward, resulting in a narrow locus of points that roughly coincides with the stellar population model.

population (and/or increasing photometric uncertainties, particularly at higher redshift).

To get a sense of the magnitude of possible intrinsic variations, we vary τ and metallicity in the model track and compare the resulting curves with the data. This is shown in Figure 4.12, where we plot the dust-corrected UVJ diagram for galaxies with $10.0 < \log M_*/M_\odot < 10.5$ in two redshift bins. The colored tracks in the left column have different τ values, but are otherwise identical (i.e., dust-free with solar metallicity). The tracks in the right column are all dust-free, $\tau = 3$ Gyr models, but with different metallicities. The large colored points indicate an age of 3 Gyr (top row) and 1 Gyr (bottom row). As can be seen, varying τ results in only slight differences in the model trajectories. However, changing the metallicity produces a significant variation, particularly in $V - J$.

Comparing these tracks to the data, we see that the overall shape of the distribution is generally consistent with the τ-model tracks, regardless of the exact value of τ. Also, the data points cluster around the solar metallicity track, and the observed scatter in $V - J$ is smaller than the range of possible colors resulting from metallicity variations. Both of these effects can plausibly be explained by the assumptions used in the SED fitting routines. In particular, τ-models were used to parametrize the star-formation history, and most modelers restricted the metallicity to solar (see Table 1 in Santini et al., 2015). Nevertheless, further

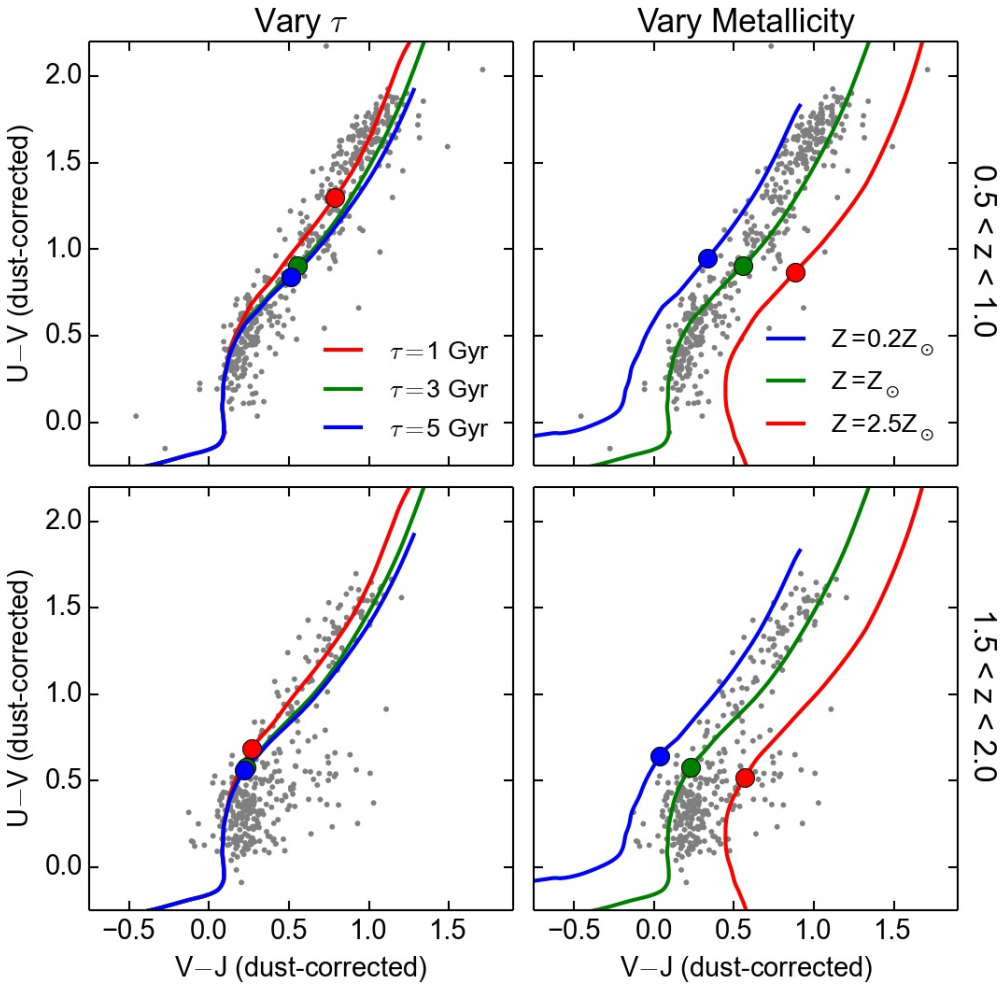

Figure 4.12: Rest-frame *dust-corrected* UVJ diagram for galaxies with $10.0 < \log M_*/M_\odot < 10.5$ in two redshift bins (gray points). Various stellar population models are plotted in each panel. Colored curves in the left column are dust-free, solar metallicity tracks with different values of τ. In the right column, the tracks are dust-free, $\tau = 3$ Gyr models of different metallicities. Colored points indicate an age of 3 Gyr (top row) and 1 Gyr (bottom row). The location of the tracks are rather insensitive to the star-formation timescale, but vary significantly with metallicity.

work is needed to probe the scatter in the dust-corrected colors and to disentangle intrinsic variations from SED fitting systematics and photometric errors. Also, it will be interesting to study the dust-corrected UVJ diagram after correcting the colors using A_V derived from independent methods, e.g., the Balmer decrement.

4.3.4 "Fading" Galaxies

Before continuing with the analysis, we first identify galaxies that are located in the star-forming region of the UVJ diagram but whose SSFRs lie below the main sequence. These "fading" galaxies represent a transition between star-forming and quiescent galaxies. At low redshift, such objects have properties distinct from actively star-forming objects. In particular, their disks are fading out as their bulges become more prominent (Fang et al., 2013). It is plausible that a similar distinction also exists among high-redshift galaxies.

Figure 4.13 plots $\Delta \log \mathrm{SSFR}_{\mathrm{UV,corr}}$, against $\Delta \log \mathrm{SMA}$,[3] for star-forming galaxies in mass and redshift bins. (See Figures 4.1 and 4.2 for the definitions of these quantities.) Points are color-coded by the SED-derived visual attenuation, A_V. Most objects lie on or close to the ridge line of the main sequence (the horizontal swaths in the panels), but a noticeable tail of low-SSFR objects is seen in nearly every panel. Moreover, these objects have smaller sizes and lower dust attenua-

[3]Because all star-forming galaxies are included, $\Delta \log$ SMA is based on the "All SF" fits of Table 4.3, i.e., the red lines in Figure 4.2. Doing so ensures that the $\Delta \log$ SMA distributions in Figure 4.13 are symmetric about zero.

tion, on average, than those on the ridge line of the main sequence. Both these traits are consistent with galaxies that are shedding their ISM and shrinking in size (due to disk fading and/or a genuine rearrangement of mass). Such objects are prime candidates for fading galaxies. The dashed red lines in each panel denote our criterion to select fading galaxies, $\Delta \log \mathrm{SSFR}_{\mathrm{UV,corr}} < -0.4$ dex. This value was chosen by eye to cleanly separate ridge-line galaxies from fading objects. The relative number of fading galaxies increases with stellar mass and with decreasing redshift, consistent with the overall evolution in the quiescent population with cosmic time (e.g., Bell et al., 2004; Faber et al., 2007; Pérez-González et al., 2008b; Muzzin et al., 2013).

Having identified fading galaxies based on $\Delta \log \mathrm{SSFR}_{\mathrm{UV,corr}}$, we show in Figure 4.14 where they lie in the UVJ diagram. By construction, fading galaxies are found in the star-forming region of the parameter space. But because they have low SSFR, they are generally found up against the quiescent boundary line (see Figure 4.5). Interestingly, their location varies as a function of mass, with low-mass (high-mass) objects having bluer (redder) colors. This variation is likely due to the increased dust content in more massive galaxies, which drives them toward redder $V - J$ (Whitaker et al., 2012). In addition, the location of the fading galaxies in UVJ may trace out (mass/redshift-dependent) quenching trajectories (Barro et al., 2014). Unless otherwise noted, fading galaxies are excluded from

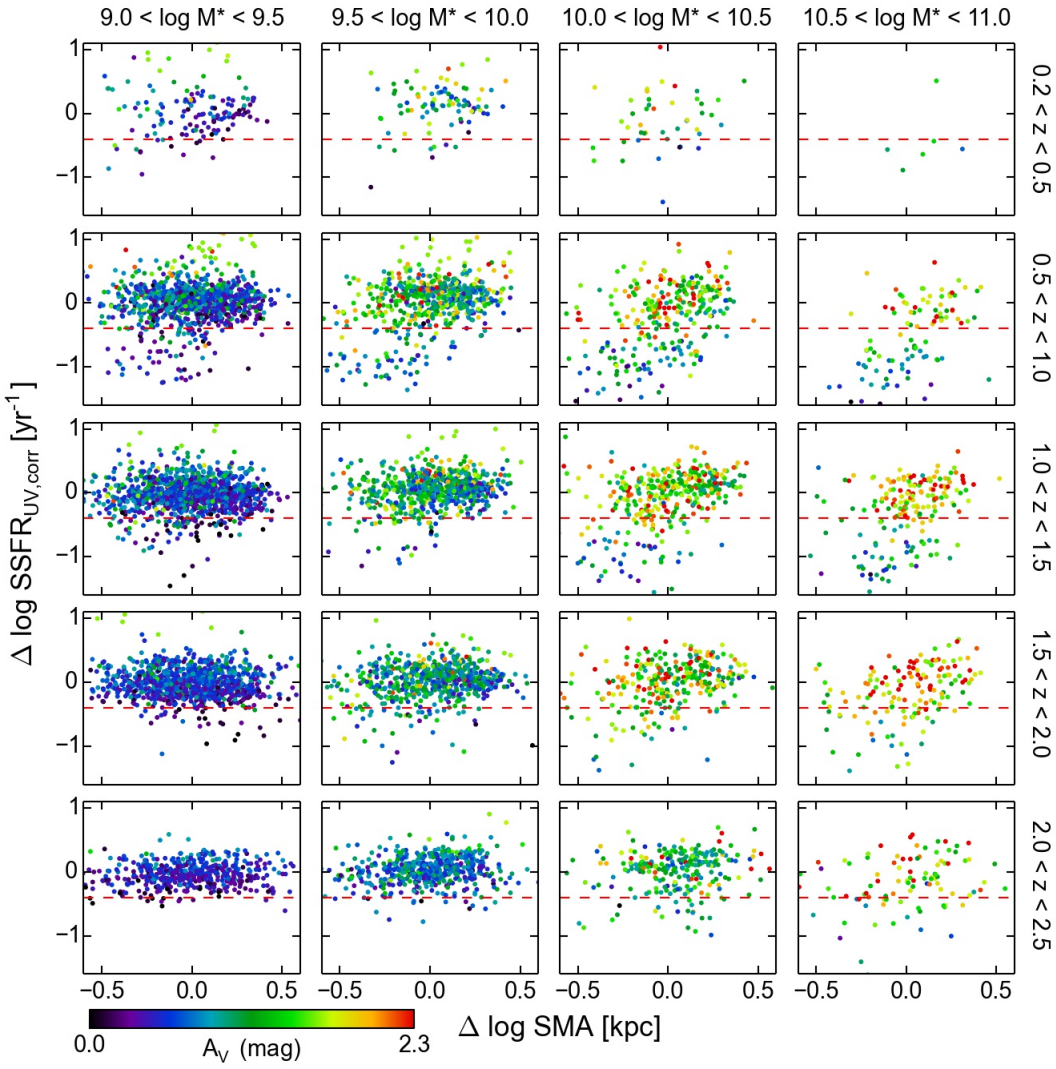

Figure 4.13: $\Delta \log \mathrm{SSFR}_{\mathrm{UV,corr}}$ vs. $\Delta \log$ SMA for galaxies that lie within the star-forming region of the UVJ diagram, divided into narrow stellar mass and redshift bins, as indicated in the figure. Points are color-coded by the SED-derived visual attenuation, A_V. A clear tail of objects with low SSFR, low A_V, and systematically smaller sizes exists in nearly every bin, which are plausibly interpreted as galaxies fading to the quiescent region of the UVJ diagram. Such fading galaxies are defined as objects with $\Delta \log \mathrm{SSFR}_{\mathrm{UV,corr}} < -0.4$ dex, lying below the dashed red lines.

our subsequent analysis, and we focus on objects located squarely on the main sequence, which we term "main-sequence ridge-line galaxies."

4.4 Correlations between Dust Attenuation and Galaxy Structure

4.4.1 Effects of Dust and Inclination in the UVJ Diagram

The diagonal extent of the star-forming sequence in the UVJ diagram is normally attributed to increasing dust reddening (e.g., Wuyts et al., 2008; Patel et al., 2012). Indeed, stellar population synthesis models assuming a Calzetti attenuation law predict a reddening vector that is nearly parallel to the star-forming locus. To verify this behavior, Figure 4.15 shows the grid of UVJ diagrams, with points color-coded by the median A_V derived from SED fitting. Only main-sequence ridge-line galaxies are shown; fading galaxies are excluded (Section 4.3.4). $V-J$ color is clearly correlated with A_V, with the most heavily attenuated galaxies populating the upper-right corner of the star-forming sequence (the "dusty region"), consistent with expectations. Note that the loci of constant A_V are nearly vertical, i.e., that $V-J$, not $(V-J)'$, is the best indicator of A_V.

The buildup of dust content with stellar mass and time is readily apparent in Figure 4.15: low-mass galaxies start out lightly attenuated and gradually in-

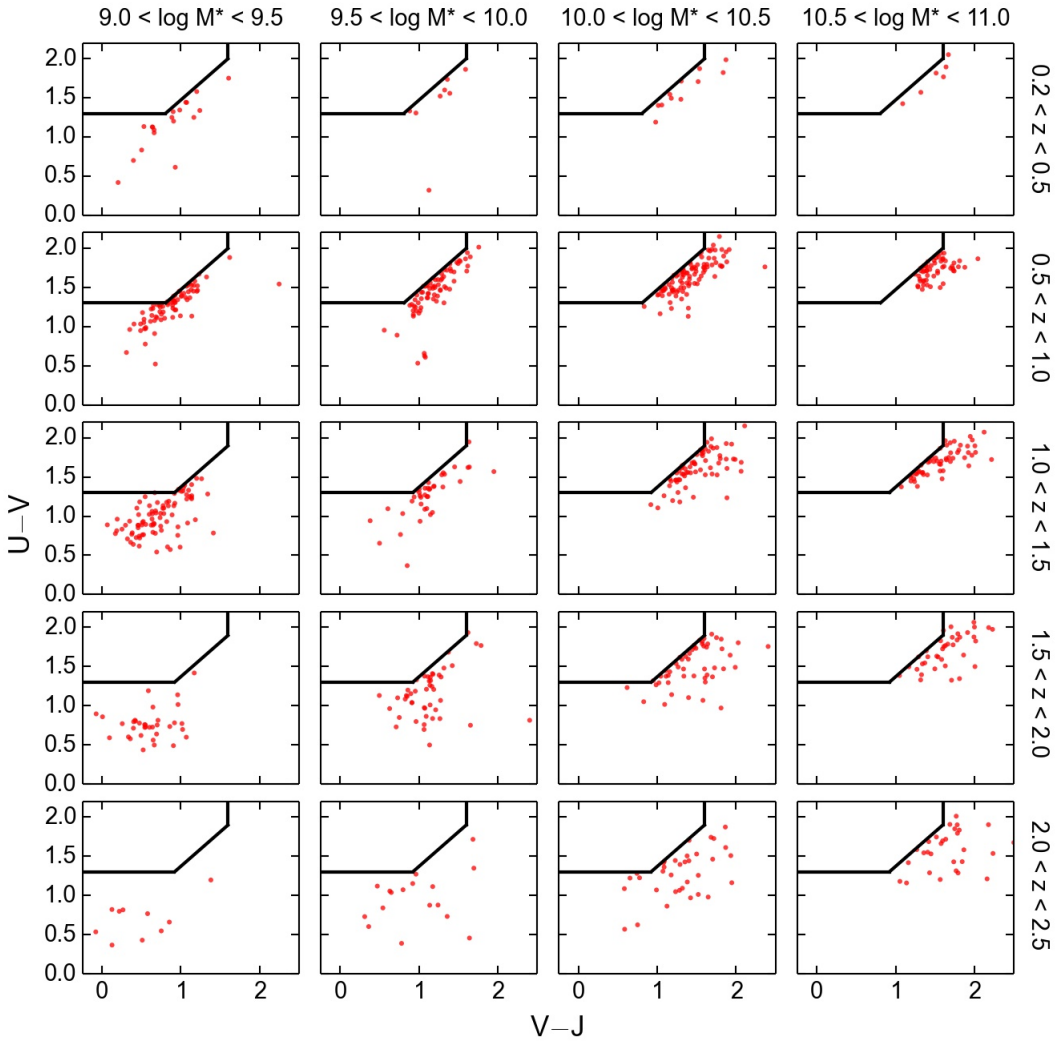

Figure 4.14: Rest-frame UVJ diagram, divided into narrow stellar mass and redshift bins, as indicated in the figure. Only fading galaxies ($\Delta \log \mathrm{SSFR}_{\mathrm{UV,corr}} < -0.4$ dex) are shown (red points). The locus of fading galaxies varies as a function of mass, suggesting that the typical quenching trajectory varies by mass when dust is included. These fading galaxies are excluded from the subsequent analysis.

crease their dust absorption with time. It is interesting that the overall trend is another example of mass-dependent evolution, this time in terms of dust content, i.e., massive galaxies tend to be more dusty earlier on, with lower-mass objects becoming more dusty only at later times. This establishes that heavy element enrichment of the interstellar medium, as evidenced by dust, also participates in downsizing. Such an effect has been seen in studies of the redshift evolution of the mass-metallicity relation (e.g., Zahid et al., 2011; Henry et al., 2013a,b). However, because *individual* measurements of (gas-phase) metallicity are challenging at high redshift (current samples above $z \sim 1$ contain only tens of objects), our much larger sample is able to provide much-needed verification of these results using a complementary approach.

While Figure 4.15 highlights the role of dust content in establishing the extent of the UVJ star-forming sequence, it is known that galaxy inclination also plays an important role in moving galaxies into the dusty region of the UVJ diagram (Patel et al., 2012). Assuming a fixed amount of dust, (disky) galaxies seen edge-on are redder than their face-on counterparts, owing to the increased path length along the line of sight (e.g., Burstein et al., 1991; Rocha et al., 2008). This effect is seen in massive galaxies at low redshift (i.e., $z \lesssim 1$ and $M_* \gtrsim 10^{10.5}\,M_\odot$; Patel et al., 2012), where fully settled disks dominate the overall galaxy population (Kassin et al., 2012). However, this effect has not yet been investigated at higher redshifts

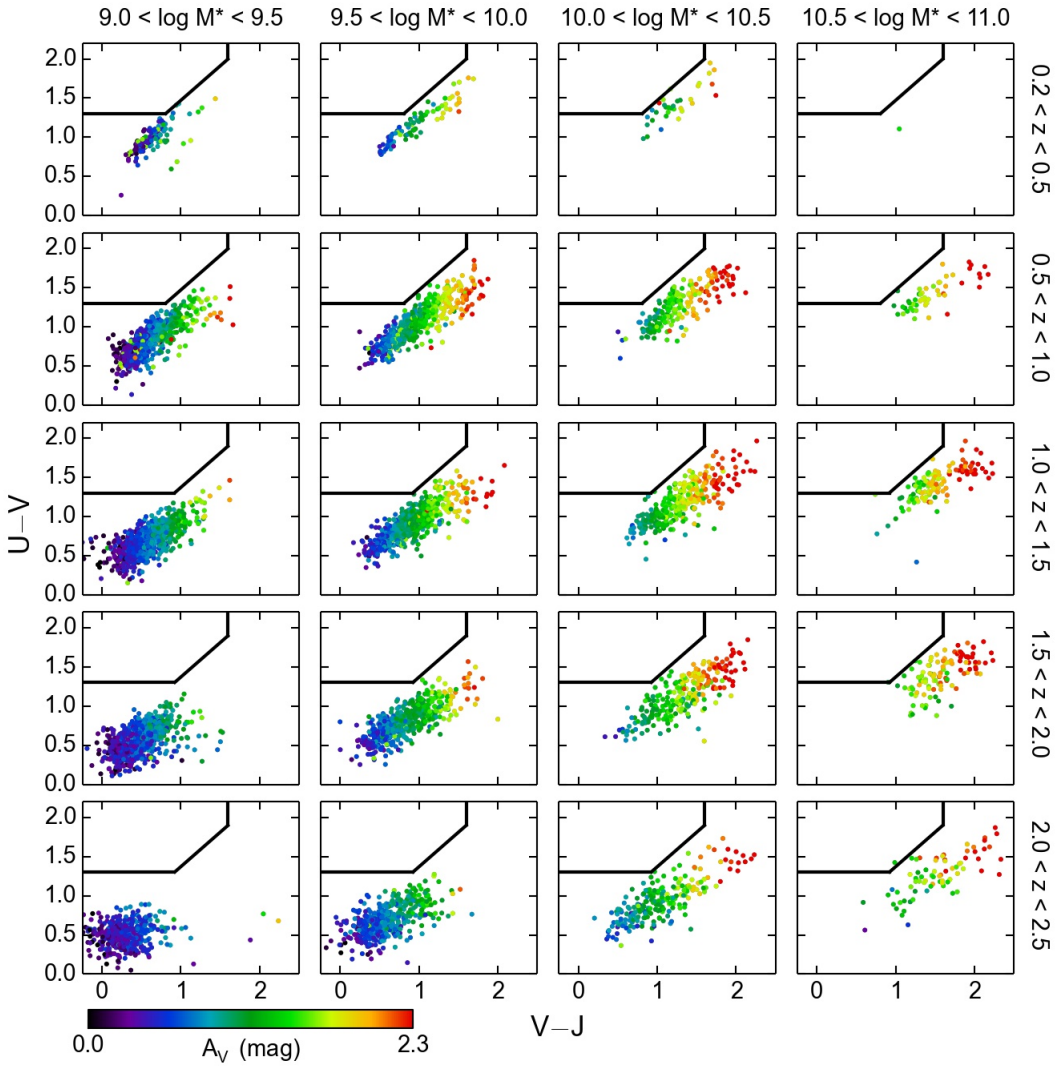

Figure 4.15: Rest-frame UVJ diagram, divided into narrow stellar mass and redshift bins, as indicated in the figure. Points are color-coded by A_V. Quiescent and fading galaxies ($\Delta \log \mathrm{SSFR}_{\mathrm{UV,corr}} < -0.4$ dex) have been excluded. A clear correlation between A_V and $V-J$ color is seen, confirming the standard interpretation that dust absorption is responsible for driving galaxies toward red $V-J$ colors.

and lower masses, where it is unclear if the high values of A_V are dominated by inclination effects or intrinsically greater dust optical depth.

To address this question, Figure 4.16 presents the same grid of UVJ diagrams, with points now color-coded by their observed axis ratio b/a. An axis ratio of 1 corresponds to a perfectly round object (e.g., a face-on disk), while smaller values of b/a indicate progressively flatter (more elongated) systems. From the figure, we see that the strongest correlation between b/a and $V - J$ is found at $z \lesssim 1$ for all masses. This confirms and extends the results of Patel et al. (2012) to lower masses. Above $z \sim 1$, the trend persists (weakly) for high-mass galaxies ($\gtrsim 10^{10}\,M_{\odot}$), but falls apart for low-mass galaxies. We note that the existence of the correlation depends on the simultaneous presence of both significant reddening *together with* highly flattened disks. Absence of either disks or dust would cause the correlation to vanish. Thus, the general weakening of the trend above $z \sim 1$ could be due to either a lack of dust or the disappearance of disks, or perhaps both. In what follows, we argue that both factors seem to play a role (see further discussion in Section 4.4.2).

Figure 4.17 shows a UVJ diagram populated with color postage stamps of a random sampling of galaxies with $9.5 < \log M_*/M_{\odot} < 10.0$ and $0.5 < z < 0.8$. The stamps are $3''$ on a side and were constructed by combining *HST*/ACS F435W, F775W, and F850LP images, roughly corresponding to rest-frame NUV, B, and V

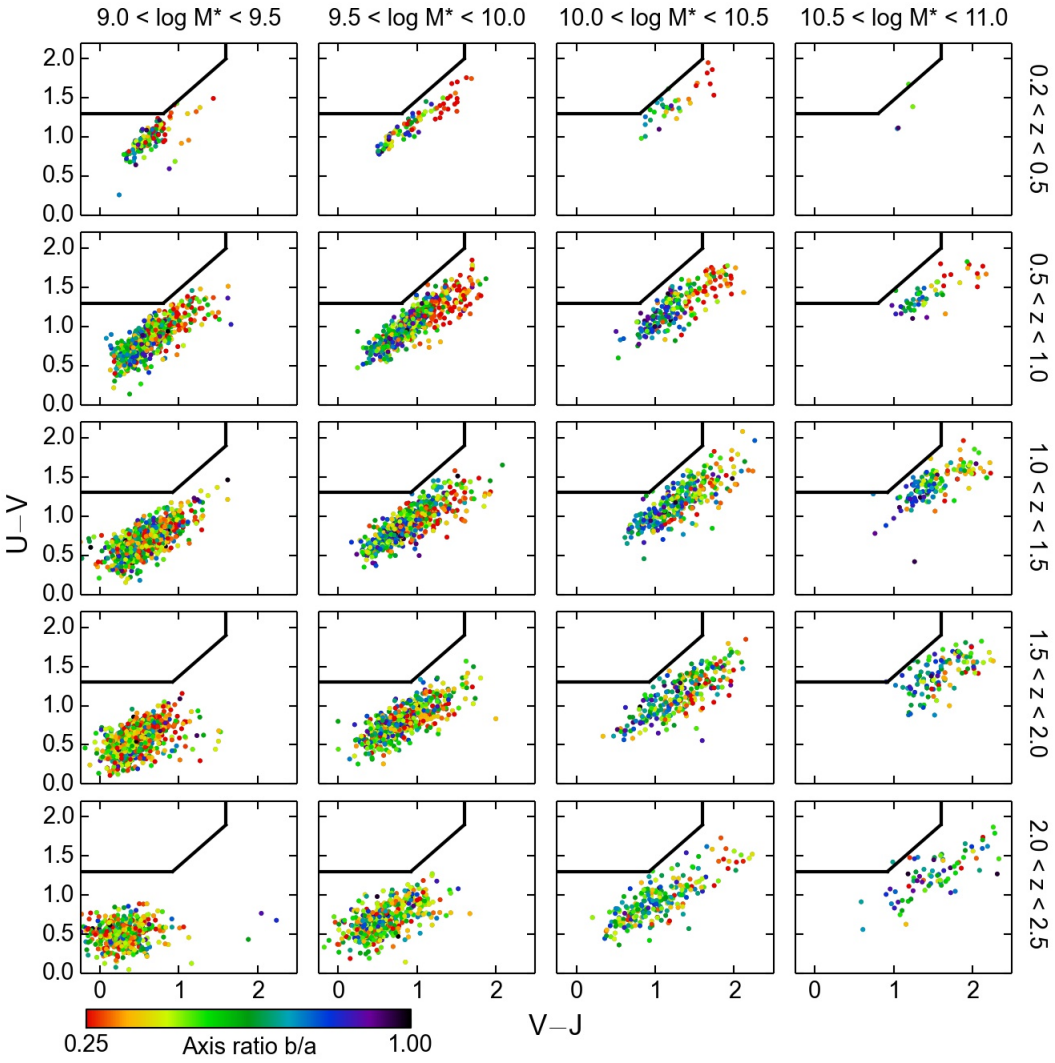

Figure 4.16: Rest-frame UVJ diagram, divided into narrow stellar mass and redshift bins, as indicated in the figure. Points are color-coded by the observed axis ratio, b/a. Quiescent and fading galaxies ($\Delta \log \mathrm{SSFR}_{\mathrm{UV,corr}} < -0.4$ dex) have been excluded. A strong trend between b/a and $V-J$ is seen toward lower redshifts, consistent with the increasing prevalence of disks, including edge-on disks that can reach the reddest $V-J$ at late times.

at these redshifts. The visual appearance of the galaxies is consistent with their location in the UVJ diagram, with quenched objects above the line appearing uniformly red and star-forming galaxies exhibiting a variety of morphologies, colors, and inclinations. In particular, galaxies in the lower-left are primarily face-on disks, while redder galaxies ($V - J \gtrsim 1$) tend to be edge-on disks. However, some are actually quite compact and round, a point we discuss further in Section 4.4.2. Also, recall that galaxies with the same SSFR lie along diagonal tracks roughly parallel to the star-forming locus. It is remarkable to find galaxies of such different sizes having the *same* SSFR.

It is worth emphasizing that the trends discussed so far emerge only when the data are subdivided into narrow bins, as we have done. Most previous works combine galaxies with a wide range in mass and/or redshift when using the UVJ diagram, effectively washing out these trends. Moreover, our sample includes low-mass galaxies ($M_* \lesssim 10^{10}\,M_\odot$), allowing us to place constraints in a regime that has heretofore been little explored.

4.4.2 Reddened Star-forming Galaxies

Figures 4.5, 4.16, and 4.17 highlight the fact that galaxies located in the dusty region of the UVJ diagram are quite diverse in their morphologies and star-formation rates. In this section, we further dissect the reddened portion of the

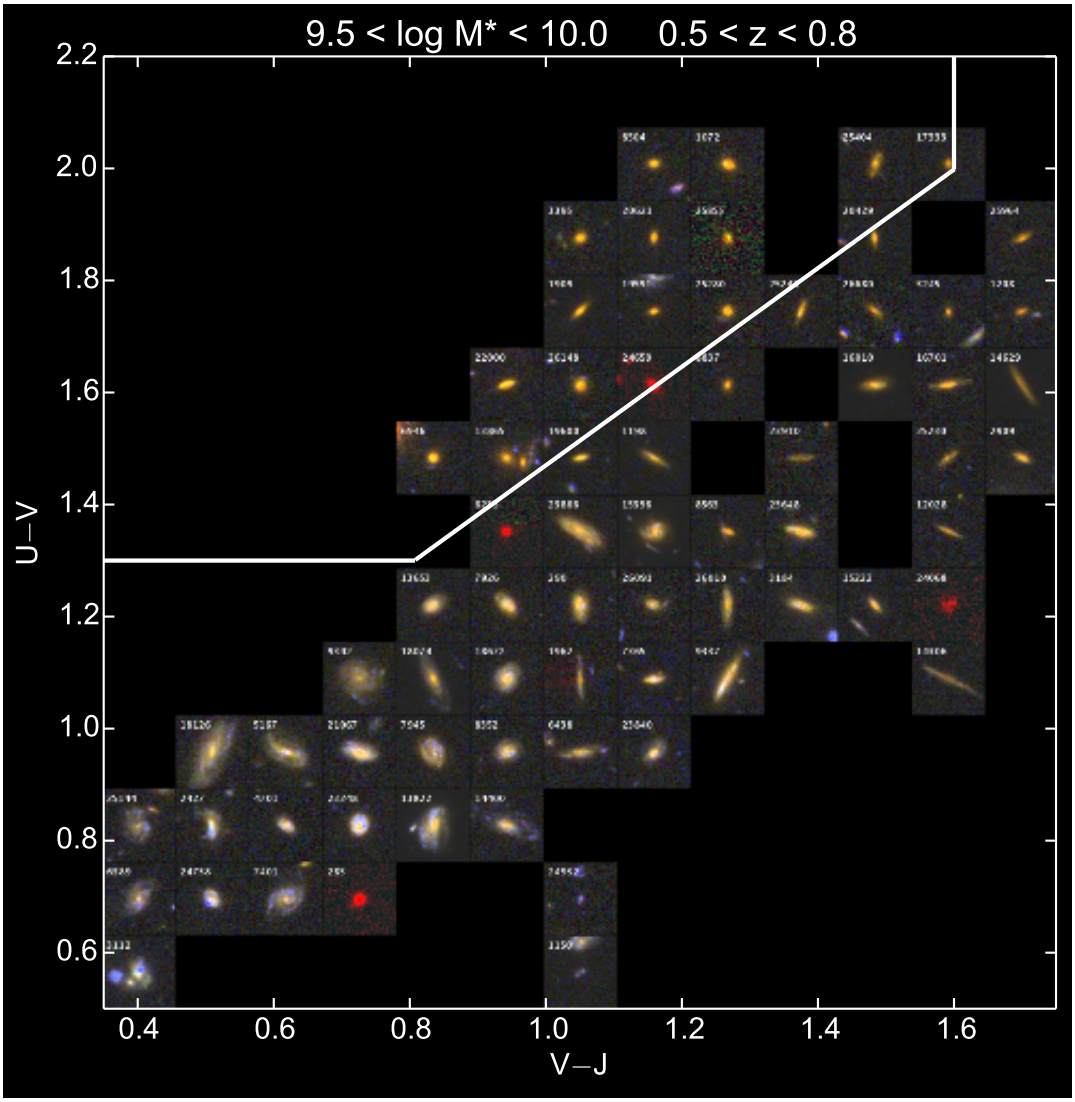

Figure 4.17: UVJ diagram, populated with color postage stamps, 3″ on a side, generated from *HST*/ACS F435W, F775W, and F850LP images, for a random sample of galaxies with $9.5 < \log M_*/M_\odot < 10.0$ and $0.5 < z < 0.8$. (Some stamps only have F850LP imaging, causing them to appear artificially red.) A clear visual distinction is apparent between star-forming and quiescent galaxies. Moreover, a rich diversity of morphologies is seen *within* the star-forming sequence. In particular, redder objects ($V-J \gtrsim 1$) can be edge-on and disky or compact and round, implying that multiple channels exist for galaxies to achieve such reddened colors.

UVJ star-forming sequence and delineate the various types of galaxies that inhabit this region, defined roughly as $V-J \gtrsim 1$. Specifically, from Figure 4.17 we identify three distinct classes of objects that are apparently heavily reddened: (1) galaxies whose star formation is going out (fading galaxies), (2) star-forming disks seen close to edge-on, and (3) compact, actively star-forming objects with intrinsically round shapes. We previously isolated the first class in Figure 4.13. As seen in Figure 4.14, a significant fraction of fading galaxies fall into the dusty region. The second class has been identified before (Patel et al., 2012) and now in our sample (Figure 4.16). To our knowledge, the third class (round, compact) has not been previously identified in a systematic way.

Focusing on the second and third classes of reddened star-forming galaxies, Figure 4.18 plots A_V versus $\Delta \log$ SMA in bins of redshift and mass. As in the previous section, fading galaxies are excluded and only main-sequence ridge-line galaxies are shown.[4] Points are color-coded by b/a. This parameter space is chosen in order to better discriminate between reddened galaxies of various sizes and inclinations.

The distribution of points changes most strongly as a function of mass, i.e., the total extent of A_V is smaller in low-mass galaxies compared to high-mass galaxies (see, e.g., Figure 4.5). Curiously, a minimum value of $A_V \approx 0.5$ is seen, even in

[4]Here, $\Delta \log$ SMA is based on the "no fading" fits of Table 4.3 (blue lines in Figure 4.2) to ensure that $\Delta \log$ SMA is not biased low by the smaller sizes of the fading galaxies.

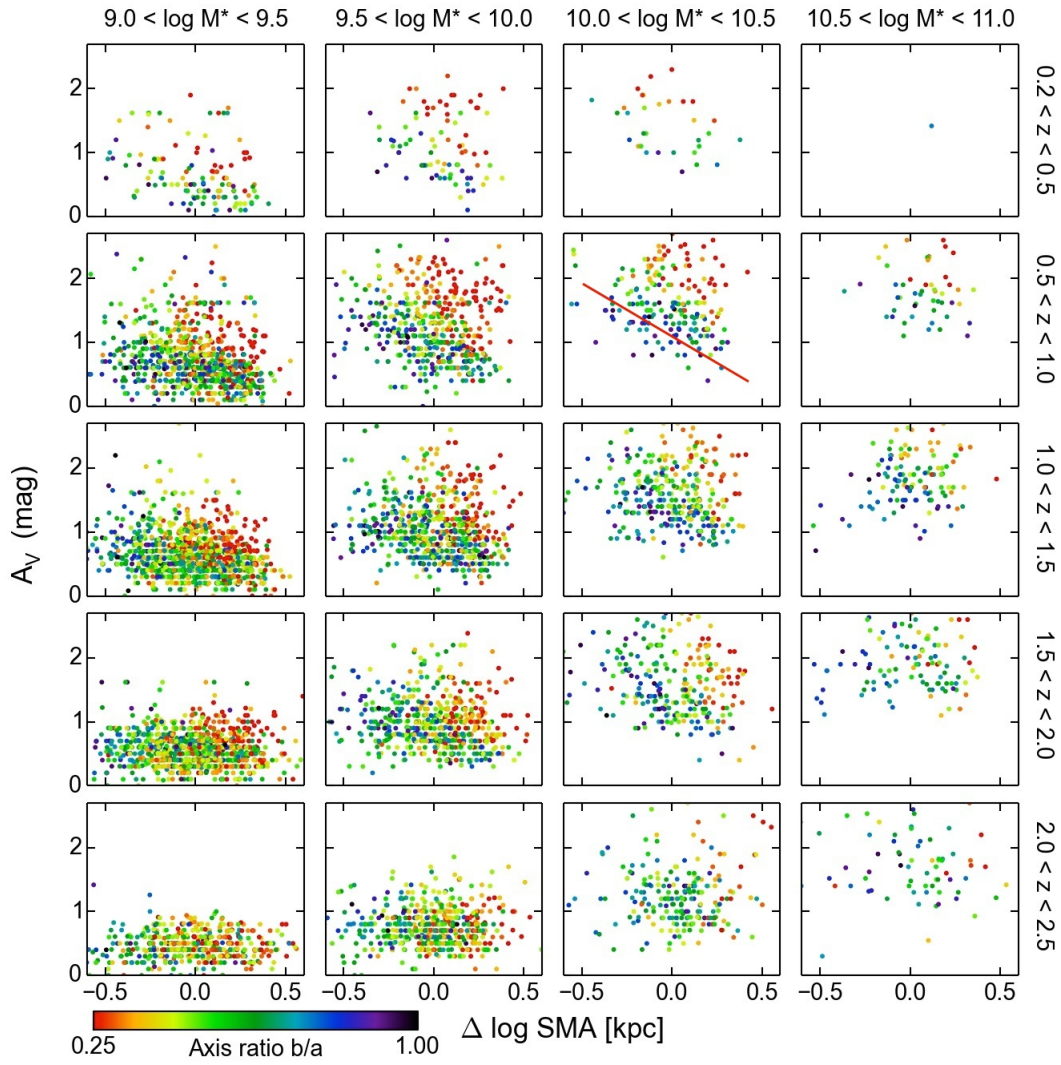

Figure 4.18: A_V vs. Δ log SMA for main-sequence ridge-line galaxies, divided into narrow stellar mass and redshift bins, as indicated in the figure. Points are color-coded by observed axis ratio b/a. At fixed A_V, galaxies over a wide range of sizes are found. In particular, highly reddened galaxies can be small and round (high b/a) as well as large and flattened (low b/a). At fixed size, A_V is anti-correlated with b/a (flatter galaxies are more attenuated), indicating the presence of disk galaxies. Moreover, the roughly diagonal contours of constant b/a (red line) imply that, at fixed b/a, smaller galaxies are more attenuated, perhaps due to a larger dust column density.

the low-mass/high-redshift regime, where one might expect essentially no dust. Whether this is a systematic effect due to the SED fitting procedure or an actual indication that young galaxies are somewhat dusty is a very important question but is beyond the scope of this work.

From Figure 4.18, we see a clear correlation between A_V and b/a at fixed size, in the sense that inclined galaxies are more attenuated. This is particularly true at higher masses and lower redshifts, where the dynamic range of A_V is larger. This trend is not surprising (Section 4.4.1), and is indicative of the presence of disk galaxies. Incidentally, this provides additional evidence for mass-dependent evolution in disk formation/settling, because the trend between A_V and b/a is seen initially in more massive galaxies.

The distribution of axis ratios in this parameter space bears further discussion. We see that contours of constant b/a run more or less diagonally (a red line is drawn in one panel to guide the eye), implying that, at fixed axis ratio, smaller galaxies are more attenuated. This statement holds for both edge-on and round galaxies, and is most apparent at higher masses and lower redshifts. If this trend between A_V and size is due to increasing dust opacity along the line of sight, then it implies that smaller galaxies have a denser ISM and larger dust column density. We quantify this trend between A_V and galaxy size and compare it to predictions based on gas scaling relations in Section 4.7.

Figure 4.19 shows a montage of color images of galaxies in the A_V-Δ log SMA plane. The visual appearance of the galaxies agrees with the quantitative measurements presented above. The trend between A_V and b/a at fixed size is apparent, particularly for the disk galaxies. In addition, objects with $A_V \gtrsim 1.5$ are mostly large, edge-on disks, but a handful of them are quite small and round, visually confirming the trends seen in Figure 4.18.

4.5 The Observed Shape Distributions of Star-forming Galaxies

The results in the previous section highlight the discriminating power of structural information to identify a previously overlooked connection between galaxy size/shape and dust attenuation and provide evidence for the mass-dependent nature of disk formation/settling. What else can be learned from galaxy shapes? Increasing attention has been paid to the distribution of galaxy shapes (particularly b/a) and how it evolves with time (e.g., Holden et al., 2012; Chang et al., 2013; van der Wel et al., 2014b). Knowledge of the axis ratio distribution provides crucial insight into galaxy formation processes, including constraining the epoch of disk formation/settling. Recently, van der Wel et al. (2014b) determined the relative fractions of star-forming disky and prolate (elongated) galaxies out

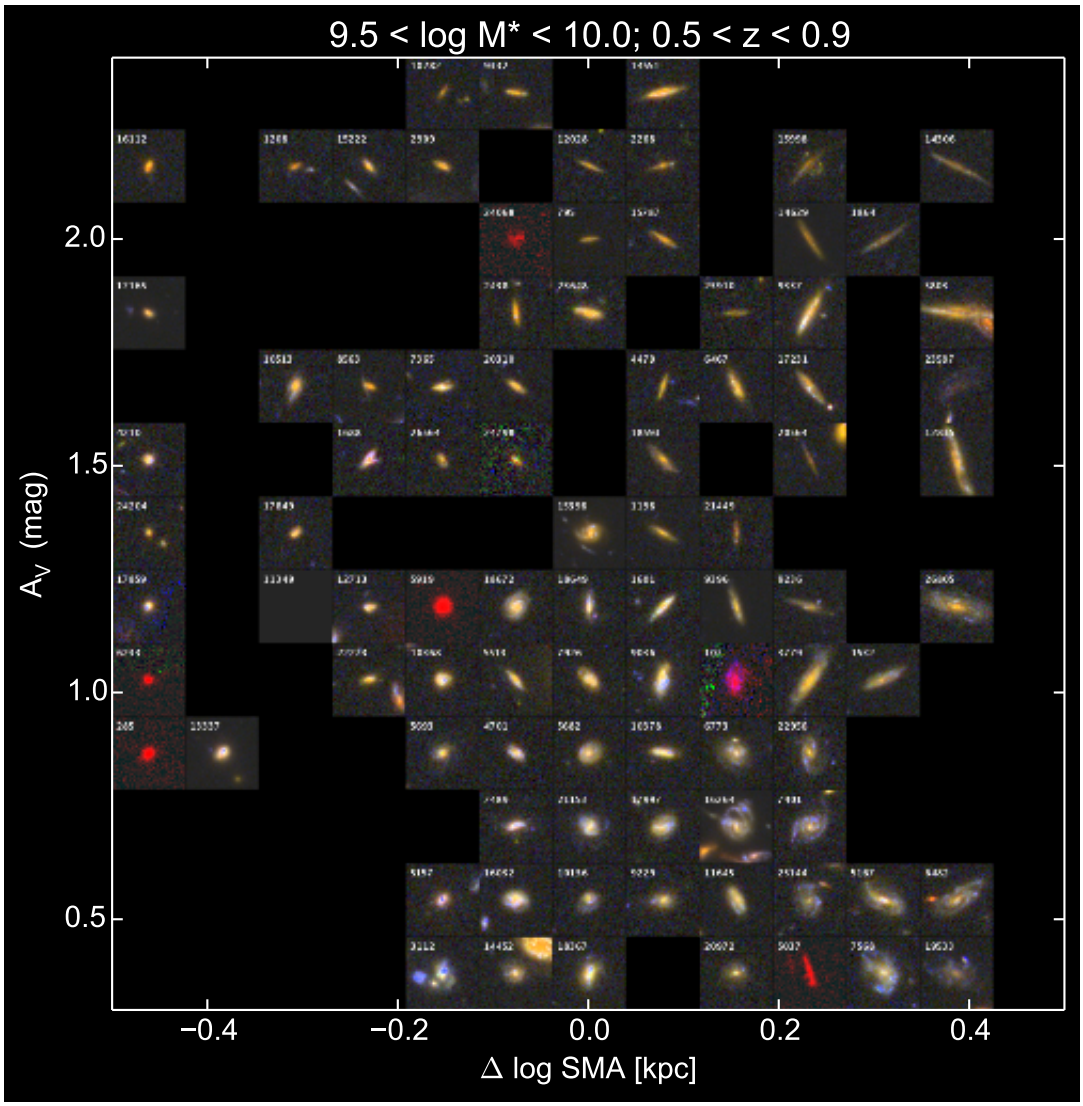

Figure 4.19: A_V vs. $\Delta \log$ SMA for main-sequence ridge-line galaxies with $9.5 < \log M_*/M_\odot < 10.0$ and $0.5 < z < 0.9$. Color postage stamps, $3''$ on a side, for a random sample of galaxies are shown. This montage visually confirms the trends seen in Figure 4.18: galaxies with low A_V are mainly face-on disks, while high-A_V galaxies are mainly edge-on disks. But a small number of round, compact objects with high A_V is also present. In addition, at fixed b/a, smaller galaxies are more reddened.

to $z \sim 2.5$ by fitting the observed b/a distributions to a synthetic population of randomly oriented triaxial galaxies. They concluded that the fraction of prolate galaxies increases toward higher redshift and lower stellar masses. However, prolate galaxies are virtually non-existent above $10^{10}\,M_{\odot}$ at all redshifts.

In this section, we examine the observed shape distribution of star-forming galaxies as a function of mass and redshift. However, whereas previous works used only the b/a distribution to derive the intrinsic shape distribution (e.g., Holden et al., 2012; Chang et al., 2013; van der Wel et al., 2014b), we add galaxy size as an additional classification parameter to better interpret the range of observed shapes. Our approach has the advantage of allowing different-sized galaxies to have different shape distributions. However, our results are qualitative at this stage, and it will be interesting to develop a theoretical model that uses both b/a and size to quantify the trends we find.

To set the stage, Figure 4.20 presents the b/a histograms for main-sequence ridge-line galaxies in bins of mass and redshift. To interpret this figure, we first describe the expected b/a distributions for two limiting cases. In each case, galaxies are assumed to be a homogeneous population with the same intrinsic distribution of shapes regardless of size or other parameters. The shapes are triaxial and characterized by three principal axes, A, B, and C. The first case assumes that star-forming galaxies are all thin, round, oblate disks (with $C \ll B = A$). Viewed

from random angles, these galaxies would show a uniform (flat) distribution in the *observed* axis ratio b/a. In the second case, galaxies are intrinsically prolate (i.e., cigar-shaped, with $B = C \ll A$). When viewed from random angles, the distribution is peaked at relatively low b/a, owing to the low probability of observing a prolate galaxy "end-on," which would appear round.

Returning to Figure 4.20, a clear variation in the b/a distributions is seen as a function of both redshift and mass. At the highest redshifts, the distributions are clearly peaked around $b/a \approx 0.4$, and they gradually become flatter with time. From the histograms alone, one might conclude that the peaky distributions are consistent with a significant prolate population, while the flatter histograms reflect the increasing prevalence of oblate disks with time. So far, our data are consistent with van der Wel et al. (2014b). However, as we show next, the picture becomes more complicated once size information is included. As mentioned in Section 4.2, we use SMA as our indicator of galaxy size because it is a more faithful indicator of intrinsic size than the circularized effective radius, which depends on viewing angle.

Figure 4.21 plots b/a against $\Delta \log$ SMA (based on the "no fading" fits in Table 4.3) for main-sequence ridge-line galaxies, in mass and redshift bins. The distribution of points in this parameter space requires some interpretation. A population of infinitely thin, purely oblate disks of various sizes would produce

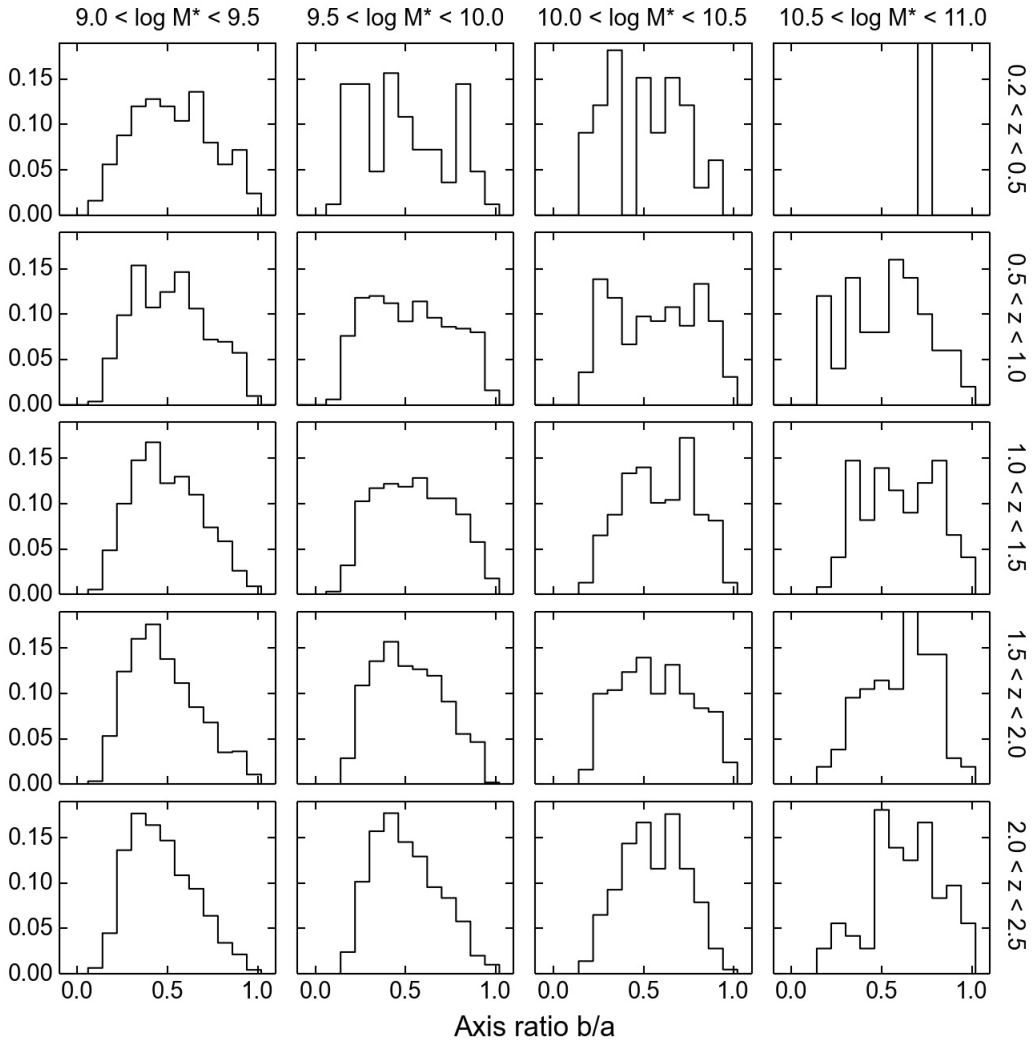

Figure 4.20: Observed axis ratio distributions for main-sequence ridge-line galaxies. A clear variation in the distribution as a function of mass and redshift is seen. In particular, low-mass/high-redshift galaxies show a peaked distribution skewed toward low b/a, while increasingly flatter distributions are seen in the remaining panels.

a uniform distribution in b/a (from zero to one) and Δ log SMA, and galaxies would occupy a rectangular region in the diagram. For disks with finite thickness, the overall distribution would remain rectangular, but galaxies would "pile up" at the intrinsic (non-zero) disk thickness. On the other hand, a population of purely prolate galaxies (with the same *intrinsic* SMA and short-to-long axis ratio C/A) would lie on a curved track in the diagram, with round objects having small *projected* SMA and elongated ones having larger projected SMA. As a representative example, the red dashed curve in Figure 4.21 plots the analytic prediction for the observed size and b/a of a prolate galaxy with $C/A = 0.2$, seen from different viewing angles (Binney & Merrifield, 1998).

Examination of Figure 4.21 shows that the real galaxy distribution falls somewhere in between these two extremes. The typical shape resembles a wedge, with a sharp, curved lower boundary in most panels. How do these two-dimensional distributions compare with the results presented in van der Wel et al. (2014b) concerning the relative contributions of prolate versus oblate galaxies?

The upper-right corner of this parameter space (i.e., large and round) is expected to be populated by face-on oblate disks, but not by prolate galaxies.[5] (For visual confirmation of this, see Figure 4.24.) Thus the presence of disks can be inferred by identifying those bins in which the upper-right corner is filled. From

[5]Spheroidal galaxies would also be found here, but such objects tend to be quenched and are not expected to contribute significantly to our sample of star-forming galaxies.

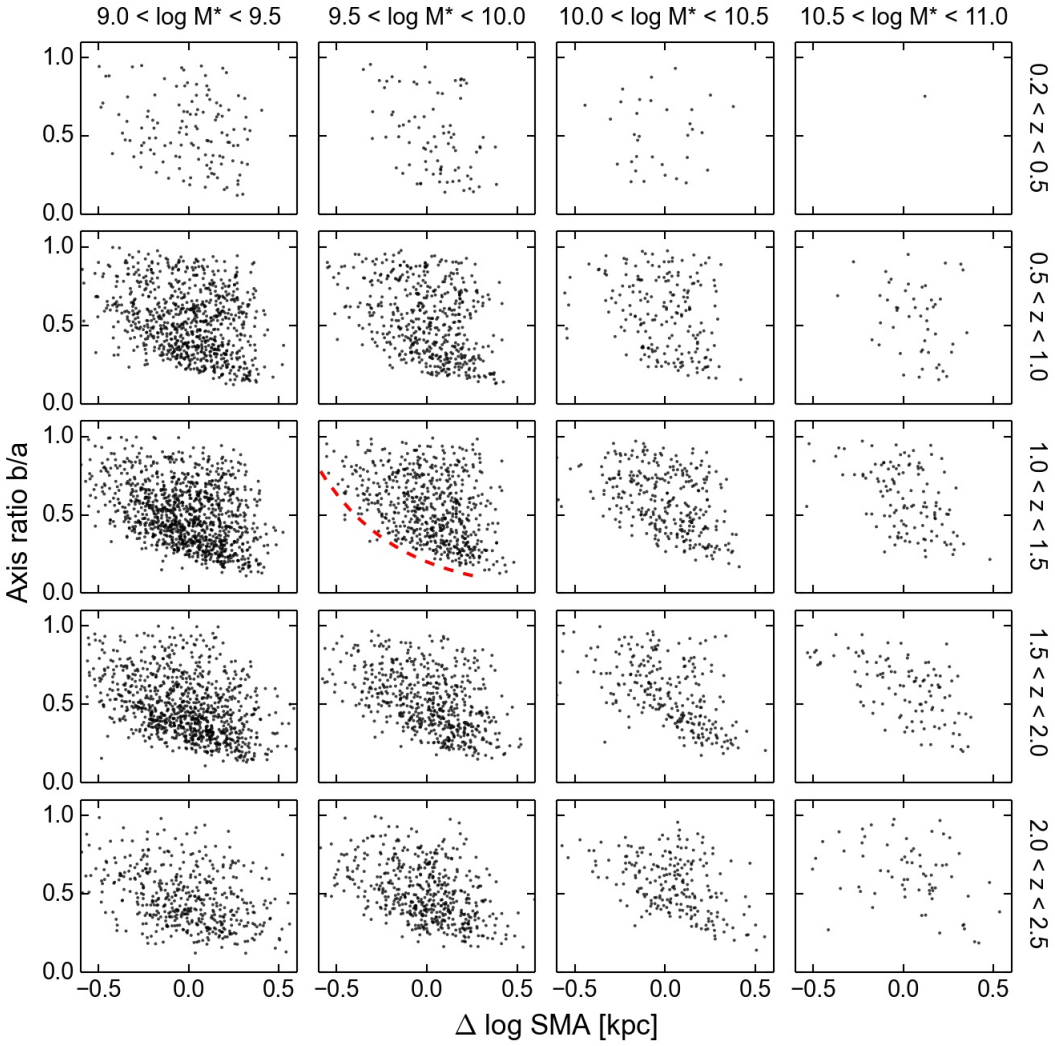

Figure 4.21: Observed axis ratio, b/a, vs. $\Delta \log$ SMA, for main-sequence ridge-line galaxies, divided into narrow stellar mass and redshift bins, as indicated in the figure. The red dashed curve is the predicted track for a prolate object with short-to-long axis ratio $C/A = 0.2$, seen from different viewing angles. For $z \gtrsim 1$ and $M_* \lesssim 10^{10}\,M_\odot$, the wedge-shaped distribution is consistent with the mix of prolate and oblate galaxies reported by van der Wel et al. (2014b). However, a similarly shaped distribution is also observed in the other bins, suggesting that smaller objects are intrinsically more spheroidal (i.e., thicker) and/or some prolate objects are found even at low redshift.

Figure 4.21, this corner is sparsely populated at high redshift and gradually gets filled in with time. After $z \sim 1.5$, the corner becomes more pronounced, indicating that mature, settled disks begin to dominate around this epoch. This is consistent with the rise in settled disks over time identified by Kassin et al. (2012), based on a kinematic study of blue galaxies. Our data are also consistent with the results of van der Wel et al. (2014b), who conclude that oblate disks become more common after $z \sim 1.5$.

In the mass and redshift ranges where van der Wel et al. (2014b) find a high fraction of prolate objects ($M_* \lesssim 10^{10}\,M_\odot$ and $z \gtrsim 1$), the curved boundaries in the corresponding panels of Figure 4.21 are consistent with being caused by a population of prolate objects. What is puzzling is that the curved boundary is seen in nearly all the other panels as well, including those low-redshift bins ($z \lesssim 1$) that van der Wel et al. (2014b) determined to have a negligible contribution of prolate objects.

One possible explanation is that the curved boundary is a selection effect, the result of a systematic bias against very small, flattened objects, which could have mis-measured or missing GALFIT parameters due to insufficient spatial resolution. However, van der Wel et al. (2012) demonstrated that even galaxies with semi-*minor* axis lengths $\leq 0\farcs02$ (0.3 pixels) could be reliably measured. We verify this claim by color-coding the points in Figure 4.21 by semi-minor axis

($= b/a \times$ SMA), expressed in arcseconds (Figure 4.22). The minimum value of the color bar (black) corresponds to $0\farcs02$ (-1.7 dex), the smallest size for which reliable GALFIT measurements are possible. We see that, in each panel, objects along the curved boundary are all comfortably larger than the minimum size. This means that intrinsically small, flat objects are not systematically excluded, and, thus the curved boundary is indeed real.

Given this, an alternative explanation for the wedge-shaped distributions at low redshift is needed. One possibility is that some low-redshift, star-forming galaxies are in fact prolate. Such galaxies could conceivably be among the objects found in the upper-left corner of the distributions, but it is rare to observe a prolate galaxy end-on (which would appear round and small). Hence, if that corner is completely prolate, then we would expect a great many more prolate galaxies seen "side-on" in the lower-right corner, and potentially *most* of the lower-right region would have to be prolate also. If that is true, then there is very little room left at the lower right for any edge-on disk galaxies, which may then be inconsistent with their observed numbers in the upper-right corner. It seems more likely that a large fraction of galaxies in the upper left are genuinely spheroidal objects, perhaps very thick disks. In other words, at low redshift, smaller objects are possibly intrinsically rounder (i.e., thicker).

The arguments above are currently qualitative, and firm conclusions must

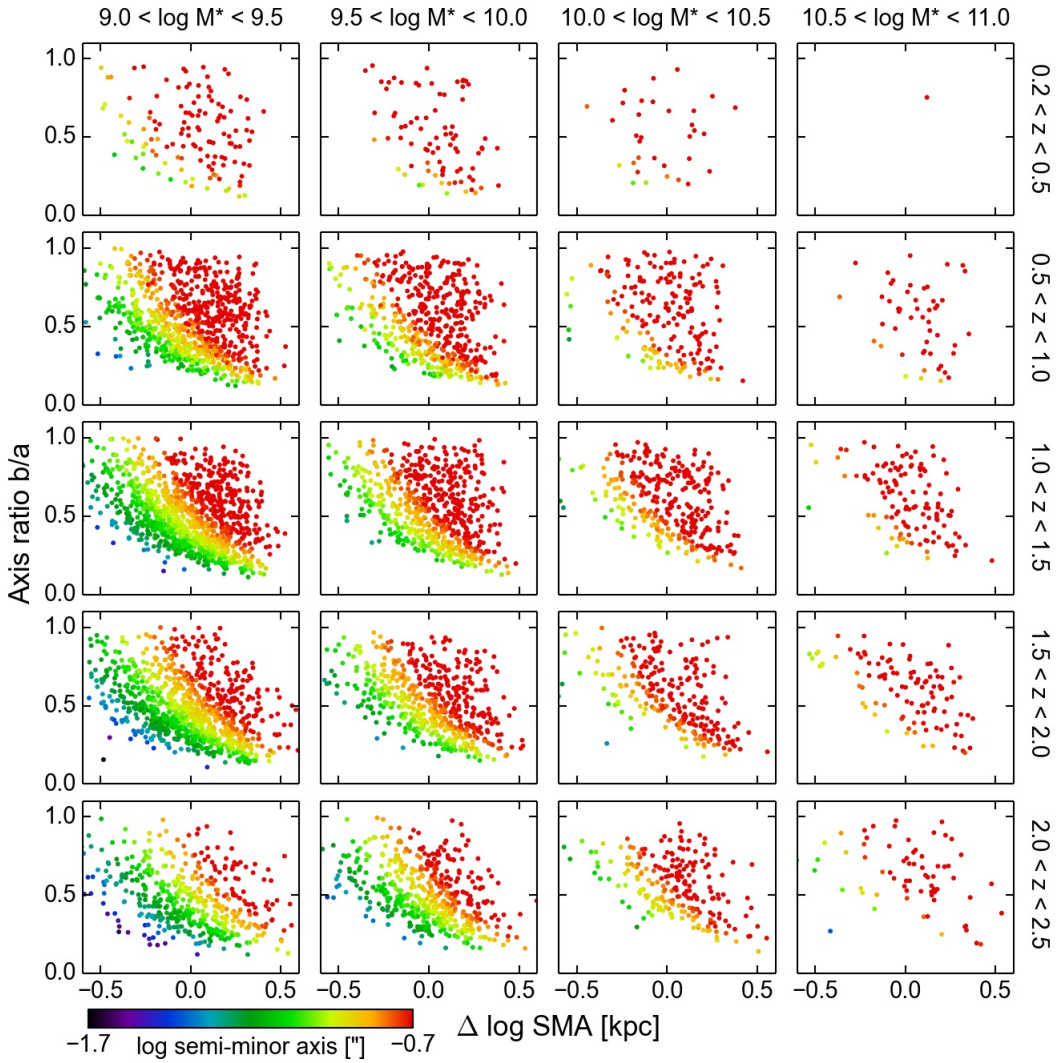

Figure 4.22: Observed axis ratio, b/a, vs. Δ log SMA, for main-sequence ridge-line galaxies, divided into narrow stellar mass and redshift bins, as indicated in the figure. Points are color-coded by semi-minor axis, in arcsec. The smallest galaxies for which GALFIT can reliably measure structural parameters have semi-minor axes $= 0\farcs02$ (-1.7 dex). In each panel, galaxies located on the curved boundary are all larger than this value, implying that the boundary is real and not the result of a systematic bias against intrinsically small, flat objects.

await quantitative modeling. However, our approach highlights the necessity of combining size information with axis ratios in order to make such arguments; b/a alone provides an incomplete description of galaxy shapes.

In passing, we also point out that there is a tendency for the most inclined objects to have the largest $\Delta \log$ SMA, i.e., the lower-right corner of each distribution "pokes out." This is possibly due to a systematic bias in the GALFIT measurements: an underestimate in b/a leads to an overestimate in SMA (van der Wel et al., 2012). Or, it may be due to a line-of-sight effect, in which the surface brightness is higher at a given radius as the path length is increased through a more inclined disk.

Is it possible to distinguish between prolate/oblate objects using something other than structure? For purely oblate disks, A_V would increase as b/a decreases, due to a longer path length for disks seen edge-on. This trend ought to be seen regardless of galaxy size. For purely prolate galaxies, the opposite is expected to be true. Figure 4.23 plots b/a against $\Delta \log$ SMA, with points color-coded by A_V. In bins where oblate disks are expected to dominate, flattened galaxies are seen to have higher attenuation than rounder objects of the same size (as seen earlier in Figure 4.18). In the bins where prolate galaxies should dominate (i.e., the lower-leftmost six panels in Figure 4.23), at best a weak trend is seen between b/a and A_V, whose strength increases toward lower redshift (when oblate disks

start to dominate). This weaker trend is consistent with having a mix of prolate and oblate objects, whose opposite trends in A_V versus b/a cancel each other out; however, it is not definitive proof. The argument requires the presence of disks as well as dust. Galaxies could be quite disky and yet exhibit low absorption, even when edge-on, because the dust is so low. This is consistent with the generally low A_V measurements for the prolate-rich bins (as seen in Figure 4.18). Thus we cannot definitively identify prolate objects simply by examining trends in A_V.

Can visual morphologies distinguish between prolate and oblate galaxies? Figures 4.24 and 4.25 show color postage stamps of main-sequence ridge-line galaxies in two mass and redshift bins, plotted in the b/a-$\Delta \log$ SMA plane. At lower redshift and higher masses (Figure 4.24), the galaxies are essentially all oblate disks. Larger galaxies ($\Delta \log \text{SMA} \gtrsim 0$) are clearly disky (with red centers) and have well-defined spiral structure. Objects in the upper-right are face-on disks, while those in the lower-right are seen edge-on. Smaller objects tend to be smoother and rounder, with less prominent spiral structure.

At higher redshift (Figure 4.25), galaxies show a similar mix of morphologies. A clear population of disks is seen in the upper-right of the diagram. Some galaxies in the lower-right corner have redder centers and bluer outskirts, which are consistent with disks, but others are more irregular. However, it is not obvious from the images alone whether these objects are just disturbed disks/mergers or

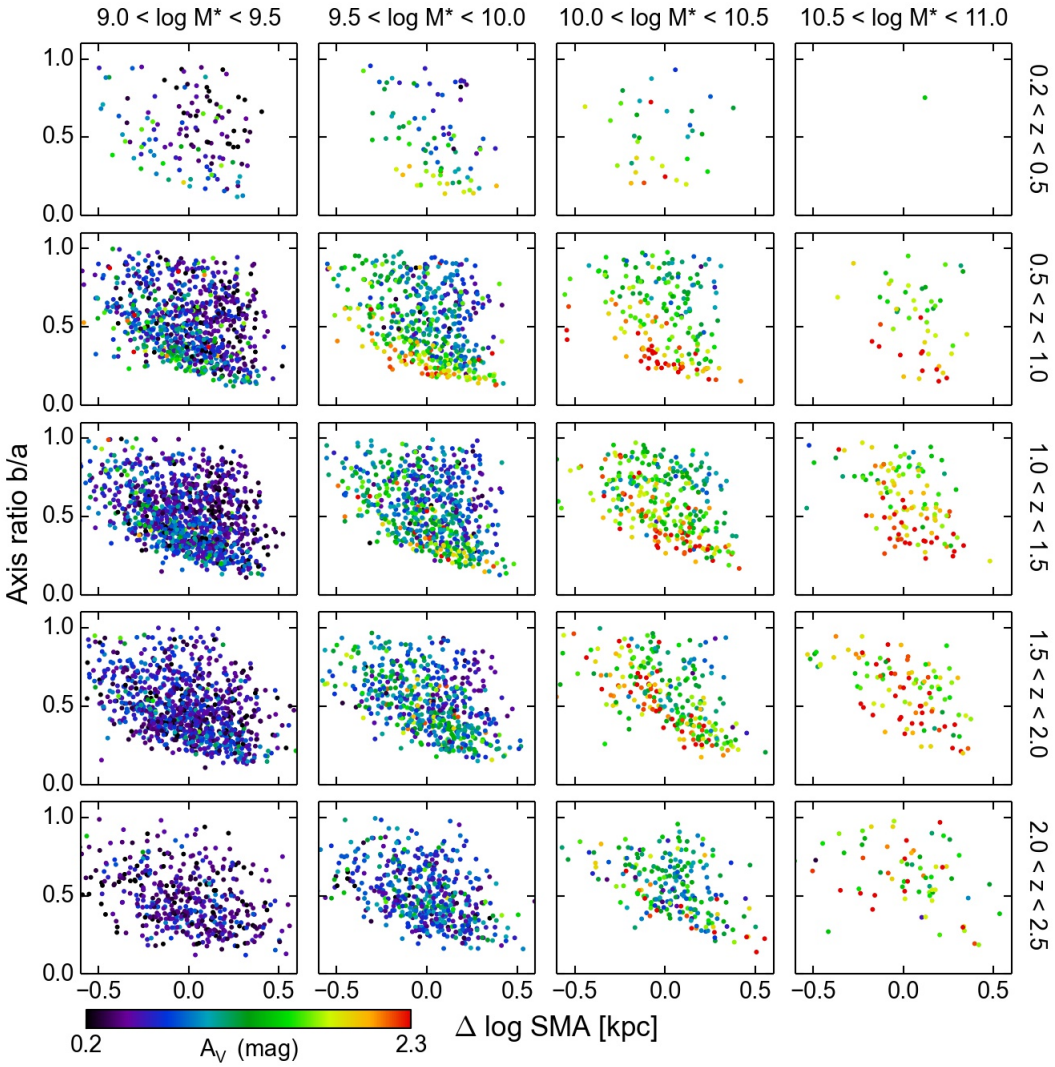

Figure 4.23: Observed axis ratio, b/a, vs. Δ log SMA, for main-sequence ridge-line galaxies, divided into narrow stellar mass and redshift bins, as indicated in the figure. Points are color-coded by visual attenuation, A_V. In bins dominated by oblate disks (i.e., $z \lesssim 1.5$ and $M_* \gtrsim 10^{10}\,M_\odot$), galaxies with small b/a (i.e., flattened) tend to be more attenuated than rounder objects, as expected. The trend is weaker in bins where prolate objects are expected to dominate (i.e., $z \gtrsim 1$ and $M_* \lesssim 10^{10}\,M_\odot$), though this is also consistent with an overall lower amount of dust at high redshift/low masses.

actually prolate. Developing criteria, both visual and quantitative, to robustly identify prolate galaxies is clearly needed in order to make further progress. Possible quantities to examine include Sersic index, asymmetry, color gradients, and central mass density. Recent hydrodynamical galaxy simulations are beginning to investigate prolate objects in detail and will help shed light on this issue (Ceverino et al., 2015).

4.6 A Lack of Correlation between SSFR and Galaxy Structure

We have shown that star-forming galaxies show a wide range of shapes and sizes, even at a given mass and redshift. We also saw that star-forming galaxies in a mass and redshift bin exhibit a wide range in SSFR, and that loci of constant SSFR form "stripes" in the UVJ diagram (Figure 4.5). A question that springs from these results is: Does SSFR correlate with galaxy structure, at a fixed mass and redshift? The qualifier is important, because previous studies have shown that SFR is (unsurprisingly) correlated with stellar mass (the star-forming main sequence; e.g., Brinchmann et al., 2004; Daddi et al., 2007; Noeske et al., 2007; Salim et al., 2007; Wuyts et al., 2011b; Whitaker et al., 2012, 2014). But our question goes deeper: does the scatter in (S)SFR show systematic trends with

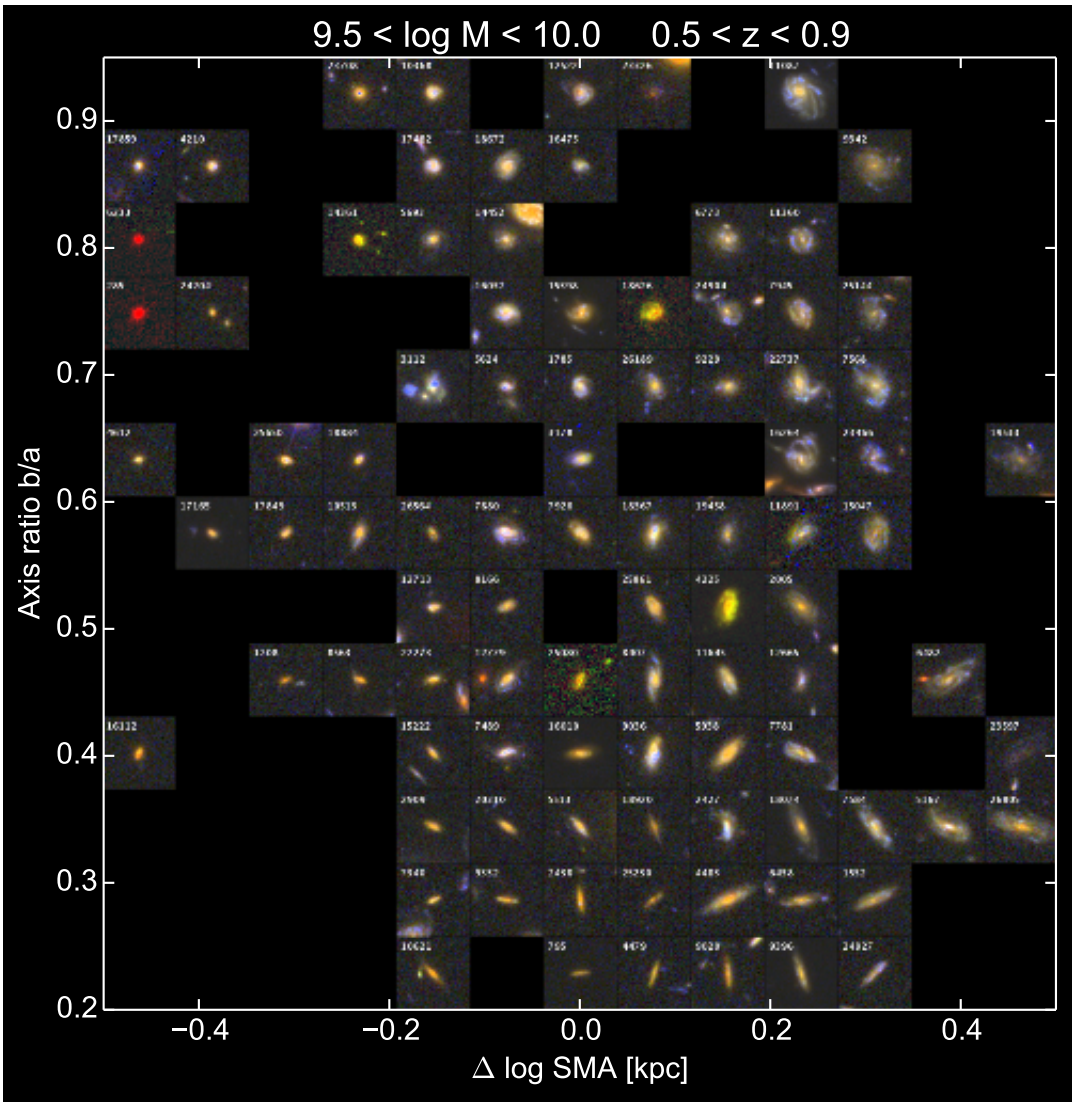

Figure 4.24: Montage of main-sequence ridge-line galaxies with $9.5 < \log M_*/M_\odot < 10.0$ and $0.5 < z < 0.9$ in the b/a-$\Delta \log$ SMA plane. Oblate disks are expected to dominate in this bin. Larger galaxies tend to show clear spiral structure, while smaller objects are featureless (or have unresolved structure). At these lower redshifts, galaxies located in the lower-right corner are predominantly edge-on, oblate disks, as evidenced by their redder central bulges and bluer outskirts.

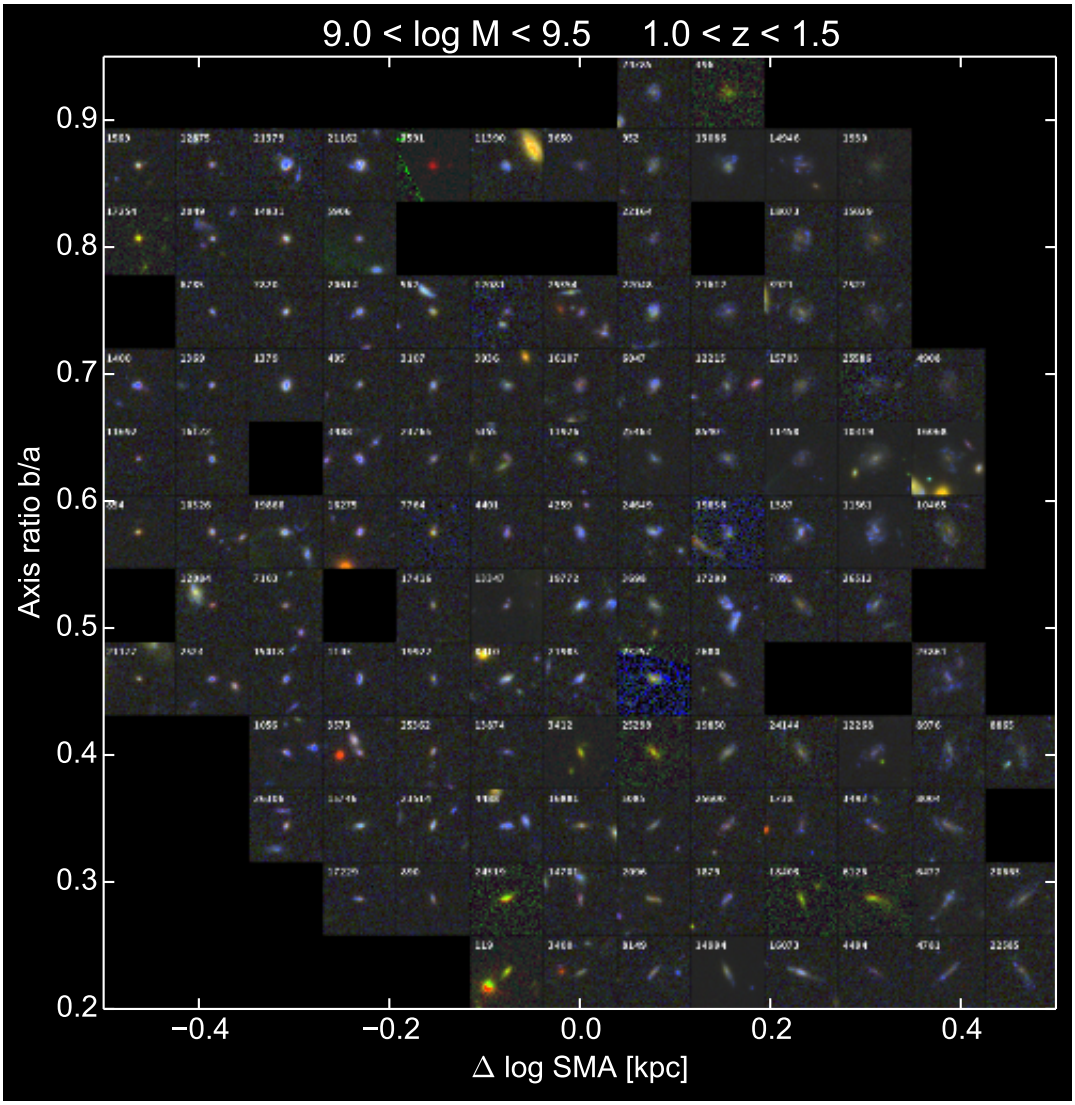

Figure 4.25: Montage of main-sequence ridge-line galaxies with $9.0 < \log M_*/M_\odot < 9.5$ and $1.0 < z < 1.5$ in the b/a-$\Delta \log$ SMA plane. Galaxies at these lower masses and higher redshifts show a similar variety of morphologies to those seen in Figure 4.24. However, some galaxies in the lower-right corner show more irregular morphologies. These could be disturbed disks, mergers, or possibly prolate galaxies.

galaxy structure (size and Sersic index), *even at fixed stellar mass*?

Previously, Wuyts et al. (2011b) examined how galaxy structure varies across the main sequence, using a similar sample of CANDELS galaxies. They found, on average, smaller galaxy sizes and larger Sersic indices for galaxies lying significantly ($\sim 10\times$) above and below the ridge line of the main sequence (their Figures 2 and 8). Little to no trend was seen for galaxies *on* the ridge line. However, their analysis used rather coarse redshift and stellar mass bins, so it is worth returning to this question with our dataset to see if their results persist when the sample is more finely dissected.

To investigate, we refer back to Figure 4.13, where $\Delta \log \mathrm{SSFR}_{\mathrm{UV,corr}}$ is plotted against $\Delta \log$ SMA. Previously we used this figure to identify fading galaxies (Section 4.3.4), but now we focus our attention on objects located on the main-sequence ridge line. For these galaxies, there is essentially *no correlation* between $\Delta \log \mathrm{SSFR}_{\mathrm{UV,corr}}$ and $\Delta \log$ SMA. Our result is consistent with Wuyts et al. (2011b), but, in addition, our method reveals that such behavior persists even in *narrow slices* of mass and redshift. In other words, the flat trend for star-forming galaxies seen in Wuyts et al. (2011b) is not due to their averaging over a much larger range of M_* and z, but is indeed real.

In addition to size, a similar result is seen with Sersic index. Figure 4.26 plots $\Delta \log \mathrm{SSFR}_{\mathrm{UV,corr}}$ against Sersic index, n, and points are color-coded by axis ratio

b/a. No correlation is seen between $\Delta \log \mathrm{SSFR}_{\mathrm{UV,corr}}$ and n, again indicating that structural variations do not appear to drive the spread in SSFR, at fixed mass and redshift. The fading galaxies (below the red dashed line) do tend to be rounder, as we noted in Section 4.3.4. Interestingly, they do not necessarily have high values of n; indeed, fading objects can span a wide range in n. Recalling from Figure 4.13 that fading objects come in a range of sizes, our results suggest that quenching does not uniformly mold galaxies into objects with small sizes and concentrated light profiles, at least not immediately.

Returning to the main-sequence ridge-line galaxies in Figure 4.26, it is worth noting that the observed range of Sersic indices changes dramatically from a broad distribution at high redshift/low masses to a peaked distribution at low redshift/high masses. In other words, the classic picture of star-forming galaxies all having exponential disks ($n \approx 1$) is generally true only for more massive objects and at later times. This again is consistent with the mass-dependent trend in disk formation that we saw earlier (see also Kassin et al., 2012). From the figure, it is also apparent that there is no systematic trend between $\Delta \log \mathrm{SSFR}_{\mathrm{UV,corr}}$ and b/a, reassuring us that inclination (which affects the line-of-sight dust attenuation) does not introduce any systematic bias in the determination of $\mathrm{SSFR}_{\mathrm{UV,corr}}$.

To summarize, we find that, at fixed mass and redshift, $\mathrm{SSFR}_{\mathrm{UV,corr}}$ for actively star-forming galaxies shows no correlation with size or Sersic index. These results

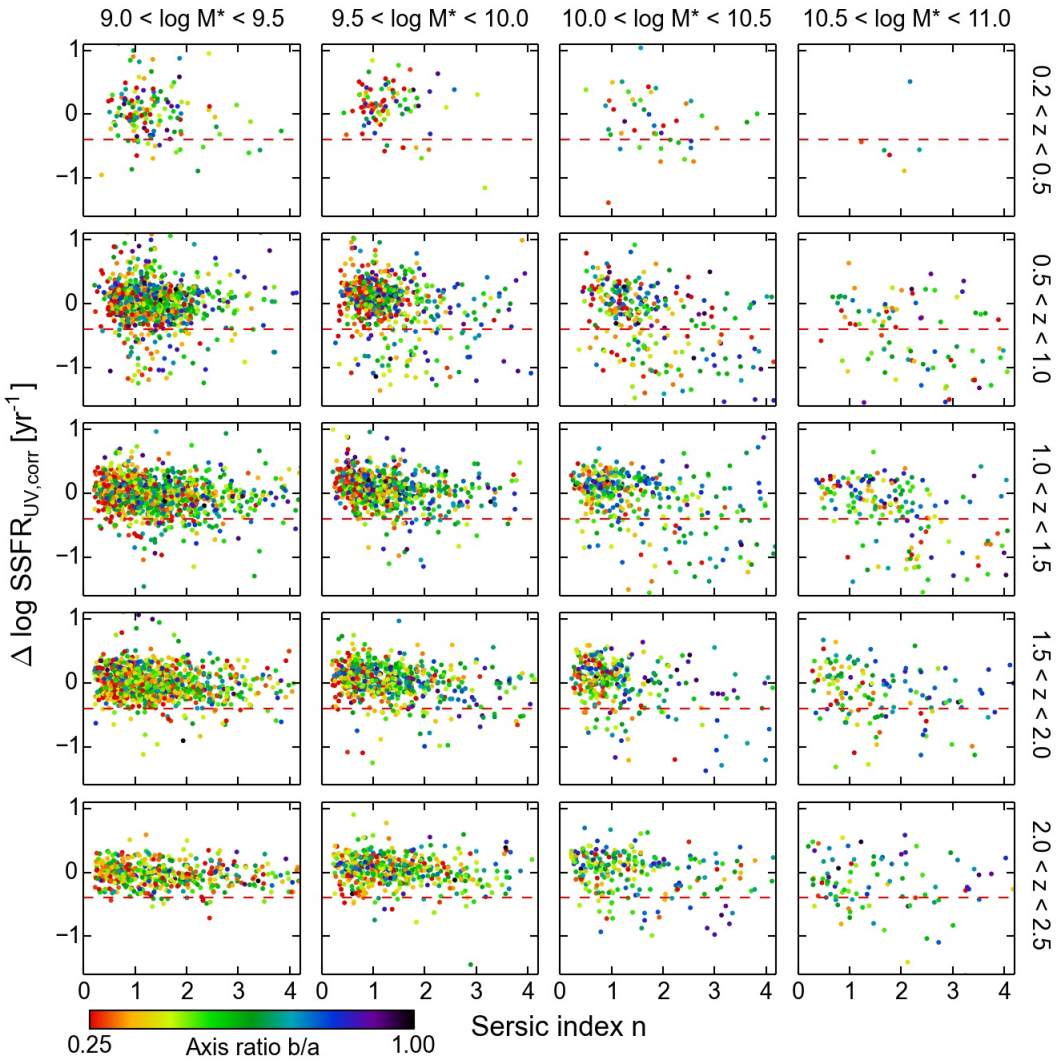

Figure 4.26: $\Delta \log \mathrm{SSFR}_{\mathrm{UV,corr}}$ vs. Sersic index n for star-forming galaxies, divided into narrow stellar mass and redshift bins, as indicated in the figure. Points are color-coded by axis ratio b/a. No correlation is seen between $\Delta \log \mathrm{SSFR}_{\mathrm{UV,corr}}$ and n on the ridge line of the main sequence. Furthermore, the distribution of n changes noticeably with M_* and z: star-forming galaxies at early times/low masses span a large range in n, while at late times/high masses they primarily have exponential profiles ($n \approx 1$). Objects below the dashed line are fading galaxies (Section 4.3.4).

confirm and bolster the conclusions of Wuyts et al. (2011b), who find the lack of a trend between star-formation rate and structure for galaxies located *within* the main sequence. The implications of this result are discussed below (Section 4.7.1).

4.7 Discussion

By exploiting the large number of objects and numerous value-added catalogs in the CANDELS survey, we have been able to subdivide our sample into narrow slices of mass and redshift. This has enabled a more comprehensive and systematic examination of trends that are often washed out when lumping together galaxies spanning a wide range in M_* and/or z. The results presented above have uncovered numerous questions about galaxy formation and evolution processes, and we highlight and discuss a few key issues below.

4.7.1 The Impact of Galaxy Structure on Star Formation and Dust Attenuation

The results presented in Section 4.6 reveal a surprising lack of correlation between $\Delta \log \mathrm{SSFR}_{\mathrm{UV,corr}}$ and galaxy structure (size and Sersic index) at fixed mass and redshift. This broadly agrees with the findings of Wuyts et al. (2011b). However, they also find a trend of decreasing size and increasing Sersic index among galaxies with significantly higher SFR ($\sim 10\times$ above the main sequence).

We do not see such behavior. Indeed, there are practically no galaxies with $\Delta \log \mathrm{SSFR}_{\mathrm{UV,corr}} \gtrsim 0.5$ dex in our sample, and those that do have higher SSFR are neither systematically smaller nor have higher n than the rest of the population (Figures 4.13 and 4.26). However, this discrepancy may not be significant, as there are very few such outliers in the Wuyts et al. (2011b) sample, and the observed scatter in size and n for these objects is large, making definitive statements difficult (e.g., their Figures 2 and 8).

This lack of correlation between SSFR and structure places constraints on the gas supply that fuels star formation. Observations of local and high-redshift galaxies have shown that the molecular gas fraction, $f_g \equiv M_g/M_*$, is correlated with SSFR and anti-correlated with stellar mass (e.g., Saintonge et al., 2011; Magdis et al., 2012; Tacconi et al., 2013; Genzel et al., 2015). Moreover, the typical scatter in f_g at fixed M_* or fixed SSFR is roughly a factor of two (Tacconi et al., 2013; Genzel et al., 2015). We now show that our results are consistent with this scatter, and, furthermore, that it should also correlate with galaxy size.

To establish why our results necessitate a scatter in f_g, we first predict how SSFR would vary as a function of galaxy size if f_g were constant. The calculation is done assuming a fixed stellar mass (and redshift). In other words, if a galaxy were shrunk in size, while keeping the same amount of gas, by how much would its SSFR increase? Clearly, its gas surface density, Σ_g, would increase, and, consequently,

so would its star formation rate surface density, $\Sigma_{\rm SFR}$, according to the Kennicutt-Schmidt relation, $\Sigma_{\rm SFR} \propto \Sigma_g^{1.4}$ (Kennicutt, 1998). Quantitatively, assuming $f_g =$ constant, the change in $\Sigma_g \propto M_g/{\rm SMA}^2$ resulting from a 0.6 dex decrease in SMA (based on the extent in $\Delta \log$ SMA in Figure 4.13) is 1.2 dex, or a factor of 16. The corresponding increase in $\Sigma_{\rm SFR} \propto \Sigma_g^{1.4}$ is 1.7 dex. This predicts a 0.5-dex increase in SFR, since ${\rm SFR} \propto \Sigma_{\rm SFR} \times {\rm SMA}^2$. Inspecting Figure 4.13, it is clear that such a steep relation is *not* seen at any mass or redshift in our sample. This suggests that gas fraction is correlated with galaxy size in such a way as to maintain a constant value of (S)SFR at fixed stellar mass.

Redoing our calculation, assuming the same 0.6-dex decrease in SMA, we find that f_g must decrease by a factor of ≈ 2.2 in order to maintain a constant SFR. Thus, we predict a scatter of a factor of ~ 2 in the gas fraction at fixed stellar mass, in good agreement with the factor ~ 2 scatter in the molecular gas scaling relations discussed above. Moreover, we predict that the observed scatter in f_g at fixed stellar mass should be correlated with galaxy size (smaller galaxies have lower f_g), which can be confirmed with existing data.

Using these estimates, we can now place constraints on the level of dust attenuation as well. The results in Figure 4.18 indicate that dust attenuation, A_V, is anti-correlated with galaxy size, at least for disk-dominated systems. One possible interpretation of this trend is that the gas (and dust) density is higher in smaller

galaxies, resulting in an increase in dust attenuation. Indeed, assuming that f_g decreases by a factor of 2.2 and size decreases by a factor of 4, we find that the gas surface density, Σ_g, increases by a factor of ~ 7. This predicts an increase in A_V by a factor of 7, assuming a fixed dust-to-gas ratio and that A_V scales linearly with the gas surface density.

Because the increase in A_V is relative, not absolute, any comparison to the data requires specifying an initial value for A_V. Consulting Figure 4.18, we see that the typical A_V for large-radii galaxies ranges from ~ 0.5 mag to ~ 1.5 mag, depending on their stellar mass. Our prediction then says that A_V increases anywhere from 3 to 9 mag, depending on the initial A_V. Comparing this prediction with Figure 4.18, however, reveals that the observed trend between A_V and size is much weaker than predicted in all bins. Our assumption that A_V scales linearly with the gas density is equivalent to assuming that all the stars are located behind a foreground screen of dust. Obviously, such an assumption is too simplistic to represent the varied star-dust geometries found in actual galaxies. A more realistic approach that agrees better with observations is to consider a model in which some fraction of the stars are more obscured and/or the dust is clumpy rather than homogeneous (e.g., Calzetti et al., 1994; Charlot & Fall, 2000; Witt & Gordon, 2000; Wild et al., 2011; Liu et al., 2013).

To get a rough sense of how patchy the dust must be, we estimate the fraction

of light that must be unobscured in order to reproduce the trend in Figure 4.18. We use a toy model in which some fraction of stars is located behind a uniform screen of dust, while the remaining fraction is totally unobscured. The dust screen is assumed to scale in proportion to the gas surface density. As stated above, a shrinkage in galaxy size by 0.6 dex translates into a factor of 7 increase in A_V, if all the stars are uniformly attenuated. In order for A_V to increase by, say, 1 mag, we estimate that $\sim 20\%$ of the light must be unobscured (assuming an initial A_V of 1 mag). This estimate is formally valid only for V-band light; the fraction at other wavelengths is likely different and would depend on the relative fraction of young and old stars producing the light. However, the point is that exact predictions of how A_V should scale with galaxy size (and also inclination) depend sensitively on the exact geometrical model, especially on how many stars are lightly obscured. The results of our toy model are crude, but they highlight a need for more accurate parameterizations of dust attenuation that account for variations in star-dust geometry and galaxy structure.

4.7.2 Connecting Galaxies to Dark Matter Halos

Our discussion so far has neglected the fact that galaxies reside in dark matter (DM) halos. It is obvious that the processes shaping a galaxy's evolution must be somehow connected to the behavior of its DM halo. In particular, is there a

correspondence between halo properties and galaxy properties that can explain the trends observed in the data?

Section 4.6 presented evidence that SSFR shows no correlation with galaxy size or Sersic index, at fixed M_* and z, for star-forming galaxies on the main sequence. An implication of this result is that a galaxy's star formation history is not a smoothly varying function of time that coincides with (or results from) changes in its structure. In other words, present data suggest that a galaxy's SSFR is independent of its internal structure (at a given mass and redshift).

How to explain this? Recent analytic models of galaxy evolution may offer a solution (e.g., Bouché et al., 2010; Dekel et al., 2013; Lilly et al., 2013; Dekel & Mandelker, 2014). Dubbed the "bathtub" model in Dekel et al. (2013), the key assumptions in this toy model are (1) the gas mass in a galaxy obeys a continuity equation that balances gas accretion onto the galaxy with gas consumption via star formation and outflows, and (2) the SFR is proportional to the accreted gas mass. As shown by Dekel et al. (2013), once a steady state is reached, the SFR is proportional to the mass accretion rate onto the halo. In other words, whatever gas is accreted is immediately converted into stars (and an accompanying outflowing galactic wind). Predictions from this simple model are broadly consistent with the observed redshift evolution in the fundamental metallicity relation, cosmic SSFR, and stellar-to-halo mass relation (Lilly et al., 2013; Dekel & Mandelker, 2014).

Our result that SSFR is independent of galaxy structure agrees with the basic tenet of the bathtub model, namely, that SFR is ultimately regulated by global gas accretion rather than by the internal structure of the galaxy. This also suggests that the intrinsic scatter in the (S)SFR-mass relation is primarily due to variations in the (specific) halo accretion rate. It will be interesting to verify this with current and future semi-analytic models and hydrodynamical simulations.

Turning to the results on galaxy shapes presented in Section 4.5, an outstanding question is the extent to which the intrinsic shape of a galaxy is a reflection of the intrinsic shape of its DM halo. N-body DM simulations show that halos are generally not spherical, and that their shapes evolve with redshift (e.g., Bullock, 2002; Jing & Suto, 2002; Allgood et al., 2006; Bett et al., 2007; Bonamigo et al., 2015). In general, simulations predict that, at fixed mass, halos start out elongated and become more spherical over time. Also, halos tend to be more elongated at their centers because early accretion occurs along thin filaments rather than isotropically (Dekel et al., 2009). Recent hydrodynamical simulations of high-redshift galaxies have found that galaxies forming in elongated halos have correspondingly elongated (prolate) stellar distributions (Ceverino et al., 2015, T. Sai, V. Tang, in preparation). Moreover, these elongated galaxies are seen almost exclusively at low mass, $M_* \lesssim 10^{9.5}\,M_\odot$, and high redshift $z \gtrsim 1.5$, which agrees with our results and those of van der Wel et al. (2014b) on the shapes

of galaxies. Simulations will also provide detailed information on the internal structure of prolate objects, which can be compared to our structural results.

It is clear that galaxies and their DM halos are intimately connected. Given this close link, it seems natural that a correspondence should exist between halo properties and galaxy properties. The most obvious example of such a correspondence is the stellar mass-halo mass relation (e.g., Behroozi et al., 2013, and references therein). Also, the bathtub model posits that SFR can be regulated by halo accretion rate alone. In addition, the radii of galaxies are plausibly linked with additional halo parameters like virial radius, concentration, and/or spin. Indeed, models of disk formation that assume a scaling between disk size and virial radius (e.g., Mo et al., 1998) can successfully reproduce key scaling relations, including the mass-size relation (Somerville et al., 2008; Lu et al., 2015) and the Tully-Fisher relation (Dutton et al., 2011). With the increasing sophistication of theoretical models, one can in principle verify how well halo parameters map onto the corresponding galaxy parameters. More crucially, these models can provide insight into the mechanisms producing the amount and shape of the *scatter* that is observed in these parameters (C. Lee, in preparation).

4.8 Summary and Conclusions

In this work, we utilize a rich database of $\sim$9,100 galaxies with $0.2 < z < 2.5$ and $9.0 < \log M_*/M_\odot < 11.0$, taken from the GOODS-S and UDS regions of the CANDELS program, to study the evolution of galaxy colors, star-formation rates, and structure. By dividing the sample into narrow mass and redshift slices, we have uncovered both a striking diversity and a surprising regularity among star-forming galaxies. Our main results are as follows.

1. Star-forming galaxies in the UVJ diagram trace out "stripes" of constant SSFR that run parallel to the star-forming locus, along the newly defined coordinate $(U-V)'$. This behavior is seen when galaxies are divided into narrow mass and redshift slices or stacked together. We find a nearly universal trend between SSFR and $(U-V)'$, suggesting that a galaxy's SSFR can be estimated just from its $U-V$ and $V-J$ colors.

2. The diagonal extent of the star-forming locus in the UVJ diagram is mainly a dust sequence: galaxies with redder $V-J$ suffer higher visual attenuation. We confirm previous results showing that inclination is a main factor in populating the reddest end of the sequence, but only for $z \lesssim 1$. We find that the red end is also populated by small, intrinsically round objects with enhanced attenuation, possibly due to a denser ISM, as well as by "fading"

objects whose star formation is going out.

3. The observed axis ratio distribution of star-forming galaxies evolves strongly with mass and redshift. At early times/low masses, the distribution is consistent with a significant contribution from prolate objects, gradually giving way to flatter oblate disks toward late times/high masses. Our use of semi-major axis in conjunction with axis ratio reveals that, for $z \lesssim 1$, galaxies with smaller sizes are intrinsically rounder (i.e., thicker) than larger-radii objects of the same mass. The fact that shape varies with size could alter the conclusions of previous analyses, which lumped all galaxies together regardless of size. The existence of small, intrinsically round galaxies could be due to the increasing prominence of bulges as disks begin to fade. Alternatively, they may represent a handful of prolate objects at low redshift, contrary to recent results.

4. Based on the evolution of galaxy structure (size, axis ratio, Sersic index), we find evidence for a mass-dependent trend in the formation and settling of disks, i.e., more massive galaxies form thin disks earlier, in agreement with previous kinematic results. We also see an associated increase in dust content (as measured by A_V), which likely reflects a buildup of metals in the ISM as galaxies evolve.

5. At fixed mass and redshift, no correlation exists between $\Delta \log \mathrm{SSFR}_{\mathrm{UV,corr}}$

(the offset from the main sequence) and galaxy structure (radius and Sersic index), for actively star-forming galaxies. We deduce from this that the gas fraction in galaxies must vary by a factor of ~ 2 at fixed stellar mass (with less gas in smaller-radii objects), in agreement with the observed scatter in molecular gas content in high-redshift galaxies. The lack of correlation agrees with the bathtub model of star formation, in which SFR is regulated by the halo accretion rate, not by conditions within the galaxy.

6. The correlation between gas fraction and galaxy size (Point 5) also places constraints on the relative increase in dust attenuation suffered by smaller galaxies of a given mass. In particular, adopting a foreground screen approximation, we predict a factor ~ 7 increase in absorption as galaxies shrink in radius by a factor of 4. However, the observed trend in the data is much weaker. We can better match the data by assuming that some fraction ($\sim 20\%$) of stars are totally unobscured, pointing to the need for more sophisticated treatments of dust attenuation that account for more realistic star-dust geometries.

This work has given a bird's-eye view of the changing demographics of star-forming galaxies over a wide range in mass and redshift. It must be noted that virtually all of these results, particularly those involving $\mathrm{SSFR_{UV,corr}}$ and A_V, depend on the validity of the SED models fitted by CANDELS team members. The

picture we describe appears plausible, but it needs to be verified before it can be fully adopted. If found correct, our results provide new and stringent constraints linking star formation with galaxy structure for future models and simulations to reproduce. In addition, CANDELS offers additional data that we have not yet utilized, e.g., quantitative morphological measures, X-ray observations to identify AGN, and radial mass, A_V, and SFR profiles to investigate the internal evolution of mass buildup and radial gradients in SFR and dust attenuation. Future work will incorporate these additional sources to refine our understanding of how star-forming galaxies evolve.

4.9 Appendix: On the Validity of Dust-corrected, UV-based SSFR

Our use of $\mathrm{SSFR_{UV,corr}}$ assumes that it is a robust tracer of star formation, at least in a relative sense. In other words, we assume that $\mathrm{SSFR_{UV,corr}}$ reliably rank-orders galaxies according to their star-formation activity. To verify the usability of $\mathrm{SSFR_{UV,corr}}$, in this appendix we compare it to SFRs based on a combination of UV and IR data. This hybrid approach has become the de facto standard because it offers a direct measurement of both dust-obscured and unobscured star formation (e.g., Kennicutt & Evans, 2012). However, SFRs involving IR data are

plagued by their own systematic biases, which we discuss before moving on to the comparison with our UV-based rates.

4.9.1 Systematic Biases in $L_{\rm IR}$ Estimates

Widely used calibrations exist to convert the total infrared luminosity, $L_{\rm IR}$, to SFR (e.g., Kennicutt et al., 2009; Hao et al., 2011; Murphy et al., 2011b). We define $L_{\rm IR}$ to be the integrated $8-1000\,\mu$m luminosity, though other definitions are also used in the literature. Typically, the available IR photometry is fit to various families of IR templates, which themselves are calibrated to observations of *local* IR-luminous galaxies (Chary & Elbaz, 2001; Dale & Helou, 2002; Rieke et al., 2009). $L_{\rm IR}$ is then computed by integrating under the best-fit IR template. If multiple IR bands are not available, recipes exist to convert single-band photometry (usually $24\,\mu$m) to $L_{\rm IR}$ (e.g., Wuyts et al., 2008; Elbaz et al., 2011; Rujopakarn et al., 2013).

Various questions surround the methods used to estimate $L_{\rm IR}$. First, how robust is the cross-matching of counterparts between the optical and IR imaging, given that confusion is severe, particularly in the far-IR, which has poor spatial resolution? Second, how well do the IR templates perform in recovering the true $L_{\rm IR}$, as a function of the number of data points available, stellar mass, and redshift? Finally, how accurate are single-band conversions used to derive $L_{\rm IR}$?

Figure 4.27 gives a visual sense of the object confusion problem. Four images at different wavelengths of the same patch of the GOODS-S field are shown. Sources in the final sample analyzed in this paper were identified based on the *HST*/WFC3 F160W image and are indicated by red circles. They are to be compared to the same regions of sky observed with *Spitzer* and *Herschel*. Note, first of all, the large number of our sources that are not detected at all at longer wavelengths. The degradation in spatial resolution in the MIPS and *Herschel* images is also painfully clear. Note, in particular, the blending seen in regions where several F160W objects are clustered together (e.g., the lower-left region). Needless to say, accurately assigning fluxes to the proper object(s) from such images is a challenging task. A fuller discussion of tackling object confusion can be found in e.g., Pérez-González et al. (2010) and Safarzadeh et al. (2015).

In our study, source identification in the MIPS and *Herschel* imaging was completed following the method described in Pérez-González et al. (2005, 2008b, 2010). Briefly, objects detected in the MIPS 24 μm image are used as priors to identify objects in the longer-wavelength PACS and SPIRE imaging. Once the positions are constrained, fluxes are measured by fitting the appropriate PSF to the source at each location. All the F160W sources located within the MIPS PSF are then assigned the full value of the IR fluxes. In order to mitigate confusion, only F160W objects that are identified as the nearest neighbor to a MIPS source

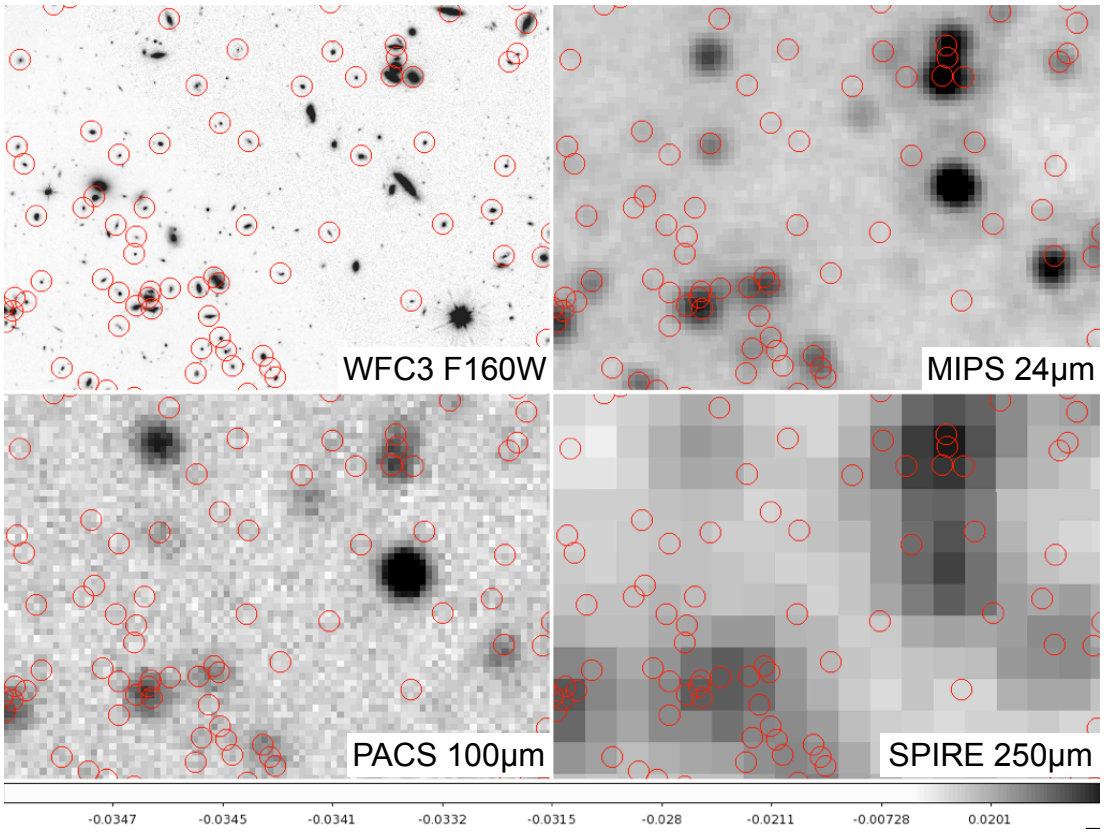

Figure 4.27: Cutouts of the same region in the GOODS-S field, as imaged at four different wavelengths. Red circles indicate objects in the present sample, which are selected from the *HST*/WFC3 F160W image (upper left). The spatial resolution of the successive images worsens dramatically, going from 0.″2 FWHM for F160W, to 6″ for MIPS 24 μm (upper right) and PACS 100 μm (lower left), to 18″ for SPIRE 250 μm (lower right). Robust IR flux measurements of F160W-selected objects is challenging owing to confusion in the MIPS and PACS/SPIRE imaging. Note also that most of the objects detected in F160W (red circles) are not detected at all at longer wavelengths.

are used. This reduces our sample from 9,135 objects to 2,425 objects (27% of the total sample). While this addresses source mis-identification between the MIPS and F160W images, there is still "residual" confusion between the MIPS and *Herschel* imaging, which may contaminate the latter measurements. Pérez-González et al. (2010) showed that the fraction of blended MIPS objects is about 15% in the PACS imaging, but reaches $\sim$ 50% in the longer-wavelength SPIRE bands. Thus, the PACS fluxes are generally robust and free from contamination due to blending, while the SPIRE measurements are more uncertain (see below).

With the IR photometry in hand, we proceed to address the other issues raised above regarding the determination of $L_{\rm IR}$. Figure 4.28 plots the ratio of $L_{\rm IR}$ determined from full SED fitting to the available far-IR photometry points, denoted $L_{\rm IR}$ (SED), to $L_{\rm IR}$ determined from the 24 μm-based conversion of Rujopakarn et al. (2013), denoted $L_{\rm IR}$ (R13), versus the mass-normalized $L_{\rm IR}$ (R13). Points are color-coded by the photometry used in the IR SED fitting. (Note that the sample is almost exclusively star-forming galaxies, by virtue of requiring objects to be detected in MIPS.) We see from the figure that galaxies have higher $L_{\rm IR}/M_*$ ratios at earlier times. Since $L_{\rm IR}$ traces star formation, this trend is simply saying that star-forming galaxies had higher (S)SFRs at earlier times, which is consistent with the observed increase in the zeropoint of the star-forming main sequence with redshift (e.g., Whitaker et al., 2012).

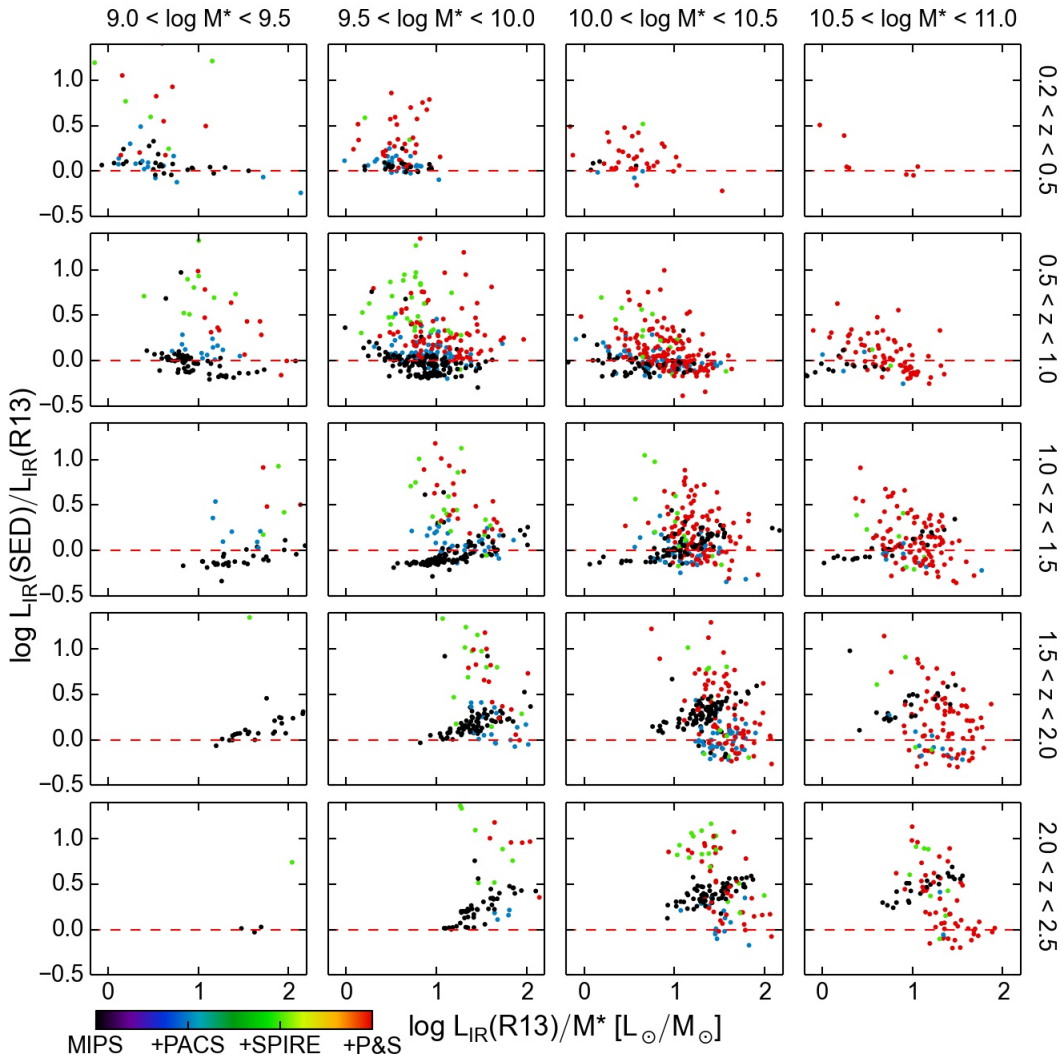

Figure 4.28: Ratio of $L_{\rm IR}$ determined from SED fitting to local IR templates, $L_{\rm IR}$ (SED), to $L_{\rm IR}$ determined from the 24 μm-based conversion of Rujopakarn et al. (2013), $L_{\rm IR}$ (R13), plotted against the mass-normalized $L_{\rm IR}$ (R13). Points are color-coded by the photometry used in the SED fitting. Outlying galaxies with high $L_{\rm IR}$ ratios are possibly affected by incorrect SPIRE data (green points). Fitting local templates to MIPS-only galaxies (black points) results in a systematic overestimate in $L_{\rm IR}$ that is due to evolution in PAH emission strength that is not accounted for in the fitting.

Nominally, galaxies should have $L_{\rm IR}$ ratios close to unity if the two methods of determining $L_{\rm IR}$ are consistent. Inspection of the figure reveals that this is *not* generally the case, and other interesting trends are also seen. First, we find that galaxies with only SPIRE for their far-IR photometry (green points) have significantly higher $L_{\rm IR}$ ratios than most of the other objects in each bin. This effect is particularly apparent in the two lowest mass bins and in the highest redshift bin. One possible explanation is that the cross-matching between catalogs was inaccurate and that the aberrant points have been assigned incorrect fluxes. In contrast, we see that the PACS-only galaxies (blue points) have ratios much closer to unity, pointing to an issue in the SPIRE photometry. It is true that some galaxies with *both* PACS and SPIRE data (red points) also have very large ratios, and it remains to be seen if the offset is driven by the (poorer?) SPIRE data.

Another trend in Figure 4.28 involves galaxies with only MIPS 24 μm data (black points). At low redshift, their $L_{\rm IR}$ ratios are close to unity, but they gradually increase with redshift, reaching $\sim$ 0.5 dex at $z \sim 2$. This effect is a manifestation of the systematic bias introduced when fitting observed-frame 24 μm data to locally calibrated IR templates (Papovich et al., 2007; Nordon et al., 2010; Elbaz et al., 2011; Murphy et al., 2011a; Rujopakarn et al., 2011; Nordon et al., 2012). That is, $L_{\rm IR}$ will be overestimated in galaxies above $z \sim 1.5$, where observed 24 μm probes PAH emission (rest-frame 8$-$12 μm; Tielens, 2008).

As proposed by Rujopakarn et al. (2013, hereafter R13), this bias is due to a systematic increase in the observed PAH emission strength relative to $L_{\rm IR}$ with redshift, which is not accounted for when local templates are used as-is to fit high-redshift galaxies. Physically, this is because star formation (and IR emission) in high-redshift objects is spatially more extended than in the local galaxies used to calibrate the IR templates (Rujopakarn et al., 2011), where star formation occurs in compact, heavily obscured regions (nuclear starbursts, mergers, etc). This increases the exposed surface area of the photodissociation regions from which PAH emission originates. Hence, for a given measured PAH luminosity in a high-redshift galaxy, fitting local IR templates will return a value of $L_{\rm IR}$ that is systematically too high. This is what is seen in Figure 4.28.

To account for this effect, the R13 method rescales the local IR templates to correct for the redshift evolution in the SED shape. This conversion produces $L_{\rm IR}$ values in reasonable agreement (0.13 dex scatter) with those based on direct FIR measurements from *Herschel* (R13). Hence we use the R13-derived $L_{\rm IR}$ in the calculation of UV+IR SFRs below, in order to reduce systematics in $L_{\rm IR}$ and maximize the number of galaxies with $L_{\rm IR}$ estimates, since more objects have MIPS data.

4.9.2 Comparing $\mathrm{SSFR_{UV,corr}}$ and $\mathrm{SSFR_{UV+IR}}$

We now investigate the extent to which $\mathrm{SSFR_{UV,corr}}$ is a reliable indicator of star-formation activity by comparing it with SSFRs derived from a combination of (unobscured) UV and IR emission, $\mathrm{SSFR_{UV+IR}}$. This hybrid approach has become popular in galaxy studies with the increasing availability of FIR data (e.g., Bell et al., 2005; Wuyts et al., 2011a). It is nominally a more faithful measure of star formation than $\mathrm{SSFR_{UV,corr}}$, since it incorporates a *direct* measure of obscured star formation, rather than relying on a (possibly inaccurate) dust correction to recover the obscured UV luminosity. Hence it serves as an *independent* check of $\mathrm{SSFR_{UV,corr}}$.

We use the formula presented in Wuyts et al. (2011a) to calculate the UV+IR SFR:

$$\mathrm{SFR_{UV+IR}}\ [M_\odot\,\mathrm{yr}^{-1}] = 1.09\times10^{-10}\,(L_{\mathrm{IR}} + 3.3L_{\mathrm{NUV}})\ [L_\odot], \tag{4.4}$$

where L_{IR} is the integrated $8-1000\,\mu$m luminosity, and $L_{\mathrm{NUV}} \equiv \nu L_\nu(2800\,\text{Å})$ is the rest-frame near-UV luminosity, measured at 2800 Å. Note that the effective coefficient in front of the UV term in Equation 4.4 is 3.60×10^{-10}, whereas our adopted conversion factor (Equation 4.1) to compute $\mathrm{SSFR_{UV,corr}}$ is 2.59×10^{-10}, which is $\approx 25\%$ smaller. This translates to a 0.1 dex offset between the two rates, which is insignificant compared to the scatter in $\mathrm{SSFR_{UV+IR}}$. Because we use the R13 method to derive L_{IR}, we label the rates as $\mathrm{SSFR_{UV+IR}}$ (R13).

Figure 4.29 compares $\mathrm{SSFR_{UV+IR}}$ (R13) with $\mathrm{SSFR_{UV,corr}}$, in our usual mass and redshift bins. The two SSFRs agree quite well in nearly all the bins. However, a systematic offset is seen in all the panels, increasing toward higher redshift. In particular, galaxies with lower $\mathrm{SSFR_{UV,corr}}$ tend to lie in a plume above the one-to-one line, producing a flatter distribution of points. One possible cause of this offset is that, for galaxies with lower SSFR, more of the IR emission may be powered by dust in the diffuse ISM that is heated by older, cooler stars (Salim et al., 2009). At $z \sim 2$, where the observed $24\,\mu$m flux is dominated by PAH features, this effect is compounded by the fact that PAH molecules can also be excited by cooler stars in the diffuse ISM (Li & Draine, 2002; Calzetti et al., 2007).

Nevertheless, the overall agreement between the two SSFRs leads us to conclude that $\mathrm{SSFR_{UV,corr}}$ is a valid measure of star formation activity, and that the R13 method is a good method to convert $24\,\mu$m flux to L_{IR}. These results are also encouraging because they demonstrate that dust-corrected, UV-based SFRs can give results comparable to those that combine UV and IR data (see also, e.g., Wuyts et al., 2011a; Rodighiero et al., 2014). Moreover, because IR data exist for only a small fraction of our total sample, we are able to maximize our sample size by using $\mathrm{SSFR_{UV,corr}}$.

Finally, we show in Figure 4.30 the UVJ diagram, with points color-coded by $\mathrm{SSFR_{UV+IR}}$ (R13). Gray points indicate galaxies excluded because they lack a

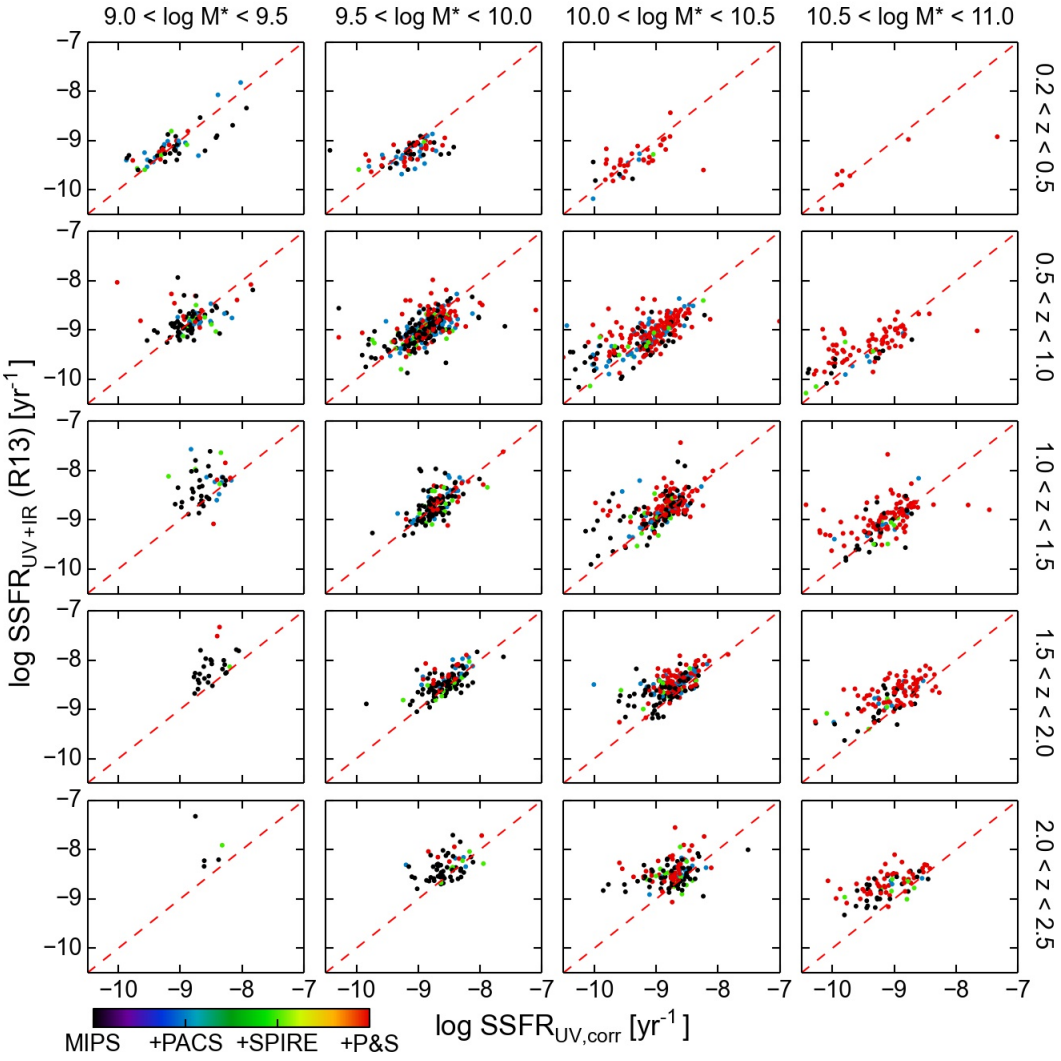

Figure 4.29: $\mathrm{SSFR_{UV+IR}}$ (R13) is compared with $\mathrm{SSFR_{UV,corr}}$ in bins of redshift and stellar mass. Points are color-coded by the IR photometry used to determine L_{IR}. The one-to-one relation is indicated in each panel by the red dashed lines. The overall agreement between $\mathrm{SSFR_{UV+IR}}$ (R13) and $\mathrm{SSFR_{UV,corr}}$ bolsters our claim that $\mathrm{SSFR_{UV,corr}}$ is a reliable measure of star-formation activity for normal star-forming galaxies.

robust MIPS detection. The lack of objects with good IR data is most pronounced at low masses, but the situation is better at higher masses. Most importantly, the gradient in SSFR along $(U-V)'$ is still seen, even when using $\mathrm{SSFR}_{\mathrm{UV+IR}}$ (R13), which confirms our earlier result using $\mathrm{SSFR}_{\mathrm{UV,corr}}$, indicating that the gradient is a real phenomenon, not just an artifact of SED modeling.

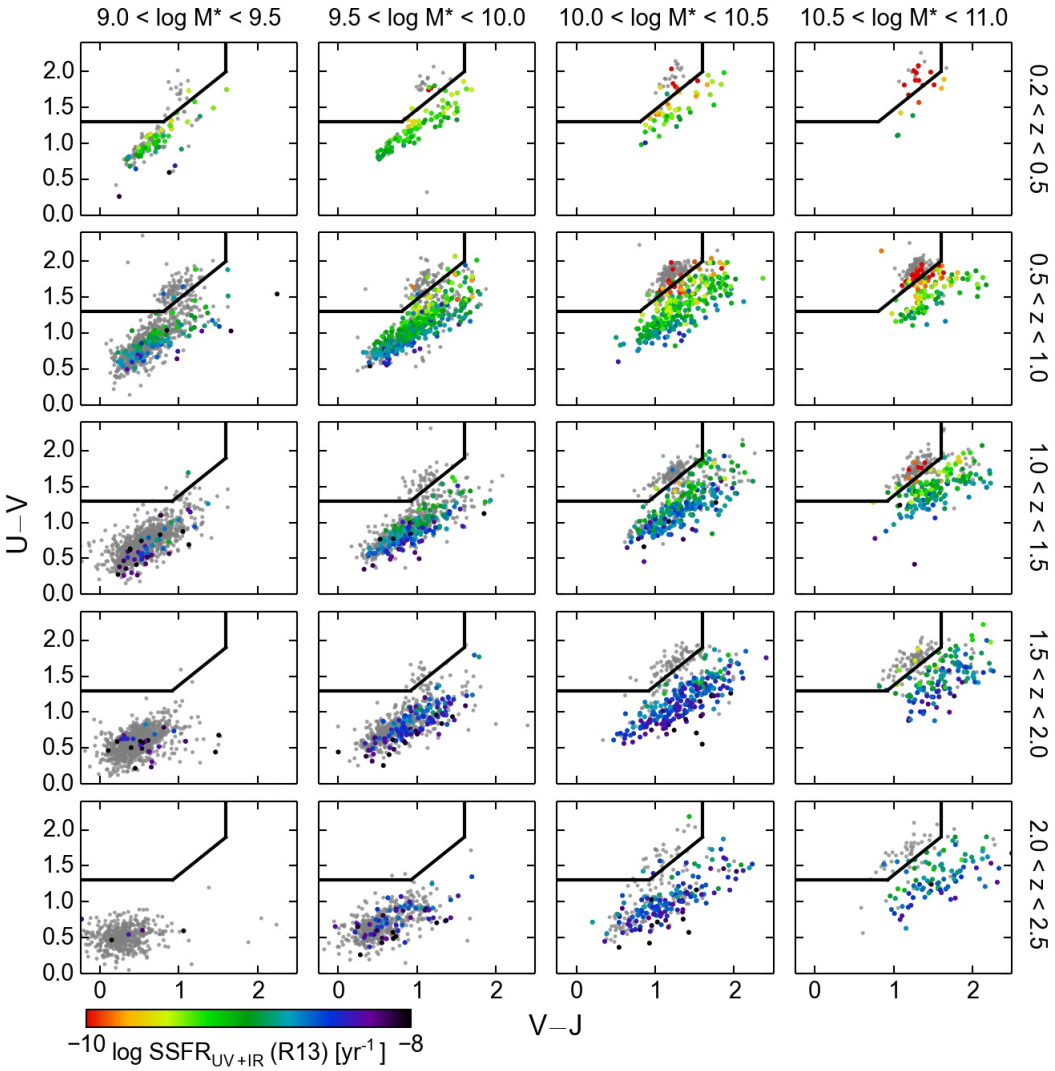

Figure 4.30: Rest-frame UVJ diagram, divided into narrow stellar mass and redshift bins, as indicated in the figure. Points are color-coded by $\mathrm{SSFR}_{\mathrm{UV+IR}}$ (R13). Gray points represent galaxies without a secure MIPS detection. Despite the reduced sample size, a clear gradient in SSFR is still seen in all panels, in agreement with the results of Figure 4.5, which uses dust-corrected, UV-based SSFR.

Bibliography

Abazajian, K. N., et al. 2009, ApJS, 182, 543

Agüeros, M. A., et al. 2005, AJ, 130, 1022

Allgood, B., Flores, R. A., Primack, J. R., Kravtsov, A. V., Wechsler, R. H., Faltenbacher, A., & Bullock, J. S. 2006, MNRAS, 367, 1781

Ammons, S. M., et al. 2011, ApJ, 740, 3

Arnouts, S., et al. 2013, A&A, 558, A67

Barro, G., et al. 2011, ApJS, 193, 13

—. 2013, ApJ, 765, 104

—. 2014, ApJ, 791, 52

Behroozi, P. S., Wechsler, R. H., & Conroy, C. 2013, ApJ, 770, 57

Bell, E. F. 2008, ApJ, 682, 355

Bell, E. F., & de Jong, R. S. 2001, ApJ, 550, 212

Bell, E. F., et al. 2004, ApJ, 608, 752

—. 2005, ApJ, 625, 23

—. 2012, ApJ, 753, 167

Bertin, E., & Arnouts, S. 1996, A&AS, 117, 393

Bett, P., Eke, V., Frenk, C. S., Jenkins, A., Helly, J., & Navarro, J. 2007, MNRAS, 376, 215

Bezanson, R., van Dokkum, P. G., van de Sande, J., Franx, M., Leja, J., & Kriek, M. 2013, ApJL, 779, L21

Binette, L., Magris, C. G., Stasińska, G., & Bruzual, A. G. 1994, A&A, 292, 13

Binney, J., & Merrifield, M. 1998, Galactic Astronomy (Princeton University Press)

Birnboim, Y., & Dekel, A. 2003, MNRAS, 345, 349

Blanton, M. R., & Moustakas, J. 2009, ARA&A, 47, 159

Blanton, M. R., & Roweis, S. 2007, AJ, 133, 734

Blumenthal, G. R., Faber, S. M., Primack, J. R., & Rees, M. J. 1984, Nature, 311, 517

Boissier, S., et al. 2008, ApJ, 681, 244

Bonamigo, M., Despali, G., Limousin, M., Angulo, R., Giocoli, C., & Soucail, G. 2015, MNRAS, 449, 3171

Bouché, N., et al. 2010, ApJ, 718, 1001

Brammer, G. B., van Dokkum, P. G., & Coppi, P. 2008, ApJ, 686, 1503

Brammer, G. B., et al. 2009, ApJL, 706, L173

—. 2011, ApJ, 739, 24

Brinchmann, J., Charlot, S., White, S. D. M., Tremonti, C., Kauffmann, G., Heckman, T., & Brinkmann, J. 2004, MNRAS, 351, 1151

Bruzual, G., & Charlot, S. 2003, MNRAS, 344, 1000

Bullock, J. S. 2002, in The Shapes of Galaxies and their Dark Halos, ed. P. Natarajan, 109–113

Burstein, D., Haynes, M. P., & Faber, M. 1991, Nature, 353, 515

Cacciato, M., Dekel, A., & Genel, S. 2012, MNRAS, 421, 818

Calzetti, D., Armus, L., Bohlin, R. C., Kinney, A. L., Koornneef, J., & Storchi-Bergmann, T. 2000, ApJ, 533, 682

Calzetti, D., Kinney, A. L., & Storchi-Bergmann, T. 1994, ApJ, 429, 582

Calzetti, D., et al. 2007, ApJ, 666, 870

Cappellari, M., et al. 2006, MNRAS, 366, 1126

—. 2012, Nature, 484, 485

Catinella, B., et al. 2010, MNRAS, 403, 683

Cattaneo, A., Dekel, A., Faber, S. M., & Guiderdoni, B. 2008, MNRAS, 389, 567

Ceverino, D., Dekel, A., & Bournaud, F. 2010, MNRAS, 404, 2151

Ceverino, D., Primack, J., & Dekel, A. 2015, ArXiv e-prints

Chang, Y.-Y., et al. 2013, ApJ, 773, 149

Charlot, S., & Fall, S. M. 2000, ApJ, 539, 718

Chary, R., & Elbaz, D. 2001, ApJ, 556, 562

Cheung, E., et al. 2012, ApJ, 760, 131

Code, A. D. 1969, PASP, 81, 475

Conroy, C., & van Dokkum, P. G. 2012, ApJ, 760, 71

Cortese, L., & Hughes, T. M. 2009, MNRAS, 400, 1225

Cowie, L. L., Songaila, A., Hu, E. M., & Cohen, J. G. 1996, AJ, 112, 839

Cox, T. J., Jonsson, P., Somerville, R. S., Primack, J. R., & Dekel, A. 2008, MNRAS, 384, 386

Croton, D. J., et al. 2006, MNRAS, 365, 11

Daddi, E., et al. 2007, ApJ, 670, 156

Dahlen, T., et al. 2013, ApJ, 775, 93

Dale, D. A., & Helou, G. 2002, ApJ, 576, 159

Davis, M., et al. 2007, ApJL, 660, L1

de Zeeuw, P. T., et al. 2002, MNRAS, 329, 513

Dekel, A., & Birnboim, Y. 2006, MNRAS, 368, 2

Dekel, A., & Mandelker, N. 2014, MNRAS, 444, 2071

Dekel, A., Sari, R., & Ceverino, D. 2009, ApJ, 703, 785

Dekel, A., & Silk, J. 1986, ApJ, 303, 39

Dekel, A., Zolotov, A., Tweed, D., Cacciato, M., Ceverino, D., & Primack, J. R. 2013, MNRAS, 435, 999

del Río, M. S., Brinks, E., & Cepa, J. 2004, AJ, 128, 89

Di Matteo, T., Springel, V., & Hernquist, L. 2005, Nature, 433, 604

Donas, J., et al. 2007, ApJS, 173, 597

Dressler, A., & Gunn, J. E. 1983, ApJ, 270, 7

Driver, S. P., et al. 2006, MNRAS, 368, 414

Dutton, A. A., et al. 2011, MNRAS, 410, 1660

Elbaz, D., et al. 2011, A&A, 533, A119

Emsellem, E., et al. 2007, MNRAS, 379, 401

Faber, S. M., et al. 2007, ApJ, 665, 265

Fabian, A. C. 2012, ARA&A, 50, 455

Fang, J. J., Faber, S. M., Koo, D. C., & Dekel, A. 2013, ApJ, 776, 63

Fang, J. J., Faber, S. M., Salim, S., Graves, G. J., & Rich, R. M. 2012, ApJ, 761, 23

Filippenko, A. V. 2003, in Astronomical Society of the Pacific Conference Series, Vol. 290, Active Galactic Nuclei: From Central Engine to Host Galaxy, ed. S. Collin, F. Combes, & I. Shlosman, 369

Finkelman, I., Moiseev, A., Brosch, N., & Katkov, I. 2011, MNRAS, 418, 1834

Fontana, A., et al. 2009, A&A, 501, 15

Forbes, J., Krumholz, M., & Burkert, A. 2012, ApJ, 754, 48

Franx, M., van Dokkum, P. G., Schreiber, N. M. F., Wuyts, S., Labbé, I., & Toft, S. 2008, ApJ, 688, 770

Galametz, A., et al. 2013, ApJS, 206, 10

Galaz, G., Dalcanton, J. J., Infante, L., & Treister, E. 2002, AJ, 124, 1360

Galaz, G., Herrera-Camus, R., Garcia-Lambas, D., & Padilla, N. 2011, ApJ, 728, 74

Genzel, R., et al. 2015, ApJ, 800, 20

Giavalisco, M., et al. 2004, ApJL, 600, L93

Gil de Paz, A., et al. 2007, ApJS, 173, 185

Goto, T. 2005, MNRAS, 357, 937

Goudfrooij, P., Hansen, L., Jorgensen, H. E., & Norgaard-Nielsen, H. U. 1994, A&AS, 105, 341

Graves, G. J., & Faber, S. M. 2010, ApJ, 717, 803

Graves, G. J., Faber, S. M., & Schiavon, R. P. 2009a, ApJ, 693, 486

—. 2009b, ApJ, 698, 1590

—. 2010, ApJ, 721, 278

Graves, G. J., Faber, S. M., Schiavon, R. P., & Yan, R. 2007, ApJ, 671, 243

Graves, G. J., & Schiavon, R. P. 2008, ApJS, 177, 446

Grogin, N. A., et al. 2011, ApJS, 197, 35

Gültekin, K., et al. 2009, ApJ, 698, 198

Guo, Y., et al. 2013, ApJS, 207, 24

—. 2015, ApJ, 800, 39

Hao, C.-N., Kennicutt, R. C., Johnson, B. D., Calzetti, D., Dale, D. A., & Moustakas, J. 2011, ApJ, 741, 124

Heckman, T. M. 1980, A&A, 87, 152

Henry, A., Martin, C. L., Finlator, K., & Dressler, A. 2013a, ApJ, 769, 148

Henry, A., et al. 2013b, ApJL, 776, L27

Hernquist, L., & Mihos, J. C. 1995, ApJ, 448, 41

Holden, B. P., van der Wel, A., Rix, H.-W., & Franx, M. 2012, ApJ, 749, 96

Hopkins, P. F., Hernquist, L., Cox, T. J., Di Matteo, T., Robertson, B., & Springel, V. 2006, ApJS, 163, 1

Hopkins, P. F., Hernquist, L., Cox, T. J., & Kereš, D. 2008, ApJS, 175, 356

Hopkins, P. F., et al. 2010, ApJ, 724, 915

Ilbert, O., et al. 2010, ApJ, 709, 644

Impey, C., & Bothun, G. 1997, ARA&A, 35, 267

Jing, Y. P., & Suto, Y. 2002, ApJ, 574, 538

Kassin, S. A., et al. 2012, ApJ, 758, 106

Kauffmann, G., Heckman, T. M., De Lucia, G., Brinchmann, J., Charlot, S., Tremonti, C., White, S. D. M., & Brinkmann, J. 2006, MNRAS, 367, 1394

Kauffmann, G., et al. 2003a, MNRAS, 341, 33

—. 2003b, MNRAS, 341, 54

—. 2007, ApJS, 173, 357

Kaviraj, S., Peirani, S., Khochfar, S., Silk, J., & Kay, S. 2009, MNRAS, 394, 1713

Kaviraj, S., et al. 2007, ApJS, 173, 619

Kennicutt, R. C., & Evans, N. J. 2012, ARA&A, 50, 531

Kennicutt, Jr., R. C. 1998, ARA&A, 36, 189

Kennicutt, Jr., R. C., et al. 2009, ApJ, 703, 1672

Kereš, D., & Hernquist, L. 2009, ApJL, 700, L1

Kereš, D., Katz, N., Weinberg, D. H., & Davé, R. 2005, MNRAS, 363, 2

Koekemoer, A. M., et al. 2011, ApJS, 197, 36

Kormendy, J., & Kennicutt, Jr., R. C. 2004, ARA&A, 42, 603

Krumholz, M. R., McKee, C. F., & Tumlinson, J. 2009, ApJ, 699, 850

Kuntschner, H., et al. 2010, MNRAS, 408, 97

La Barbera, F., Ferreras, I., Vazdekis, A., de la Rosa, I. G., de Carvalho, R. R., Trevisan, M., Falcón-Barroso, J., & Ricciardelli, E. 2013, MNRAS, 433, 3017

Lahav, O., Lilje, P. B., Primack, J. R., & Rees, M. J. 1991, MNRAS, 251, 128

Laidler, V. G., et al. 2007, PASP, 119, 1325

Lawrence, A., et al. 2007, MNRAS, 379, 1599

Lemonias, J. J., et al. 2011, ApJ, 733, 74

Li, A., & Draine, B. T. 2002, ApJ, 572, 232

Li, C., Wang, L., & Jing, Y. P. 2013, ApJL, 762, L7

Lilly, S. J., Carollo, C. M., Pipino, A., Renzini, A., & Peng, Y. 2013, ApJ, 772, 119

Liu, G., et al. 2013, ApJL, 778, L41

Lotz, J. M., Jonsson, P., Cox, T. J., Croton, D., Primack, J. R., Somerville, R. S., & Stewart, K. 2011, ApJ, 742, 103

Lu, Y., Mo, H. J., & Wechsler, R. H. 2015, MNRAS, 446, 1907

Madau, P., & Dickinson, M. 2014, ARA&A, 52, 415

Madau, P., Pozzetti, L., & Dickinson, M. 1998, ApJ, 498, 106

Magdis, G. E., et al. 2012, ApJ, 760, 6

Magnelli, B., et al. 2013, A&A, 553, A132

Mandelker, N., Dekel, A., Ceverino, D., Tweed, D., Moody, C. E., & Primack, J. 2014, MNRAS, 443, 3675

Mannucci, F., Cresci, G., Maiolino, R., Marconi, A., & Gnerucci, A. 2010, MNRAS, 408, 2115

Marchesini, D., van Dokkum, P. G., Förster Schreiber, N. M., Franx, M., Labbé, I., & Wuyts, S. 2009, ApJ, 701, 1765

Marino, A., Bianchi, L., Rampazzo, R., Thilker, D. A., Annibali, F., Bressan, A., & Buson, L. M. 2011, ApJ, 736, 154

Martig, M., Bournaud, F., Teyssier, R., & Dekel, A. 2009, ApJ, 707, 250

Martin, D. C., et al. 2005, ApJL, 619, L1

—. 2007, ApJS, 173, 342

McBride, J., Fakhouri, O., & Ma, C.-P. 2009, MNRAS, 398, 1858

Mendel, J. T., Simard, L., Ellison, S. L., & Patton, D. R. 2013, MNRAS, 429, 2212

Mihos, J. C., & Hernquist, L. 1994, ApJL, 437, L47

Mo, H. J., Mao, S., & White, S. D. M. 1998, MNRAS, 295, 319

Moffett, A. J., Kannappan, S. J., Baker, A. J., & Laine, S. 2012, ApJ, 745, 34

Morganti, R., et al. 2006, MNRAS, 371, 157

Morris, A. M., et al. 2015, AJ, 149, 178

Moster, B. P., Naab, T., & White, S. D. M. 2013, MNRAS, 428, 3121

Moustakas, J., et al. 2013, ApJ, 767, 50

Mullaney, J. R., et al. 2012, MNRAS, 419, 95

Murphy, E. J., Chary, R.-R., Dickinson, M., Pope, A., Frayer, D. T., & Lin, L. 2011a, ApJ, 732, 126

Murphy, E. J., et al. 2011b, ApJ, 737, 67

Muzzin, A., et al. 2013, ApJ, 777, 18

Noeske, K. G., et al. 2007, ApJL, 660, L47

Noordermeer, E., van der Hulst, J. M., Sancisi, R., Swaters, R. A., & van Albada, T. S. 2005, A&A, 442, 137

Nordon, R., et al. 2010, A&A, 518, L24

—. 2012, ApJ, 745, 182

O'Connell, R. W. 1999, ARA&A, 37, 603

Oke, J. B. 1974, ApJS, 27, 21

Pahre, M. A., Ashby, M. L. N., Fazio, G. G., & Willner, S. P. 2004, ApJS, 154, 235

Papovich, C., et al. 2007, ApJ, 668, 45

—. 2015, ApJ, 803, 26

Patel, S. G., Holden, B. P., Kelson, D. D., Franx, M., van der Wel, A., & Illingworth, G. D. 2012, ApJL, 748, L27

Patel, S. G., Kelson, D. D., Holden, B. P., Franx, M., & Illingworth, G. D. 2011, ApJ, 735, 53

Patel, S. G., et al. 2013, ApJ, 778, 115

Peirani, S., Crockett, R. M., Geen, S., Khochfar, S., Kaviraj, S., & Silk, J. 2010, MNRAS, 405, 2327

Peng, C. Y., Ho, L. C., Impey, C. D., & Rix, H.-W. 2002, AJ, 124, 266

Peng, Y.-j., et al. 2010, ApJ, 721, 193

Pérez-González, P. G., Trujillo, I., Barro, G., Gallego, J., Zamorano, J., & Conselice, C. J. 2008a, ApJ, 687, 50

Pérez-González, P. G., et al. 2005, ApJ, 630, 82

—. 2008b, ApJ, 675, 234

—. 2010, A&A, 518, L15

Perlmutter, S., et al. 1999, ApJ, 517, 565

Quintero, A. D., et al. 2004, ApJ, 602, 190

Rampazzo, R., et al. 2007, MNRAS, 381, 245

Reddy, N. A., Pettini, M., Steidel, C. C., Shapley, A. E., Erb, D. K., & Law, D. R. 2012, ApJ, 754, 25

Reddy, N. A., et al. 2015, ArXiv e-prints

Rees, M. J., & Ostriker, J. P. 1977, MNRAS, 179, 541

Rich, R. M., et al. 2005, ApJL, 619, L107

Rieke, G. H., Alonso-Herrero, A., Weiner, B. J., Pérez-González, P. G., Blaylock, M., Donley, J. L., & Marcillac, D. 2009, ApJ, 692, 556

Riess, A. G., et al. 1998, AJ, 116, 1009

Rocha, M., Jonsson, P., Primack, J. R., & Cox, T. J. 2008, MNRAS, 383, 1281

Rodighiero, G., et al. 2014, MNRAS, 443, 19

Rujopakarn, W., Rieke, G. H., Eisenstein, D. J., & Juneau, S. 2011, ApJ, 726, 93

Rujopakarn, W., Rieke, G. H., Weiner, B. J., Pérez-González, P., Rex, M., Walth, G. L., & Kartaltepe, J. S. 2013, ApJ, 767, 73

Safarzadeh, M., Ferguson, H. C., Lu, Y., Inami, H., & Somerville, R. S. 2015, ApJ, 798, 91

Saintonge, A., et al. 2011, MNRAS, 415, 32

Salim, S., Fang, J. J., Rich, R. M., Faber, S. M., & Thilker, D. A. 2012, ApJ, 755, 105

Salim, S., & Rich, R. M. 2010, ApJL, 714, L290

Salim, S., et al. 2007, ApJS, 173, 267

—. 2009, ApJ, 700, 161

Santini, P., et al. 2015, ApJ, 801, 97

Sarzi, M., et al. 2010, MNRAS, 402, 2187

Schawinski, K., Thomas, D., Sarzi, M., Maraston, C., Kaviraj, S., Joo, S.-J., Yi, S. K., & Silk, J. 2007, MNRAS, 382, 1415

Schechter, P. 1976, ApJ, 203, 297

Schiavon, R. P. 2007, ApJS, 171, 146

Schiminovich, D., et al. 2007, ApJS, 173, 315

Seibert, M., et al. 2005, ApJL, 619, L23

Sersic, J. L. 1968, Atlas de galaxias australes

Shapiro, K. L., et al. 2010, MNRAS, 402, 2140

Shen, S., Mo, H. J., White, S. D. M., Blanton, M. R., Kauffmann, G., Voges, W., Brinkmann, J., & Csabai, I. 2003, MNRAS, 343, 978

Silk, J. 1977, ApJ, 211, 638

Silk, J., & Mamon, G. A. 2012, RAA, 12, 917

Snyder, G. F., Cox, T. J., Hayward, C. C., Hernquist, L., & Jonsson, P. 2011, ApJ, 741, 77

Somerville, R. S., & Davé, R. 2014, ArXiv e-prints

Somerville, R. S., Hopkins, P. F., Cox, T. J., Robertson, B. E., & Hernquist, L. 2008, MNRAS, 391, 481

Stoughton, C., et al. 2002, AJ, 123, 485

Strateva, I., et al. 2001, AJ, 122, 1861

Strauss, M. A., et al. 2002, AJ, 124, 1810

Szomoru, D., Franx, M., van Dokkum, P. G., Trenti, M., Illingworth, G. D., Labbé, I., & Oesch, P. 2013, ApJ, 763, 73

Tacchella, S., et al. 2015, Science, 348, 314

Tacconi, L. J., et al. 2013, ApJ, 768, 74

Tal, T., et al. 2014, ApJ, 789, 164

Taylor, E. N., et al. 2011, MNRAS, 418, 1587

Thilker, D. A., et al. 2005, ApJL, 619, L79

—. 2007, ApJS, 173, 538

—. 2010, ApJL, 714, L171

Thomas, D., Maraston, C., Bender, R., & Mendes de Oliveira, C. 2005, ApJ, 621, 673

Thomas, D., Maraston, C., Schawinski, K., Sarzi, M., & Silk, J. 2010, MNRAS, 404, 1775

Tielens, A. G. G. M. 2008, ARA&A, 46, 289

Toomre, A., & Toomre, J. 1972, ApJ, 178, 623

Trager, S. C., Faber, S. M., Worthey, G., & González, J. J. 2000, AJ, 119, 1645

Tremaine, S., et al. 2002, ApJ, 574, 740

Tremonti, C. A., et al. 2004, ApJ, 613, 898

Trujillo, I., et al. 2006, ApJ, 650, 18

Trump, J. R., Hsu, A. D., Fang, J. J., Faber, S. M., Koo, D. C., & Kocevski, D. D. 2013, ApJ, 763, 133

van de Sande, J., Kriek, M., Franx, M., Bezanson, R., & van Dokkum, P. G. 2014, ApJL, 793, L31

van der Wel, A., et al. 2012, ApJS, 203, 24

—. 2014a, ApJ, 788, 28

—. 2014b, ApJL, 792, L6

van Dokkum, P. G., et al. 2010, ApJ, 709, 1018

van Driel, W., & van Woerden, H. 1991, A&A, 243, 71

Wake, D. A., Franx, M., & van Dokkum, P. G. 2012a, ArXiv e-prints

Wake, D. A., van Dokkum, P. G., & Franx, M. 2012b, ApJL, 751, L44

Wang, J., et al. 2011, MNRAS, 412, 1081

Wechsler, R. H., Bullock, J. S., Primack, J. R., Kravtsov, A. V., & Dekel, A. 2002, ApJ, 568, 52

Whitaker, K. E., Kriek, M., van Dokkum, P. G., Bezanson, R., Brammer, G., Franx, M., & Labbé, I. 2012, ApJ, 745, 179

Whitaker, K. E., et al. 2014, ApJ, 795, 104

White, S. D. M., & Frenk, C. S. 1991, ApJ, 379, 52

White, S. D. M., & Rees, M. J. 1978, MNRAS, 183, 341

Wild, V., Charlot, S., Brinchmann, J., Heckman, T., Vince, O., Pacifici, C., & Chevallard, J. 2011, MNRAS, 417, 1760

Williams, C. C., et al. 2014, ApJ, 780, 1

Williams, R. J., Quadri, R. F., Franx, M., van Dokkum, P., & Labbé, I. 2009, ApJ, 691, 1879

Williams, R. J., Quadri, R. F., Franx, M., van Dokkum, P., Toft, S., Kriek, M., & Labbé, I. 2010, ApJ, 713, 738

Witt, A. N., & Gordon, K. D. 2000, ApJ, 528, 799

Wong, O. I., et al. 2012, MNRAS, 420, 1684

Woo, J., Dekel, A., Faber, S. M., & Koo, D. C. 2015, MNRAS, 448, 237

Woo, J., et al. 2013, MNRAS, 428, 3306

Wuyts, S., Labbé, I., Schreiber, N. M. F., Franx, M., Rudnick, G., Brammer, G. B., & van Dokkum, P. G. 2008, ApJ, 682, 985

Wuyts, S., et al. 2007, ApJ, 655, 51

—. 2011a, ApJ, 742, 96

—. 2011b, ApJ, 742, 96

—. 2012, ApJ, 753, 114

Wyder, T. K., et al. 2009, ApJ, 696, 1834

Yan, R., & Blanton, M. R. 2012, ApJ, 747, 61

Yan, R., Newman, J. A., Faber, S. M., Konidaris, N., Koo, D., & Davis, M. 2006, ApJ, 648, 281

Yang, X., Mo, H. J., van den Bosch, F. C., Zhang, Y., & Han, J. 2012, ApJ, 752, 41

Yesuf, H. M., Faber, S. M., Trump, J. R., Koo, D. C., Fang, J. J., Liu, F. S., Wild, V., & Hayward, C. C. 2014, ApJ, 792, 84

Yi, S. K., et al. 2005, ApJL, 619, L111

York, D. G., et al. 2000, AJ, 120, 1579

Zahid, H. J., Kewley, L. J., & Bresolin, F. 2011, ApJ, 730, 137

Zhong, G. H., Liang, Y. C., Hammer, F., Chen, X. Y., Deng, L. C., & Flores, H. 2010, A&A, 520, A69

Zhong, G. H., Liang, Y. C., Liu, F. S., Hammer, F., Hu, J. Y., Chen, X. Y., Deng, L. C., & Zhang, B. 2008, MNRAS, 391, 986